

中国科学技术大学

博士学位论文



基于 ATLAS 探测器上 ZZ 玻色子到全轻子 衰变道的事例对电弱对称性破缺过程的研 究

作者姓名： 祝鹤龄
学科专业： 粒子与原子核物理
导师姓名： 赵政国 马宏
完成时间： 二〇二〇年九月二十七日

University of Science and Technology of China
A dissertation for doctor's degree



**Studies of Electroweak Symmetry
Breaking in ZZ Production in Purely
Leptonic Decay with ATLAS Detector**

Author: Heling Zhu

Speciality: Particle and Nuclear Physics

Supervisors: Zhengguo Zhao, Hong Ma

Finished time: September 27, 2020

摘要

论文介绍了本人在粒子物理领域基于大型强子对撞机 (LHC) 上 ATLAS 实验做的研究工作。大型强子对撞机是当今世界上最大的、能量最高的对撞机，是建立在理论和实验之间的重要桥梁。而 ATLAS 实验是 LHC 上的一个通用粒子探测器实验，同时也是体积最大的探测器。基于 ATLAS 实验在 LHC 上收集到的亮度为 139 fb^{-1} 能量为 13 TeV 的质子-质子对撞数据，本文重点介绍了两个 Z 玻色子衰变到四轻子末态过程的一系列研究。包括，标准模型 (SM) 下 ZZ 到四轻子过程截面的测量、矢量玻色子散射 (VBS) 过程在 ZZ 到四轻子末态的观测，和寻找重共振态衰变到 ZZ 到四轻子末态的过程。

ZZ 到四轻子过程截面的测量结果为 $\sigma_{ZZjj}^{tot} = 1.27 \pm 0.12(\text{stat}) \pm 0.02(\text{theo}) \pm 0.07(\text{exp}) \pm 0.01(\text{bkg}) \pm 0.03(\text{lumi})$ ，总体相对误差为 11%。在误差范围内，该结果和标准模型预言值 $1.14 \pm 0.04(\text{stat}) \pm 0.20(\text{theo})$ 相吻合。同时，在两个 Z 玻色子伴随着两个喷注 (jets) 末态的电弱相互作用过程的寻找中，我们观测到偏离本底假说超过 5 倍标准差 (5.5σ) 的明显偏差。在此基础上，本文也介绍了对于下一代高亮度大型强子对撞机 (HL-LHC) 在两个 Z 玻色子伴随着两个喷注 (jets) 末态的电弱相互作用过程的模拟预言。

另一方面，本文介绍了在一对 Z 玻色子衰变至四轻子末态过程中寻找重共振态的实验。根据不同的信号模型，寻找的粒子质量区间设置在 200 GeV 到 2000 GeV 之间。基于该测量结果，没有证据可以证明重共振态的存在。因此，研究给出了基于不同信号模型的截面上限，包括在不同衰变宽度假说下自旋为 0 的共振态，以及基于 Randall–Sundrum 模型的自旋为 2 的引力子 (graviton)。在该分析中，我们认为，信号主要可通过 gluon-gluon Fusion (ggF) 和 Vector Boson Fusion (VBF) 过程产生。在自旋为 0 的窄衰变宽度模型下，我们对 ggF 和 VBF 两个过程都进行了研究。而对于大宽度模型，由于在质量很高的区间分辨率很差以及 VBF 过程的统计量太小等客观原因，只对 ggF 过程进行了研究。对于自旋为 2 的模型，实验给出了 Randall–Sundrum 模型的引力子的理论质量下限，为 1500 GeV 。

28

ABSTRACT

This dissertation presents my research in the field of Particle Physics with the ATLAS experiment at the Large Hadron Collider (LHC). The LHC is the world's largest and most powerful collider, and it was built as a bridge between the theories and the experiment. The ATLAS experiment is a general-purpose particle detector experiment with the largest volume at the LHC. This dissertation focus on the studies with two Z bosons production decaying into $\ell\ell\ell'\ell'$ final state, where ℓ stands for electron or muon, using 139 fb^{-1} of 13 TeV proton-proton (pp) collision data collected by ATLAS experiment at the LHC. The ZZ production in $\ell\ell\ell'\ell'$ channel provides a most clean and sensitive tool to test the Standard Model (SM) at the energy frontier and to study the *Higgs* physics. Studies including the measurement on SM $ZZjj$ production cross section, the observation of Vector Boson Scattering (VBS) process as well as the searches of heavy resonances in ZZ production decaying into $\ell\ell\ell'\ell'$ final state are reported in this dissertation.

The fiducial cross section for SM $ZZjj$ production is measured to be $\sigma_{ZZjj}^{tot} = 1.27 \pm 0.12(\text{stat}) \pm 0.02(\text{theo}) \pm 0.07(\text{exp}) \pm 0.01(\text{bkg}) \pm 0.03(\text{lumi})[\text{pb}]$ with a total relative uncertainty of 11% for the $\ell\ell\ell'\ell'$ final state, and found to be compatible with the SM prediction of $1.14 \pm 0.04(\text{stat}) \pm 0.20(\text{theo})[\text{pb}]$. The electroweak production of two jets in association with a Z -boson pair (EW- $ZZjj$) is observed with a significant deviation from the background-only hypothesis corresponding to a statistical significance of 5.5σ . Following with the observation, the prospect study for the EW- $ZZjj$ production at the High luminosity LHC (HL-LHC) using 3000 fb^{-1} simulated pp collision data at a centre-of-mass energy of 14 TeV is presented, with a expected significance of around 7σ .

A search for heavy resonances decaying into a pair of Z bosons to $\ell\ell\ell'\ell'$ final state is also conducted in this dissertation. Different mass ranges for the hypothetical resonances are considered, depending on the signal models and spanning between 200 GeV and 2000 GeV. Data is found to agree with a background-only hypothesis, thus, the results are interpreted as upper limits on production cross section for sevaral different models, including heavy Higgs like (spin-0) narrow-width approximation (NWA) and large-width approximation (LWA), as well as the Randall–Sundrum model with a graviton excitation spin-2 resonance (RSG). The signal is assumed to generate dominatly via gluon-gluon Fusion (ggF) production mode and Vector Boson Fusion (VBF) production mode. Both ggF and VBF channels are studied in NWA, while for LWA, only ggF channel is studied due to worse resolution in higher mass region and the lack of statistic for VBF process. In

Abstract

- 61 addition, mass of RS Graviton is constrained, $m(G_{KK}) < 1500$ GeV is excluded at 95%
- 62 CL by $ZZ \rightarrow \ell\ell\ell'\ell'$ analysis.

63

64

Acknowledgments

65 First of all, I would like to express my great gratitude to my supervisors Prof. Zhao
66 Zhengguo and Dr. Ma Hong, for their guidance and patience during my Ph.D years. It's
67 Zhengguo, who inspire me with his deep physics insight when I was an undergraduate
68 student and led me enter the field of Particle Physics. I will never forget how I was
69 attracted by his broad knowledge and the amazing picture of particles he showed me,
70 which became the reason I choose the Particle Physics as my major. It's always relaxed
71 and benificial greatly when chating with him, which broads my version, makes me to be
72 more confident and helps me step out of so many difficulties.

73 Thanks to Hong, for giving me the oppotunity to study in Brookhaven National Lab
74 (BNL) that I can work with so many senior and brilliant physicists, and teaching me a lot
75 in the details of physics. As the chair of physics department at BNL, can you imagine
76 that he managed to take time sitting with me every week, teaching me the details and
77 techniques of my analysis as well as helping me to parepre my talks at conference.

78 Thank you both for leading me to the field of physics, showing me how beautiful the
79 science and the world are. And thank you for providing me so many oppotunities and
80 tremendous supports to work at physics frontier and work with people all over the world.
81 It's my greatest honor to be your student. Your strong personalitis will definitely influence
82 my future life and career.

83 I would like to give my large gratitude to Prof. Zhou Bing. It's Bing who introduced
84 me to ATLAS experiment when I was a junior. As a professor and group leader of ATLAS
85 group in University of Michigan with busy schedule, Bing still took time to teach me in
86 physics start from simple formulas and help me to prepare my first academic presentation
87 patiently when I was a undergraduate student. Also it's my great fortune that I can have
88 opportunities to work with you and learn from you in so many analyses during these years.
89 Your kind and patience, your high standard influence me deeply in all these years.

90 Moreover, I really want to give my sincere grattitude to Dr. Xu Lailin. Thank you,
91 Lailin, for all your helps during the passing five years. Thanks for teaching me in all the
92 analysis details, coding techniques, presentation skills hand by hand. You are really a
93 very good and patient teacher and give me as many knowledges as you can. Your broad
94 knowledge, your perseverance in science and your very hard working indeed affect me a
95 lot.

96 In the meantime, I want to give my special thanks to Dr. Li Bing, who helped me

Acknowledgments

97 a lot in several different analyses (low-mass 4μ resonance search, VBSZZ analysis, Z'
98 search), he never hesitated to give his hand to me when I faced difficulties.

99 I would like to express my gratitude to many colleagues in both USTC and BNL team.
100 Thanks to Prof. Sun Yongjie, who is the supervisor of my undergraduate thesis, helped
101 me start my first detector project on MRPC. Also thanks Dr. Liu Zhen who taught me
102 in details in this project, and helped me a lot for my life at BNL too. Thanks to Prof.
103 Peng Haiping, Prof. Zhu Yingchun and Dr. Hu Qipeng for helping me all the details
104 and techniques in HWW analysis when I was a beginner. Thanks to Dr. Dai Tiesheng,
105 I have learnt quite a lot in the project of Monitored Drift Tubes (MDT) when working
106 with you at CERN and also thank you for all the help in regular life since that was my
107 first time to Europe. Thanks to Dr. Chen Hucheng, who is the supervisor of my ATLAS
108 qualification task on LAr Trigger Digitizer Boards (LTDB) and the person lead me into
109 this interesting electronic project. And my appreciation to Dr. Xu Hao, Dr. Chen Kai and
110 Dr. Liu Hongbin who taught me in patience for this project as I was really a freshman on
111 electronics. Thanks to Prof. Yuji Enari and Dr. Georges Aad for the help in LAr software
112 tasks when I moved from BNL to CERN. In the meantime, I would really like to give
113 my gratitude to Dr. Michael Begal, Dr. Marc-Andre Pleier, Dr. Alessandro Tricoli, Dr.
114 George Redlinger, Dr. Viviana Cavalieri, Dr. Gaetano Barone and many senior physicists
115 in BNL omaga group. I have learnt a lot from every chat with you and every seminar you
116 hosted. Also I want to thanks to Prof. Wu Yusheng, Prof. Qian Jianming, Prof. Liu
117 Yanwen, Dr. Ju Xiangyang for teaching me in lots of details in different physics analyses.

118 Moreover, I want to give my thanks to friends I met at USTC, BNL and CERN during
119 my Ph.D years. Thanks to Dr. Yang Qian, Dr. Chu Xiaoxuan, Dr. Tu Biao, Dr. Gao
120 Shanshan, Dr. Liu Feng, Dr. Yuan Guangyuan, and many other friends I met at BNL.
121 Thanks to Prof. Geng Cong, Dr. Li Peilian, Dr. Zhang Liqing, Dr. Guo Yicheng, Dr. Xu
122 Tairan, Dr. Wang Rongkun, Chen Jing, He Fudong, Guo Qianying, Chen Ye, Xu Hao,
123 Wang Tao, Xie Xiangyu, Liu Xiangtian and all friends I met at USTC and CERN. Thank
124 you all my friends! I will always remember all the happiness with you, and best wishes
125 to you in the future!

126 Last but not least, I would give my greatest gratitude to my families. Thanks my
127 parents for giving me all your endless loves and supports in my whole life. My deep
128 appreciation to my three aunts for loving and caring me so much since I was born and
129 help me to accompany with my mother when I was thousands miles far away from home.
130 And my husband, Lin, thank you for your understanding and walk through all difficulties
131 with me in these years especially when we were in a foreign country.

Contents

132	Acknowledgments	IV
134	Chapter 1 Introduction	1
135	Chapter 2 Theory	3
136	2.1 The Standard Model of Particle Physics	3
137	2.1.1 Elementary particles in the Standard Model	3
138	2.1.2 Electroweak theory	4
139	2.1.3 Higgs mechanism and Electroweak symmetry breaking	6
140	2.1.4 Beyond the SM Higgs sector	9
141	2.2 Phenomenology of Large Hadron Collider	10
142	2.2.1 Physics at hadronic collision	11
143	2.2.2 Higgs physics at the LHC	13
144	2.2.3 Diboson physics at the LHC	15
145	Chapter 3 The Large Hadron Collider and the ATLAS Detector	19
146	3.1 The Large Hadron Collider	19
147	3.1.1 Operation history and machine layout	19
148	3.1.2 Luminosity and pile-up	22
149	3.2 ATLAS detector	24
150	3.2.1 Detector overview	24
151	3.2.2 Physics requirement	26
152	3.2.3 Magnet system	26
153	3.2.4 Inner detector	27
154	3.2.5 Calorimeters	30
155	3.2.6 Muon spectrometer	31
156	3.2.7 Trigger system	33
157	Chapter 4 Simulation and Event Reconstruction for the ATLAS Experiment	37
158	4.1 Event simulation	37
159	4.2 Event reconstruction	40
160	4.2.1 Track	40
161	4.2.2 Primary vertex	42
162	4.2.3 Electron	43

Contents

164	4.2.4 Muon	48
165	4.2.5 Jets	52
166	4.2.6 Missing transverse energy	56
167	Chapter 5 Statistical treatment of searching for new particles or processes	59
169	5.1 The likelihood function	59
170	5.2 Test statistic	60
171	5.3 The CLs upper limit	62
172	5.4 Nuisance parameters	63
173	Chapter 6 Studies of SM ZZ production in $\ell\ell\ell'\ell'$ final state using pp collision data collected by ATLAS detector from 2015 to 2018	64
176	6.1 Introduction	64
177	6.2 Data and MC samples	65
178	6.2.1 Data samples	65
179	6.2.2 MC simulations	66
180	6.3 Objects and Event selection	67
181	6.3.1 Objects selection	67
182	6.3.2 Event selection	68
183	6.4 Background estimation	69
184	6.4.1 QCD backgrounds	69
185	6.4.2 Reducible backgrounds	70
186	6.5 Systematics	74
187	6.5.1 Theoretical systematics	74
188	6.5.2 Experimental systematics	76
189	6.6 Measurement of fiducial cross section	79
190	6.6.1 Calculation of C-factor	79
191	6.6.2 Result of fiducial cross section	80
192	6.7 Search for EW- $ZZjj$	80
193	6.7.1 MD discriminant	80
194	6.7.2 Fitting procedure	80
195	6.7.3 Result of fit	82
196	6.8 Prospect study of EW- $ZZjj$ production in HL-LHC	84
197	6.8.1 The ATLAS detector at HL-LHC	85

198	6.8.2 Simulation	85
199	6.8.3 Event selection	85
200	6.8.4 Systematics	86
201	6.8.5 Results	88
202	6.9 Conclusion	91
203	Chapter 7 Search for heavy resonances decaying into a pair of Z bosons in $\ell\ell\ell'\ell'$ final state using pp collision data collected by ATLAS detector from 2015 to 2018	92
206	7.1 Introduction	92
207	7.2 Data and MC samples	93
208	7.2.1 Data samples	93
209	7.2.2 Background MC simulations	93
210	7.2.3 Signal MC simulations	94
211	7.3 Analysis selections	95
212	7.3.1 Objects selection	95
213	7.3.2 Event selection	96
214	7.3.3 Event categorizations	98
215	7.3.4 Signal acceptance	106
216	7.4 Background estimation	107
217	7.4.1 Irreducible backgrounds	108
218	7.4.2 Reducible backgrounds	112
219	7.5 Signal modelling	113
220	7.5.1 Modelling of narrow-width signal	114
221	7.5.2 Modelling of large-width signal	114
222	7.5.3 Modelling of interference	118
223	7.5.4 Modelling of spin-2 RS Graviton signal	122
224	7.6 Systematic uncertainties	123
225	7.6.1 Theoretical uncertainties	124
226	7.6.2 Experimental systematics	126
227	7.7 Results in $\ell\ell\ell'\ell'$ channel	126
228	7.7.1 Statistical procedure	127
229	7.7.2 For to likelihood function under background-only hypothesis for MVA-based analysis	128
231	7.7.3 Interpretations	128
232	7.8 Conclusion	138

Contents

233	Chapter 8 Summary	139
234	Bibliography	142

List of Figures

235	2.1	The elementary particles of the Standard Model.	3
237	2.2	The Feynman diagrams of interactions that form the basis of the standard model.	5
239	2.3	The Higgs potential $V(\phi)$ with $\mu^2 > 0$ (left) and $\mu^2 < 0$ (right).	7
240	2.4	Schematic view of a hadron-hadron collision ^[8]	11
241	2.5	The PDF4LHC15 NLO PDFs at a low scale $\mu^2 = Q^2 = 4\text{GeV}^2$ (left) and at $\mu^2 = Q^2 = 100\text{GeV}^2$ (right) as a function of x.	12
243	2.6	Feynman diagrams of the Higgs production modes: (a) ggF; (b) VBF; (c) VH; (d) ttH.	14
245	2.7	The SM Higgs boson production cross sections for various production modes as a function of the centre-of-mass energy for pp collision.	14
247	2.8	Higgs boson production cross section for various production modes as a function of the Higgs mass for $\sqrt{s} = 13 \text{ TeV}$ (left) and 14 TeV (right) for pp collision.	14
250	2.9	SM Higgs decay channels.	15
251	2.10	Branching ratio of Higgs decays in various channels as a function of Higgs mass ^[14]	16
253	2.11	The tree-level Feynman diagrams of diboson production at the LHC.	16
254	2.12	Total production cross-section presented by ATLAS as a function of centre-of-mass energy \sqrt{s} from 7 to 13 TeV for some selected processes, the diboson measurements are scaled by a factor 0.1 to allow a presentation without overlaps.	17
258	2.13	Feynman diagrams of the vector boson scattering.	17
259	2.14	Feynman diagrams of vertexes involving QGC, TGC and Higgs.	18
260	3.1	Cumulative luminosity as a function of time in years from 2011 to 2018 for ATLAS detector.	20
262	3.2	CERN accelerator complex ^[20]	21
263	3.3	Integrated luminosity in ATLAS.	23
264	3.4	Number of Interactions per Crossing from 2015-2018 in ATLAS.	23
265	3.5	Coordinate system used by the ATLAS experiment at the LHC ^[22]	24
266	3.6	Cut-away view of the ATLAS detector ^[23]	25

List of Figures

267	3.7	Schematic diagram of the ATLAS magnet system.	27
268	3.8	Schematic diagram of the ATLAS inner detector ^[25] .	28
269	3.9	Schematic diagram of the ATLAS 4-Layer Pixel Detector.	28
270	3.10	SCT (a) barrel module and (b) end-cap ^[29] .	29
271	3.11	Cut-away view of the ATLAS calorimeters. The LAr calorimeters are seen 272 inside the scintillator-based tile hadronic calorimeters ^[31] .	30
273	3.12	Schematic diagram of a LAr EM calorimeter barrel module.	31
274	3.13	Schematic diagram of tile calorimeter module ^[33] .	32
275	3.14	Cut-away view of the ATLAS muon spectrometer ^[35] .	32
276	3.15	Schematic diagram of the ATLAS trigger and data acquisition system in run-2.	34
277	3.16	An examples of L1 calorimeter trigger tower for electron and photon trig- 278 gers ^[37] .	35
279	3.17	The HLT trigger algorithm sequence ^[37] .	36
280	4.1	The flow of the ATLAS simulation software.	37
281	4.2	Sketch of a hardon-hardon collision simulated by MC event generator. The 282 red blob in center denotes the hard collision, surrounded by tree-like struc- 283 tures representing Bremsstrahlung which is simulated by Parton Showers. 284 The purple blob stands for a secondary hard scattering event. The light green 285 blobs indicate the parton-to-hardon transitions and the dark green blobs rep- 286 resents hardon decays. The yellow lines are soft photon radiations.	39
287	4.3	The flowchart of the ATLAS data processing.	40
288	4.4	Schematic view of the ATLAS inner detector showing all the corresponding 289 components.	41
290	4.5	Schematic of the impact parameters of a track in the transverse plane (left) 291 and RZ-plane (right), as defined in the global ATLAS tracking frame ^[59] .	46
292	4.6	The efficiencies of three electron identification WPs from $Z \rightarrow ee$ (left) 293 events and hadrons misidentified as electrons estimated using di-jet MC sam- 294 ples (right).	47
295	4.7	Distributions of $E_T^{cone0.2}$ (left) and $p_T^{varcone0.2}$ (right) for electrons from $ZZ \rightarrow ee$ events in data and MC simulation. The simulated events (full histograms) 296 are normalized to data.	48
298	4.8	Muon reconstruction efficiency as a function of η for: Medium (and Loose), 299 Tight and High- p_T working points.	51
300	4.9	Muon reconstruction efficiency for Low- p_T working point as a function of η .	52

301	4.10	Distributions of the calorimeter-based (right) and the track-based (left) relative isolation variables measured in $Z \rightarrow \mu\mu$ events	53
302			
303	4.11	A overview schematic of ATLAS jet reconstruction ^[65]	53
304			
305	4.12	A overview schematic of ATLAS jet calibration ^[66]	54
306			
307	4.13	MV2c10 BDT output for b- (solid blue), c- (dashed green) and light-flavour (dotted red) jets in $t\bar{t}$ events ^[67]	56
308			
309	4.14	Measured E_T^{miss} distribution for $Z \rightarrow \mu\mu$ events (left) and $W \rightarrow e\nu$ events (right)	57
310			
311	5.1	(a) Illustration of the relationship between the observed t_μ and its p -value. (b) The relationship between p -value and the observed significance Z , where $\phi(x)$ is a standard normal distribution	61
312			
313	6.1	Typical diagrams for the production of $ZZjj$, including the relevant EW VBS diagrams (first row) and QCD diagrams (second row)	65
314			
315	6.2	Pre-fit m_{ZZ} and m_{jj} distribution in QCD-enriched CR	71
316			
317	6.3	Fake factor for $Z+jets$ background, constructed with additional electron, as a function of p_T (left) and η (right)	72
318			
319	6.4	Fake factor for $Z+jets$ background, constructed with additional muon, as a function of p_T (left) and η (right)	72
320			
321	6.5	Fake factor for $t\bar{t}$ background, constructed with additional electron, as a function of p_T (left) and η (right)	73
322			
323	6.6	Fake factor for $t\bar{t}$ background, constructed with additional muon, as a function of p_T (left) and η (right)	73
324			
325	6.7	The theoretical uncertainties for $gg \rightarrow ZZ$ background in particle-level SR (left) and CR (right)	76
326			
327	6.8	MD distribution for QCD- $ZZjj$ process in low and high pile-up events for SR (left) and CR (right)	78
328			
329	6.9	MD shape difference for QCD $q\bar{q} \rightarrow ZZ$ background between different Sherpa theoretical uncertainties and sample from MadGraph5_aMC@NLO on SR (left) and CR (right)	78
330			
331	6.10	Observed and post-fit expected multivariate discriminant distributions after the statistical fit in the $\ell\ell\ell'\ell'$ SR (left) and QCD CR (right). The error bands include the experimental and theoretical uncertainties, as well as the uncertainties in μ_{EW} and $\mu_{\text{QCD}}^{\ell\ell\ell'jj}$. The error bars on the data points show the statistical uncertainty on data	82
332			
333			
334			

335	6.11 Observed and post-fit expected m_{jj} distributions in SR (left) and QCD CR 336 (right). The error bands include the expected experimental and theoretical 337 uncertainties. The error bars on the data points show the statistical uncer- 338 tainty. The contributions from the QCD and EW production of $ZZjj$ events 339 are scaled by 0.96 and 1.35, respectively, corresponding to the observed nor- 340 malization factors in the statistical fit. The last bin includes the overflow 341 events.	83
342	6.12 Observed and post-fit expected m_{ZZ} spectrum in SR. The error bands include 343 the expected experimental and theoretical uncertainties. The error bars on the 344 data points show the statistical uncertainty. The contributions from the QCD 345 and EW production of $ZZjj$ events are scaled by 0.96 and 1.35, respectively, 346 corresponding to the observed normalization factors in the statistical fit. The 347 last bin includes the overflow events.	83
348	6.13 Display of an event candidate of EW- $ZZjj$ production in $2e2\mu$ channel in 349 last MD bin ($0.875 < \text{MD} < 1.0$). The invariant mass of the di-jet (four-lepton) 350 system is 2228 (605) GeV.	84
351	6.14 Detector-level distributions of EW- and QCD- $ZZjj$ processes with selected 352 events in defined phase space at 14 TeV of (a) m_{jj} , (b) m_{ZZ} , (c) $ \Delta\phi(ZZ) $, 353 (d) ZZ centrality, normalized to 3000 fb^{-1}	87
354	6.15 Jet variations on m_{jj} distribution for EW- $ZZjj$ (left) and QCD- $ZZjj$ (right) 355 processes with luminosity of 3000 fb^{-1} at 14 TeV. <i>Upgrade Performance</i> 356 <i>Function</i> is used to extract the uncertainties with <i>baseline</i> setting.	88
357	6.16 The expected significance of EW- $ZZjj$ processes as a function of differ- 358 ent m_{jj} cut with 3000 fb^{-1} , under conditions of different sizes of theoretical 359 uncertainties on the QCD- $ZZjj$ background modelling. The statistical un- 360 certainty is estimated from expected data yield at 14 TeV with 3000 fb^{-1} . 361 Different uncertainties are summed up quadratically.	89
362	6.17 The projected differential cross-sections at 14 TeV for the EW- $ZZjj$ pro- 363 cesses as a function of m_{jj} (left) and m_{ZZ} (right). The top panel shows mea- 364 surement with statistical only case, where statistical uncertainty is estimated 365 from expected data yield at 14 TeV with 3000 fb^{-1} . The bottom panel shows 366 impact of different sizes of systematic uncertainties.	89
367	7.1 (a) VBF DNN architecture diagram. (b) ggF DNN architecture.	102

368	7.2	(a) $m_{4\ell}$ distribution of raw (unweighted) training events for VBF signal (blue) 369 and background (black); (b) $m_{4\ell}$ distribution of weighted VBF signal (blue) 370 and background (black) used at training time.	103
371	7.3	(a) $m_{4\ell}$ distribution of raw (unweighted) training events for ggF signal (blue) 372 and background (black); (b) $m_{4\ell}$ distribution of weighted ggF signal (blue) 373 and background (black) used at training time.	103
374	7.4	The output score of “ggF-classifier” (a) and “VBF-classifier” (b) with the 375 events passing the common event selections for the data, the SM backgrounds 376 and an example of a NWA signal with a mass of 600 GeV. For the “VBF- 377 classifier”, an additional requirement of at least two jets in the event is ap- 378 plied. The signals cross section are set to one hundred times of the observed 379 limit for the “ggF-classifier” and fifty times of the observed limit for the 380 “VBF -classifier”. The $Z Z$ backgrounds are scaled by the normalisation fac- 381 tors shown in Table 7.15. The lower panels show the ratio of data to predic- 382 tion. Only statistical and experimental systematic uncertainties are included. 383 105	
384	7.5	Significance improvements of the MVA-based over the cut-based categoriza- 385 tion of the VBF (ggF) category for VBF (ggF) signal samples from 300 to 386 2000 GeV for seven different cuts on the VBF (ggF) output score. The op- 387 timal cut of 0.8 (0.5) for VBF (ggF) score is chosen as the solid line, while 388 other alternative cuts are plotted with dashed lines. For VBF category, results 389 at 2000 GeV for cuts of 0.8 and 0.9 are missing due to a lack of background 390 events passing this tight selection.	105
391	7.6	Illustration of the MVA-based VBF and ggF event classification for events 392 with (a) $N_{\text{jets}} < 2$ and (b) $N_{\text{jets}} \geq 2$	107
393	7.7	NWA acceptance as a function of m_H for the MVA-based categorization for 394 the samples of (a) ggF production; (b) VBF production.	107
395	7.8	NWA acceptance as a function of m_H for the Cut-based categorization for the 396 samples of (a) ggF production mode; (b) VBF production mode.	108
397	7.9	Distributions of the $m_{4\ell}$ invariant mass fit projections of the $q\bar{q} \rightarrow ZZ$ back- 398 ground samples for the 4μ , $4e$ and $2\mu 2e$ final states in the ggF-CBA-enriched 399 category, and the 4ℓ inclusive VBF-CBA-enriched category. Cut-based cat- 400 egorization is used.	109

401	7.10	Distributions of the $m_{4\ell}$ invariant mass fit projections of the $gg \rightarrow ZZ$ background samples for the 4μ , $4e$ and $2\mu2e$ final states in the ggF-CBA-enriched category, and the 4ℓ inclusive VBF-CBA-enriched category. Cut-based categorization is used.	110
405	7.11	Distributions of the $m_{4\ell}$ invariant mass fit projections of the $q\bar{q} \rightarrow ZZ$ (EW) background samples for the 4μ , $4e$ and $2\mu2e$ final states in the ggF-CBA-enriched category, and the 4ℓ inclusive VBF-CBA-enriched category. Cut-based categorization is used.	110
409	7.12	Distributions of the $m_{4\ell}$ invariant mass fit projections of the $q\bar{q} \rightarrow ZZ$ background samples for the 4μ , $4e$ and $2\mu2e$ final states in the ggF-MVA-high category, the 4ℓ inclusive ggF-MVA-low category and VBF-MVA-enriched category. DNN-based categorization is used.	111
413	7.13	Distributions of the $m_{4\ell}$ invariant mass fit projections of the $gg \rightarrow ZZ$ background samples for the 4μ , $4e$ and $2\mu2e$ final states in the ggF-MVA-high category, the 4ℓ inclusive ggF-MVA-low category and VBF-MVA-enriched category. DNN-based categorization is used.	111
417	7.14	Distributions of the $m_{4\ell}$ invariant mass fit projections of the $q\bar{q} \rightarrow ZZ$ (EW) background samples for the 4μ , $4e$ and $2\mu2e$ final states in the ggF-MVA-high category, the 4ℓ inclusive ggF-MVA-low category and VBF-MVA-enriched category. DNN-based categorization is used.	112
421	7.15	Distributions of the $m_{2\mu2e}$ and fit projection for signal samples between 200 to 3000 GeV for ggF production mode. Three MC campaigns, mc16a, mc16d and mc16e, are combined. The lower panel in each plot shows the pull distribution.	115
425	7.16	Polynomial fits of the parameters μ , f_C , σ_G , σ_C , n_C and α_C for the signal $C + G$ model in the $2\mu2e$ channel as a function of m_H for the ggF production mode. The combination of the mc16a, mc16d and mc16e MC campaigns is used.	116
428	7.17	The difference between MC simulation and parameterization of 4μ (left), $4e$ (middle) and $2\mu2e$ (right) for the ggF production mode. The combination of the mc16a, mc16d and mc16e MC campaigns is used.	116
431	7.18	The final signal shapes for the ggF production mode, interpolated from the polynomial fit parameters.	116
433	7.19	Comparison of the analytical shape to a truth $m_{4\ell}$ distribution of gg2VV MC samples for $m_H = 450$ GeV (top), 700 GeV (bottom) and width equal to 5% (left), 10% (middle), 15% (right) of the mass.	118

436	7.20	Comparison between the analytical shape convoluted with detector effects and the reconstructed $m_{2\mu 2e}$ MC distribution for mass points ranging from 400 to 1800 GeV and width equal to 15% of the mass.	119
437			
438			
439	7.21	The interference (H-B) model fitted to the truth $m_{4\ell}$ MC distribution after signal region selection for $2\mu 2e$ channel.	121
440			
441	7.22	The signal modelling for the large-width scenario at m_H of 400 GeV (top), 600 GeV (middle) and 800 GeV (bottom), as well as three different signal width: 5% (left), 10% (middle) and 15% (right). The contribution of the interference between heavy Higgs and SM Higgs (H-h) is shown together with the one between heavy Higgs and SM $gg \rightarrow ZZ$ background (H-b).	123
442			
443			
444			
445			
446	7.23	Fitted parameters of the graviton RBW, m_{RBW} and Γ_{RBW} , as a function of the graviton resonance mass, m_G	124
447			
448	7.24	Reconstructed $m_{4\ell}$ distributions in the $2\mu 2e$ channel with the final signal model superimposed for each RS graviton signal sample at masses of 600 GeV, 1600 GeV and 2000 GeV. The lower panel in each plot shows the pull distribution. The dashed green lines show the truth-level graviton signal models for reference.	124
449			
450			
451			
452			
453	7.25	Distribution of the four-lepton invariant mass $m_{4\ell}$ in the $\ell\ell\ell'\ell'$ search for (a), (b), (c) the ggF-MVA-high categories, (d) the ggF-MVA-low category and (e) the VBF-MVA-enriched category. The backgrounds are determined from a combined likelihood fit to the data under the background-only hypothesis. The simulated signal at 600 GeV is normalized to a cross section corresponding to one hundred times the observed upper limit given in section 7.7.3. The error bars on the data points indicate the statistical uncertainty, while the systematic uncertainty in the prediction is shown by the hatched band. The lower panels show the ratio of data to prediction.	129
454			
455			
456			
457			
458			
459			
460			
461			
462	7.26	Pulls and constraints of nuisance parameters after a background only fit to (a) Asimov data and (b) observed data in the $\ell\ell\ell'\ell'$ channel. The Asimov data is generated with background data only, and the observed data includes datasets from 2015 to 2018.	130
463			
464			
465			
466	7.27	Correlation of nuisance parameters after a background only fit to Asimov data in the $\ell\ell\ell'\ell'$ channel. The Asimov data is generated with background data only.	131
467			
468			

469	7.28	The expected and observed upper limits at 95% CL on $\sigma \times BR(H \rightarrow ZZ)$ using the MVA-based analysis for ggF (left) and VBF (right) production. The green and yellow bands represent the $\pm 1\sigma$ and $\pm 2\sigma$ uncertainties in the expected limits.	131
470			
471			
472			
473	7.29	The expected and observed upper limits at 95% CL on $\sigma \times BR(H \rightarrow ZZ)$ using the cut-based analysis for ggF (left) and VBF (right) production. The green and yellow bands represent the $\pm 1\sigma$ and $\pm 2\sigma$ uncertainties in the expected limits.	132
474			
475			
476			
477	7.30	The upper limits at 95% confidence level on $\sigma_{ggF} \times BR(H \rightarrow ZZ)$ as a function of the heavy resonance mass m_H for the ggF production mode with an intrinsic width of 1% (top left), 5% (top right), 10% (bottom left) and 15% (bottom right) for both the case where interference with Standard Model processes is considered. The green and yellow bands represent the $\pm 1\sigma$ and $\pm 2\sigma$ uncertainties in the expected limits.	133
478			
479			
480			
481			
482			
483	7.31	The upper limits at 95% confidence level on $\sigma_{ggF} \times BR(G_{KK} \rightarrow ZZ)$ as a function of the heavy resonance mass $m(G_{KK})$ for the ggF production mode in RS Graviton model. The green and yellow bands represent the $\pm 1\sigma$ and $\pm 2\sigma$ uncertainties in the expected limits.	133
484			
485			
486			
487	7.32	The expected (left) and observed (right) upper limits at 95% confidence level on $\sigma \times BR(S \rightarrow ZZ)$ for ggF production mode at different assumptions.	135
488			
489	7.33	Comparisons of the expected upper limits at 95% CL on the cross section times branching ratio as a function of the heavy resonance mass m_H for the ggF production mode (left) and for the VBF production mode (right) in the case of the NWA. The expected limits from the previous publication are shown in the green dashed line and are projected to the 139 fb^{-1} as shown in the blue dashed line. In addition, the current results based on either cut-based categorisation or the multivariate-based categorisation are shown in red and black lines.	137
490			
491			
492			
493			
494			
495			
496			
497	7.34	Display of one candidate event in 4μ final state with the mass of 1.35 TeV.	137

List of Tables

499	3.1	Summary of design parameters of the LHC for pp collisions.	20
500	4.1	Overview of the contributions to E_T^{miss} .	58
501	6.1	Overlap removal criteria between pre-selection objects for the $\ell\ell\ell'\ell'$ channel. The overlap removal follows the order shown in this table. Once an object has been marked as removed, it does not participate in the subsequent stages of the overlap removal procedure.	68
505	6.2	Summary of selection of physics objects and candidate events at detector level in the $\ell\ell\ell'\ell'jj$ signal region.	69
507	6.3	Observed data and expected signal and background yields in 139 fb^{-1} of luminosity. Minor backgrounds are summed together as ‘Others’. Uncertainties on the predictions include both statistical and systematic components.	69
510	6.4	Observed data and expected signal and background yields in 139 fb^{-1} of luminosity. Diboson background in table includes all the other diboson processes discussed in section 6.2.2, except those with four-lepton final state. Uncertainties include only MC statistic. No events from $Z+jets$ and $t\bar{t}$ MC samples pass the selection, and are indicated as 0 in the table.	70
515	6.5	Fake background estimations in the SR. For nominal value, the 2D fake factor together with the $Z+jets$ and $t\bar{t}$ combination applied. The other lines show the estimations with different uncertainty variations.	74
518	6.6	Summary of different variations for EW- and QCD- $ZZjj$ theoretical uncertainties measurement.	75
520	6.7	Summary of theoretical uncertainties for the fiducial volume (SR) for both EW and QCD qq -initial processes.	75
522	6.8	Summary of theoretical uncertainties for the control region for EW and qqQCD processes.	75
524	6.9	Experimental systematic uncertainties in $\ell\ell\ell'\ell'$ channel with the luminosity of 139 fb^{-1} . The “Electron Exp.”, “Muon Exp.” and “Jet Exp.” represent the quadrature of the respective sources from electron, muon, and jets.	77
527	6.10	C Factor of different $ZZjj$ processes.	79
528	6.11	Measured and predicted fiducial cross-sections in $\ell\ell\ell'\ell'jj$ final-state. Uncertainties due to different sources are presented.	80

530	6.12	Input features for the training of MD.	81
531	6.13	Observed μ_{EW} and $\mu_{\text{QCD}}^{\ell\ell\ell'jj}$, as well as the observed and expected significance from the individual $\ell\ell\ell'\ell'$ channel. The full set of systematic uncertainties are included.	82
534	6.14	Comparison of event yields for signal ($N_{\text{EW-ZZjj}}$) and background ($N_{\text{QCD-ZZjj}}$) processes, and expected significance of EW-ZZjj processes, normalized to 3000 fb^{-1} data at 14 TeV, with baseline and alternative selections. Uncertainties in the table refer to expected data statistical uncertainty at 14 TeV with 3000 fb^{-1}	86
539	6.15	Summary of expected cross-section measured with different theoretical uncertainties. The statistical uncertainty is computed from expected data yield with 3000 fb^{-1} at 14 TeV. Different uncertainties are treated as uncorrelated and summed quadratically.	90
543	7.1	Summary of the recorded integrated luminosity (lumi), average and peak pile-up (PU) of data from 2015 to 2018.	93
545	7.2	Summary of the p_T (E_T) trigger thresholds (in GeV) employed for the muon (electron) trigger selection in the year of 2015, 2016, 2017, and 2018.	96
547	7.3	Summary of the object and event selection requirements.	99
548	7.4	Cutflow table for a narrow-width ggF signal sample at $m_H = 600$ GeV. N_{event} denotes the number of events selected after each cut is applied, normalized to 139 fb^{-1} , according to the expected upper limit on the cross section. The acceptances (the proportion of events selected relative to the initial number of events) are also included.	100
553	7.5	Cutflow table for a narrow-width ggF signal sample at $m_H = 1000$ GeV. N_{event} denotes the number of events selected after each cut is applied, normalized to 139 fb^{-1} , according to the expected upper limit on the cross section. The acceptances (the proportion of events selected relative to the initial number of events) are also included.	100
558	7.6	Cutflow table for a narrow-width VBF signal sample at $m_H = 600$ GeV. N_{event} denotes the number of events selected after each cut is applied, normalized to 139 fb^{-1} , according to the expected upper limit on the cross section. The acceptances (the proportion of events selected relative to the initial number of events) are also included.	101

563	7.7	Cutflow table for a narrow-width VBF signal sample at $m_H = 1000$ GeV. N_{event} denotes the number of events selected after each cut is applied, nor- malized to 139 fb^{-1} , according to the expected upper limit on the cross sec- tion. The acceptances (the proportion of events selected relative to the initial number of events) are also included.	101
564			
565			
566			
567			
568	7.8	Input features used in the “VBF-classifier” for the $\ell\ell\ell'\ell'$ analysis. The RNN stands for the recurrent neural network and MLP for the multilayer percep- tron.	104
569			
570			
571	7.9	Input features used in the “ggF-classifier” for the $\ell\ell\ell'\ell'$ analysis. The RNN stands for the recurrent neural network and MLP for the multilayer percep- tron.	106
572			
573			
574	7.10	Summary of acceptance uncertainties of PDF, QCD scale and parton shower variations for ggF production. The MVA-based categorization is used.	125
575			
576	7.11	Summary of acceptance uncertainties of PDF, QCD scale and parton shower variations for VBF production. The MVA-based categorization is used.	125
577			
578	7.12	Summary of acceptance uncertainties of PDF, scale, and parton showering variations for QCD $q\bar{q} \rightarrow ZZ$ background. The MVA-based categorization is used.	126
579			
580			
581	7.13	A list of the experimental systematics considered in this analysis. The NPs have been separated by whether they only affect the normalisation (left col- umn) or if they affect the shape (right column) of the $m_{4\ell}$ distribution. They are further subdivided into the primary objects that they affect.	134
582			
583			
584			
585	7.14	Expected and observed numbers of events for $m_{4\ell} > 200$ GeV, together with their systematic uncertainties, for three MVA-based categories. The expected number of events, as well as their uncertainties, are obtained from a likelihood fit to the data under the background-only hypothesis. The uncertainties of the ZZ normalisation factors, presented in table 7.15, are also taken into account.	135
586			
587			
588			
589			
590			
591	7.15	ZZ normalization factor in each category, obtained from a likelihood fit to the data under the background-only hypothesis.	135
592			

593	7.16	Impact of the leading systematic uncertainties, the data statistic uncertainties, as well as the total uncertainties on the predicted signal event yield with the cross section times branching ratio being set to the expected upper limit, ex- pressed as a percentage of the signal yield for the ggF (left) and VBF (right) production modes at $m_H = 400$ and 1000 GeV.	136
594			
595			
596			
597			

Dedicated to my mother!

献给我的母亲！

602 **Chapter 1 Introduction**

603 The goal of particle physics is to understand how our universe works at its most funda-
604 mental level. It can be accomplished by pursuing the mysteries of the basic construction of
605 matter and energy, probing the interactions between elementary particles, and exploring
606 the basic nature of space and time itself.

607 **Elementary particles**

608 From around the 6th century BC, ancient Greek philosophers Leucippus, Democritus,
609 and Epicurus brought up a philosophical idea that everything is composed of “uncuttable”
610 elementary particles. In the 19th century, John Dalton, through his work on stoichiometry,
611 concluded that each element of nature was composed of a single, unique type of particle.
612 The particle was named as “atom” after the Greek word atomos, with the meaning of “in-
613 divisible”. However this Dalton’s atom theory was strongly challenged later. Near the
614 end of 19th century, physicists discovered that Dalton’s atoms are not, in fact, the funda-
615 mental particles of nature, but conglomerates of even smaller particles. Electron was dis-
616 covered by J. J. Thomson in 1897, and then its charge was carefully measured by Robert
617 Andrews Millikan and Harvey Fletcher in their “oil drop experiment” of 1909. In early
618 20th-century, Rutherford’s “gold foil experiment” showed that the atom is mainly empty
619 space, with almost all its mass concentrated in a tiny positively charge atomic nucleus.
620 Then the discoveries of anti-particles (the positron in 1932) and other particles (e.g. the
621 muon in 1936) show that more discoveries could be expected in future experiments.

622 Starting from 1950s, more accelerator facilities were put into service. Throughout
623 the 1950s and 1960s, a bewildering variety of particles were found in collisions of parti-
624 cles from increasingly high-energy beams. It was referred to informally as the “particle
625 zoo”. In 1964, the quark model was independently proposed by physicists Murray Gell-
626 Mann and George Zweig, and experimentally confirmed of their existence in mid-1970s.
627 In 1970s, the establishment of quantum chromodynamics (QCD) postulated the funda-
628 mental strong interaction, experienced by quarks and mediated by gluons.

629 The well-known Standard model (SM) was developed in stages throughout the lat-
630 ter half of the 20th century. Since then, confirmation of the top quark (1995), the tau
631 neutrino (2000), and the Higgs boson (2012) have added further credence to the Standard
632 Model. Now, the quarks, leptons and gauge bosons are the elementary constituents in a
633 framework of Standard Model of particle physics, which theoretically describes three of
634 the four known fundamental forces (the electromagnetic, weak, and strong interactions,

635 and not including the gravitational force) in the universe, as well as classifies all
636 known elementary particles.

637 **Higgs mechanics and electroweak symmetry breaking**

638 In 1961, Sheldon Glashow, Steven Weinberg and Abdus Salam together brought for-
639 ward a unified electroweak theory to combine the electromagnetic and weak interactions.
640 In the standard model, if under the condition that the energy is high enough but elec-
641 troweak symmetry is unbroken, all elementary particles are massless. But measurements
642 show the fact that the W and Z bosons actually have masses. Later on, the Higgs mechan-
643 ics resolves this conundrum. The simplest description of the mechanism adds a Higgs
644 field that permeates all space to the Standard Model. Below some extremely high energy,
645 the field causes spontaneous symmetry breaking during interactions. All massive parti-
646 cles in the Standard Model, including the W and Z bosons, interact with Higgs boson to
647 acquire their mass.

648 Over the past few decades, with the combination of electroweak theory, Higgs me-
649 chanics and strong interactions has been widely accepted. But the Higgs boson, which is
650 essential to explain the mechanics of the property “mass” for gauge bosons and fermions,
651 had been the final missing piece in the Standard Model of particle physics at that time.
652 The mass of Higgs boson was not specifically predicted, and it has been searched in sev-
653 eral large experiments (eg. LEP at CERN, Tevatron at Fermilab, and LHC at CERN) with
654 different energy. In 2012, the discovery of Higgs boson was finally announced by the
655 ATLAS and CMS collaborations at the Large Hadron Collider (LHC) with its mass round
656 125 GeV. Peter Higgs and Francois Englert were award the 2013’s Nobel Prize in Physics
657 for their theoretical discovery of a mechanism that contributes to our understanding of the
658 origin of mass of subatomic particles.

659 **Contents of this thesis**

660 This dissertation is organized as follows. Section 2 briefly introduces the Standard
661 Model of particle physics, the Higgs mechanism related to the dissertation and the LHC
662 phenomenology. Section 3 gives an overview of the LHC and the ATLAS detector. The
663 detector simulation and the reconstruction of physics objects are described in section 4.
664 And then section 5 focuses on the Standard model ZZ production cross section measure-
665 ment in $ZZ \rightarrow \ell\ell\ell'\ell'$ channel, where ℓ stands for electron or muon, and the observa-
666 tion of its electroweak component as well as its further prospects in High luminosity LHC
667 (HL-LHC). Section 6 present the search of possible heavy resonances in $ZZ \rightarrow \ell\ell\ell'\ell'$
668 channel. In the end, section 7 gives the summary and outlook for future physics in LHC.

669

Chapter 2 Theory

670 2.1 The Standard Model of Particle Physics

671 The standard model (SM) reflects our current understanding of elementary particles
 672 and several basic interactions. It is a gauge quantum field theory containing the inter-
 673 nal symmetries of the unitary product group $SU(3) \times SU(2) \times U(1)$, in which the color
 674 group $SU(3)$ presents the strong interaction, and $SU(2) \times U(1)$ describes the electroweak
 675 interactions. Over the past decades, the SM has been widely tested through various ex-
 676 periments with extremely high precision.

677 2.1.1 Elementary particles in the Standard Model

678 The elementary particles in SM can be classified into 3 class: *fermions*, *gauge bosons*
 and the *Higgs boson* as shown in Figure 2.1.

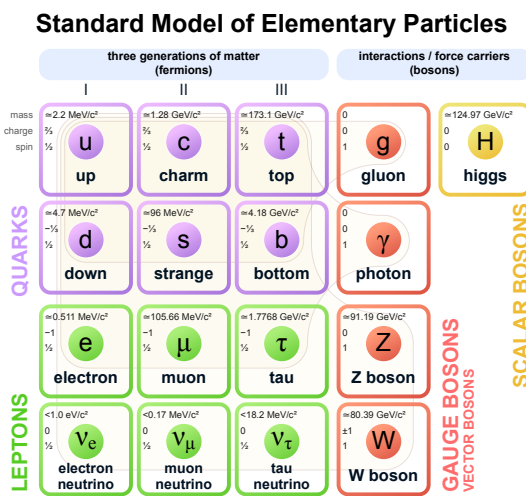


Fig. 2.1 The elementary particles of the Standard Model.

679

680 **Fermions** The Standard Model includes 12 elementary particles of spin- $\frac{1}{2}$ obeying the
 681 Fermi-Dirac statistics, known as fermions. They are classified into two types: *leptons* and
 682 *quarks* according to their interactions. The *leptons* include three generations: electron
 683 (e) and electron neutrino (ν_e); muon (μ) and muon neutrino (ν_μ); tau (τ) and tau neutrino
 684 (ν_τ). The e , μ and τ carry electric charge of -1 and three neutrinos are electrically neutral.
 685 All the leptons can participate in electroweak interactions. Also there are three generations
 686 of *quarks*: up (u) and down (d); charm (c) and strange (s); top (t) and bottom (b). The
 687 defining property of the quarks is that they carry color charge (while leptons don't), and
 688 hence interact via the strong interaction, letting them to be strongly bound from one to

another, forming color-neutral composite particles (known as hadrons) containing either a quark and an antiquark (mesons) or three quarks (baryons). In the meantime, u , c and t -quark carry electric charge of $2/3$, and d , s and b -quark carry electric charge of $-1/3$. Hence they interact via all three interactions described in SM. Each fermion also has a corresponding antiparticles.

Gauge bosons act as force carriers that mediate the strong, weak, and electromagnetic interactions in SM. They are spin-1 particles obeying the Bose-Einstein statistics. There are three types of gauge bosons:

- The eight massless *gluons* mediate the strong interactions between color charged particles (quarks).
- The massless *photons* mediate the electromagnetic force between electrically charged particles.
- The W^+ , W^- and Z bosons mediate the weak interactions between particles of different flavors (all quarks and leptons). All these three bosons are massive, the W^\pm carries an electric charge of $+1$ and -1 and couples to the electromagnetic interaction while Z boson is electrically neutral.

Figure 2.2 shows the Feynman diagrams of corresponding interactions in SM.

Higgs boson is a massive scalar elementary particle with spin-0. It plays a unique role in the SM by explaining the origin of masses of massive gauge bosons (W^\pm and Z) and fermions. And it is the last discovered particle in SM.

2.1.2 Electroweak theory

The electroweak interaction is the unified description of two of the four known fundamental interactions of nature: electromagnetism and the weak interaction. It is based on the gauge group of $SU(2)_L \times SU(1)_Y$, in which L is the left-handed fields and Y is the weak hypercharge^[1]. It follows the Lagrangian of

$$L_{EW} = L_{gauge} + L_{Higgs} + L_{fermion} + L_{Yukawa} \quad (2.1)$$

L_{gauge} is the **gauge term** part

$$L_{gauge} = -\frac{1}{4} W_{\mu\nu}^i W^{\mu\nu i} - \frac{1}{4} B_{\mu\nu} B^{\mu\nu} \quad (2.2)$$

where W_μ^i and B_μ present the $SU(2)_L$ and $SU(1)_Y$ gauge fields respectively, with the

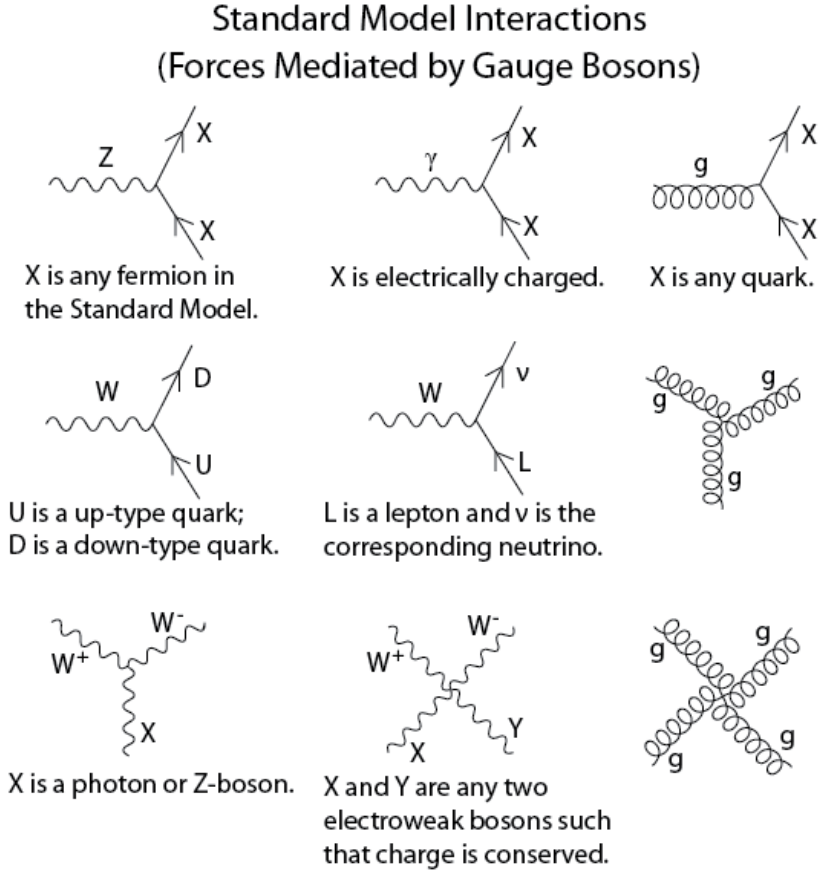


Fig. 2.2 The Feynman diagrams of interactions that form the basis of the standard model.

716 corresponding field strength tensors of

$$\begin{aligned} B_{\mu\nu} &= \partial_\mu B_\nu - \partial_\nu B_\mu \\ W_{\mu\nu}^i &= \partial_\mu W_\nu^i - \partial_\nu W_\mu^i - g \epsilon_{ijk} W_\mu^j W_\nu^k \end{aligned} \quad (2.3)$$

717 In the equations above, g is the $SU(2)_L$ gauge coupling and ϵ_{ijk} is the totally antisymmetric tensor. The gauge Lagrangian has three and four-point self interactions of W^i , which result in triple and quartic gauge boson couplings.

720 The second term of the Lagrangian is the **scalar part**:

$$L_{Higgs} = (D^\mu \phi)^\dagger D_\mu \phi - V(\phi) \quad (2.4)$$

721 where $\phi = \begin{pmatrix} \phi^+ \\ \phi^0 \end{pmatrix}$ is a complex Higgs scalar, and $V(\phi)$ is the Higgs potential which is 722 restricted into the form of

$$V(\phi) = +\mu^2 \phi^\dagger \phi + \lambda (\phi^\dagger \phi)^2 \quad (2.5)$$

723 due to the combination of $SU(2)_L \times SU(1)_Y$ invariance and renormalizability. In Eq. 2.5,

724 μ is a mass-dependent parameter and λ is the quartic Higgs scalar coupling, which rep-
 725 resents a quartic self-interaction between the scalar fields. When $\mu^2 < 0$, there will be
 726 spontaneous symmetry breaking (more details in section 2.1.3). To maintain vacuum sta-
 727 bility, $\lambda > 0$ is required. And in Eq. 2.4, the gauge covariant derivative is defined as

$$D_\mu \phi = \left(\partial_\mu + ig \frac{\tau^i}{2} W_\mu^i + \frac{ig'}{2} B_\mu \right) \phi \quad (2.6)$$

728 in which τ^i represents the Pauli matrices, and g' is the $U(1)_Y$ gauge coupling. The square
 729 of the covariant derivative results in three and four -point interactions between the gauge
 730 and scalar fields.

731 The third term of the Lagrangian is the **fermion part**

$$\begin{aligned} L_{fermion} = & \sum_{m=1}^F (\bar{q}_{mL}^0 \gamma_\mu D_\mu q_{mL}^0 + \bar{l}_{mL}^0 \gamma_\mu D_\mu l_{mL}^0 + \bar{u}_{mR}^0 \gamma_\mu D_\mu u_{mR}^0 \\ & + \bar{d}_{mR}^0 \gamma_\mu D_\mu d_{mR}^0 + \bar{e}_{mR}^0 \gamma_\mu D_\mu e_{mR}^0 + \bar{\nu}_{mR}^0 \gamma_\mu D_\mu \nu_{mR}^0) \end{aligned} \quad (2.7)$$

732 In Eq. 2.7, m is the family index of fermions, F is the number of families. The subscripts
 733 $L(R)$ stand for the left (right) chiral projection $\psi_{L(R)} \equiv (1 \mp \gamma_5) \psi / 2$.

$$q_{mL}^0 = \begin{pmatrix} u_m^0 \\ d_m^0 \end{pmatrix}_L \quad l_{mL}^0 = \begin{pmatrix} v_m^0 \\ e_m^{-0} \end{pmatrix}_L \quad (2.8)$$

734 are the $SU(2)$ doublets of left-hand quarks and leptons, while u_{mR}^0 , d_{mR}^0 , e_{mR}^{-0} and ν_{mR}^0 are
 735 the right-hand singlets.

736 The last term in Eq. 2.1 is **Yukawa term**

$$\begin{aligned} L_{Yukawa} = & - \sum_{m,n=1}^F [\Gamma_{mn}^u \bar{q}_{mL}^0 \tilde{\phi} u_{nR}^0 + \Gamma_{mn}^d \bar{q}_{mL}^0 \phi d_{nR}^0 \\ & + \Gamma_{mn}^e \bar{l}_{mL}^0 \phi e_{nR}^0 + \Gamma_{mn}^\nu \bar{l}_{mL}^0 \tilde{\phi} \nu_{nR}^0] + h.c. \end{aligned} \quad (2.9)$$

737 the matrices Γ_{mn} refer to the Yukawa couplings between single Higgs doublet (ϕ) and the
 738 various flavors of quarks (m) and leptons (n).

739 2.1.3 Higgs mechanism and Electroweak symmetry breaking

740 As shown in previous subsection, the Lagrangian L_{gauge} does not involve any mass
 741 term due to the requirement of gauge invariance. So all the W and B bosons should be
 742 massless. But experimental observations show that the gauge bosons are massive. There-
 743 fore, the gauge invariance must be broken spontaneously. The Higgs field is introduced
 744 to break the $SU(2)_L \times U(1)_Y$ symmetry and gauge bosons and fermions can interact with

745 Higgs filed to acquire their masses. And this specific process is named *Higgs mechanism*
 746 in SM.

747 The Higgs field ϕ is a doublet and can be written in a Hermitian basis as

$$\phi = \begin{pmatrix} \phi^+ \\ \phi^0 \end{pmatrix} = \frac{1}{\sqrt{2}} \begin{pmatrix} \phi_1 - i\phi_2 \\ \phi_3 - i\phi_4 \end{pmatrix} \quad (2.10)$$

748 where $\phi_i = \phi_i^+$ stand for four Hermitian field. In this new basis, the Higgs potential in
 749 Eq. 2.5 can be expressed as:

$$V(\phi) = \frac{1}{2}\mu^2 \left(\sum_{i=1}^4 \phi_i^2 \right) + \frac{1}{4}\lambda \left(\sum_{i=1}^4 \phi_i^2 \right)^2 \quad (2.11)$$

750 To simplify the situation, the axis in this four-dimensional space can be chosen to satisfied
 751 $\langle 0 | \phi_i | 0 \rangle = 0$ for $i = 1, 2, 4$, and $\langle 0 | \phi_3 | 0 \rangle = v$. Thus,

$$V(\phi) \rightarrow V(v) = \frac{1}{2}\mu^2 v^2 + \frac{1}{4}\lambda v^4 \quad (2.12)$$

752 The minimization of this potential depends on the sign of μ^2 as shown in figure 2.3. When
 753 $\mu^2 > 0$ the minimum occurs at $v = 0$, namely the vacuum is empty space and $SU(2)_L \times$
 754 $U(1)_Y$ symmetry is unbroken. In the case of $\mu^2 < 0$, the $v = 0$ symmetric point is no
 755 longer stable and the minimum occurs at nonzero value of $v = (-\mu^2/\lambda)^{1/2}$ which breaks
 the $SU(2)_L \times U(1)_Y$ symmetry. Thus, the classical vacuum ϕ_0 of Higgs doublet can be

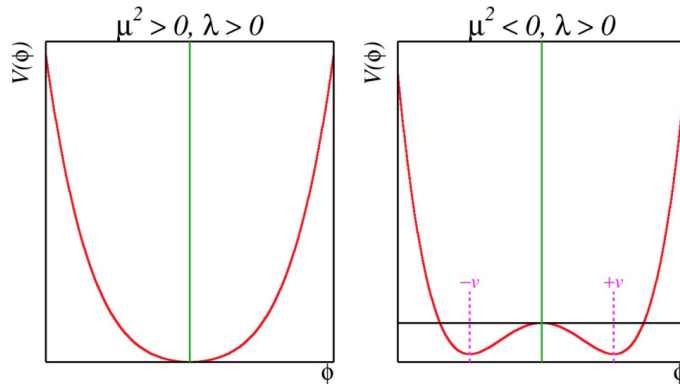


Fig. 2.3 The Higgs potential $V(\phi)$ with $\mu^2 > 0$ (left) and $\mu^2 < 0$ (right).

756

757 expressed by

$$\phi_0 = \frac{1}{\sqrt{2}} \begin{pmatrix} 0 \\ v \end{pmatrix} \quad (2.13)$$

758 And to quantize around the classical vacuum in a general form:

$$\phi = \frac{1}{\sqrt{2}} \begin{pmatrix} 0 \\ v + H \end{pmatrix} \quad (2.14)$$

759 Where H is a Hermitian field for physical Higgs scalar. In this gauge, the Lagrangian

760 L_{Higgs} in Eq. 2.4 takes a simple form

$$\begin{aligned} L_{Higgs} &= (D^\mu \phi)^\dagger D_\mu \phi - V(\phi) \\ &= M_W^2 W^{\mu+} W_\mu^- \left(1 + \frac{H}{v}\right)^2 + \frac{1}{2} M_Z^2 Z^\mu Z_\mu \left(1 + \frac{H}{v}\right)^2 \\ &\quad + \frac{1}{2} (\partial_\mu H)^2 - V(\phi) \end{aligned} \quad (2.15)$$

761 where the W and Z fields are

$$\begin{aligned} W^\pm &= \frac{1}{\sqrt{2}} (W^1 \mp iW^2) \\ Z &= -\sin\theta_W B + \cos\theta_W W^3 \end{aligned} \quad (2.16)$$

762 Therefore, in Eq. 2.15 spontaneous symmetry breaking brings out masses for the W and

763 Z gauge bosons

$$\begin{aligned} M_W &= \frac{gv}{2} \\ M_Z &= \sqrt{g^2 + g'^2} \frac{v}{2} = \frac{M_W}{\cos\theta_W} \end{aligned} \quad (2.17)$$

764 where θ_W is the weak angle defined as

$$\sin\theta_W = \frac{g'}{\sqrt{g^2 + g'^2}} \quad \cos\theta_W = \frac{g}{\sqrt{g^2 + g'^2}} \quad \tan\theta_W = \frac{g'}{g} \quad (2.18)$$

765 Then another gauge boson photon remains massless with the field of

$$A = \cos\theta_W B + \sin\theta_W W^3 \quad (2.19)$$

766 After the symmetry breaking, the Higgs potential in unitary gauge can be written into

$$V(\phi) = -\frac{\mu^4}{4\lambda} - \mu^4 H^2 + \lambda v H^3 + \frac{\lambda}{4} H^4 \quad (2.20)$$

767 The first term in V is a constant, while the second term denotes a (tree-level) mass of

768 Higgs boson

$$M_H = \sqrt{-2\mu^2} = \sqrt{2\lambda} v \quad (2.21)$$

769 Due to the unknown of quartic Higgs coupling λ , the Higgs mass is not predicted. The

770 third and fourth terms in the Higgs potential V denote the induced cubic and quartic in-
 771 teractions of the Higgs scalar.

772 Through the Higgs mechanism, fermions can also acquire their masses. In the unitary
 773 gauge, Yukawa Lagrangian (L_{Yukawa}) can be written as a simple form of^[2]

$$L_{Yukawa} = - \left(1 + \frac{H}{v} \right) (m_d \bar{d}d + m_u \bar{u}u + m_l \bar{l}l) \quad (2.22)$$

774 in which $m_f = \frac{y_f v}{\sqrt{2}}$ for $f = d, u, l$.

775 2.1.4 Beyond the SM Higgs sector

776 After the discovery of the Higgs boson by the ATLAS and CMS Collaborations at the
 777 LHC^[3-4] in 2012, one question comes out: if this Higgs boson at around 125 GeV is fully
 778 responsible for the unitarization of the scattering amplitudes? The possibility that this
 779 discovered particle is just a part of the extended Higgs sector by various extensions cannot
 780 be ruled out. Many models, motivated by hierarchy and naturalness arguments, predicted
 781 the extended Higgs sector, such as the electroweak-singlet model^[5] and the two-Higgs-
 782 doublet models (2HDM)^[6].

783 Singlet scalar extension of the SM

784 The electroweak singlet model can be considered as the minimal extension of the SM
 785 Higgs sector, encompassing a single gauge singlet real scalar field S . In this model, a
 786 heavy, real singlet is introduced in addition to the SM one. The associated zero tempera-
 787 ture, tree-level scalar potential can be written as:

$$V = V_{SM} + V_{HS} + V_S \quad (2.23)$$

788 where

$$\begin{aligned} V_{SM} &= \mu^2 (H^\dagger H) + \bar{\lambda}_0 (H^\dagger H) \\ V_{HS} &= \frac{a_1}{2} (H^\dagger H) S + \frac{a_2}{2} (H^\dagger H) S^2 \\ V_S &= \frac{b_2}{2} S^2 + \frac{b_3}{3} S^3 + \frac{b_4}{4} S^4 \end{aligned} \quad (2.24)$$

789 where H stands for the SM scalar field of the original Higgs mechanism. After elec-
 790 troweak symmetry breaking, this model gives rise to two CP -even Higgs bosons, in which
 791 the lighter one is the Higgs boson that has been discovered at around 125 GeV. And the new
 792 heavy scalar (S) is allowed to have both SM and non-SM decays. One would expect to
 793 see suppressions of the branching ratio to SM Higgs decay modes, as the branching ratio
 794 to the pair of singlet-like scalars would be considerable.

795 **Two Higgs Doublet Model**

796 The two-Higgs-doublet model (2HDM) is another extension of SM Higgs sector carried
797 by an additional scalar doublet. In this model, through electroweak symmetry breaking,
798 there are five physical Higgs bosons: two CP-even, one CP-odd, and two charged ones.

799 The most general CP-conserving 2HDM has seven free parameters:

- 800 • The Higgs boson masses: m_h , m_H , m_A and $m_{H^{\pm}}$.
801 • $\tan\beta$: the ratio of the vacuum expectation values of the two doublets.
802 • α : the mixing angle between the CP-even Higgs bosons.
803 • m_{12}^2 : the potential parameter that mixes the two Higgs doublets.

804 where the m_h can be identified as the mass of observed Higgs boson at around 125 GeV,
805 and m_H is another heavy scalar with similar properties as h boson. The coupling of the
806 neutral Higgs bosons to the W and Z are the same:

- 807 1. The coupling of the light Higgs, h , to either WW or ZZ is the same as the Standard
808 Model coupling times $\sin(\beta - \alpha)$
- 809 2. The coupling of the heavier Higgs, H , is the same as the Standard Model coupling
810 times $\cos(\alpha - \beta)$.
- 811 3. The coupling of the pseudoscalar, A , to vector bosons vanishes.

812 The two Higgs doublets, Φ_1 and Φ_2 , can couple to fermions (leptons and up- and down-
813 type quarks) in several ways, which leads to several types of 2HDM models:

- 814 • Type-I model: all quarks and leptons couple only to Φ_2 .
- 815 • Type-II model: down-type quarks and leptons couple to Φ_1 , and up-type quarks
816 couple to Φ_2 .
- 817 • The “lepton-specific” model: leptons couple to Φ_1 , while all quarks couple to Φ_2 .
- 818 • The “flipped” model: down-type quarks couple to Φ_1 , while up-type quarks and
819 leptons couple to Φ_2 .

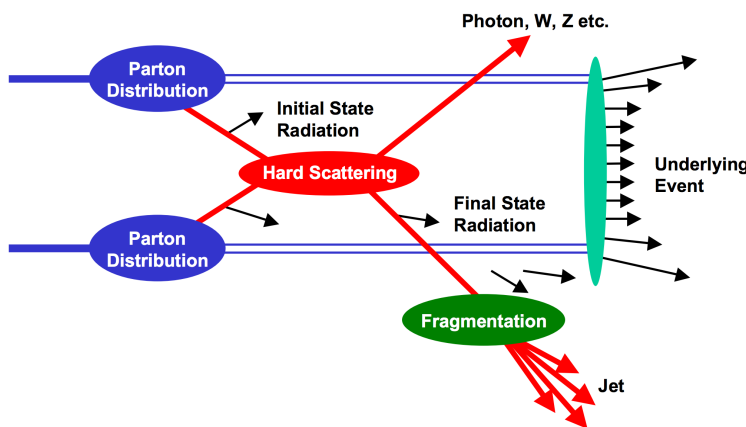
820 **2.2 Phenomenology of Large Hadron Collider**

821 The Large Hadron Collider (LHC) was built as a bridge between the theories and the
822 experiment. Physicists hope that the LHC can help to answer some of the fundamental
823 open questions in physics, concerning the basic laws of interactions and forces among the
824 elementary particles, the deep structure of space and time, and in particular the interrela-
825 tion between quantum mechanics and general relativity. This section will talk about firstly
826 the general introduction of Physics inside hadronic collision, then followed by two im-
827 portant LHC phenomenologies of the Higgs physics and Diboson physics that are related

828 closely to this dissertation.

829 2.2.1 Physics at hadronic collision

830 Protons are not the elementary particle, which actually are composed of quarks and
 831 gluons. So in proton-proton (pp) collision at the LHC, it is not protons themselves interact
 832 but quarks and gluons. Scattering processes can then be further classified into either *hard*
 833 or *soft* processes according to the momentum transfer during the interaction^[7]. QCD, as
 834 an underlying theory for both processes, its approach and level of understandings in two
 835 cases are quite different. For hard process, eg. Higgs, vector bosons and jets production,
 836 the rates and event properties can be precisely predicted based on perturbation theory.
 837 However, for soft processes like total cross-section, the underlying events, the rates and
 838 properties are dominated by non-perturbative QCD effects that are less understood. For
 839 many hard processes, the hard interactions are accompanied by soft ones. An example of
 the hadronic collision is illustrated in figure 2.4. and the typical features are summarized



840
 841 **Fig. 2.4 Schematic view of a hadron-hadron collision^[8].**

842

843 as below:

- 844 • **Parton Distribution Function (PDF):** $f_i(x, Q^2)$ gives the probability of finding a
 845 parton with flavor i (quark or gluon), carrying a momentum fraction of x and with
 846 the scale of momentum transfer Q in a proton. Parton distribution function cannot
 847 be fully calculated by perturbative QCD because of the inherent non-perturbative
 848 nature of partons. There are many different sets of PDFs that are determined by
 849 fits to data from experimental observables in various processes. As an example,
 figure 2.5 shows the *PDF4LHC15 NLO PDFs*, which are based on the combination
 of the *CT14*, *MMHT14* and *NNPDF3.1 NNLO* PDF sets^[9].
- 850 • **Fragmentation and hadronization:** The processes to produce final state particles

(or jets) from the partons produced in hard scattering.

- **Initial/Final state radiation:** The incoming and outgoing partons that carry color charge can emit QCD radiation, which gives rise to additional jets. Also the charged incoming and outgoing particles can emit Quantum Electrodynamics (QED) radiations with photons.
- **Underlying events:** Products from soft processes (not come from the primary hard scattering) as the remnants of scattering interactions.

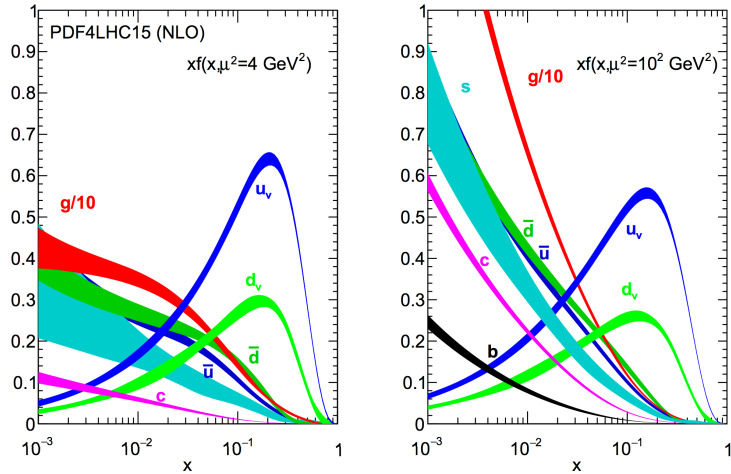


Fig. 2.5 The PDF4LHC15 NLO PDFs at a low scale $\mu^2 = Q^2 = 4\text{GeV}^2$ (left) and at $\mu^2 = Q^2 = 100\text{GeV}^2$ (right) as a function of x .

858 Cross section of hard scattering

859 According to *QCD factorization theorems*^[10], the perturbative calculations can be applied to many important hard processes involving hadrons. The basic problem addressed by factorization theorems is how to calculate high energy cross sections. Consider the process of scattering between two hardons A and B to produce a final state X, the cross section σ can be obtained by summing over all the subprocess cross section $\hat{\sigma}$ ^[11]

$$\sigma_{AB} = \int dx_a dx_b f_{a/A}(x_a) f_{b/B}(x_b) \hat{\sigma}_{ab \rightarrow X} \quad (2.25)$$

864 where $f_{q/A}(x_q)$ is the parton distribution functions of parton q . Taking into account the 865 leading order correction:

$$\sigma_{AB} = \int dx_a dx_b f_{a/A}(x_a Q^2) f_{b/B}(x_b Q^2) \hat{\sigma}_{ab \rightarrow X} \quad (2.26)$$

866 where Q^2 represents large momentum scale that characterizes the hard scattering. Later 867 on, since the finite corrections were not universal and had to be calculated separately for 868 each process, the perturbative $O(\alpha_S^n)$ corrections to the leading logarithm cross section

869 in Eq. 2.26 need to be applied, one can get:

$$\sigma_{AB} = \int dx_a dx_b f_{a/A}(x_a \mu_F^2) f_{b/B}(x_b \mu_F^2) \hat{\sigma}_{ab \rightarrow X}(\alpha_S, \mu_R, \mu_F) \quad (2.27)$$

870 in which μ_F is *factorization scale* which can represent the scale that separates the long-
 871 and short-distance physics, and μ_R is the *renormalization scale* for QCD running coupling.
 872 $\hat{\sigma}_{ab \rightarrow X}$ is the parton-level hard scattering cross section that can be calculated perturbatively
 873 in QCD with the form of

$$\hat{\sigma}_{ab \rightarrow X}(\alpha_S, \mu_R, \mu_F) = (\alpha_S)^n \left[\hat{\sigma}^{(0)} + (\alpha_S/2\pi) \hat{\sigma}^{(1)}(\mu_R, \mu_F) + (\alpha_S/2\pi)^2 \hat{\sigma}^{(2)}(\mu_R, \mu_F) + \dots \right] \quad (2.28)$$

874 where $\hat{\sigma}^{(0)}$ stands for the leading-order (LO) partonic cross section, while $\hat{\sigma}^{(1)}$ and $\hat{\sigma}^{(2)}$ are
 875 the next-to-leading-order (NLO) and next-to-next-to-leading-order (NNLO) cross section.

876 μ_R and μ_F depend on the order of truncation in Eq. 2.28. In principle, if cross sec-
 877 tion is calculated to all orders, it is invariant under changes in these parameters. The
 878 choices of μ_R and μ_F are arbitrary. To avoid unnaturally large logarithms reappearing in
 879 the perturbation series, it is sensible to choose μ_R and μ_F values of the order of the typical
 880 momentum scales of the hard scattering process and $\mu_R = \mu_F$ is also often assumed. Take
 881 Drell–Yan process as an example, the standard choice is $\mu_R = \mu_F = m_{ll}$, where m_{ll} is the
 882 invariant mass of di-lepton pair.

883 2.2.2 Higgs physics at the LHC

884 One important physics purpose of the LHC is searching for the Higgs boson, which
 885 was the last missing part in the SM. This section will discuss both the production and
 886 decay modes of the SM Higgs boson in proton-proton collision.

887 Higgs productions

888 The Higgs boson can be produced through several processes. There are 4 main produc-
 889 tion modes at the LHC: gluon-gluon Fusion (ggF), vector boson Fusion (VBF), associated
 890 production with vector-bosons (VH) (also called the Higgs Strahlung) and associated pro-
 891 duction with a pair of top/anti-top quarks ($t\bar{t}H$)^[12]. Figure 2.6 shows the corresponding
 892 Feynman diagrams of each process (at LO). For pp collisions, the cross section of pro-
 893 duction of Higgs boson is a function of centre-of-mass energy \sqrt{s} . Figure 2.7 depicts
 894 the cross section of SM Higgs, whose mass is 125 GeV, for several different produc-
 895 tion modes when centre-of-mass energy varying from 6 to 15 TeV. Figure 2.8 shows the
 896 prospect of production cross section as a function of Higgs mass from 10 to 2000 GeV for
 897 pp collision at the centre-of-mass energy of 13 TeV and 14 TeV^[13].

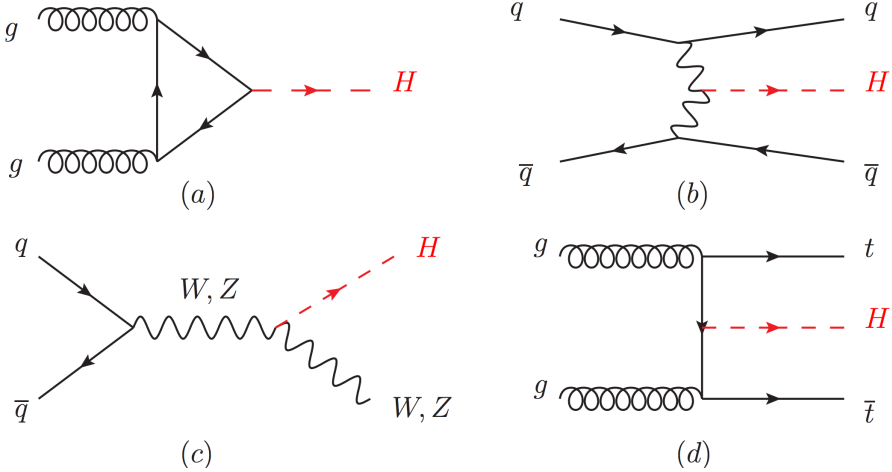


Fig. 2.6 Feynman diagrams of the Higgs production modes: (a) ggF; (b) VBF; (c) VH; (d) ttH.

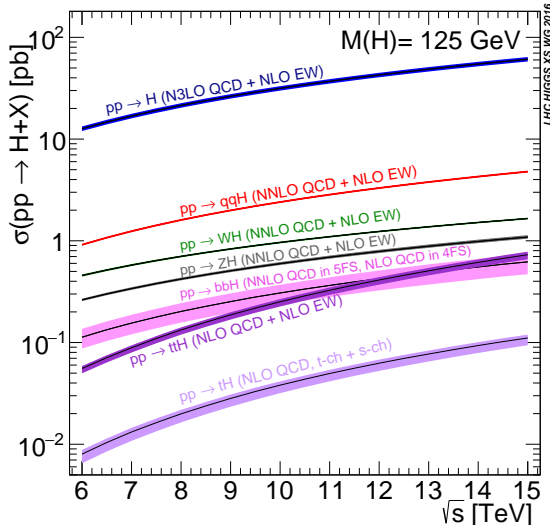


Fig. 2.7 The SM Higgs boson production cross sections for various production modes as a function of the centre-of-mass energy for pp collision.

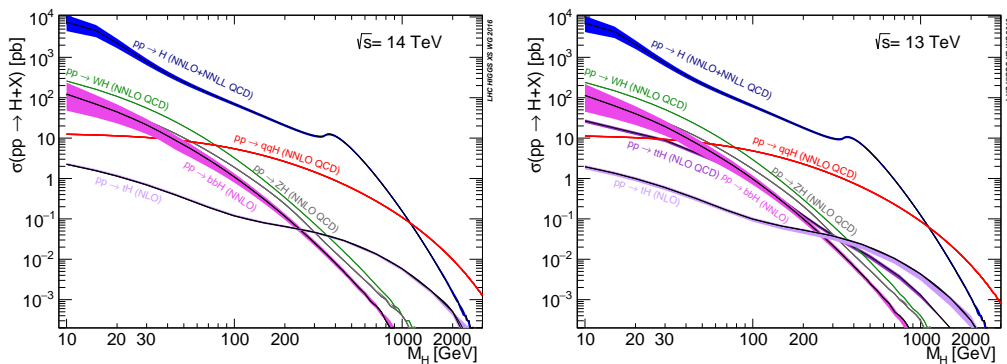


Fig. 2.8 Higgs boson production cross section for various production modes as a function of the Higgs mass for $\sqrt{s} = 13 \text{ TeV}$ (left) and 14 TeV (right) for pp collision.

and the Yukawa coupling as introduced in section 2.1.3. Figure 2.9 depicts the Feynman diagrams of various possible Higgs decay channels. The branching ratio of Higgs boson

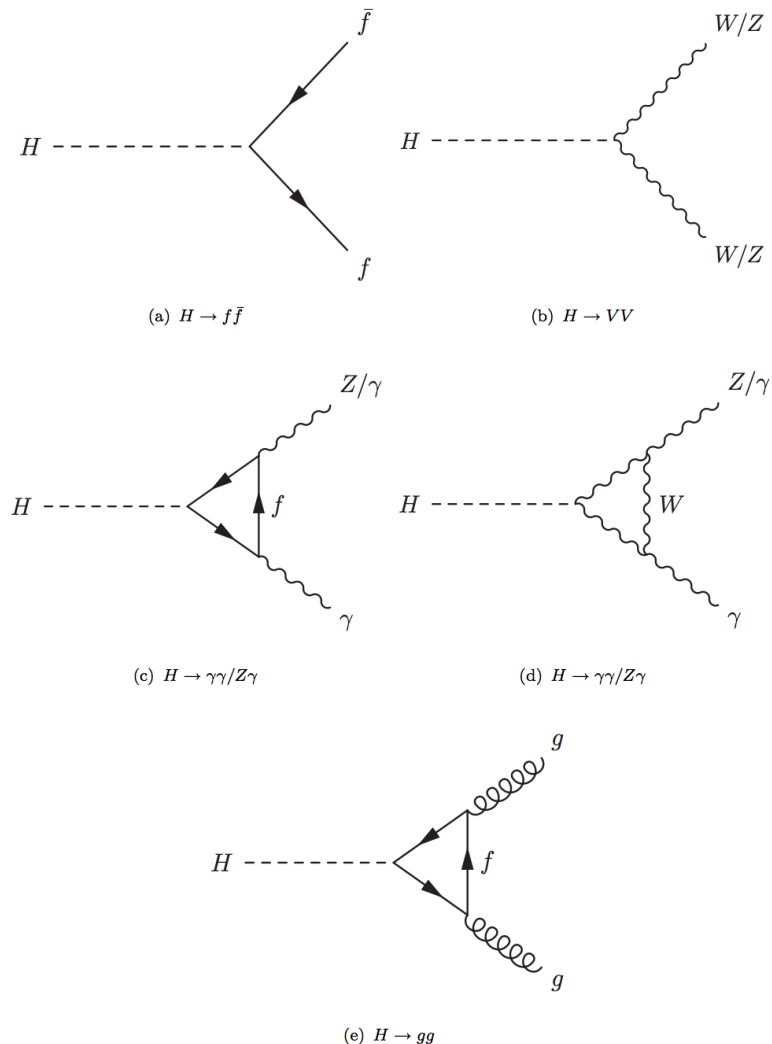


Fig. 2.9 SM Higgs decay channels.

901

902 decaying into different final states as a function of Higgs mass is shown in figure 2.10.

2.2.3 Diboson physics at the LHC

The study of diboson physics is another important test for SM of particle physics in electroweak sector, while the Vector Boson Scattering (VBS) is a key process for probing the mechanism of the electroweak symmetry breaking (EWSB). In the meantime, the non-resonant diboson productions are crucial backgrounds for Higgs studies at the LHC, which make the precise measurement of their cross section becomes very important.

909 Diboson productions

About 90% of diboson productions at hadron collider is from quark-antiquark annihilation, while others are from gluon initiated process. Figure 2.11 shows the tree-level

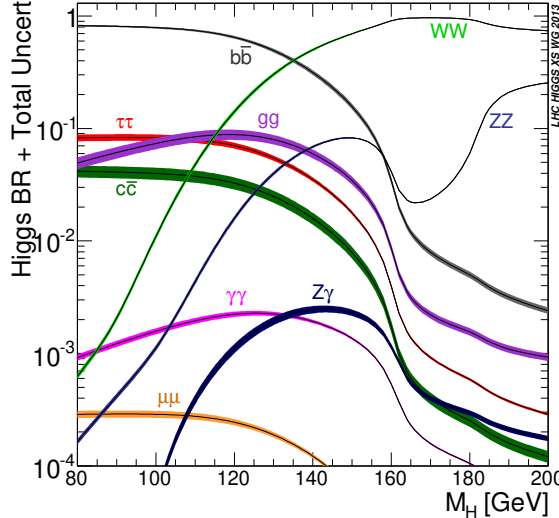


Fig. 2.10 Branching ratio of Higgs decays in various channels as a function of Higgs mass^[14].

Feynman diagrams of diboson production. Then figure 2.12 illuminates the total produc-

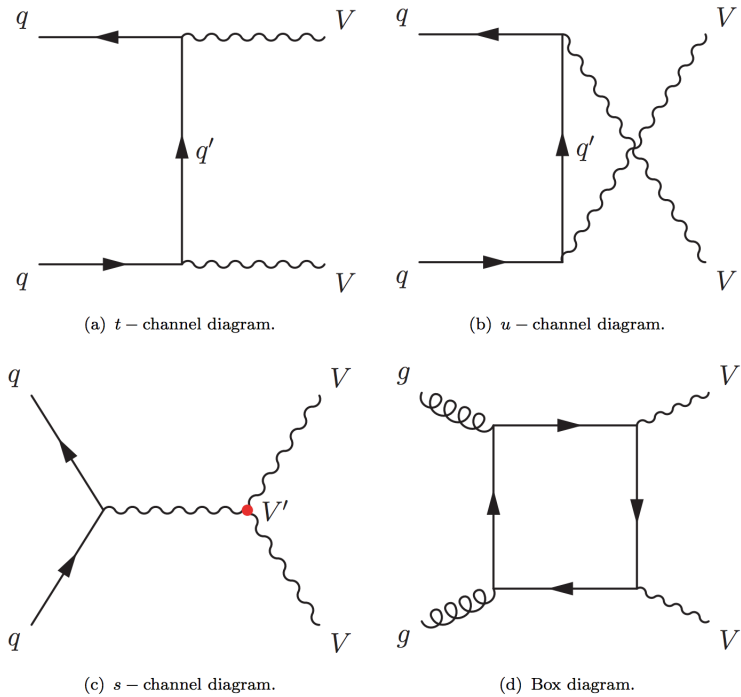


Fig. 2.11 The tree-level Feynman diagrams of diboson production at the LHC.

912

913 tion cross-section presented by ATLAS as a function of centre-of-mass energy \sqrt{s} from
 914 7 to 13 TeV for several diboson processes compared to some other major processes in
 915 hadron collision. The cross section for diboson processes are calculated at next-to-next
 916 leading order (NNLO).

917

Vector boson scattering

918 The $SU(2)_L \times U(1)_Y$ structure in SM predicts self-interactions between electroweak
 919 gauge bosons. Those self-couplings can involve either three or four gauge bosons at a

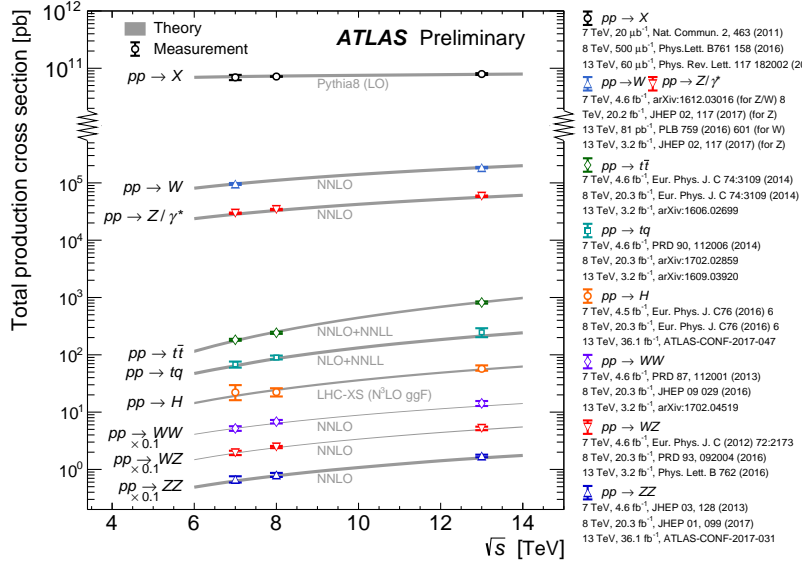


Fig. 2.12 Total production cross-section presented by ATLAS as a function of centre-of-mass energy \sqrt{s} from 7 to 13 TeV for some selected processes, the diboson measurements are scaled by a factor 0.1 to allow a presentation without overlaps.

single vertex, known as triple gauge coupling (*TGC*) or quartic gauge couplings (*QGC*), respectively. Vector boson scattering (*VBS*) is carried out by four electroweak vector bosons, namely Z , W^\pm and photon (γ) as the Feynman diagrams shown in figure 2.13. And the vertexes include either those self-interactions or the interactions with the Higgs boson are described in figure 2.14.

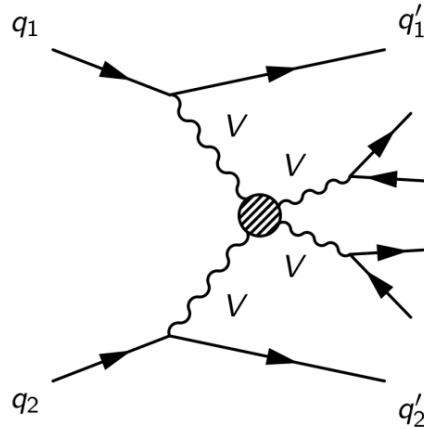


Fig. 2.13 Feynman diagrams of the vector boson scattering.

924

925 The amplitudes of leading-order (LO) VBS can be expressed as^[15]:

$$iM_{TGC}^{s-channel} = -i \frac{g_1^2}{4m_W^4} [s(t-u) - 3m_W^2(t-u)] \quad (2.29)$$

$$iM_{TGC}^{t-channel} = -i \frac{g_1^2}{4m_W^4} \left[(s-u)t - 3m_W^2(s-u) + \frac{8m_W^2}{s} u^2 \right]$$

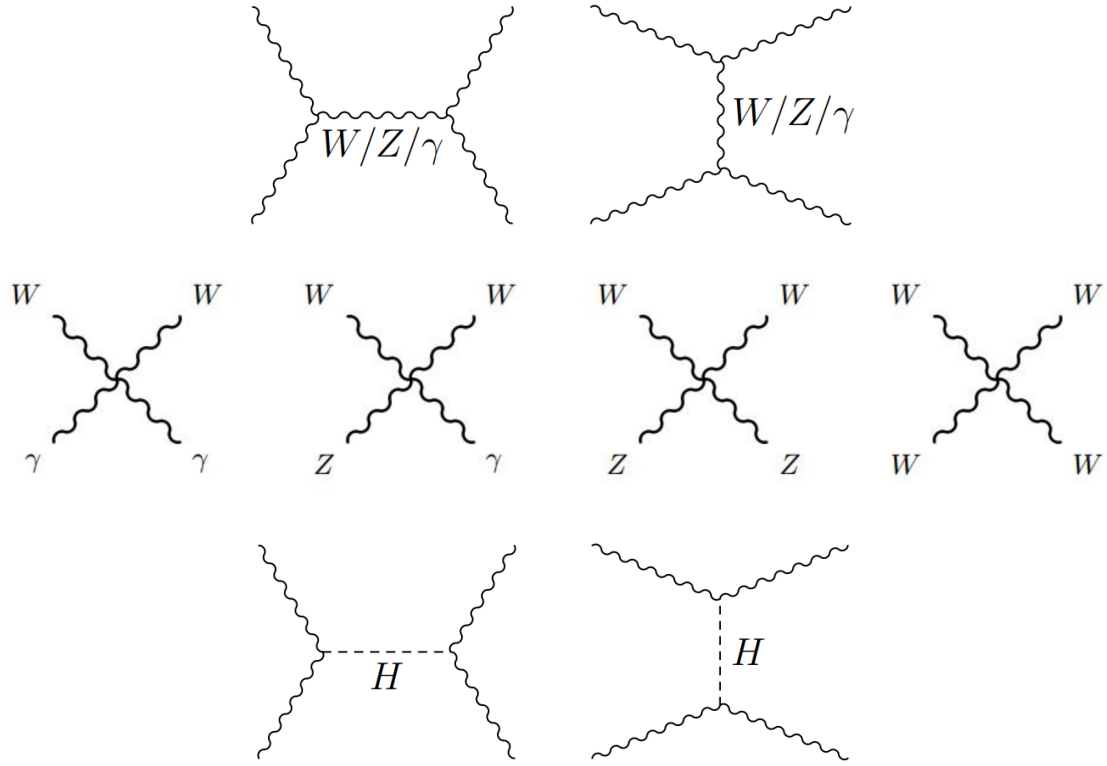


Fig. 2.14 Feynman diagrams of vertexes involving QGC, TGC and Higgs.

$$iM_{QGC} = i \frac{g_1^2}{4m_W^4} \left[s^2 + 4st + t^2 - 4m_W^2(s+t) - \frac{8m_W^2 ut}{s} \right] \quad (2.30)$$

$$\begin{aligned} iM_{Higgs} &= -i \frac{C_v^2 g_1^2}{4m_W^2} \left[\frac{(s-2m_W^2)^2}{s-m_H^2} + \frac{(t-2m_W^2)^2}{t-m_H^2} \right] \\ &\simeq -i \frac{C_v^2 g_1^2}{4m_W^2} (s+t) \end{aligned} \quad (2.31)$$

926 Combining s- and t-channel of TGC in Eq. 2.29 and the QGC term in Eq. 2.30:

$$iM_{TGC} + iM_{QGC} = i \frac{g_1^2}{4m_W^2} (s+t) + O((s/m_W^2)^0) \quad (2.32)$$

927 In Eq. 2.32, the amplitude grows as a function of centre-of-mass energy (\sqrt{s}), which
928 violates the unitarity in the TeV region. Considering the Higgs term in Eq. 2.31 can
929 perfectly cancel out this growing, and the remaining term $O((s/m_W^2)^0)$ only depends on
930 the total amplitude in SM.
931

932 In conclusion, the Higgs boson acts as "moderator" to unitarize high-energy longi-
933 tudinal vector boson scattering as introducing the Higgs restores the unitarity of total
934 amplitude in high energy region.

Chapter 3 The Large Hadron Collider and the ATLAS Detector

937 3.1 The Large Hadron Collider

Located near the French-Swiss border at the European Organization for Nuclear Research (CERN), the Large Hadron Collider (LHC) is the world's largest and most powerful particle collider. It's the proton-proton collider with the centre-of-mass energy up to 14 TeV. The beams inside the LHC are made to collide at four locations around its 27-kilometer accelerator ring, corresponding to the positions of four particle detectors - ATLAS, CMS, ALICE and LHCb. With its unprecedented energy, the LHC is designed to observe physics that involve highly massive particles, which have never been observed in previous accelerators with lower energies.

3.1.1 Operation history and machine layout

Operation history

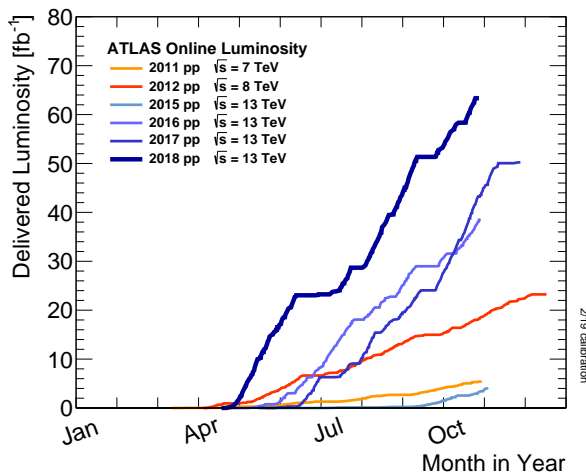
The LHC^[16-19] is a two-ring-superconducting-hadron accelerator and collider lies in a tunnel 27 kilometres in circumference and as deep as 175 metres underground. It's designed to provide proton-proton (pp) collisions at the centre-of-mass energy (\sqrt{s}) up to 14 TeV with a unprecedented luminosity of $10^{34} \text{ cm}^{-2} \text{ s}^{-1}$. In the meantime, it can also collide heavy (Pb) ions with an energy of 2.8 TeV per nucleon and a peak luminosity of $10^{27} \text{ cm}^{-2} \text{ s}^{-1}$. Table 3.1 shows the main design parameters of the LHC for proton-proton collisions.

The LHC was built from 1998 to 2008. It started its first beam in September 2008, but then was interrupted by a quench incident only after a few days running. Then it resumed the operation in November 2009 with a low energy beams. From March 2010, physics runs took place at the centre-of-mass energy of 7 TeV. Later on, this energy was increased in 2012 to $\sqrt{s} = 8$ TeV, with an integrated luminosity of 20.3 fb^{-1} , and this period is called “run-1”. After run-1, the LHC was shut down for two years for hardware maintenance and upgrade, starting from February 2013.

The second operation period with higher centre-of-mass energy at 13 TeV started from 2015 called “run-2”. And it continued to the end of 2018 with total integrated luminosity reaching about 147 fb^{-1} for ATLAS experiment. Figure 3.1 shows the cumulative luminosity as a function of time in month delivered to ATLAS experiment during stable beams in years from 2011 to 2018.

Table 3.1 Summary of design parameters of the LHC for pp collisions.

Circumference	26.7 km
Beam energy at collision	7 TeV
Beam energy at injection	0.45 TeV
Dipole field at 7 TeV	8.33 T
Luminosity	$10^{34} \text{ cm}^{-2} \text{ s}^{-1}$
Beam current	0.56 A
Protons per bunch	1.1×10^{11}
Number of bunches	2808
Nominal bunch spacing	24.95 ns
Normalized emittance	$3.75 \mu\text{m}$
Total crossing angle	$300 \mu\text{rad}$
Energy loss per turn	6.7 keV
Critical synchrotron energy	44.1 eV
Radiated power per beam	3.8 kW
Stored energy per beam	350 MJ
Stored energy in magnets	11 GJ
Operating temperature	1.9 K

**Fig. 3.1 Cumulative luminosity as a function of time in years from 2011 to 2018 for ATLAS detector.**

967 Machine layout

968 The layout of CERN accelerator complex is shown in figure 3.2. The protons are
 969 accelerated by a series of machines before being injected into the main ring. At begin-
 970 ning, the 50 MeV protons are produced in the linear particle accelerator LINAC2, and
 971 further accelerated to 1.4 GeV in Proton Synchrotron Booster (PSB). The protons are

then injected into the Proton Synchrotron (PS) to gain the energy of 26 GeV and further accelerated to 450 GeV in Super Proton Synchrotron (SPS). At the end, they are injected into the main ring, and can reach a maximum energy of 7 TeV.

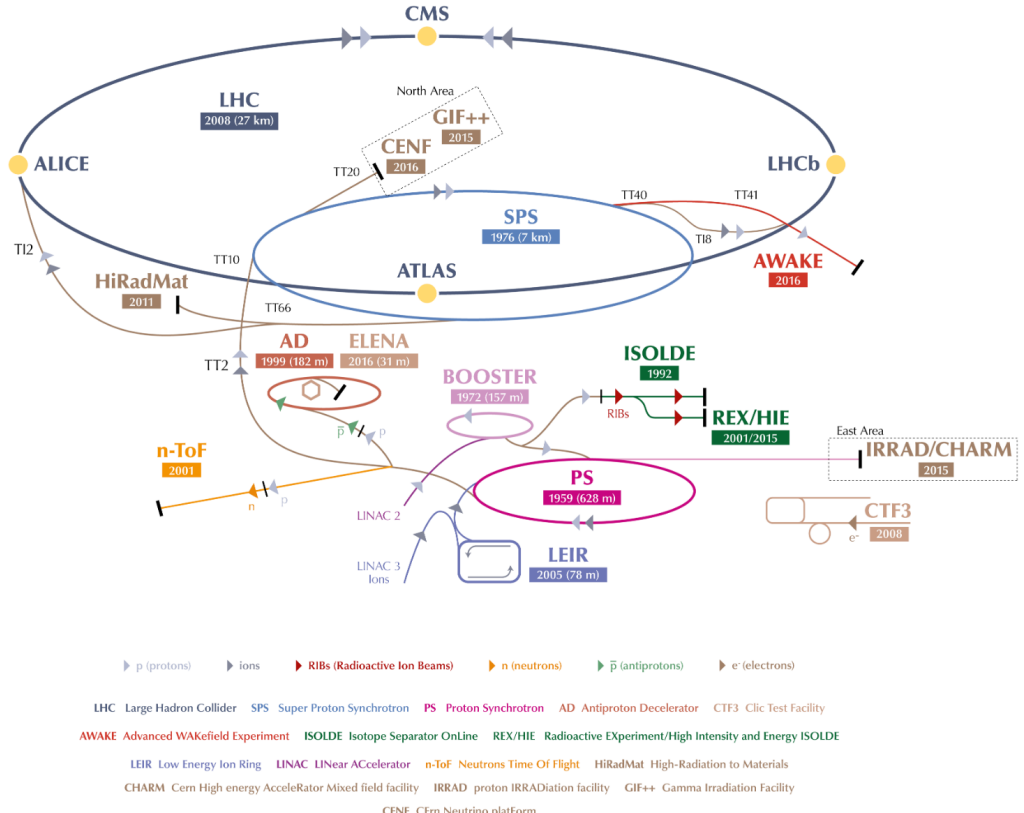


Fig. 3.2 CERN accelerator complex^[20].

The collisions can occur in 4 points, with corresponding 4 major detector experiments that are briefly described as follows:

- **ATLAS:** A Toroidal LHC ApparatuS, one of the two general-purpose particle detector experiments and detector with largest volume at the LHC. It is designed to search for the Higgs boson, test the stardand model of particle physics and search for possible beyond SM physics.
- **CMS:** Compact Muon Solenoid, another large general-purpose particle physics detector, with the same physics goal (also cross check) as ATLAS.
- **ALICE:** A Large Ion Collider Experiment, it is optimized to study heavy-ion ($Pb-Pb$ nuclei) collisions at a centre-of-mass energy of 2.76 TeV per nucleon pair.
- **LHCb:** Large Hadron Collider beauty, it is a specialized b-physics experiment, designed primarily to measure the parameters of CP violation in the interactions of b-hadrons.

3.1.2 Luminosity and pile-up

Luminosity

In beam-beam collisions, the event rate for a process is given by^[19]:

$$N = \mathcal{L}\sigma \quad (3.1)$$

where σ is the cross section of the process, and \mathcal{L} is the luminosity. For the studies of rare events, \mathcal{L} must be as high as possible. The luminosity only depends on the beam parameters, and can be written as:

$$\mathcal{L} = \frac{N_b^2 n f_r \gamma}{4\pi \epsilon_n \beta^*} \quad (3.2)$$

where N_b denotes the number of particles per bunch, n is the number of bunches per beam, f_r is the revolution frequency, γ represents relativistic γ factor, ϵ_n is the normalized transverse emittance and β^* denotes the β function at the collision point. To reduce the beam-beam interaction effects, the bunches must have a crossing angle, which produces a geometrical luminosity reduction factor F :

$$F = 1/\sqrt{1 + \left(\frac{\theta_c \sigma_Z}{2\sigma^*}\right)} \quad (3.3)$$

where θ_c denotes the crossing angle at the interaction point, σ_Z is the root mean square (RMS) bunch length and σ^* is the transverse RMS beam size at crossing point.

The luminosity expressed in Eq. 3.2 is normally the instantaneous luminosity. In fact the running conditions usually vary with time, so the luminosity can change as well. To take into account the time dependence, integrated luminosity is invited, by integrating the instantaneous luminosity over time:

$$L = \int \mathcal{L}(t) dt \quad (3.4)$$

The unit of integrated luminosity we commonly use is b^{-1} that satisfying $1b^{-1} = 10^{24} cm^{-2}$. Figure 3.3 shows integrated luminosity as a function of time delivered to ATLAS (green), recorded by ATLAS (yellow), and certified to be good quality data (blue) during run-2 pp collisions. For most physics analysis, the data with good quality (require to satisfy *Good Run List*) is used.

Pile-up

In collisions, multiple interactions can happen in one single bunch crossing, which is called “pile-up”. The variable $\langle \mu \rangle$, representing the average number of interactions per

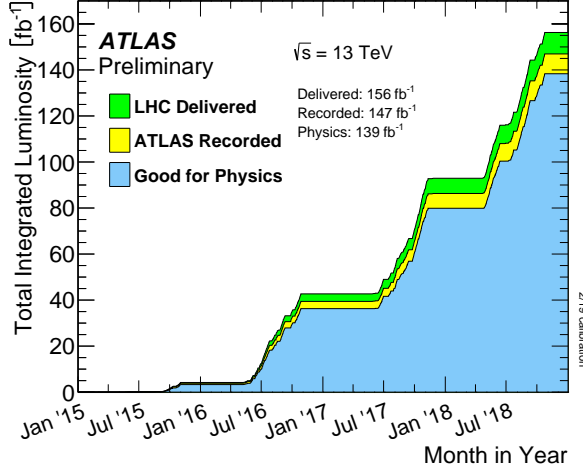


Fig. 3.3 Integrated luminosity in ATLAS.

bunch crossing, is defined to describe pile-up effect:

$$\langle \mu \rangle = \frac{L_{tot}\sigma}{f_r n_{bunch}} \quad (3.5)$$

where L_{tot} is the instantaneous luminosity, σ is the inelastic cross section, f_r is the LHC revolution frequency and n_{bunch} is the number of colliding bunches. Normally, with increasing luminosity, the pile-up becomes more significant. Figure 3.4 shows the luminosity-weighted distribution of the mean number of interactions per crossing for pp collision data from 2015 to 2018 (full run-2), the challenge of pile-up increased in each year.

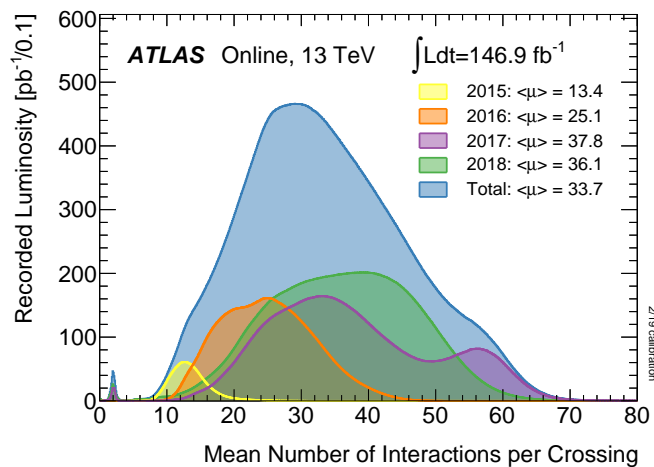


Fig. 3.4 Number of Interactions per Crossing from 2015-2018 in ATLAS.

1019

1020 **3.2 ATLAS detector**

1021 **3.2.1 Detector overview**

1022 ATLAS (A Toroidal LHC ApparatuS) is the largest volume detector ever constructed
 1023 for a particle collider. It is a cylinder with 46 meters long, 25 meters in diameter, and sits
 1024 in a cavern 100 meters below ground. The detector contains about 3000 km of cables and
 1025 it weights 7000 tonnes.

1026 This paragraph briefly summarizes the coordinate system and nomenclature used to
 1027 describe the ATLAS detector^[21]. As depicted in figure 3.5, we define the nominal inter-
 1028 action point as the origin of the coordinate system, the beam direction as the z -axis and
 1029 the x - y plane is transverse to the beam direction. The positive x -axis is defined to be the
 1030 direction pointing to the center of the LHC ring, while the positive y -axis is pointing up-
 wards. There are two sides of detector A and C, in which A (C) -side is in the positive

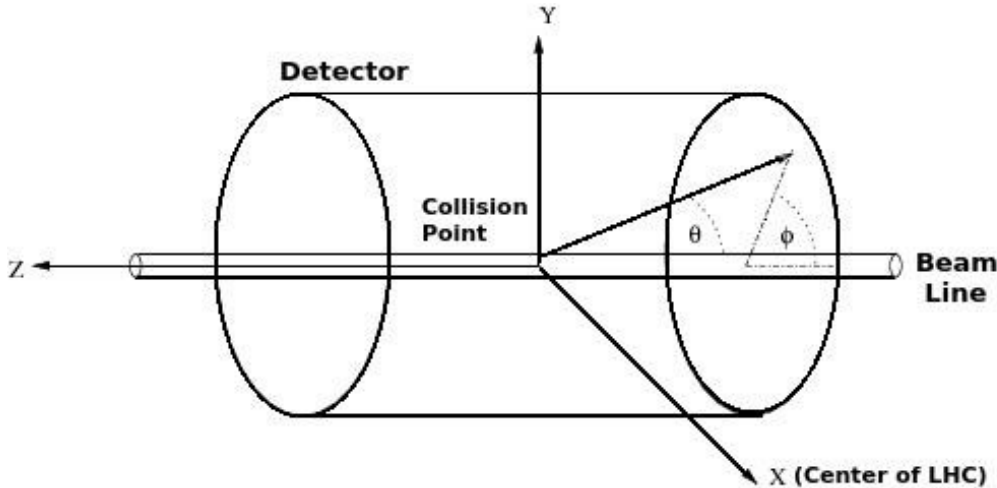


Fig. 3.5 Coordinate system used by the ATLAS experiment at the LHC^[21].

1031
 1032 (negative) z direction. The azimuthal angle ϕ is measured as usual around the beam axis,
 1033 while the polar angle θ is the angle from the beam axis. In physics analysis, we usually
 1034 use the pseudorapidity instead of θ angle, which is designed as $\eta = -\ln \left[\tan \left(\frac{\theta}{2} \right) \right]$.

1035 For massive objects (eg. jets), the rapidity $y = \frac{1}{2} \ln \left[\frac{E+p_z}{E-p_z} \right]$ is used. In addition, the
 1036 transverse momentum p_T , transverse energy E_T and the missing transverse energy E_T^{miss}
 1037 are defined in x - y plane. The ΔR , a commonly used distance measurement, is defined in
 1038 the pseudorapidity-azimuthal angle space as $\Delta R = \sqrt{\Delta\eta^2 + \Delta\phi^2}$.

1039 The overall ATLAS layout is shown in figure 3.6, which is forward-backward sym-
 1040 metric with respect to the interaction point. The magnet configuration comprises a thin
 1041 superconducting solenoid surrounding the inner-detector cavity, and three large super-
 1042 conducting toroids (one barrel and two end-caps) arranged with an eight-fold azimuthal

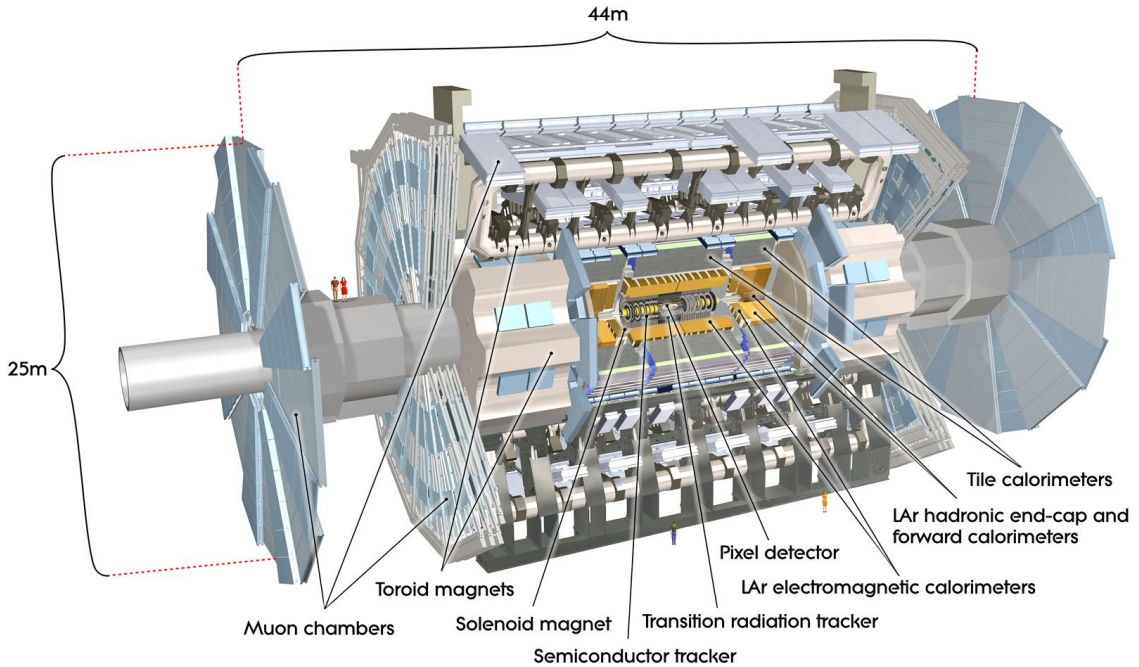


Fig. 3.6 Cut-away view of the ATLAS detector^[23].

1043 symmetry around the calorimeters.

1044 **The inner detector**, which is the innermost part of ATLAS, is immersed in a 2 T
 1045 solenoidal magnetic field. It's used for pattern recognition, momentum and vertex mea-
 1046 surements and electron identification, with the combination of tracking system.

1047 **The calorimeter** is outside the solenoid, for electromagnetic and hadronic en-
 1048 ergy measurements. The high granularity liquid-argon (LAr) electromagnetic sampling
 1049 calorimeters is used to measure energy and position with range up to $|\eta| < 3.2$ for
 1050 electrons and photons. For hadron, a scintillator-tile calorimeter is used in the range of
 1051 $|\eta| < 1.7$, and the liquid-argon hadronic endcap calorimeters (HEC) is used in end-cap re-
 1052 gion. And then the LAr forward calorimeters provide both electromagnetic and hadronic
 1053 energy measurements with the coverage in forward region up to $|\eta| = 4.9$.

1054 **The muon spectrometer** is the outermost layer. It's a air-core toroid system, with
 1055 a long barrel and two inserted end-cap magnets that provides strong bending power in a
 1056 large volume within a light and open structure. A set of chambers measuring the tracks
 1057 of muons with high spatial precision and accurate time-resolution are used. Multiple-
 1058 scattering effects are minor, and excellent muon momentum resolution can be achieved.

3.2.2 Physics requirement

As mentioned previously, ATLAS is one of two general-purpose particle detector experiment at the LHC. It's designed to take advantage of the unprecedented energy at the LHC, as the discovery of Higgs boson is one of its benchmark. Lots of precise tests and measurements of SM physics are ongoing with ATLAS experiment. While, in the meantime, ATLAS is also designed to observe the phenomena that involve highly massive particles, which can also explore the possibility of extra dimensions proposed by several models in TeV region. To fulfil many diverse physics goals, a set of general requirements are needed:

- The high-speed and radiation-hard electronics are required due to the experimental conditions at the LHC.
- High detector granularity is needed to reduce the overlapping events and handle the particle fluxes.
- Large acceptance in pseudorapidity and azimuthal angle coverage is needed.
- For inner detector, good charged-particle momentum resolution and reconstruction efficiency are crucial. And the vertex detectors close to the interaction region are required to be able to observe secondary vertices for offline tagging of τ -lepton and b -jets.
- Good electromagnetic (EM) calorimetry for electron and photon, as well as full-coverage hadronic calorimetry for accurate jet and missing transverse energy measurements, are essentially required, since these measurements form the basis of many studies.
- Good muon spectrometer is also required for muon identification and momentum measurement over a wide range of momenta.
- Highly efficient but with sufficient background rejection triggers are also needed and extremely important for objects with low transverse-momentum.

More detailed descriptions of each sub-system will be given in the following subsections.

3.2.3 Magnet system

A strong magnetic field is required for precise measurement of charged particle momenta. The ATLAS detector uses two large superconducting magnet systems, a hybrid system of a central superconducting solenoid and three outer superconducting toroids, to bend charged particles^[24]. The total magnet system is 22 m in diameter and 26 m in length as shown in figure 3.7.

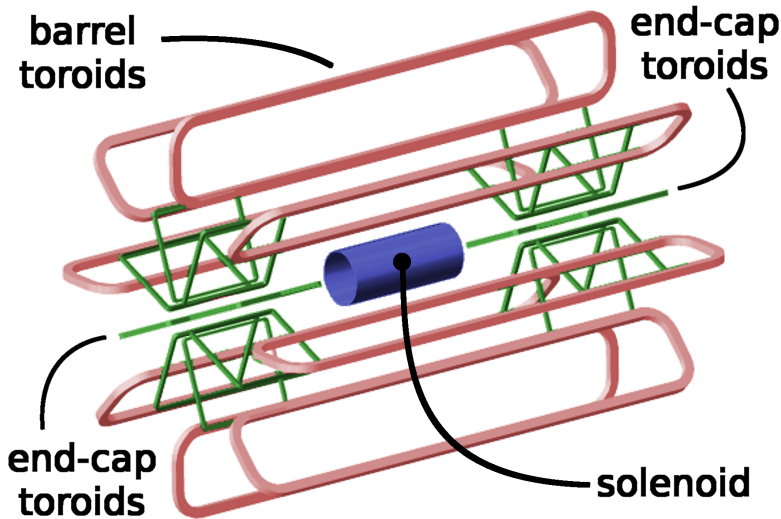


Fig. 3.7 Schematic diagram of the ATLAS magnet system.

1093 The central solenoid produces two Tesla (T) magnetic field surrounding the inner De-
 1094 tector. When obtaining such high field strength, at the same time, the solenoid needs to
 1095 be thin in order to reduce the material in front of the calorimeter.

1096 The outer toroid system comprises one barrel superconducting toroid and two end-
 1097 caps. The barrel one is composed of eight coils encased in individual racetrack-shaped,
 1098 stainless-steel vacuum vessels and produces the magnetic field in the cylindrical volume
 1099 surrounding the calorimeters. Each end-cap toroid consists of a single cold mass built up
 1100 from eight flat, square coil units and eight keystone wedges and provides a magnetic field
 1101 of approximately 1 T for the muon detectors in the end-cap regions.

1102 3.2.4 Inner detector

1103 The inner detector, as shown in figure 3.8, is the detector closest to beam pipe. It's
 1104 used to measure the position of charged particle tracks in high precision together with
 1105 good momentum resolution, among which the measurement of primary and secondary
 1106 vertices and electron identification are especially important. Due to the extremely high
 1107 luminosity produced by the LHC, the precise measurements of vertex and momentum
 1108 becomes tough and fine-granularity detectors are crucial. The inner detector consists of
 1109 three subdetectors described as below:

1110 **Pixel detector**

1111 The pixel detector^[26] is the innermost part of ATLAS tracking system. With finest
 1112 granularity of materials, it has the best spatial resolution and 3-dimensional space-point
 1113 measurement in inner detector. ATLAS Pixel Detector for the LHC run-2 is composed of
 1114 4 layers of barrel pixel detector and two end-caps with three pixel disks each, as shown in

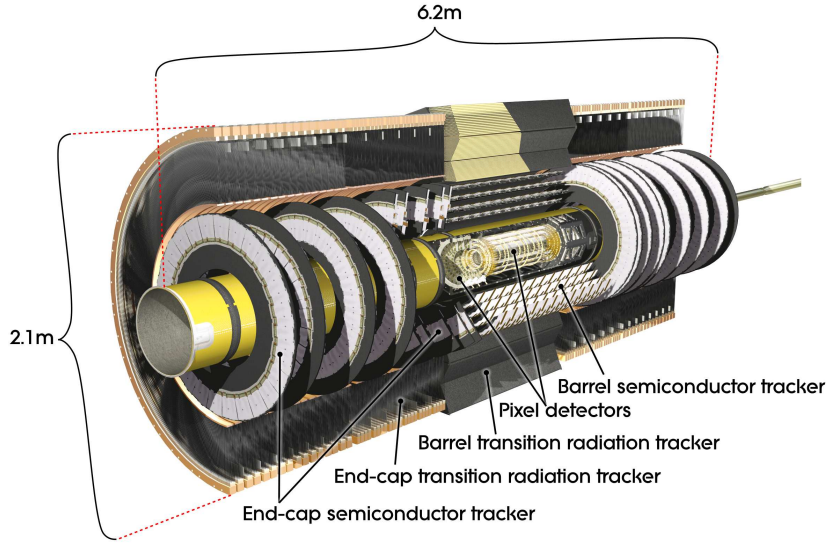


Fig. 3.8 Schematic diagram of the ATLAS inner detector^[25].

figure 3.9. There are three outer layers that originally installed for run-1 and one additional layer called Insertable B-Layer (IBL) that newly constructed in run-2^[27]. Now the 4-layer pixel detector has very good reconstruction of primary and secondary vertices, which is even crucial for long-lived particles like τ -lepton and b-quark.

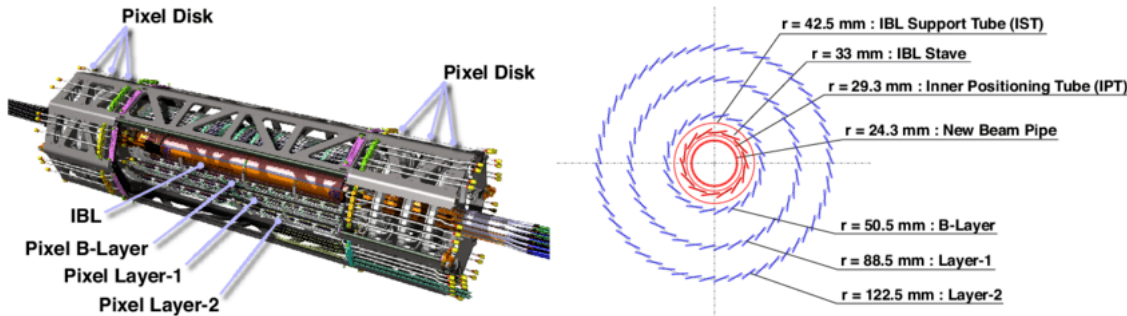


Fig. 3.9 Schematic diagram of the ATLAS 4-Layer Pixel Detector.

Semiconductor Tracker

The Semiconductor Tracker (SCT)^[28] installed outside the pixel detector is the middle component of the inner detector. It has similar function as pixel detector but with long and narrow strips instead of small pixels, which makes a much larger coverage than pixel detector. The SCT consists of 4088 modules, and contains four concentric layers in barrel (2112 modules) and nine disks in each of the two end-caps (1976 modules) as shown in figure 3.10. And it measures particles over a large area with 6.3 million readout channels and a total area of 61 square meters. The SCT is the most critical part of the inner detector for 2D track hit reconstruction. In barrel, the hit precision is $17 \mu\text{m}$ in the $r\phi$ coordinate and $580 \mu\text{m}$ in z coordinate. In end-caps, the precision is $17 \mu\text{m}$ in the $z\phi$ coordinate and $580 \mu\text{m}$ in r coordinate.

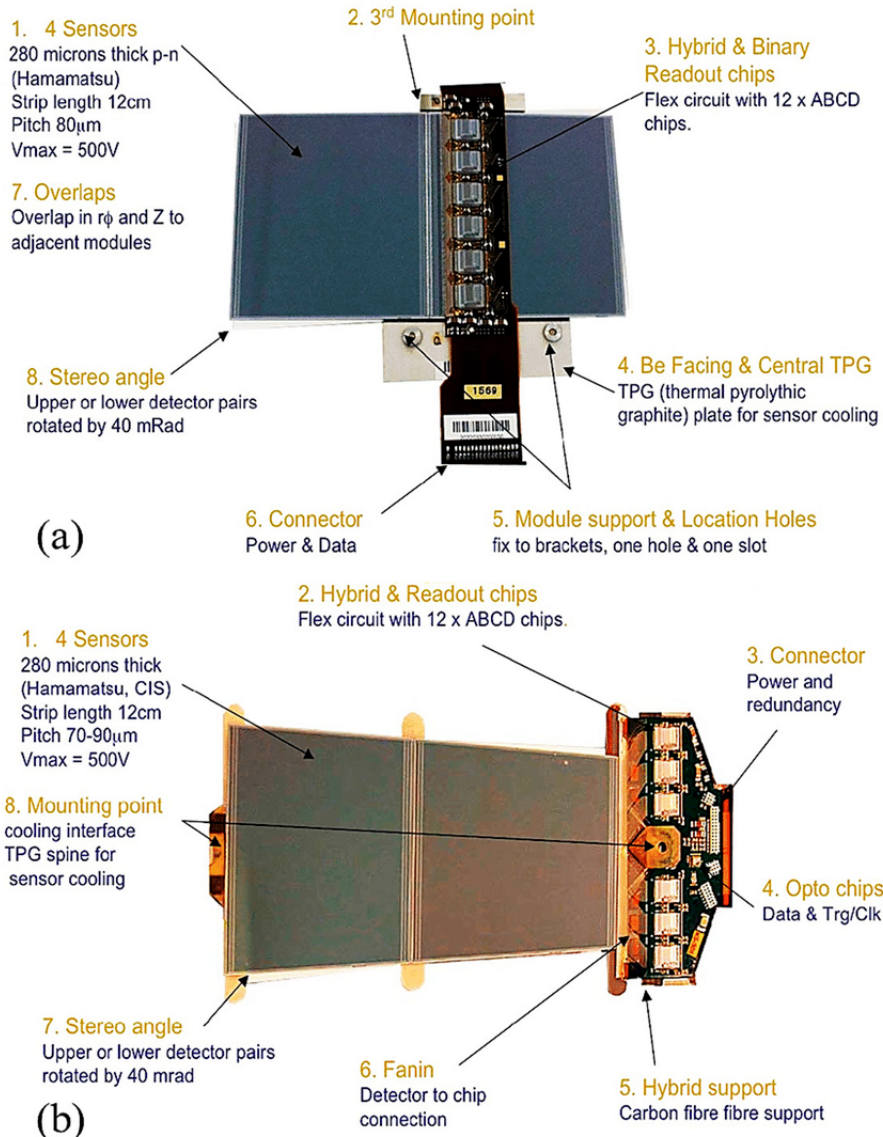


Fig. 3.10 SCT (a) barrel module and (b) end-cap^[29].

Transition radiation tracker

The transition radiation tracker (TRT)^[30] is the outermost part of inner detector, which has a very different design comparing to the two previously described sub-detectors. It can be separated into three parts: one barrel and two end-cap regions with the $|\eta|$ coverage up to 2.0. There are 73 barrel layers and 224 end-cap layers (112 in each) with 372000 straws in total, and about 351000 readout channels for TRT. The TRT provides better z resolution but much worse $r\phi$ resolution (about 130 μ m) comparing to the pixel detector and SCT per straw. But the straw hits still make significant contributions to momentum measurement, since its lower precision per point (compared to silicon) can be compensated by the large number of measurements and long track length.

3.2.5 Calorimeters

The calorimeters are designed to measure the energy from particles by absorbing them. They are located outside the solenoidal magnet that surrounds the inner detector. The ATLAS calorimeters are comprised of a number of sampling calorimeters with full ϕ -symmetry and the pseudorapidity range of $|\eta| < 4.9$. Figure 3.11 shows the layout of the ATLAS calorimeter system. There are two basic calorimeter systems: an inner electromagnetic (EM) calorimeter and an outer hadronic calorimeter. The EM calorimeter is designed for precise measurements of electrons and photons with fine granularity; while the hadronic one has relative coarser granularity but satisfies the physics requirements for jets reconstructions and E_T^{miss} measurements. Two different sampling techniques are used, the EM calorimeter is purely based on liquid-argon (LAr) technology, while the hadronic one uses both LAr and scintillating tiles calorimeters. More details are described as below:

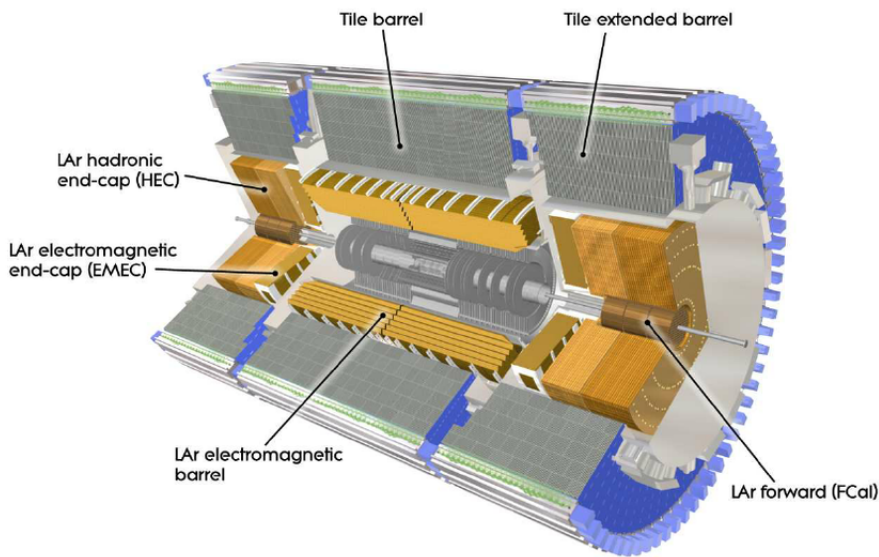


Fig. 3.11 Cut-away view of the ATLAS calorimeters. The LAr calorimeters are seen inside the scintillator-based tile hadronic calorimeters^[31].

Liquid Argon calorimeter

The LAr calorimeter uses liquid-argon as active medium. The LAr sampling calorimeter technique with “accordion-shaped” electrodes is used for all electromagnetic calorimetry covering the pseudorapidity range of $|\eta| < 3.2$; and for hadronic calorimetry with range from $|\eta| = 1.4$ to the acceptance limit $|\eta| = 4.9$ ^[32]. Figure 3.12 depicts a segment of the barrel calorimeter, which had “accordion-shaped” electrodes and absorber. For barrel EM calorimeter, the absorbing material is lead-liquid argon, while the hadronic end-cap calorimeter uses copper plates. In addition, the forward calorimeter is split into

1161 three parts, an EM sector in which copper is used as absorbing material and two hadronic sectors using tungsten outside the EM sector.

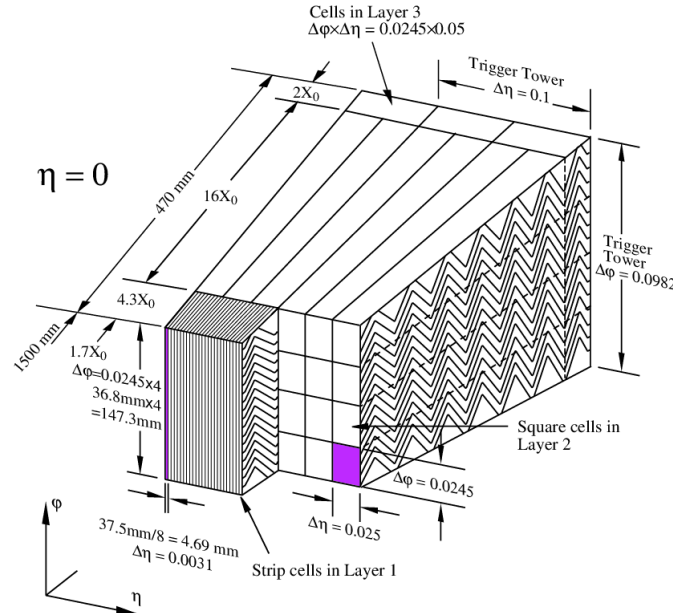


Fig. 3.12 Schematic diagram of a LAr EM calorimeter barrel module.

1162

1163 Tile calorimeter

1164 Tile calorimeter is a sampling calorimeter using scintillating plates as active medium
 1165 and steel as absorber. It consists of three sections: the central barrel with the pseudorapidity range of $|\eta| < 1.0$ and two extended barrels with $0.8 < |\eta| < 1.7$. Figure 3.13 shows
 1166 the design of one tile calorimeter module. It's used for energy reconstruction of jets and
 1167 E_T^{miss} measurement by combining the measurements with the end-cap and forward LAr
 1168 hadronic calorimeter.
 1169

1170

3.2.6 Muon spectrometer

1171 Muon spectrometer^[34] is the outermost part of the ATLAS detector with an extremely
 1172 large tracking system. It measures a large range of muon momentum, and the accuracy is
 1173 about 3% at 100 GeV and 10% at 1 TeV. The muon spectrometer comprises three main
 1174 parts: a magnetic field produced by three toroidal magnets; a set of chambers measur-
 1175 ing the tracks of muons with high spatial precision; and triggering chambers with accu-
 1176 rate time-resolution. Figure 3.14 shows the schematic of ATLAS muon spectrometer that
 1177 consists of four types of muon chambers (*MDT*, *CSC*, *RPC*, *TGC*) as well as the magnet
 1178 systems (barrel and end-cap toroid).

1179

More details of four chambers are given as below:

1180

- **Monitored Drift Tubes (MDT).** MDTs provide the precise momentum measure-

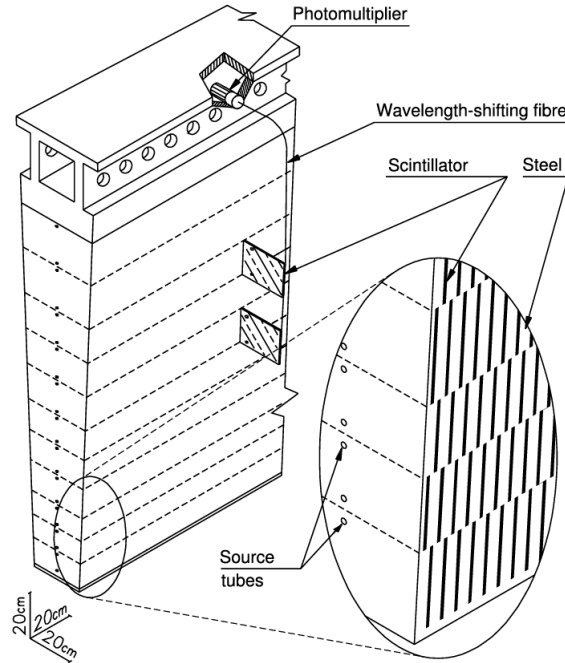


Fig. 3.13 Schematic diagram of tile calorimeter module^[33].

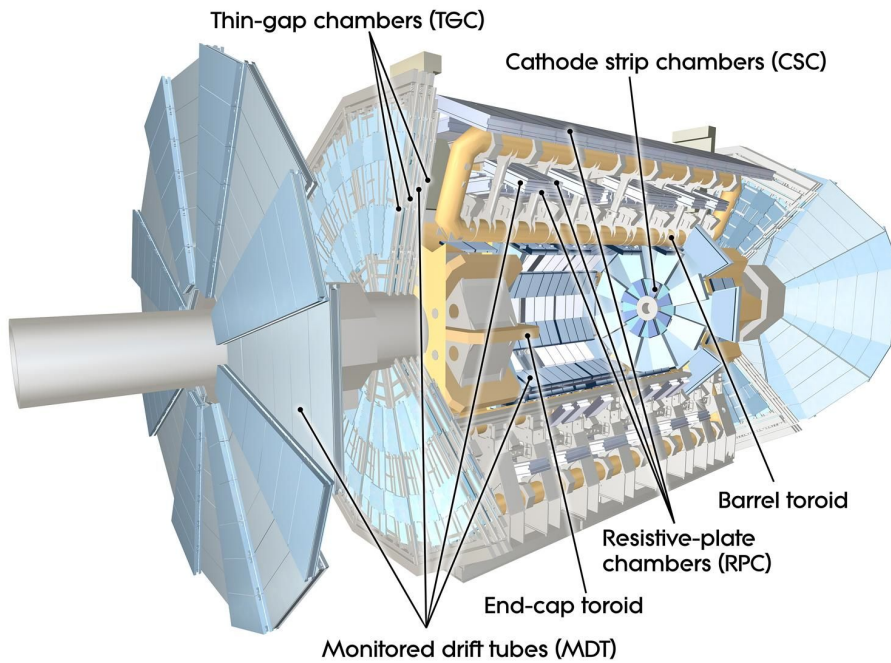


Fig. 3.14 Cut-away view of the ATLAS muon spectrometer^[35].

ment with the $|\eta|$ range up to 2.7, except in the innermost end-cap layer where the coverage is limited to $|\eta| < 2.0$. The chambers comprises three or four layers of drift tubes, with a diameter of 29.970 mm, operated with Ar/CO₂ gas (93/7) at 3 bar. The average resolution can reach 80 μm per tube and 30 μm per chamber.

- **Cathode strip chambers (CSC).** CSCs are used in the forward region of $2 < |\eta| < 2.7$ in the innermost tracking layers, due to their good time resolution and high

rate capability. The CSCs are multi-wire proportional chambers (MWPC) with the cathode planes segmented into strips in orthogonal directions, which allows both coordinates to be measured from the induced-charge distribution. The resolution of a chamber is about $40 \mu\text{m}$ for bending plane and 5 mm for the transverse plane.

- **Resistive plate chambers (RPC).** The RPCs serve as fast triggers in the barrel region of $|\eta| < 1.05$ due to the high rate capability and good spatial and time resolution. It is a gaseous parallel electrode-plate detector without any wires. There are three concentric cylindrical layers around the beam axis, as three trigger stations. Each station consists of two independent layers to measure the transverse coordinates of η and ϕ .
- **Thin gap chambers (TGC).** TGCs are used as trigger system for the end-cap region of $1.5 < |\eta| < 2.4$, and works based on the same principle as multi-wire proportional chambers. In addition, they can also provide the second azimuthal coordinate to complement the measurement of MDT in bending direction.

3.2.7 Trigger system

Trigger system in ATLAS is a very essential component, which is responsible for deciding whether to keep a given collision event for later study or not. In the LHC run-2, higher energy, luminosity and pile-up lead to a large increase of event rate by up to a factor of five, which causes to a even larger challenge and more strict requirement of trigger system.

The trigger system in run-2 consists of a hardware-based first level trigger (Level-1) and a software-based high level trigger (HLT)^[36]. As depicted in figure 3.15, in Level-1, the inputs from coarse granularity calorimeter and muon detector information together with some other subsystems are sent to the Central Trigger Processor to determine Regions-of-Interest (RoIs) in the detector. The event rate can be reduced by Level-1 triggers from 30 MHz to 100 kHz. After that, the RoI information from Level-1 is sent to HLT, in which more sophisticated selection algorithms are run for regional reconstruction. The HLT reduces the rate from Level-1 from 100 kHz to about 1 kHz on average. At the end, the events that accepted by HLT are transferred to local storage at experimental site for offline reconstruction. Details about Level-1 and HLT trigger systems are described as below:

Level-1 trigger

Substantial upgrades have been delivered in ATLAS Level-1 trigger system for run-2 data taking. The upgrades took place in both hardware and detector readout, allow the

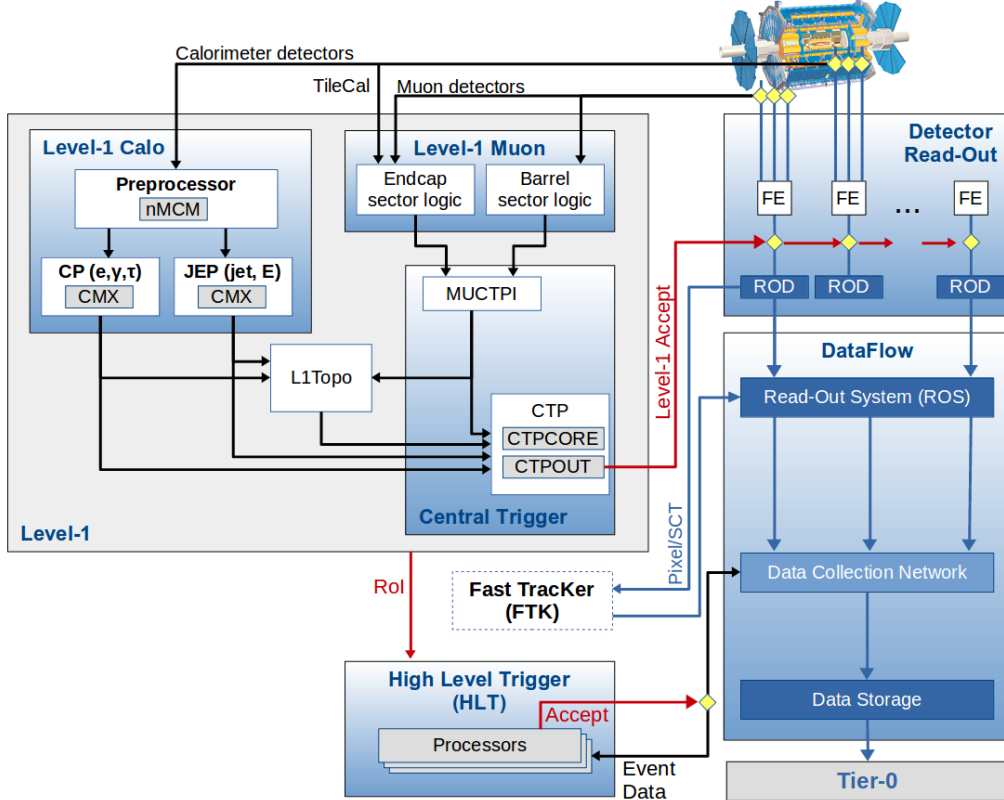


Fig. 3.15 Schematic diagram of the ATLAS trigger and data acquisition system in run-2.

trigger rate increasing from 70 kHz (in run-1) to 100 kHz (in run-2). There are two major parts of Level-1 triggers, including Level-1 calorimeter (L1calo) trigger and Level-1 muon (L1mu) trigger.

Level-1 Calorimeter trigger uses the reduced granularity information from the electromagnetic and hadronic calorimeters to search for electrons, photons, taus and jets and missing transverse energy (E_T^{miss}). It can identify an Region-of-Interest (RoI) as a 2×2 trigger tower cluster in the EM calorimeter as shown in figure 3.16, and 4×4 or 8×8 trigger tower for Jet RoIs. One important upgrade was that, the new FPGA-based (field-programmable gate array) Multi-Chip Modules are used to replace the ASICs (application-specific integrated circuits) included in the modules used in run-1, which allows the use of auto-correlation filters to suppress pile-up.

The Level-1 Muon trigger system includes one barrel section (RPC) and two end-cap section (TGC), which provides fast trigger signals from the muon detectors for the Level-1 trigger decision. By requiring a coincidence with hits from the innermost muon chambers, it can reduce the L1_MU15 rate by about 50% in the region of $1.3 < |\eta| < 1.9$ with only a loss of around 2% signal efficiency. In addition, the coverage was extended by around 4% due to installing new chambers in the feet region of the muon detector.

1238 **High Level Trigger**

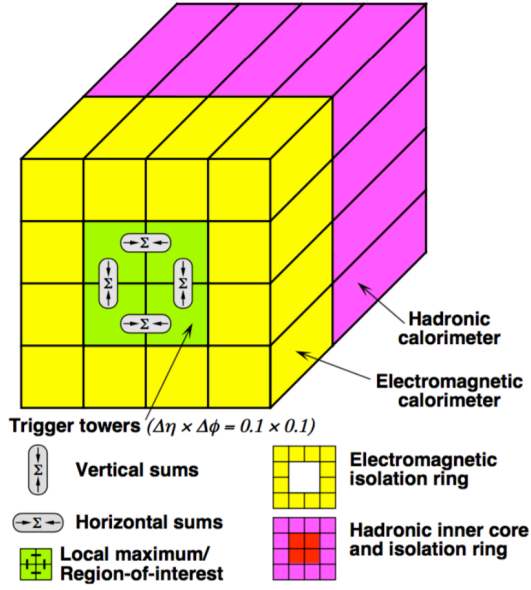


Fig. 3.16 An examples of L1 calorimeter trigger tower for electron and photon triggers^[37].

1239 In run-1, the Event Filter computer clusters and Level-2 trigger system were separated,
 1240 while now in run-2, they have been merged into a single HLT event processing. The new
 1241 arrangement helps to reduce the complexity and duplication of algorithm, which leads to a
 1242 more flexible high level trigger system. During the long-shutdown between the LHC run-
 1243 1 and run-2, lots of reoptimizations have been done for trigger reconstruction algorithms
 1244 as well as the offline analysis selections, which can improve the efficiency by more than
 1245 a factor of two in some cases like hadronic tau triggers. For some triggers, the HLT
 1246 processing performed within RoIs also allows to aggregate from RoIs to single objects.
 1247 This improvement reduces the CPU processing for events with overlapping RoIs, and the
 1248 average output rate has been increased from 400 Hz to 1 kHz.

1249 The HLT reconstruction algorithm can be divided into fast and precision online re-
 1250 construction steps. As illuminated by figure 3.17, the initial fast reconstruction helps to
 1251 reduce the event rate, and to seed into precision reconstruction. Then the final online
 1252 precision reconstruction is improved and uses offline-like algorithms as much as possi-
 1253 ble. In particular, multivariate analysis techniques (based on machine learning) have been
 1254 introduced online in many aspects.

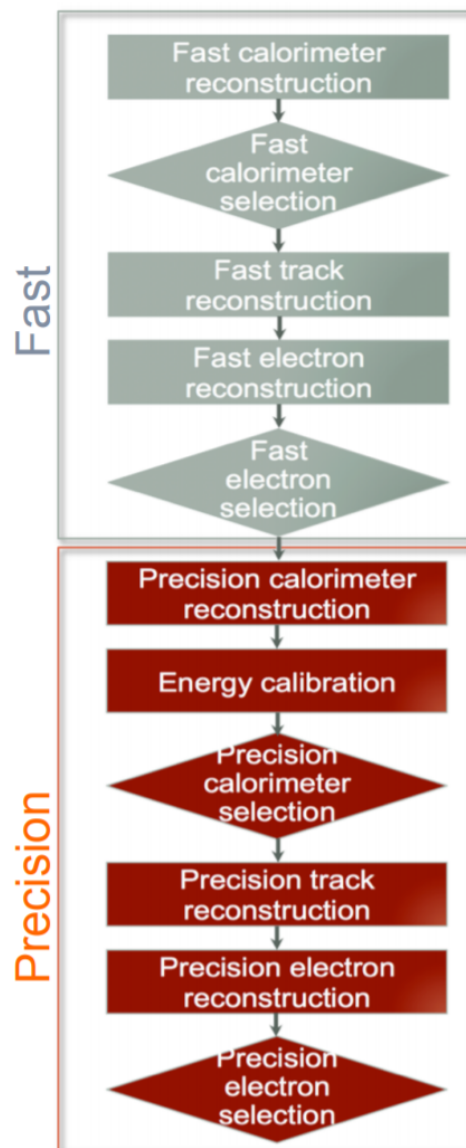


Fig. 3.17 The HLT trigger algorithm sequence^[37].

1255 Chapter 4 Simulation and Event Reconstruction for 1256 the ATLAS Experiment

1257 In current LHC pp collision, bunches of protons collide every 25 nanoseconds (ns),
1258 which gives a large challenge to event reconstruction and selections. To predict and model
1259 each process, Monte Carlo simulations of physics events are essential for high-energy
1260 physics experiments. This section will briefly discuss the event simulation and recon-
1261 struction programs based on the ATLAS software framework.

1262 4.1 Event simulation

1263 The ATLAS simulation program is integrated into the ATLAS software framework
1264 called *Athena*^[38], which uses Python as an object-oriented scripting and interpreter lan-
1265 guage to configure and load C++ algorithms and objects. Figure 4.1 shows the overview
1266 of ATLAS simulation data flow^[39]. In the diagrams, the square-cornered boxes represents
algorithms and applications to be run and round-cornered boxes denote data objects.

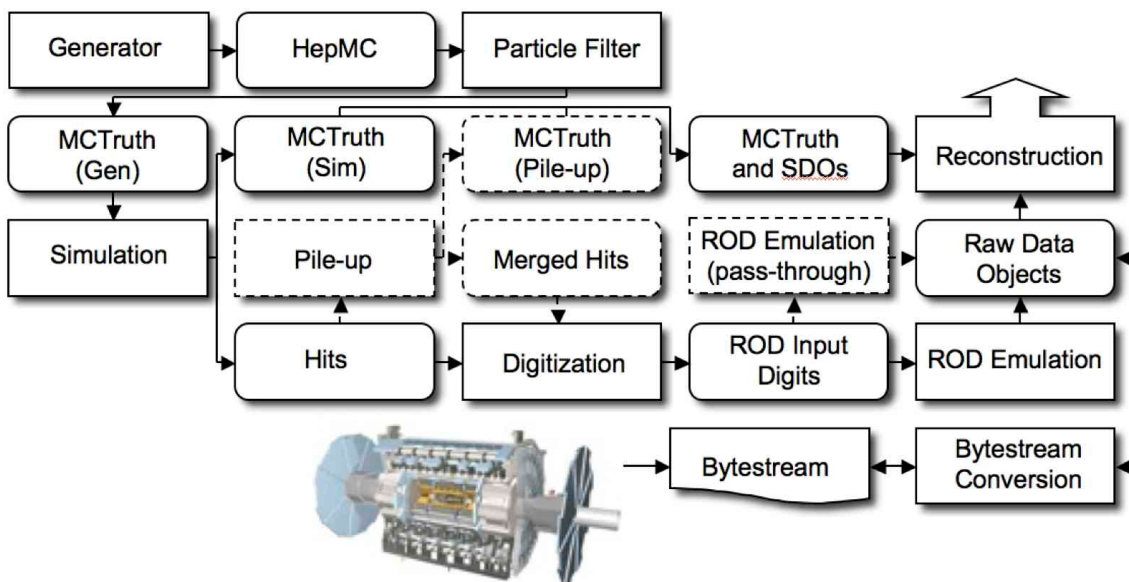


Fig. 4.1 The flow of the ATLAS simulation software.

1267
1268 First of all, events are produced by MC generators in standard HepMC format and
1269 then read into the simulation. During the simulation, particles are propagated through the
1270 full ATLAS detector whose configurations can be set by users via GEANT4 toolkit. The
1271 energies deposited in the sensitive regions of the detector are recorded as *hits* that contains
1272 the total energy deposition, position and time, and are written to a simulation hit file. In

the meantime, the events in “truth” format are also recorded to contain the history of the interactions from the generator, including incoming and outgoing particles. Simulated Data Objects (SDOs) are created from truth, which are maps between hits in sensitive portions of the detector and truth information of particles in simulation. The files are then sent to digitization, with constructs “digits” inputs and be written into Raw Data Object (RDO) file used for reconstruction.

In conclusion, there are three main parts of framework: *Generation*, *Simulation* and *Digitization*. More details are given as below:

Event generation

As shown in figure 4.2^[40], at hardon colliders, multiple scattering and rescattering effects arise, which needs to be simulated by Monte Carlo (MC) event generators to reflect the full complexity of those event structures. Several MC event generators can be used to generate events in HepMC format. The events can be filtered at generation time with some certain requirements (eg. decay channel or missing energy above a certain threshold). The generator is responsible for any prompt decays (e.g. W or Z bosons) and stores any “stable” particle expected to propagate through a part of the detector. During the generation steps, any interactions with detector are ignored and only immediate decays are considered.

There are several MC generators that have been widely used with general purpose, including Sherpa^[41], Herwig++^[42], PowhegBox^[43], MC@NLO^[44] and Pythia8^[45].

Simulation

GEANT4 is used as standard simulation toolkit for the ATLAS experiment, which transports physics particles through the detector’s geometry. During the generation level, the entire connected chain of the HepMC event is stored as the Monte Carlo truth. Only the stable particles are read into GEANT4 for further simulation and selection, and transformations can be applied to these events to select certain processes. During the simulation, many secondary tracks can be produced, therefore only information from the interactions of interest are stored, including the incoming particles, step sequence, vertex as well as outgoing particles. The output of GEANT4 is called *hit file*, which contains metadata describing the configuration of the simulation during the run, all requested truth information and a collection of hits for each subdetector.

Since the standard ATLAS detector simulation cost very large computing resources to accurately model the complex detector geometry and physics descriptions, some fast simulation programss are developed according to different user purpose. Some popular fast-sim toolkits include *Fast G4 Simulation*^[46], *ATLFAST-I*^[47] and *ATLFAST-II*^[48].

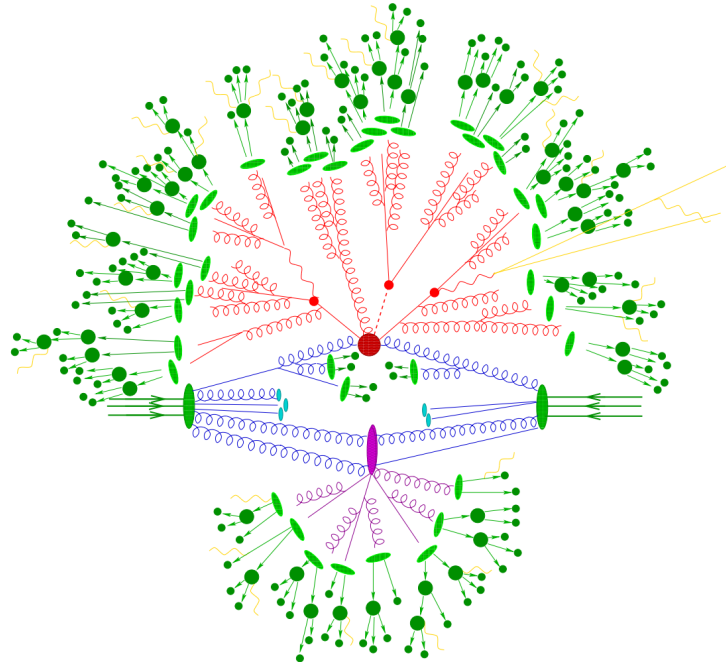


Fig. 4.2 Sketch of a hardon-hardon collision simulated by MC event generator. The red blob in center denotes the hard collision, surrounded by tree-like structures representing Bremsstrahlung which is simulated by Parton Showers. The purple blob stands for a secondary hard scattering event. The light green blobs indecate the parton-to-hardon transitions and the dark green blobs represents hadron decays. The yellow lines are soft photon radiations.

1308 Digitization

1309 The hit outputs from simulated events, including hard scattering signal, minimum
 1310 bias, beam halo, beam gas and cavern background events, are then sent into digitization
 1311 procedure, converted into detector response called “digits”. Before converted into detec-
 1312 tor signal as “digits” formart, each type of event can be overlaid at a user-specified rate.
 1313 Those overlay, called “pile-up”, can be done during digitization to save the CPU time. At
 1314 this stage, the detector noise and the first level trigger that implemented with hardware on
 1315 the real detector are added into events. The digitization firstly constructs “digits” inputs to
 1316 the readout drivers (RODs) in the detector electronics. Then the ROD functionality is em-
 1317 ualuted, and the output digits are written out as Raw Data Object (RDO) file. In addition,
 1318 the digitization algorithms can also produce Simulated Data Objects (SDOs), which con-
 1319 tain information about all the particles, noise and the amount of energy that contributed
 1320 to the signal. Then all information are sent into reconstruction level described in next
 1321 subsection.

4.2 Event reconstruction

The data flow of ATLAS data processing is sketched in figure 4.3^[49]. Data from detector is firstly filtered by online trigger system before sending to the *Tier-0* (*T0*) for initial processing by offline reconstruction software based on Athena. A small amount of data named “express stream” is processed in almost real time in *T0* for online data quality monitoring. In addition, some other dedicated data streams are sent out at trigger level for detector alignment and calibration. These calibration and alignment information are then used for bulk reconstruction in *T0*. At the end of the reconstruction chain, the data are delivered into *Tier-1* (*T1*) and *Tier-2* (*T2*) centers around the world for further analysis and production of simulated data. *T1* centers are also responsible for data reprocessing by re-running data reconstruction with improved calibration and alignment constants and with improved reconstruction algorithms.

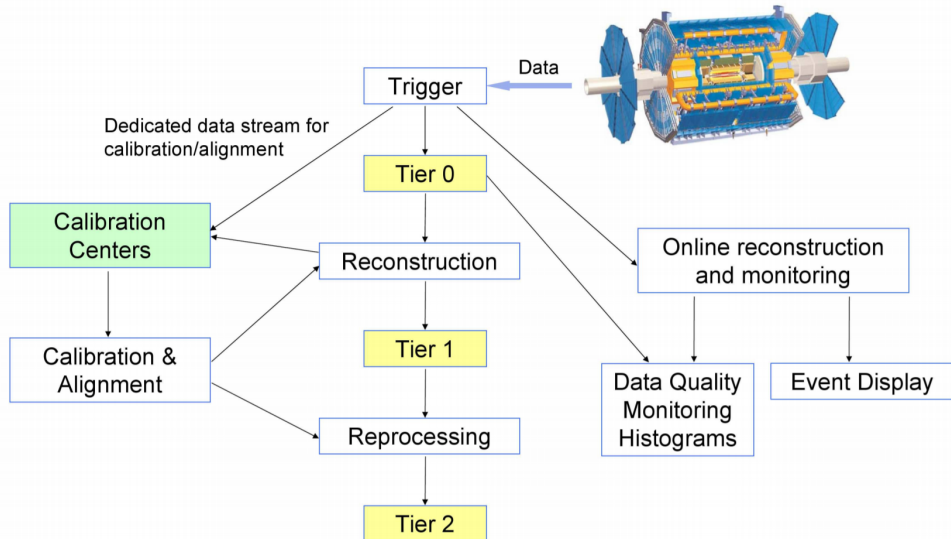


Fig. 4.3 The flowchart of the ATLAS data processing.

This section describes the reconstruction of some important physics objects in ATLAS experiment: tracks, vertices, electrons, muons, jets, and missing energies.

4.2.1 Track

The ATLAS detector is composed of two independent tracking systems: the Inner Detector (ID) close to the interaction point, and the Muon Spectrometer (MS) located in the outermost region. The reconstructed charged-particle trajectories in the ID and MS are referred to as ID tracks and MS tracks respectively. The challenge of ID reconstruction is that it needs to handle high track density that imposes a large number of combinatorial track candidates, while the MS reconstruction is however largely limited by the huge

amount of inert material, the large background and the highly inhomogeneous magnetic field^[50]. More details of these two types of track are given as below:

1345 **Inner detector track**

1346 Figure 4.4 sketches the ID system used for detecting charge-particle tracks. The ID
1347 track reconstructions contains two sequences: *inside-out* track reconstruction and *outside-in* one.

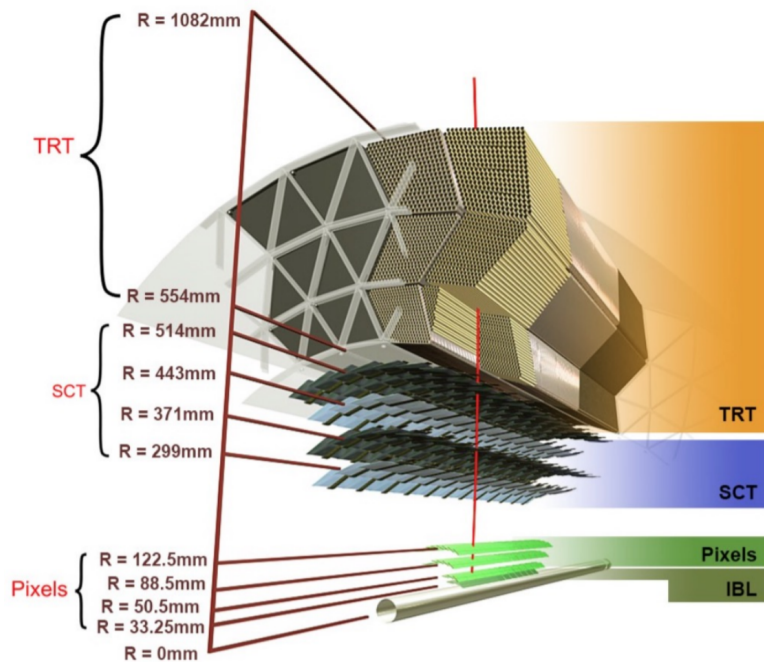


Fig. 4.4 Schematic view of the ATLAS inner detector showing all the corresponding components.

1348
1349 For inside-out tracking, it exploits the high granularity of the pixel and SCT detectors
1350 to discover prompt tracks originating from the interaction point. In first step, the track
1351 seeds are formed by combining the information of space-points in the three pixel layers
1352 and the first SCT layer. Then, these seeds are extended throughout the SCT to build track
1353 candidates. After that, these candidates are fitted with some quality cuts applied to remove
1354 the outlier clusters, reject the fake tracks and resolve ambiguities in the cluster-to-track
1355 association. The selected tracks are then further extended to TRT, and refitted with the
1356 full information from pixel, SCT and TRT detectors.

1357 Another complementary approach, outside-in, searches for unused track segments
1358 start from TRT instead. These segments are then extended into the SCT and pixel detec-
1359 tors to improve the tracking efficiency for secondary tracks from conversions or decays
1360 of long-lived particles.

1361 **Muon spectrometer track**

1362 The MS track reconstruction^[51] starts from searching hit patterns inside each muon
 1363 chamber to form segments. In each MDT chamber and nearby trigger chamber, a Hough
 1364 transform^[52] is used to search the hits lie on a certain trajectory in the bending plane of the
 1365 detector. The MDT segments are reconstructed by performing a linear fit to the hits found
 1366 in each layer. The RPC or TGC hits can be built by measuring the coordinate orthogonal to
 1367 the bending plane. And the segments of CSC can be built using a separate combinatorial
 1368 search in the η and ϕ detector planes.

1369 Then muon track candidates are built by fitting hits from segments in different layers
 1370 together. This task makes use of the algorithm by performing a segment-seeded combi-
 1371 natorial search, which starts by using the segments generated in the middle layers of the
 1372 detector where more trigger hits are available as seeds. The search is then extended to use
 1373 the segments as seeds from the inner and outer layers. The segments are selected based
 1374 on criteria of hit multiplicity and fit quality, and are matched using their relative positions
 1375 and angles. To build a track, at least two matching segments are required, except in the
 1376 barrel-endcap transition region where a single high-quality segment with η and ϕ infor-
 1377 mation can be used to build a track. At beginning, the same segment can be used to build
 1378 more than one track candidates. Later on, an overlap removal algorithm is performed to
 1379 select the best assignment to a single track, or decide whether allows the certain segment
 1380 to be shared between two tracks.

1381 The hits associated with each track candidate are then fitted using a global χ^2 fit. The
 1382 algorithm accepts the track candidate if its fitting χ^2 passes the selection criteria. Hits
 1383 with large contribution to χ^2 are removed and the track fit is repeated. In addition, the
 1384 algorithm performs a hit recovery procedure looking for additional hits consistent with
 1385 the candidate trajectory, and the track candidate is refit if additional hits are found.

1386 4.2.2 Primary vertex

1387 The reconstruction of primary vertex (PV) uses the reconstructed tracks introduced in
 1388 previous section as inputs. The tracks must satisfy the following criteria^[53]:

- 1389 • $p_T > 400$ MeV
- 1390 • $|\eta| < 2.5$
- 1391 • Number of silicon hits $\geq \begin{cases} 9 & \text{if } |\eta| \leq 1.65 \\ 11 & \text{if } |\eta| > 1.65 \end{cases}$
- 1392 • IBL hits + B-layer hits ≥ 1
- 1393 • A maximum of 1 shared module (1 shared pixel hit or 2 shared SCT hits)
- 1394 • Pixel holes = 0

1395 • SCT holes ≤ 1

1396 A candidate vertex is formed by requiring two tracks passing these selection criteria.

1397 The reconstruction of PV can be divided into two steps^[54]: vertex finding and vertex
1398 fitting. The first step is the pattern recognition process, namely the association of recon-
1399 structed tracks to vertex candidates. The latter one works on the reconstruction of the
1400 actual vertex position and its covariance matrix. More details are described as below:

1401 First of all, a set of tracks passing the selection criteria mentioned above is selected.
1402 Then a seed position for the first vertex is chosen. This seed position is determined by
1403 beam spot in the transverse plane. The starting point for x- and y- coordinates are di-
1404 rectly from the centre of the beam spot, while the one for z-coordinate is calculated as
1405 the mode of z-coordinates of tracks at their respective points with closest approach to the
1406 reconstructed centre of the beam spot.

1407 After determining the seed position, the iterative primary vertex finding procedure
1408 starts. An vertex fitting algorithm is adopted to find the optimal vertex position by per-
1409 forming an iterative χ^2 minimization, in which the seed position is used as the start point
1410 and the reconstructed tracks are used as input measurements. For this fitting procedure,
1411 the input tracks are assigned weights to reflect their compatibility with the vertex estima-
1412 tion, and the vertex position is re-calculated based on these weighted tracks. Then the
1413 iterative procedure is repeated by re-calculating the track weight according to the new
1414 vertex position. After the last iteration, the final weight of each track used in vertex fit is
1415 estimated. And those incompatible tracks ($> 7\sigma$) are then rejected from this vertex candi-
1416 date and moved back to the unused pool for next vertex finding. Then iteration procedure
1417 describes above are repeated again by using the remaining tracks, until no un-associated
1418 tracks are left or no additional vertex can be found in remaining tracks.

1419 At the end, the vertices with at least two associated tracks passing through are treated
1420 as possible PV candidates. And the output of this vertex reconstruction algorithm is the in-
1421 formation of three dimensional vertex positions and their covariance matrices. In physics
1422 analysis, it's most often to choose the one with highest sum of transverse momentum
1423 ($\sum p_T^2$) as PV.

1424 4.2.3 Electron

1425 Many interesting physical processes are with the involvement of one or more elec-
1426 trons (or positrons) at the LHC. But these electrons can be subjected to large amount of
1427 backgrounds such as hadrons, non-prompt electrons from photon conversions and non-
1428 isolated electrons from heavy flavor hadon decays. It is therefore essential to efficiently

1429 reconstruct and identify electrons as well as, in the meantime, to keep high background
1430 rejection.

1431 In ATLAS, in central region, the electrons leave tracks in inner detector (ID) and
1432 deposit the energies in the electromagnetic (EM) calorimeter. Firstly the signals from
1433 calorimeter are used for L1 trigger system, and then combined with the information from
1434 ID tracks to reconstruct electron candidates that will be used for the high level trigger
1435 (HLT) decision algorithms^[55]. The backgrounds mentioned above can then be further
1436 suppressed by using several identification criteria. In addition, electrons are required to
1437 be isolated from other activities to be further distinguished from background.

1438 More details of electron *reconstruction*, *identification* and *isolation* are described as
1439 below.

1440 **Electron reconstruction**

1441 Several steps are proceeded for electron reconstruction in the central region of ATLAS
1442 detector ($|\eta| < 2.47$):

1443 1. **Seed-cluster reconstruction:** A sliding window with size of 3×5 in unit of
1444 $\Delta\eta^{tower} \times \Delta\phi^{tower} = 0.025 \times 0.025$ in $\eta \times \phi$ space is utilized to search for elec-
1445 tron cluster seeds with total cluster transverse energy greater than 2.5 GeV. Then
1446 a clustering algorithm^[56] is applied to form the clusters around the seeds, which
1447 can take advantage of removing the duplications. The kinematics of clusters are
1448 then reconstructed by using an extended window depending on the cluster position.
1449 The efficiency of cluster search is from about 95% at $E_T = 7GeV$ to 99% for
1450 $E_T \geq 15GeV$.

1451 2. **Track reconstruction:** The track reconstruction can be divided into two steps: pat-
1452 tern recognition and track fit. The standard pattern recognition in ATLAS uses pion
1453 hypothesis for energy loss caused by interactions with detector material. If a track
1454 seed with $p_T > 1$ GeV cannot be successfully extended to a full track required at
1455 least seven hits using this pion hypothesis, but still falls inside one of the EM clus-
1456 ter region of interest, as a second attempt, the pattern recognition using electron
1457 hypothesis is then used to allow larger energy loss. Depending on the pattern used
1458 in previous stage, the track candidates are then fitted with either the pion hypothesis
1459 or the electron hypothesis by using ATLAS Global χ^2 Track Fitter^[57]. If a track
1460 candidate fails the fit by using pion hypothesis, it can be refit with the electron hy-
1461 pothesis again. In this method, a specific electron-oriented algorithm is integrated
1462 into the ATLAS standard track reconstruction, which improves the performance for
1463 electron and as well as maintain minimal interference with the main track recon-

1464 struction.

1465 **3. Electron specific track fit:** Once the tracks are obtained, they are loosely matched
1466 to EM cluster using the distance in η and ϕ between the position of track (after ex-
1467 trapolation) in calorimeter's middle layer and the cluster barycentre. The matching
1468 conditions take into account the energy loss of bremsstrahlung and the number of
1469 precise hits in silicon detector.

1470 **4. Electron candidate reconstruction:** The electron candidate is reconstructed by
1471 matching the track candidate to EM cluster seed to eventually completes the electron
1472 reconstruction procedure. If more than one track satisfy the matching condition,
1473 one track is chosen as primary track based on the information of the cluster-track
1474 distance R , the number of pixel hits and the presence of a hit in the first silicon
1475 layer^[58]. In addition, the electron candidates are removed from electron pool if it's
1476 without any associated precise hit tracks, and moved into photon candidates pool.
1477 Then we reformed the electron clusters by using 3×7 (5×5) longitudinal towers
1478 of cells in barrel (end-caps) in EM calorimeter. The measured energy is calibrated
1479 to original electron energy based on MC simulated samples by using multivariate
1480 techniques (MVA).

1481 In addition, in physics analysis, to reduce the background from photon conversions
1482 and secondary particles, the track associated with electron is required to be compatible
1483 with the primary vertex of the hard collision. Practically, the impact parameters cuts such
1484 as $d_0/\sigma_{d_0} < 5$ and $z_0 \sin\theta < 0.5$ mm are usually applied, where d_0 is the closest distance of
1485 the track to the measured beam-line, z_0 is the distance along the beam-line between the
1486 point where d_0 is measured and the beam-spot position, and θ is polar angle of the track,
1487 σ_{d_0} denotes the estimated uncertainty of d_0 parameter. Figure 4.5 depicts the definition of
1488 each track impact parameter.

1489 **Electron identification**

1490 The electron identifications are applied to determine whether the reconstructed elec-
1491 tron candidate is more signal-like or background-like object. The identification algorithms
1492 make use of quantities of related variables from electron cluster and track measurements
1493 including calorimeter shower shapes, track properties, as well as variables measuring
1494 bremsstrahlung effects for distinguishing signal from background. Taking the advantage
1495 of new IBL in run-2, the number of hits in this innermost pixel layer is utilized for discrim-
1496 inating between electrons and converted photons. In addition, a likelihood method based
1497 on the TRT high-threshold hits is adopted to compensate the lower transition radiation
1498 absorption probability of the argon.

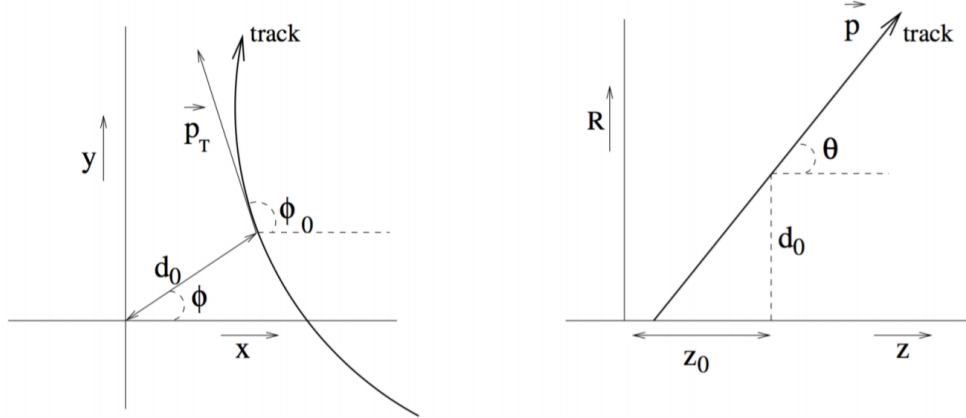


Fig. 4.5 Schematic of the impact parameters of a track in the transverse plane (left) and RZ-plane (right), as defined in the global ATLAS tracking frame^[59].

1499 The baseline identification algorithm introduced for ATLAS run-2 data analysis is the
 1500 likelihood-based (LH) method, which uses a MVA technique to simultaneously evaluate
 1501 several properties of electron candidates when making a decision. The LH method utilizes
 1502 the probability density functions (PDFs) of signal and background as the input discrimi-
 1503 nating variables. Based on these PDFs, it can calculate overall probabilities of the object
 1504 to be signal or background. Then the probabilities of signal and background are combined
 1505 together into a discriminant $d_{\mathcal{L}}$:

$$d_{\mathcal{L}} = \frac{\mathcal{L}_S}{\mathcal{L}_S + \mathcal{L}_B}, \quad \mathcal{L}_{S(B)}(\mathbf{x}) = \prod_{i=1}^n P_{s(b),i}(x_i) \quad (4.1)$$

1506 where \mathbf{x} denotes the vector of discriminating variables and $P_{s(b),i}(x_i)$ represents the value
 1507 of signal (background) PDF of the i^{th} variable as x_i .

1508 Three levels of working points (WPs) for electron identification are provided: *Loose*,
 1509 *Medium* and *Tight*, in order of increasing background rejection. Samples selected by a
 1510 looser WP are subsets of a tighter one, for example, the electrons passing Medium can
 1511 all be selected by Loose. The identification efficiency varies as function of transverse
 1512 energy (E_T) as shown in figure 4.6. For evaluations, the electron candidates from MC
 1513 simulation of $Z \rightarrow ee$ decays (di-jet) are used as signal (background). Depending on the
 1514 working point, the signal (background) efficiencies for reconstructed electron candidates
 1515 at $E_T = 25 GeV$ are in the range of 78 to 90% (0.3 to 0.8%), and increase (decrease) with
 1516 E_T .

1517 **Electron isolation**

1518 In addition to the identification criteria, most analyses have electron isolation require-
 1519 ment to further distinguish signal from background. To quantify the energy of particles

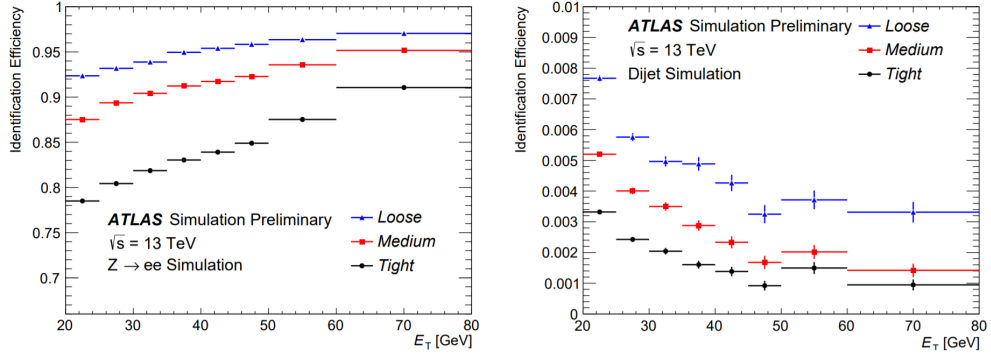


Fig. 4.6 The efficiencies of three electron identification WPs from $Z \rightarrow ee$ (left) events and hadrons misidentified as electrons estimated using di-jet MC samples (right).

around the electron candidate, the isolation variables can help to separate the prompt electron from other non-isolated electrons, like the electrons from converted photons or from heavy flavour hadron decays. There are two kinds of discriminating variables that have been designed:

• **Calorimeter-based variable:** $E_T^{topocone20}$. It's defined as the sum of transverse energies of topological clusters^[60], calibrated at EM scale within a cone of $\Delta R = 0.2$ around the candidate electron cluster. It only considers the clusters with positive reconstructed energy. In addition, a correction as a function of (E_T, η) values is applied to account for the electron energy leakage outside the cluster.

• **Track-based variable:** $p_T^{varcone20}$. It's calculated as the sum of transverse momentum of all satisfied tracks within a cone of $\Delta R = \min(0.2, 10\text{GeV}/E_T)$ around the candidate electron track. To calculate the sum, it requires the tracks are originating from the reconstruction PV of hard collision, and exclude the associated tracks of electron itself.

Based on the values of $E_T^{topocone20}/p_T$ and $p_T^{varcone20}/p_T$, a series of working points with different selection requirements are defined. The resulting WPs are divided into two kinds:

- Efficiency targeted working points: varying requirements to obtain a certain isolation efficiency, which can either be a constant or as a function of E_T .
- Fixed requirement working points: set the constant upper thresholds on isolation variables.

The distribution of two discriminating variables are shown in figure 4.7 for $ZZ \rightarrow ee$ events with $E_T > 27\text{GeV}$ and satisfying *Tight* requirement.

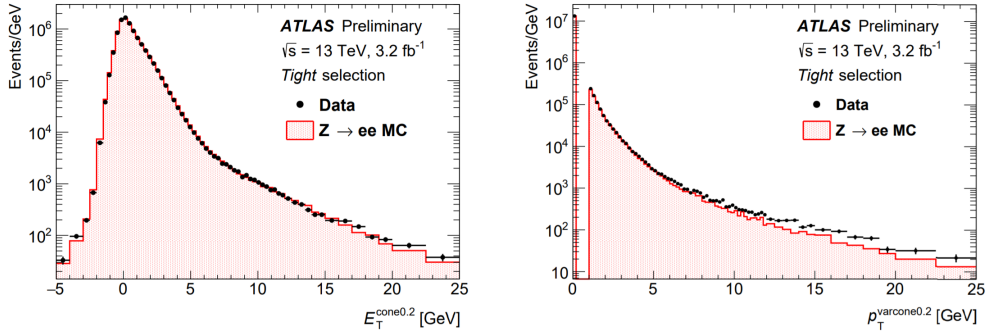


Fig. 4.7 Distributions of $E_T^{cone0.2}$ (left) and $p_T^{varcone0.2}$ (right) for electrons from $ZZ \rightarrow ee$ events in data and MC simulation. The simulated events (full histograms) are normalized to data.

4.2.4 Muon

Muons are distinctive signatures in final states of many physics analyses at the LHC including the Higgs analyses, SM measurements, BSM searches and so on. High performance of muon reconstruction and identifications are crucial. This section briefly describes some more details of the *reconstruction, identification and isolation* of muon.

Muon reconstruction

Muon reconstruction is firstly performed in inner detector (ID) and muon spectrometer (MS) independently as given in section 4.2.1. The information from each individual detector is then combined together to form the muon tracks for physics analyses. The combined ID-MS reconstruction is developed according to several algorithm based on the information from ID, MS and calorimeters. Four different muon types are defined^[51]:

- **Combined (CB) muons:** a combined track is formed by using the reconstructed tracks performed independently in ID and MS with a global refit. To improve the fit quality, the hits from MS may be added to or removed from the track. The outside-in pattern recognition is utilized for the reconstruction of most muons, in which the muons are first reconstructed in MS and then extrapolated inward to match the ID track. In the meantime, the inside-out pattern is also used as a complementary method.
- **Segment-tagged (ST) muons:** a reconstructed track in ID is defined as muon, if it can be associated with at least one track segment in MDT or CSC chambers. These ST muons are used when they can only pass across one layer of MS chambers due to their low p_T or falling into regions with less MS acceptance.
- **Calorimeter-tagged (CT) muons:** a reconstructed track in ID is categorized as muon if it's matched to the energy deposit in calorimeter which is recognized with

1566 a minimum-ionizing particle. This CT muons have lowest purity amount all types
1567 of muons, but it covers the region where ATLAS muon spectrometer is only par-
1568 tially constructed. For the region of $|\eta| < 0.1$ and $15GeV < p_T < 100GeV$, the
1569 identification of CT muons are optimal.

- 1570 • **Extrapolated (ME) muons:** the muon is reconstructed based only on the MS track
1571 and a loose requirement of originating from the interaction point. In general, this
1572 type of muon needs to pass at least two (three) layers of MS chambers to provide
1573 a track measurement in barrel (forward) region. ME muons are designed to extend
1574 the acceptance for muon reconstruction into the region $2.5 < |\eta| < 2.7$ where ID
1575 doesn't cover.

1576 Before collecting those muons for physics analyses, overlap removals are performed
1577 between different muon types with the priority of CB > ST > CT, when two types of muons
1578 share the same ID track. Besides, the overlaps with ME muons are resolved by analyzing
1579 the track hit content, and selecting the track with better fit quality and larger number of
1580 hits.

1581 **Muon identification**

1582 After reconstruction, the muon identification is then performed to further discrimi-
1583 nate between signal and background, especially to suppress backgrounds from pion and
1584 kaon decays by requiring prompt muons with high efficiency and guaranteeing a robust
1585 momentum measurement. The muon identification is defined by using the fit quality of
1586 combined track. The variables utilized in judgement for CB tracks include:

- 1587 • *q/p significance*, the absolute difference between q/g (charge over momentum) of
1588 muons measured in ID and MS divided quadratic sum of their corresponding un-
1589 certainties;
- 1590 • ρ' , the absolute value of difference between the p_T (transverse momentum) mea-
1591 sured in ID and MS, divided by the p_T of combined track;
- 1592 • *Nomalized χ^2* of the combined track fit;
- 1593 • *Number of hits in ID and MS*

1594 In addition, some new variables used for *LowPt* muon working point what will be de-
1595 scribed later^[61]:

- 1596 • *Momentum balance significance (MBS)* is computed as momentum difference be-
1597 tween the ID and MS standalone measurements with respect to the uncertainty σ
1598 on energy lost in the calorimeter system.
- 1599 • *Scattering neighbor significance (SNS)* is defined to estimated the significance of a
1600 change in trajectory along the track, expected in the presence of a hadron decaying

1601 to a muon.

- 1602 • *Scattering curvature significance (SCS)* is defined as the normalized integral of the
1603 scattering angle significances, corrected for large kinks along the trajectory.

1604 Five selection working points are developed to satisfy the different needs for different
1605 physics goals: *LowPt*, *Loose*, *Medium*, *Tight* and *HighPt*. The *Tight*, *Medium*, *Loose* are
1606 subsets from the tighter one to looser one. More detailed definition of each working point
1607 is given as follow:

- 1608 • *Loose*: this working point is designed to maximize the reconstruction efficiency
1609 while keeping good-quality of muon tracks. And they are specifically developed
1610 for reconstructing the Higgs boson candidates from four-lepton final states. All
1611 four muon types are used for this selection level. The CB and ME muons passing
1612 Medium WP that will mentioned below are all included into Loose category. In
1613 addition, the CT and ST muons are restricted to $|\eta| < 0.1$ region. In the range of
1614 $|\eta| < 2.5$, around 97.5% Loose muons are CB muons, and about 1.5% are CT while
1615 remaining 1% are ST muons.
- 1616 • *Medium*: this working point is the default criteria of muon identification in ATLAS.
1617 This selection minimizes the systematic uncertainties of muon reconstruction and
1618 calibration. In this category, we only use CB and ME muons. For CB muons, at
1619 least 3 hits in at least two layers of MDT are required, except $|\eta| < 0.1$ region,
1620 in which tracks with ≥ 1 MDT layer but ≤ 1 MDT hole layer are allowed. For
1621 ME muons, at least 3 MDT/CSC layers are required. Furthermore, a loose cut on
1622 the compatibility between measured momentum in ID and MS is applied to reduce
1623 the fake muons from hadrons misidentification. Besides, the q/p-significance is
1624 required to be less than 7.
- 1625 • *Tight*: this working point is used to maximize the purity of muons but with sacrifice
1626 of some selection efficiency. Only CB muons with hits in ≥ 2 stations of MS and
1627 passing Medium criteria are selected. In addition, the normalized χ^2 of combined
1628 track fit should be smaller than 8. Then, a two-dimensional cut of q/p-significance
1629 and ρ' is adopted as a function of muon p_T to ensure tighter background rejection
1630 for momentum below 20 GeV, in which the fake rate is usually higher.
- 1631 • *High- p_T* : this set of selections aims to maximize the momentum resolution for
1632 tracks with $p_T > 100\text{GeV}$ region. The selection is especially optimized for search-
1633 ing high-mass Z' and W' resonances. CB muons satisfying Medium selection and
1634 with ≥ 3 hits in 3 MS stations are chosen. The specific region in MS where align-
1635 ment is suboptimal are removed as a precaution.

- 1636 • *Low- p_T* : this type of muon is newly designed for physics analyses with ATLAS
 1637 software release version 21. It's designed to obtain a optimal muon identification
 1638 with very low transverse momentum of $3GeV < p_T < 5GeV$, which is crucial for
 1639 B-physics measurement in ATLAS. In this muon requirement, only CB muons are
 1640 used. In the range of $|\eta| < 1.3$, it requests muons hit at least one MS station; in
 1641 $1.3 < |\eta| < 1.55$, a least two MS stations are required; while in region of $|\eta| > 1.55$,
 1642 *Medium WP* is required. In addition, cuts are applied to suppress fakes as: $|\text{MBS}| < 3.0$, $|\text{SNS}| < 3.0$ and $|\text{SCS}| < 3.0$.
 1643

1644 Figure 4.8 and 4.9 show the selection efficiency of different muon identification work-
 1645 ing points. For *Medium (Loose)*, *Tight* and *High- p_T* : $Z \rightarrow \mu\mu$ events with $p_T > 10GeV$
 1646 are used for measurement. In the top figure of figure 4.8, the efficiency of the Loose selec-
 1647 tion (squares) is shown comparing to Medium one, where significant difference can be ob-
 1648 served in region of $|\eta| < 0.1$. For *LowPt*, $J/\Psi \rightarrow \mu\mu$ events with $3GeV < p_T < 10GeV$
 are used for measurement.

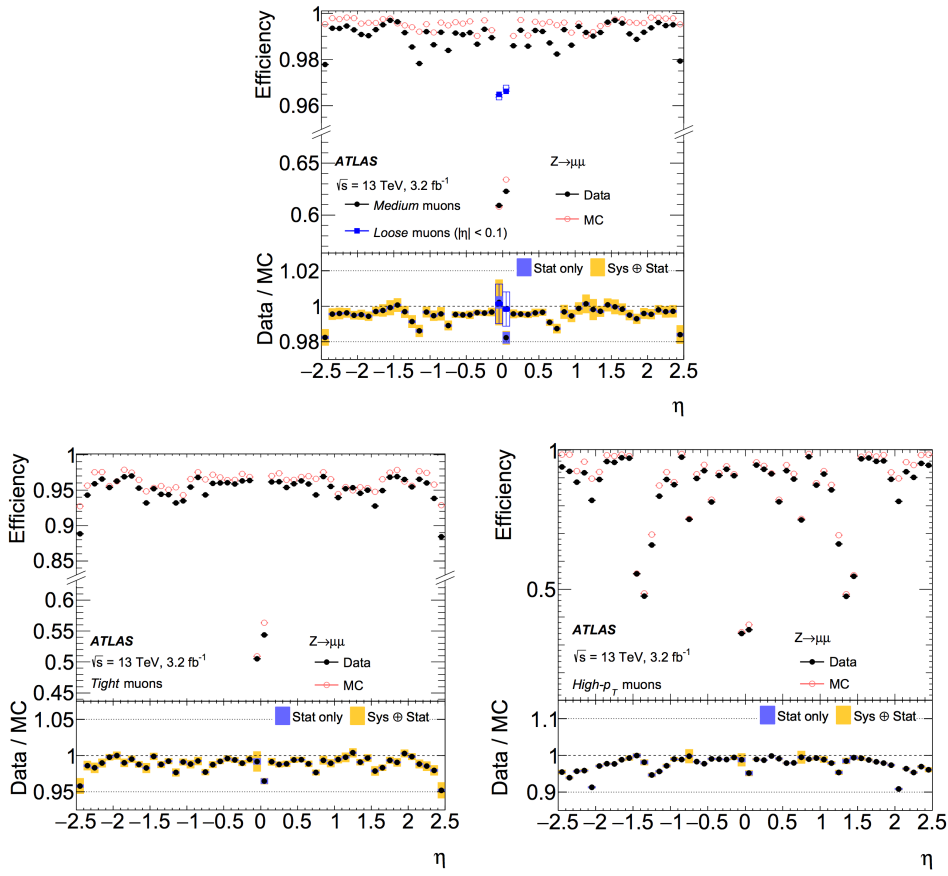


Fig. 4.8 Muon reconstruction efficiency as a function of η for: Medium (and Loose), Tight and High- p_T working points.

1649

1650

Muon isolation

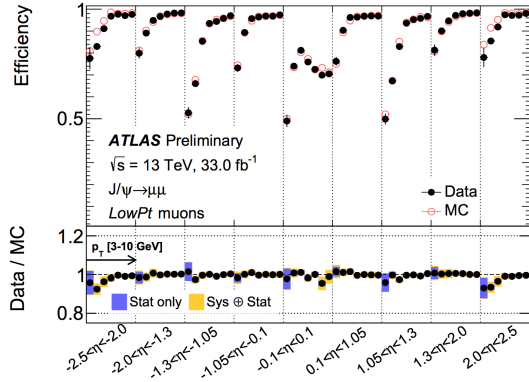


Fig. 4.9 Muon reconstruction efficiency for Low- p_T working point as a function of η .

Similar to electron, the muon isolation is used to further distinguish the prompt muon from non-prompt backgrounds. There are also two types of isolation variables for muon:

- **Calorimeter-based variable:** $E_T^{topocone20}$. It's defined as the sum of the transverse energy of topological clusters within a cone of size $\Delta R = 0.2$ around the candidate muon, after subtracting the contribution from the energy deposit of the muon itself and correcting for pile-up effects. The contributions from pile-up and underlying events are computed using the ambient energy-density technique^[62] and are corrected on an event-by-event basis.
- **Tracked-based variable:** $p_T^{varcone30}$. It's computed as the scalar sum of the transverse momenta of the tracks with $p_T > 1\text{GeV}$ in a cone size of $\Delta R = \min(10\text{GeV}/p_T^\mu, 0.3)$ around the candidate muon whose transverse momenta is p_T^μ after excluding the muon track itself. This p_T -dependent cone size can help to improve the performance for muons produced in the decay of particles with a large transverse momentum.

Then the isolation selections are applied based on *relative isolation variables*, which are computed as the ratio of the track- or calorimeter-based isolation variables to the transverse momentum of the muon. Figure 4.10 shows the distribution of those relative isolation variables by using $Z \rightarrow \mu\mu$ events for muons passing *Medium* identification criteria.

4.2.5 Jets

Jets are another important features for many physics analyses at the LHC, and especially the key signatures for vector boson fusion/scattering (VBF/VBS) processes. In ATLAS detector, jets are reconstructed as groups of topologically associated energy deposits in the calorimeters, tracks associated with charged particles measured in the inner

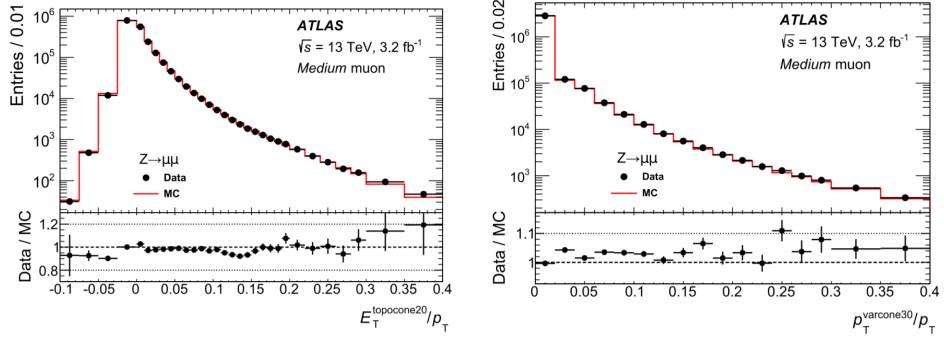


Fig. 4.10 Distributions of the calorimeter-based (right) and the track-based (left) relative isolation variables measured in $Z \rightarrow \mu\mu$ events.

tacking detector, or simulated particles. This section introduces the jet reconstruction, jet energy scale (JES) calibration and the b-jet tagging techniques.

Jet reconstruction

Jets are reconstructed using anti- k_t algorithm^[63] and with radius parameter of $R = 0.4$ in most cases. The FastJet software package^[64] is utilized for jet finding and reconstruction. A collection of four-vectors are used as inputs at each combination step in jet clustering, the total four-momentum is therefore computed as the sum of four-vector of all its constituents. There are three types of jets in ATLAS:

- *Truth jets*: the inputs to jet algorithm are simulated particles.
- *Track jets*: the inputs are charged tracks measured from inner detector.
- *Calorimeter jets*: the inputs are energy deposits in calorimeters.

Figure 4.11 shows the schematic of ATLAS jet reconstruction.

Jet reconstruction

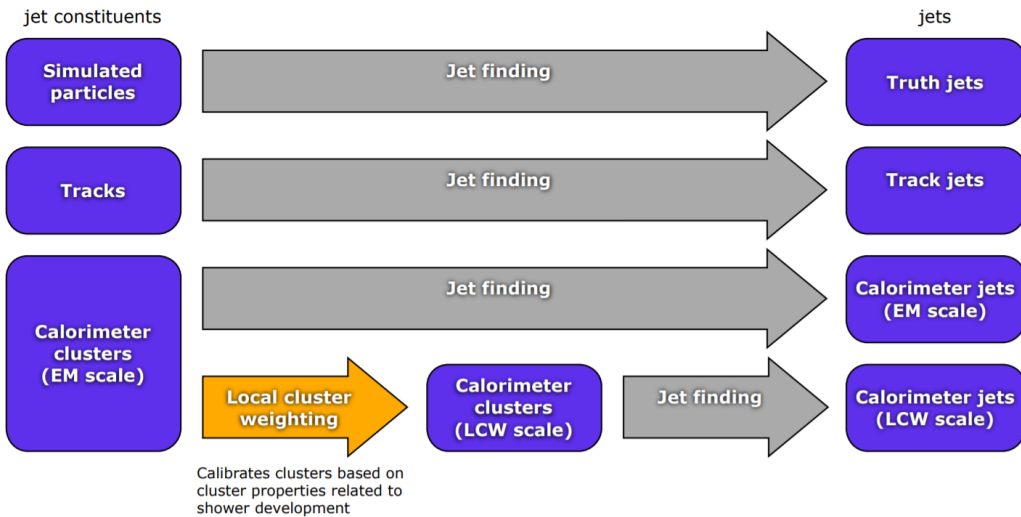


Fig. 4.11 A overview schematic of ATLAS jet reconstruction^[65].

1686

1687 The *truth jets* are reconstructed using anti- k_t algorithm with $R = 0.4$ by using final-

state, stable particles from MC simulation as inputs. It requires the candidate particles with lifetime $c_\tau > 10$ mm and excludes the particles from pile-up. Truth jets with $p_T > 7\text{GeV}$ and $|\eta| < 4.5$ are then used for jets calibration described later.

The *track jets* are reconstructed from charged particles within the full acceptance of inner detector ($|\eta| < 2.5$). The track reconstruction has been introduced in section 4.2.1. Reconstructed jets with $p_T > 500\text{MeV}$ and associated with primary vertex are then selected. Tracks are assigned to jets using ghost association^[62], a procedure that treats selected tracks as four-vectors of infinitesimal magnitude during the jet reconstruction and assigns them to the jet which they are clustered with. In addition, muon track segments are used as a compensation for those uncaptured jet energy carried by energetic particles passing through the calorimeters without being completely absorbed. Similar to the ID track, muon segments are assigned to jets using the method of ghost association mentioned above as well.

The *calorimeter jets* are reconstructed using a set of three-dimensional, positive-energy topological clusters (topo-clusters) made of calorimeter cell energies as input to the anti- k_t algorithm^[66]. Topo-clusters are built from near-by calorimeter cells that contains a significant energy above a noise threshold, which is estimated from measurements of calorimeter electronic noise and simulated pile-up noise. Those calorimeter cell energies are measured at electromagnetic energy scale (EM scale) corresponding to the energy deposited by electromagnetically interacting particles. And jets passing a p_T threshold of 7 GeV are reconstructed with the anti- k_t algorithm.

1709 Jet energy scale calibration

Figure 4.12 depicts an overview of ATLAS jet calibration scheme for EM-scale calorimeter jets. In this procedure, the jet energies are scaled to truth jets, which is reconstructed at the particle-level. Each step of the calibration corrects the full four-momentum unless otherwise stated, scaling the jet p_T , energy, and mass.

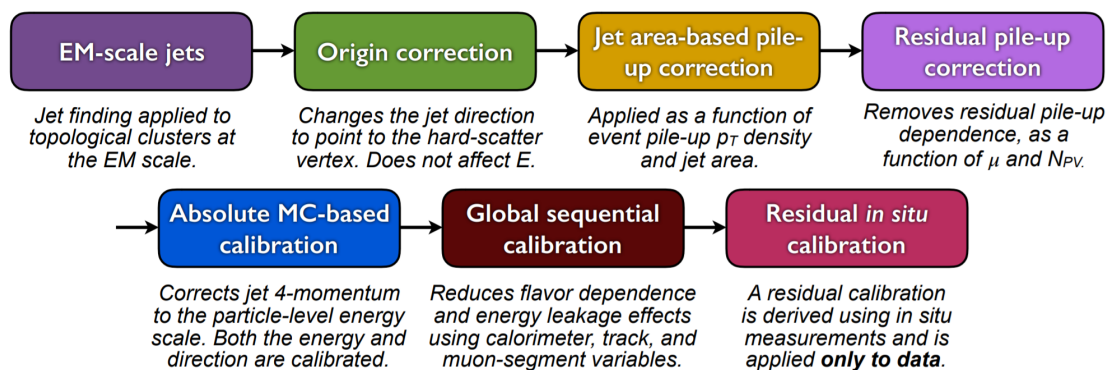


Fig. 4.12 A overview schematic of ATLAS jet calibration^[66].

1713 First of all, the origin correction recompute the four-momentum of jets to point them to
1714 the hard-scatter primary vertex instead of the centre of detector, and in the meantime keep
1715 the jet energy unchanged. This correction improves the η resolution of jets by roughly
1716 25% at a jet p_T of 20 GeV and > 5 times improvement for jet with p_T above 200 GeV,
1717 as measured from the difference between reconstructed jets and truth jets in MC simu-
1718 lation. Secondly, the pile-up correction is adopted to remove the excess energy due to
1719 in-time and out-of-time pile-up, which consists of two processes: an area-based p_T den-
1720 sity subtraction applied on the top of each event; and a residual correction derived from
1721 the simulation. Thirdly, the absolute JES calibration corrects the jet four-momentum to
1722 the particle-level energy scale, using truth jets in di-jet MC events. Furthermore, the step
1723 of global sequential calibration uses calorimeter, track and MS-based variables to reduce
1724 the flavor dependence and energy leakage effects. Finally, the residual in situ calibration
1725 is adopted to correct jets in data by using well-measured objects eg. photons, Z bosons
1726 and calibrated jets.

1727 **B-jet tagging**

1728 Tagging of b-jets plays a important role in many physics analyses involving b- or t-
1729 quark. In the meantime, lots of analyses need to apply b-jet veto to suppress $t\bar{t}$ process.
1730 There are three major types of algorithms that have been developed to distinguish b-quark
1731 jets from light-quark (u,d,s) jets^[67]:

- 1732 • **Impact parameter based algorithms (IP2D and IP3D):** b-hadrons usually have
1733 long lifetime (~ 1.5 ps, $c_\tau \sim 450$ μm), which leads to large impact parameter for
1734 tracks produced from b-hadron decay. The impact parameter taggers are devel-
1735 oped based on these variables. The IP2D tagger makes use of the transverse im-
1736 pact parameter significance $d_0/\sigma(d_0)$ as discriminant, while IP3D tagger uses two-
1737 dimensional discriminant of both transverse and longitudinal impact parameter sig-
1738 nificances: $d_0/\sigma(d_0)$ and $z_0 \sin\theta/\sigma(z_0)$.
- 1739 • **Secondary vertex finding algorithm (SV1)** makes use of the secondary vertex
1740 formed by decay products of b-hadron within the jet. All track pairs within a jet are
1741 tested for a two-track vertex hypothesis, and removed if they are likely to originate
1742 from a long-live particle decay (eg. K_s or Λ), hadronic interactions or photon con-
1743 versions. After that, a new vertex is fitted with all tracks from remaining two-track
1744 vertices, and the outliers are removed from this set of tracks.
- 1745 • **Decay chain multi-vertex algorithm (JetFitter)**^[68] exploits the topological struc-
1746 ture of weak b- and c- hadron decays inside the jet and tries to reconstruct the full

1747 b-hadron decay chain. A Kalman filter is adopted to find a common line between
 1748 primary vertex and b/c- vertices, as well as their position in this line, which gives
 1749 a approximated flight path for the b-hadron. In this approach, the b- and c-hadron
 1750 vertices, whenever resolution allows, can be resolved, even when there is only a
 1751 single track associated to them.

1752 The final discrimination commonly used in many physics analyses is called **Multivariate**
 1753 **Algorithm (MV2)**, which is based on Boosted Decision Tree (BDT) implemented in the
 1754 TMVA package^[69] by combining the outputs from underlying taggers mentioned above.
 1755 The MV2 was trained using jets in $t\bar{t}$ sample, where the b-jets are treated as signal while
 1756 the c- and light-flavor jets are treated as backgrounds. There are three kinds of MV2
 1757 depending on the fraction of c-jets in background for training: *MV2c00*, *MV2c10* and
MV2c20. Figure 4.13 presents the output score of MV2c10 for different flavor jets.

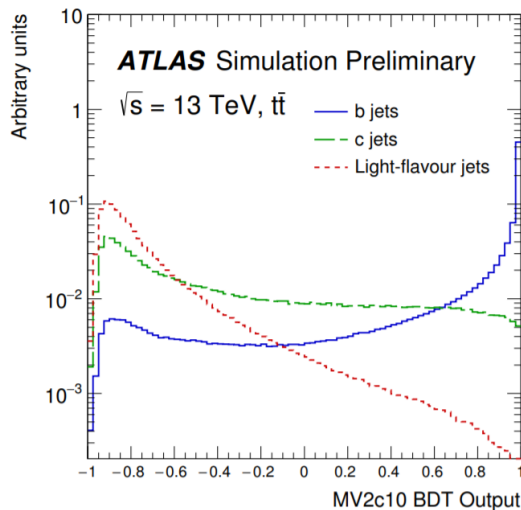


Fig. 4.13 MV2c10 BDT output for b- (solid blue), c- (dashed green) and light-flavour (dotted red) jets in $t\bar{t}$ events^[67].

1758

1759 4.2.6 Missing transverse energy

1760 Many interesting physics processes are with the involvement of neutrinos. Since they
 1761 do not interact with any materials in the detector, neutrinos cannot be detected directly;
 1762 but instead, they can result in imbalance in the plane transverse to the beam axis, where
 1763 momentum conservation is assumed. It is known as the missing transverse momentum
 1764 denoted as E_T^{miss} , which is obtained from the negative vector sum of the momenta of all
 1765 particles detected in a proton-proton collision event.

1766 The E_T^{miss} is measured using selected, reconstructed and calibrated hard objects in an

1767 event. Its x- and y- components can be calculated as follow^[70]:

$$E_{x(y)}^{miss} = E_{x(y)}^{miss,e} + E_{x(y)}^{miss,\gamma} + E_{x(y)}^{miss,\tau} + E_{x(y)}^{miss,jets} + E_{x(y)}^{miss,\mu} + E_{x(y)}^{miss,soft} \quad (4.2)$$

1768 where each object term is given by the negative vectorial sum of the momenta of the
 1769 respective calibrated objects. The calorimeter signals are associated with the recon-
 1770 structed objects in the following order: electrons, photons, hadronically decaying taus,
 1771 jets, muons. The soft term is reconstructed from detected objects not match any hard
 1772 object passing the selections, but associated with the primary vertex. Details of applied
 1773 selections for each term are summarized in table 4.1.

1774 Based on $E_{x(y)}^{miss}$, the magnitude of E_T^{miss} and the azimuthal angle ϕ^{miss} are computed:

$$\begin{aligned} E_T^{miss} &= \sqrt{(E_x^{miss})^2 + (E_y^{miss})^2} \\ \phi^{miss} &= \arctan(E_y^{miss}/E_x^{miss}) \end{aligned} \quad (4.3)$$

1775 In equation 4.2, each objects are required to pass certain reconstruction and calibrated
 1776 criteria and selections mentioned above before taken as inputs.

1777 In figure 4.14, left plot shows the observed E_T^{miss} distribution for data and MC of $Z \rightarrow$
 1778 $\mu\mu$ events without genuine missing transverse momentum; and right plot shows the E_T^{miss}
 1779 distribution for $W \rightarrow e\nu$ events that has genuine (true) missing transverse momentum
 due to real neutrino.

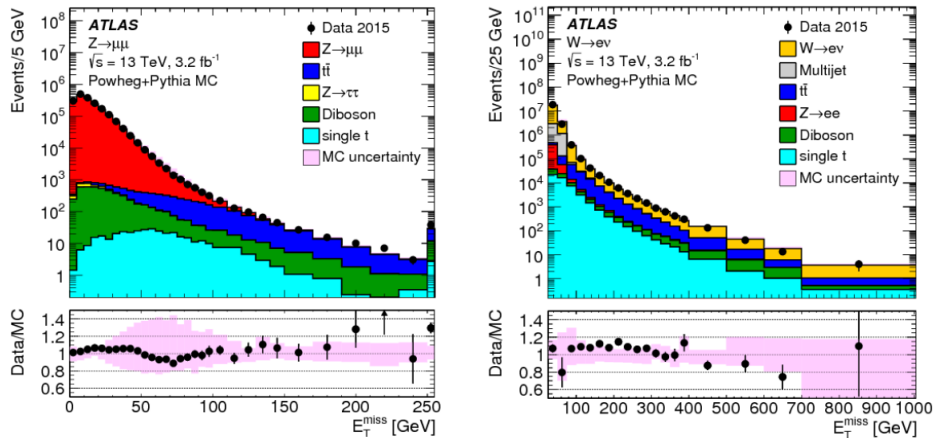


Fig. 4.14 Measured E_T^{miss} distribution for $Z \rightarrow \mu\mu$ events (left) and $W \rightarrow e\nu$ events (right).

1780

Table 4.1 Overview of the contributions to E_T^{miss} .

Objects contributing to E_T^{miss}				
Priority	Type	Selections	Variables	Comments
(1)	e	$ \eta < 1.37 \text{ or } 1.52 < \eta < 2.47$ $p_T > 10GeV$	$E_T^{miss,e}$	all e^\pm passing kinematic selections and medium reconstruction quality
(2)	γ	$ \eta < 1.37 \text{ or } 1.52 < \eta < 2.47$ $p_T > 25GeV$	$E_T^{miss,\gamma}$	all γ passing kinematic selections and tight reconstruction quality, and without overlapping with (1)
(3)	τ_{had}	$ \eta < 1.37 \text{ or } 1.52 < \eta < 2.47$ $p_T > 20GeV$	$E_T^{miss,\tau}$	all τ_{had} passing kinematic selections and medium reconstruction quality, and without overlapping with (1) and (2)
(4)	μ	$ \eta < 2.7$ $p_T > 10GeV$	$E_T^{miss,\mu}$	all μ passing kinematic selections and medium reconstruction quality
(5)	jet	$ \eta < 4.5$ $p_T > 60GeV$ --- or --- $2.4 < \eta < 4.5$ $20GeV < p_T < 60GeV$ --- or --- $ \eta < 2.4$ $20GeV < p_T < 60GeV$ $JVT > 0.59$	$E_T^{miss,jet}$	all jets passing kinematic selections and reconstruction quality (jet cleaning), and without overlap with (1)–(4)
(6)	ID track	$p_T > 400MeV$ $ d_0 < 1.5mm$ $ z_0 \sin\theta < 1.5mm$ $\Delta R(track, e/\gamma cluster) > 0.05$ $\Delta R(track, \tau_{had}) > 0.2$	$E_T^{miss,soft}$	all ID tracks from the hard-scattering vertex passing kinematic selections and reconstruction quality, and not associated with any particle from (1), (3) or (4), or associated with a jet from (5)

1781 **Chapter 5 Statistical treatment of searching for new 1782 particles or processes**

1783 In the experiments of particle physics, one often searches for particles or processes
1784 that have been predicted but not yet observed, such as the two analysis presented in this
1785 dissertation: searching for the vector boson scattering process and searching for the heavy
1786 resonance(s). Usually two hypotheses are defined:

- 1787 • H_0 : null hypothesis, in most cases are designated as background-only hypothesis.
1788 • H_1 : signal plus background hypothesis, where signal is a new model one would
1789 like to search for.

1790 For the purpose of discovering a new signal process, the H_0 hypothesis is tested against
1791 the alternative H_1 . When setting limits, the H_1 hypotheses with different signal strengths
1792 are tested against the H_0 .

1793 The level of agreement between observed data and a given hypothesis can be quantified
1794 by computing the p -value, the probability under this hypothesis assumption, or
1795 its equivalent Gaussian significance. This section describes the statistical treatment for
1796 searches related to this dissertation.

1797 5.1 The likelihood function

1798 The likelihood function is defined as the product of a set of the probability density
1799 functions (pdfs) of variables x , that used to evaluate the probability of the observed
1800 dataset:

$$\mathcal{L}(x_1, \dots, x_N; \theta_1, \dots, \theta_M) = \prod_i^N f(x_i; \theta_1, \dots, \theta_M) \quad (5.1)$$

1801 where $\theta_1, \dots, \theta_M$ are the nuisance parameters that can be written as $\boldsymbol{\theta}$, and x_1, \dots, x_N
1802 denote the observables of dataset. Usually one measures the variable x by constructing a
1803 histogram $\mathbf{n} = (n_1, \dots, n_N)^{[71]}$. The expectation value of the i th bin n_i can be written as:

$$E[n_i] = \mu s_i + b_i \quad (5.2)$$

1804 where μ is the signal strength, s_i and b_i are the number of signal and background events
1805 in that bin. In addition to the histogram \mathbf{n} , in some cases, one would like to use subsidiary
1806 measurements to help further constrain the nuisance parameters. For instance, due to the
1807 lack of background simulation or the mismodelling issue of one MC sample, one can

choose a control region and construct another histogram $\mathbf{m} = (m_1, \dots, m_M)$ to constrain the contribution of one certain background in data. For this measurement, the expectation value of the i th bin m_i can be written as:

$$E[m_i] = u_i(\boldsymbol{\theta}) \quad (5.3)$$

In most particle experiments, the number of these events observed in one bin follows the Poisson distribution, by combining the equation 5.2 and 5.3, one can get the likelihood function for all bins as:

$$\mathcal{L}(\mu, \boldsymbol{\theta}) = \prod_{i=1}^N \frac{(\mu s_i + b_i)^{n_i}}{n_i!} e^{-(\mu s_i + b_i)} \prod_{k=1}^M \frac{u_k^{m_k}}{m_k!} e^{-u_k} \quad (5.4)$$

Then to test the hypothesized value of μ , the profile likelihood ratio is defined as:

$$\lambda(\mu) = \frac{\mathcal{L}(\mu, \hat{\boldsymbol{\theta}})}{\mathcal{L}(\hat{\mu}, \hat{\boldsymbol{\theta}})} \quad (5.5)$$

where numerator denotes to a local maximum-likelihood for a specific μ , $\hat{\boldsymbol{\theta}}$ is the value of $\boldsymbol{\theta}$ that maximizes the numerator. And the denominator is the global maximum-likelihood with the $\hat{\mu}$ and $\hat{\boldsymbol{\theta}}$ as their best fit value.

5.2 Test statistic

To test the level of agreement between the data and the hypothesized value μ , a test statistic t_μ can be defined as:

$$t_\mu = -2 \ln \lambda(\mu) \quad (5.6)$$

From the definition of $\lambda(\mu)$ in equation 5.5, one can see that $0 \leq \lambda \leq 1$, and a λ with value close to 1 implies good agreement between data and μ . Thus, smaller value of t_μ means the increase of compatibility between data and μ . To quantify the level of disagreement, one can calculate the p -value as:

$$p_\mu = \int_{t_{\mu,obs}}^{\infty} f(t_\mu | \mu) dt_\mu \quad (5.7)$$

in which $t_{\mu,obs}$ is the value of test statistic from observed data, and $f(t_\mu | \mu)$ is the pdf of t_μ under the assumption of hypothesized value μ . This is a one-side p -value with its

1827 corresponding observed significance, Z , can be defined as:

$$Z = \Phi^{-1}(1 - 2p_\mu) \quad (5.8)$$

1828 The relationship between the t_μ , p -value and significance Z are depicted in figure 5.1.
 1829 When searching for a signal process, such as Higgs boson, the particle physics commu-
 1830 nity tends to claim a discovery when the rejection of background-only hypothesis has a
 1831 significance of at least $Z = 5$.

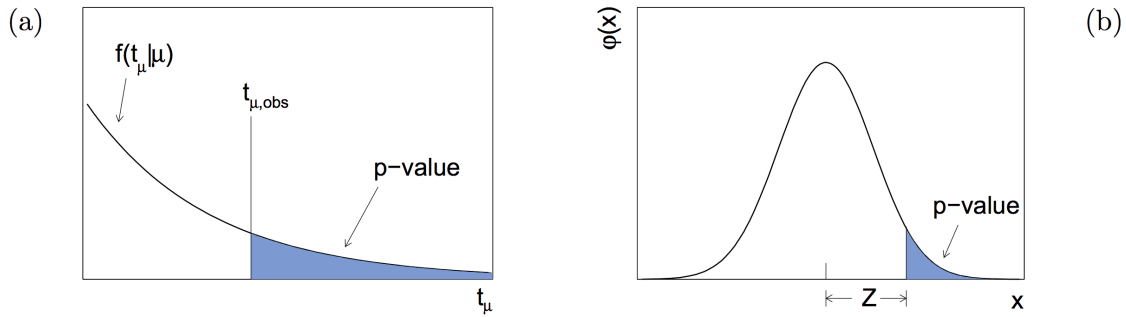


Fig. 5.1 (a) Illustration of the relationship between the observed t_μ and its p -value. (b) The relationship between p -value and the observed significance Z , where $\phi(x)$ is a standard normal distribution.

1832 In most cases, one assumes that the presence of a new signal can only increase the
 1833 event rate comparing to the background only model, then the signal strength $\mu \geq 0$. And
 1834 for the case of discovery, the hypothesis of a positive signal strength should be tested
 1835 against to the background-only (null) hypothesis by using the test statistic called p_0 :

$$p_0 = \begin{cases} -2\ln(\lambda(0)) & \hat{\mu} \geq 0 \\ 0 & \hat{\mu} < 0 \end{cases} \quad (5.9)$$

1836 which corresponds to the p -value called p_0 :

$$p_0 = \int_{q_{0,obs}}^{\infty} f(q_0|0)dq_0 \quad (5.10)$$

1837 to quantify the level of disagreement between the data and the null hypothesis ($\mu = 0$).

5.3 The CLs upper limit

For a signal hypothesized value μ , one can compute the probability that this hypothesis (called S+B hypothesis) gives a **greater** test statistic value than the observed one q_{obs} as:

$$p_{s+b} = \int_{q_{obs}}^{\infty} f(q_{\mu}|\mu) dq_{\mu} \quad (5.11)$$

In the meantime, the probability that the background-only hypothesis gives a **smaller** test statistic than observed data can also be calculated as:

$$1 - p_b = \int_{-\infty}^{q_{obs}} f(q_{\mu}|0) dq_{\mu} \quad (5.12)$$

Then we define the CLs^[72] of a hypothesized value μ as:

$$CLs = \frac{p_{s+b}}{1 - p_b} \quad (5.13)$$

For purpose of excluding a signal hypothesis, a threshold CLs of 0.05 is often used. For this reason, usually under the circumstance that no significant derivation between data and background-only hypothesis is found, one would like to find the value of hypothesized signal strength μ by requiring its $CLs = 0.05$ (called 95% CLs upper limit) for exclusion.

The sensitivity of an experiment to exclude a new signal process is quantified by *median upper limit*, which is obtained using “Asimov dataset”. The Asimov dataset is defined such that when one uses it to evaluate the estimators for all parameters, one obtains the true parameter values. Moreover, it is useful to use Asimov dataset to compute how much the sensitivity is expected to vary, given the expected fluctuations in the data. The $\hat{\mu}$ is assumed to follow a Gaussian distribution with a mean value of μ' and the standard deviation of σ . First of all, the test statistic from profile likelihood ratio can be approximated as^[71]:

$$-2\ln\lambda(\mu) = \frac{(\mu - \hat{\mu})^2}{\sigma^2} + \mathcal{O}(1/\sqrt{N}) \quad (5.14)$$

Given that the Asimov dataset corresponding to a signal strength μ' , one finds:

$$-2\ln\lambda_A(\mu) \approx \frac{(\mu - \mu')^2}{\sigma^2} = q_{\mu,A} \quad (5.15)$$

where $q_{\mu,A} = -2\ln\lambda_A(\mu)$ is the observed test statistic of Asimov dataset. Then the stan-

1858 dard derivation can be computed as:

$$\sigma_A^2 = \frac{(\mu - \hat{\mu})^2}{q_{\mu,A}} \quad (5.16)$$

1859 In a special situation where one wants to find the median exclusion significance for the
1860 hypothesis μ assuming that there is no signal ($\mu' = 0$), one gets:

$$\sigma_A^2 = \frac{\hat{\mu}^2}{q_{0,A}} \quad (5.17)$$

1861 **5.4 Nuisance parameters**

1862 The expected numbers and pdf shapes of signal and background events also depend on
1863 a series of systematic uncertainties, which are described as a set of nuisance parameters
1864 (NPs). As showed in equation 5.1, θ is a set of NPs that plays as an additional “penalty”
1865 term to likelihood function, which will increase the negative log likelihood when any
1866 nuisance parameter is shifted from its nominal value. Usually those NPs are constrained
1867 by using Gaussian function with their estimated uncertainties provided by the experiment
1868 condition.

1869 **Chapter 6 Studies of SM ZZ production in $\ell\ell\ell'\ell'$ final** 1870 **state using pp collision data collected by ATLAS** 1871 **detector from 2015 to 2018**

1872 6.1 Introduction

1873 After the discovery of Higgs boson^[3,4], the examination of electroweak symmetry
1874 breaking (EWSB) becomes a main focus at the LHC. In addition to measuring the prop-
1875 erties of Higgs boson directly, the vector boson scattering (VBS) process is another key
1876 avenue to probe EWSB^[73-75]. As introduced in section 2.1.3, in Standard Model (SM),
1877 the Higgs boson acts as “moderator” to unitarize high-energy longitudinal VBS ampli-
1878 tudes at the TeV scale. Therefore, studying high-energy behaviours of VBS is crucial to
1879 understand the mechanism of EWSB.

1880 Since no VBS process was observed prior to the LHC era, LHC provides an exception-
1881 able opportunity to study them due to its unprecedented high energy and luminosity. At
1882 the LHC, the VBS process is typically studied through the measurements of electroweak
1883 (EW) production of two vector bosons radiated from quark-quark initial state, plus a pair
1884 of hadronic jets with high energy in the back and forward regions (denoted as EW- $VVjj$).
1885 The quantum chromodynamics (QCD) production of $VVjj$ containing two QCD vertices
1886 at the lowest order (denoted as QCD- $VVjj$) is an irreducible background to the search
1887 of EW- $VVjj$ production. The features of EW- $VVjj$ production including a large invari-
1888 ant mass of jet pair (m_{jj}) and a significant separation of rapidity between two jets (Δy_{jj}).
1889 Figure 6.1 presents some typical Feynman diagrams of EW- and QCD- $ZZjj$ processes.
1890

1891 The first evidence of the EW- $VVjj$ process was seen in same-sign WW channel
1892 (EW- $W^\pm W^\pm jj$) by ATLAS collaboration with 20.3 fb^{-1} 8 TeV data^[76], in which a 3.6σ
1893 excess was observed in data over the background-only prediction. In the LHC run-2, the
1894 observation (with $> 5 \sigma$ statistical significance) of EW- $W^\pm W^\pm jj$ process has been re-
1895 ported in both ATLAS and CMS collaboration with 36 fb^{-1} 13 TeV data^[77-78]. In WZ
1896 channel (EW- $WZjj$), an observation with 5.3σ excess was also reported by the AT-
1897 LAS collaboration recently^[79]. As for the EW- $ZZjj$ production, it was searched by
1898 CMS using 35.9 fb^{-1} 13 TeV data but no evidence was found^[80]. The EW production in
1899 ZZ final state (EW- $ZZjj$) is typically rare, whose fiducial cross section has an order of
1900 $O(0.1) \text{ fb}^{-1}$ in the final state where both Z bosons decay leptonically. But in the mean-

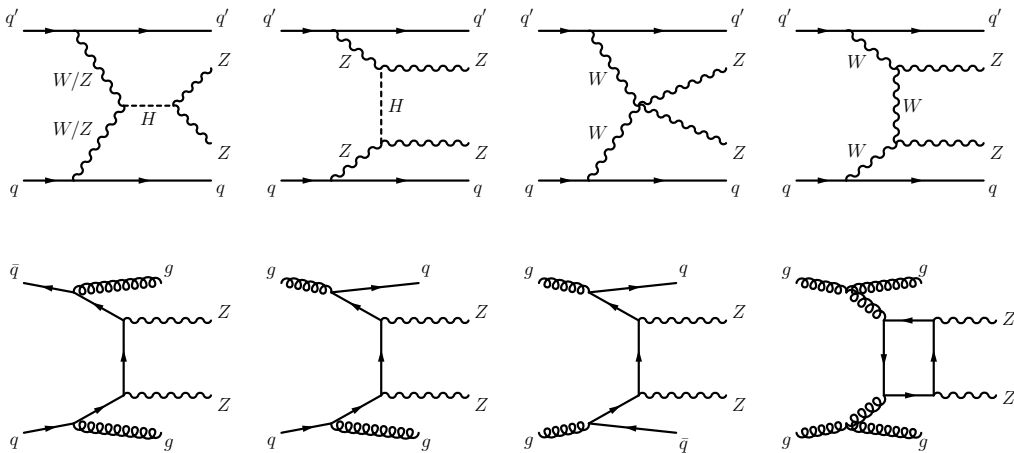


Fig. 6.1 Typical diagrams for the production of $ZZjj$, including the relevant EW VBS diagrams (first row) and QCD diagrams (second row).

time, $ZZ \rightarrow \ell\ell\ell'\ell'$ process offers an extremely clean channel than all the others. So with more data collected in the LHC, the observation of EW- $ZZjj$ becomes possible.

This section presents the first observation of EW- $ZZjj$ production decaying to four charged leptons with two jets ($\ell\ell\ell'\ell' jj$) by ATLAS collaboration using the complete set of the LHC run-2 data with 139 fb^{-1} luminosity. It is a new milestone in the study of EWSB at the LHC, and completes the last missing part of observation of weak boson scattering for massive bosons. In the meantime, the measurement of fiducial cross-sections for SM ZZ production including both EW and QCD processes is also reported. The $ZZjj$ production involving intermediate τ -leptons from Z decays is considered as signal but has a negligible contribution to the selected events. Reducible backgrounds give minor contributions in the $\ell\ell\ell'\ell' jj$ channel are also studied. To further separate the EW signal and the QCD background, multivariate discriminant (MD) is trained using event kinematic information from simulated samples. The MD distribution is then used as discriminant in statistical fit to evaluate the signal strength of EW process.

6.2 Data and MC samples

6.2.1 Data samples

The datasets for this analysis include the full run-2 pp collision data collected by the ATLAS experiment during the years from 2015 to 2018. Data event is only used if it passed the latest Good Run List (GRL) released by the Data Quality group from ATLAS experiment, corresponding to an integrated luminosity of $139.0 \pm 2.4 \text{ fb}^{-1}$.

1921 6.2.2 MC simulations

1922 The EW- $Z Z jj$ production is modelled using MadGraph5_aMC@NLO 2.6.1^[81] with
1923 the matrix elements (ME) calculated in the leading-order (LO) approximation in pertur-
1924 bative QCD (pQCD) and with the NNPDF2.3LO^[82] parton distribution functions (PDF).
1925 The VBF Higgs process is also included.

1926 The QCD- $Z Z jj$ production is modelled using Sherpa 2.2.2^[83] with the
1927 NNPDF3.0NNLO^[84] PDF, where events with up to one (three) outgoing partons
1928 are generated at NLO (LO) in pQCD. The production of $Z Z jj$ from the gluon-gluon
1929 initial state with a four-fermion loop or with an exchange of the Higgs boson has an
1930 order of α_S^4 in QCD, and is not included in the Sherpa simulation. A separate gg induced
1931 $Z Z + 2\text{jets}$ sample is modelled using Sherpa 2.2.2 with the NNPDF3.0NNLO PDF and
1932 with an additional 1.7 k-factor^[85] being applied. Then the interference between EW- and
1933 QCD- $Z Z jj$ is modelled with MadGraph5_aMC@NLO 2.6.1 calculated at LO.

1934 The diboson productions from QCD $WW \rightarrow \ell\nu qq$ as well as QCD and EW $WZ \rightarrow$
1935 $\ell\ell qq$ are modelled using Sherpa 2.2.2 with the NNPDF3.0NNLO PDF. The productions
1936 of semileptonic decays ($WW \rightarrow \ell\nu qq$ and $WZ \rightarrow qq\ell\ell$) are modelled using Powheg-
1937 Box v2^[86] with the CT10 PDF^[87]. The triboson production is modelled using Sherpa
1938 2.2.2 with the NNPDF3.0NNLO PDF.

1939 For top-quark pair ($t\bar{t}$) production, the Powheg-Box v2 is used with the CT10 PDF.
1940 The single top-quark production in t -channel, s -channel and Wt -channel are simulated
1941 using the Powheg-Box v1 event generator^[88-90]. The productions of $t\bar{t}$ in association with
1942 vector boson(s) ($t\bar{t}V$) are modelled with MadGraph5_aMC@NLO 2.3.3 for $t\bar{t}W$ and $t\bar{t}Z$
1943 with $Z \rightarrow \nu\nu/qq$ decays, with Sherpa 2.2.1 for $t\bar{t}Z$ where the Z decays to dilepton, and
1944 with MadGraph5_aMC@NLO 2.2.2 for $t\bar{t}WW$ respectively.

1945 The $Z+jets$ processes are modelled using Sherpa 2.2.1 with the NNPDF3.0NNLO
1946 PDF, in which the ME is calculated for up to two partons with next-to-leading-order
1947 (NLO) accuracy in pQCD and up to four partons with LO accuracy.

1948 For all the samples except those from Sherpa, the parton showering is modelled with
1949 Pythia8^[45] using the NNPDF2.3^[82] PDF set, and the A14 set of tuned parameters^[91].
1950 While for Sherpa samples, the parton showering is simulated within the programme.

1951 All simulated events are processed with detector response simulation based on Geant4
1952 described in section 4.1. In addition, simulated inelastic pp collisions are overlaid to
1953 model additional pp collision in the same and neighbouring bunch crossings (pile-up),
1954 and reweighted to match the pile-up conditions in data. Moreover, all simulated events
1955 are processed using the same reconstruction algorithms as data. And the leptons and

1956 jets reconstruction, energy scale and resolution, and the leptons identification, isolation,
 1957 trigger efficiencies for simulated events, as described in section 4.2, are all corrected to
 1958 match the data measurements.

1959 **6.3 Objects and Event selection**

1960 **6.3.1 Objects selection**

1961 The selection of analysis relies on the definition of multiple objects: *electrons*, *Muons*,
 1962 and *jets*. Details of definition for each object are described as below:

1963 **Muon:** To increase the acceptance range in reconstruction (reco) -level for $\ell\ell\ell'\ell'$
 1964 channel, all four types of muons (CB, ST, CT, ME muons, described in section 4.2.4)
 1965 are used. The identified muons are then required to pass $p_T > 7$ GeV and $|\eta| < 2.7$,
 1966 and satisfy the *Loose* identification criterion (see definition in sec 4.2.4). The impact
 1967 parameter cuts are further applied to suppress the contribution from cosmic muons and
 1968 non-prompt muons, with the value of: $|d_0/\sigma(d_0)| < 3.0$ and $|z_0 \sin\theta| < 0.5$ mm, where d_0
 1969 is the transverse impact parameter relative to the beam line, $\sigma(d_0)$ is its uncertainty, and
 1970 z_0 is the longitudinal impact parameter relative to the primary vertex. In order to avoid
 1971 muons associated with jets, all muons are required to be isolated and pass *FixedCutLoose*
 1972 isolation criteria of $E_T^{\text{topocone}20}/p_T < 0.3$ and $p_T^{\text{varcone}30}/p_T < 0.15$.

1973 **Electron:** As described in section 4.2.3, electrons are reconstructed from energy de-
 1974 posits in the EM calorimeter matched to a track in the inner detector. The electron candi-
 1975 dates must satisfy the *Loose* criterion defined by the likelihood-based (LH) method. And
 1976 electrons are required to have $p_T > 7$ GeV and $|\eta| < 2.47$. Moreover, the impact param-
 1977 eter requirements of $|d_0/\sigma(d_0)| < 5.0$ and $|z_0 \sin\theta| < 0.5$ mm are applied. Same as muon,
 1978 all electrons are required to satisfy *FixedCutLoose* isolation criteria, which, for electrons,
 1979 is $E_T^{\text{topocone}20}/p_T < 0.2$ and $p_T^{\text{varcone}20}/p_T < 0.15$.

1980 **Jets:** Jet are key signatures for VBS processes. This analysis use the jets clustered
 1981 using the anti- k_t algorithm with radius parameter $R = 0.4$, more details of jets' reconstruc-
 1982 tion can be found in section 4.2.5. The jets are required to satisfy $p_T > 30$ (40) GeV in
 1983 the $|\eta| < 2.4$ ($2.4 < |\eta| < 4.5$) region. To further reduce the effects of pile-up jets, a jet
 1984 vertex tagger (JVT) is applied to jets with $p_T < 60$ GeV and $|\eta| < 2.4$ to select jets from
 1985 hard-scattering vertex^[92].

1986 **Overlap removal:** An overlap-removal procedure is applied to selected leptons and
 1987 jets. To enhance the selection efficiency, leptons are given higher priority to be kept when
 1988 overlapping with jets. More details of the strategy is summarized in table 6.1.

	Reference objects	Criteria
Remove electrons	electrons	Share a track or have overlapping calorimeter cluster. Keep higher p_T electron
Remove muons	electrons	Share track and muon is calo-tagged
Remove electrons	muons	Share track
Remove jets	electrons	$\Delta R_{e-jet} < 0.2$
	muons	$\Delta R_{\mu-jet} < 0.2$ OR muon track is ghost-associated to jet AND ($N_{Trk}(jet) < 3$ OR ($p_T^{jet}/p_T^\mu < 2$ and $p_T^\mu/\Sigma_{TrkP_t} > 0.7$))

Table 6.1 Overlap removal criteria between pre-selection objects for the $\ell\ell\ell'\ell'$ channel. The overlap removal follows the order shown in this table. Once an object has been marked as removed, it does not participate in the subsequent stages of the overlap removal procedure.

6.3.2 Event selection

The events are required to additionally be recorded by single or multi-lepton triggers, with transverse momentum (p_T) thresholds varying from 8 to 26 GeV. The overall trigger efficiency for selected inclusive $\ell\ell\ell'\ell' jj$ signal events in the analysis region are from 95 to 99%.

The $\ell\ell\ell'\ell'$ quadruplets are formed by two opposite-sign, same-flavour (OSSF) lepton pairs ($\ell^+\ell^-$), in which leptons are required to be separated by $\Delta R > 0.2$ in table 6.1. At most one muon is allowed to be ME or CT muon. The p_T threshold of first three leading leptons are 20, 20 and 10 GeV. If more than one quadruplets are found, the one with minimum sum of difference between two dilepton pair masses and Z boson mass ($|m_{l_1^+ l_1^-} - m_Z| + |m_{l_2^+ l_2^-} - m_Z|$) is selected. Both two dilepton pair masses are required to be between 66 to 116 GeV. In addition, the invariant masses of all possible OSSF pairs are required to be greater than 10 GeV to reject events from J/ϕ or Y decay.

For VBS topology, the two most energetic jets in different detector side ($y_{j1} \times y_{j2} < 0$) are selected. Furthermore, the invariant mass of two jets (m_{jj}) is required to be greater than 300 GeV, while Δy_{jj} is required to be larger than 2. Table 6.2 summarizes the above selection requirements, which is defined as signal region (SR).

Electrons	$p_T > 7 \text{ GeV}$, $ \eta < 2.47$ $ d_0/\sigma_{d_0} < 5$ and $ z_0 \times \sin \theta < 0.5 \text{ mm}$
Muons	$p_T > 7 \text{ GeV}$, $ \eta < 2.7$ $ d_0/\sigma_{d_0} < 3$ and $ z_0 \times \sin \theta < 0.5 \text{ mm}$
Jets	$p_T > 30$ (40) GeV for $ \eta < 2.4$ ($2.4 < \eta < 4.5$)
$Z Z$ selection	$p_T > 20, 20, 10 \text{ GeV}$ for the leading, sub-leading and third leptons Two OSSF lepton pairs with smallest $ m_{\ell^+\ell^-} - m_Z + m_{\ell'^+\ell'^-} - m_Z $ $m_{\ell^+\ell^-} > 10 \text{ GeV}$ for all OSSF lepton pairs $\Delta R(\ell, \ell') > 0.2$ $66 < m_{\ell^+\ell^-} < 116 \text{ GeV}$
Dijet selection	Two most energetic jets with $y_{j_1} \times y_{j_2} < 0$ $m_{jj} > 300 \text{ GeV}$ and $\Delta y_{jj} > 2$

Table 6.2 Summary of selection of physics objects and candidate events at detector level in the $\ell\ell\ell'\ell' jj$ signal region.

6.4 Background estimation

Table 6.3 summarizes the background yields for $Z Z jj \rightarrow \ell\ell\ell'\ell' jj$ process in 139 fb^{-1} . Uncertainties on the predictions include both statistical and systematic components. ‘‘Others’’ includes minor contributions from non- $Z Z$ processes including $Z+jets$, top-quark, triboson and $t\bar{t}V$ processes. Details of estimation for each source are described as below.

Process	$\ell\ell\ell'\ell' jj$
EW- $Z Z jj$	20.6 ± 2.5
QCD- $q\bar{q} \rightarrow ZZ$	77 ± 25
QCD- $gg \rightarrow ZZ$	13.1 ± 4.4
Others	3.2 ± 2.1
Total	114 ± 26
Data	127

Table 6.3 Observed data and expected signal and background yields in 139 fb^{-1} of luminosity. Minor backgrounds are summed together as ‘‘Others’’. Uncertainties on the predictions include both statistical and systematic components.

6.4.1 QCD backgrounds

The QCD- $Z Z jj$ production, which include both qq and gg initial processes, is the irreducible background in the search of EW- $Z Z jj$ production. A QCD-enriched control region, named as QCD CR, is defined to constrain the normalization of $Z Z$ background

2016 by reverting either the m_{jj} or Δy_{jj} requirements as:

$$m_{jj} < 300 \text{ GeV} \text{ OR } \Delta y_{jj} < 2 \quad (6.1)$$

2017 Then this normalization factor is included into statistical fit as a free parameter to properly
2018 treat the uncertainty correlations between SR and CR, while the shapes are taken from MC
2019 simulation. Table 6.4 shows the event yields of each background components in this CR.
Uncertainties are statistical one only. The distributions of invariant mass of $\ell\ell\ell'\ell'$ and

Process	$\ell\ell\ell'\ell' jj$
EW-ZZjj	3.9 ± 0
QCD-ZZjj	136.9 ± 0.6
QCD-ggZZjj	16.8 ± 0.1
Diboson	0.3 ± 0.1
Triboson	1.6 ± 0.1
Z+jets	0
t̄t	0
Total	159.5 ± 0.62
Data	152

Table 6.4 Observed data and expected signal and background yields in 139 fb^{-1} of luminosity.

Diboson background in table includes all the other diboson processes discussed in section 6.2.2, except those with four-lepton final state. Uncertainties include only MC statistic. No events from Z+jets and t̄t MC samples pass the selection, and are indicated as 0 in the table.

2020

2021 dijet in QCD CR are shown in figure 6.2.

2022 6.4.2 Reducible backgrounds

2023 Backgrounds from Z+jets, top-quark and WZ processes called reducible back-
2024 grounds can be estimated by data-driven method. These events usually contain two or
2025 three leptons from Z/W decays, together with heavy-flavor jets or misidentified compo-
2026 nents of jets reconstructed as leptons called “fake leptons”. A *fake factor* method is used
2027 to estimate these backgrounds, where the lepton misidentification is measured in data with
2028 the region enhances contributions from Z+jets and top-quark processes. The method is
2029 described as below:

2030 1. Define a dedicated background dominant region to derive the fake factor for this

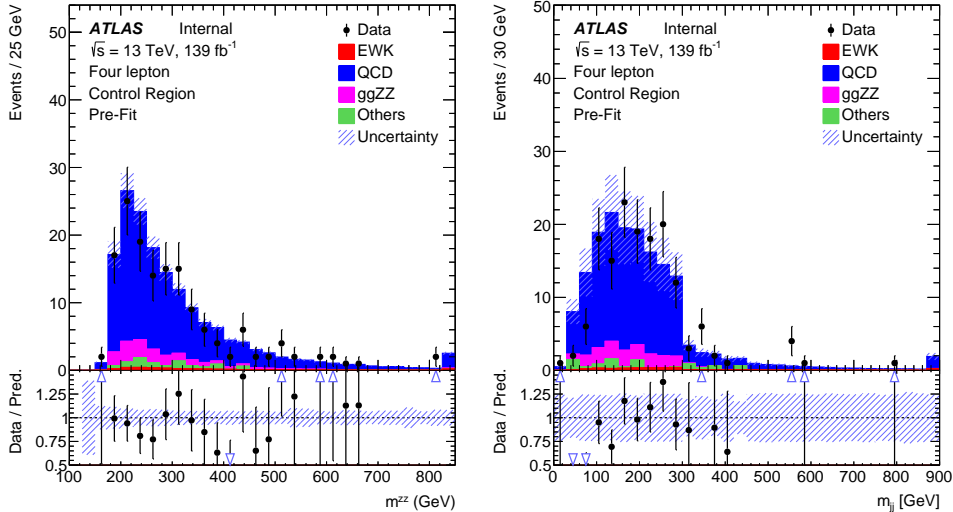


Fig. 6.2 Pre-fit m_{ZZ} and m_{ll} distribution in QCD-enriched CR.

background. The *fake factor* is defined as:

$$\mathcal{F} = \mathcal{N}_{good}/\mathcal{N}_{pool} \quad (6.2)$$

where \mathcal{N}_{good} refers to the number of good leptons passing all SR selection, while \mathcal{N}_{pool} denotes the number of poor leptons passing most SR selection but fail one certain requirement.

2. Define a fake control region, where one or two lepton(s) pass *poor* requirement while all the other leptons are required to pass SR selection.
3. The number of fake events are calculated as:

$$\mathcal{N}_{fake} = (N_{gggp} - N_{ggp}) \times \mathcal{F} - (N_{gppg} - N_{gpp}) \times \mathcal{F}^2 \quad (6.3)$$

with the subtraction of ZZ contribution, and the double counting between N_{gggp} and N_{gppg} .

For the definition of *poor* leptons: The poor electrons are defined as failing “Fixed-CutLoose” isolation requirement, or failing “LooseLH” electron ID requirement but satisfying “VeryLooseLH” WP. The poor muons are required to fail the “FixedCutLoose” isolation requirement or invert the impact parameter cut to be $3 < d_0/\sigma(d_0) < 10$. The dedicated $Z+jets$ and $t\bar{t}$ dominant regions are defined to calculate the fake factor respectively in the following subsections.

1. Fake factor for $Z+jets$

Fake factor for $Z+jets$ background is calculated in $Z+jets$ enriched region, where

events with one OSSF lepton pair around Z mass associated with two jets are selected.

The value of fake factor is driven from data, and is a function of p_T and η as shown in

2050 figure 6.3 for electrons and figure 6.4 for muons. During calculation, the contributions
 2051 from non- $Z+jets$ backgrounds ($t\bar{t}$, ZZ , WZ) have been subtracted from data. The values
 calculated directly from $Z+jets$ MC are also shown in plots for comparison.

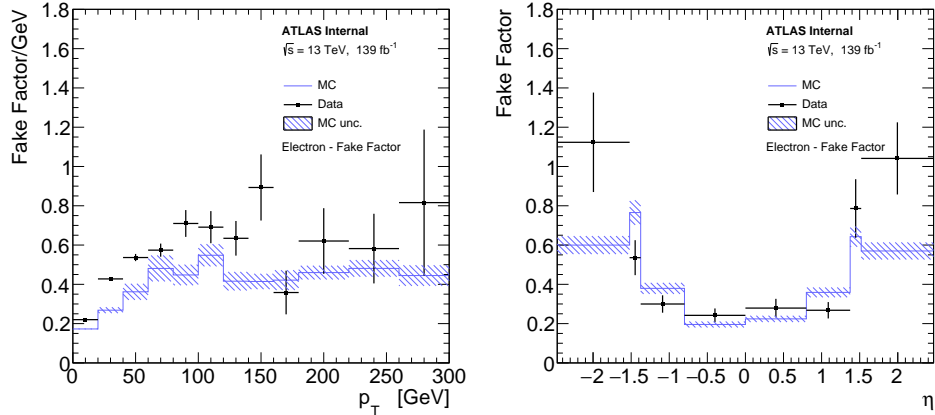


Fig. 6.3 Fake factor for $Z+jets$ background, constructed with additional electron, as a function of p_T (left) and η (right).

2052

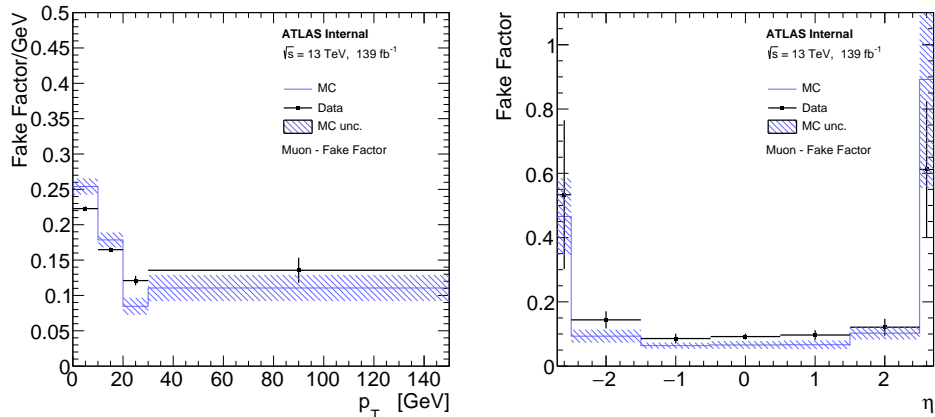


Fig. 6.4 Fake factor for $Z+jets$ background, constructed with additional muon, as a function of p_T (left) and η (right).

2053

2. Fake factor for $t\bar{t}$

2054 The fake factor for $t\bar{t}$ are calculated in $t\bar{t}$ dominant region by selecting the events that
 2055 have one $e\mu$ -pair with additional two jets. For events with three leptons, $m_T^W < 60 \text{ GeV}$ cut
 2056 is applied to reject the contribution from $t\bar{t} + W$ events. The m_T^W is defined as below:

$$m_T^W = \sqrt{2p_T^{l_3}E_T^{\text{miss}} \left[1 - \cos(\Delta\phi(p_T^{l_3}, E_T^{\text{miss}})) \right]} \quad (6.4)$$

2057 In addition, at least one b-jet is required to enhance the top component. The fake factors of
 2058 $t\bar{t}$ calculated from data as the function of p_T and η are shown in figure 6.5 for electrons and
 2059 6.6 for muons. The non- $t\bar{t}$ contributions including $Z+jets$, ZZ and WZ , are subtracted

from data.

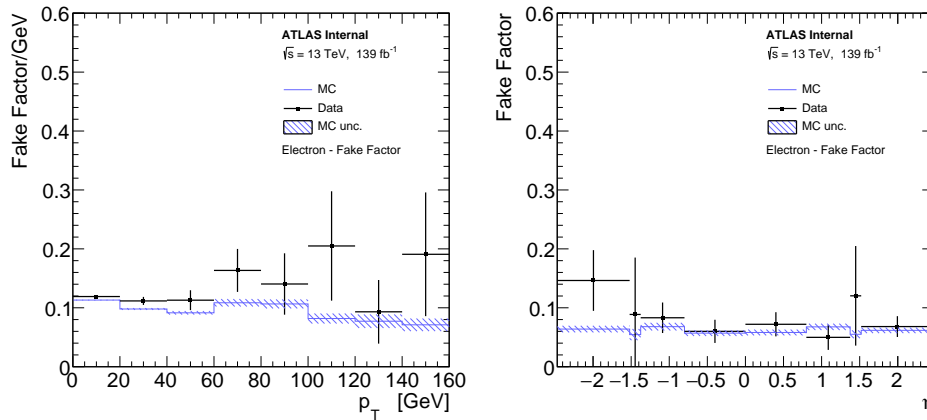


Fig. 6.5 Fake factor for $t\bar{t}$ background, constructed with additional electron, as a function of p_T (left) and η (right).

2060

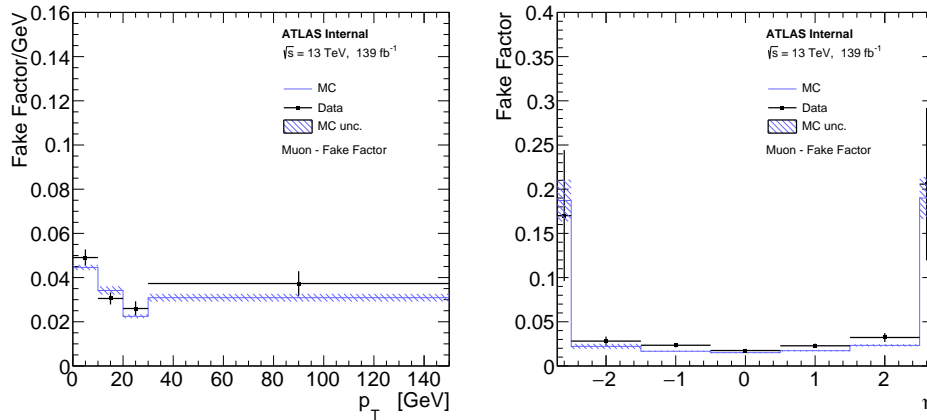


Fig. 6.6 Fake factor for $t\bar{t}$ background, constructed with additional muon, as a function of p_T (left) and η (right).

2061

3. Systematics of fake estimation and results

2062

The systematics of fake factor method can be measured by varying the parameters and selection requirements in fake factor calculation. In addition, due to the very limited data statistic in $\ell\ell\ell'\ell'$ channel, to be more conservative, the difference between data measurement and MC simulation are also considered as additional systematics component.

2065

The sources of systematics that have been included are listed as below:

2067

- Variations of isolation cut for the poor lepton definition up and down scaled by a factor of two.
- Variations of the yields of those subtracted MC in fake control region scaled by 30% up and down.
- The difference of fake factors between driven from data and from MC simulation.

2068

2069

2070

- The difference of fake factors when changing to one bin measurement (instead of p_T or η dependent).
- The statistical uncertainties on fake factor in fake control region.

Table 6.5 summarizes the contribution of fake backgrounds in signal region under different systematic conditions mentioned above as well as the nominal one, together with their statistical uncertainties.

channel	4e	2e2 μ	4 μ	inclusive
Nominal estimate	0.678 ± 0.652	1.023 ± 0.740	0.566 ± 0.240	2.268 ± 1.015
F stat. uncertainty varied down	0.698 ± 0.622	0.872 ± 0.652	0.509 ± 0.214	2.079 ± 0.926
F stat. uncertainty varied up	0.657 ± 0.685	1.173 ± 0.840	0.622 ± 0.267	2.452 ± 1.116
One bin F	0.653 ± 0.590	0.594 ± 0.558	0.646 ± 0.313	1.892 ± 0.870
MC F	0.534 ± 0.471	1.415 ± 0.993	0.439 ± 0.184	2.389 ± 1.114
Isolation varied down	0.938 ± 0.686	0.552 ± 0.466	0.215 ± 0.107	1.704 ± 0.837
Isolation varied up	0.723 ± 0.646	1.104 ± 0.739	0.559 ± 0.237	2.386 ± 1.010
MC corr. varied down	0.697 ± 0.695	1.048 ± 0.811	0.832 ± 0.385	2.577 ± 1.136
MC corr. varied up	0.660 ± 0.614	0.984 ± 0.687	0.316 ± 0.159	1.961 ± 0.935

Table 6.5 Fake background estimations in the SR. For nominal value, the 2D fake factor together with the $Z+jets$ and $t\bar{t}$ combination applied. The other lines show the estimations with different uncertainty variations.

2077

2078 6.5 Systematics

2079 The analysis includes both the statistical fit to MD distribution to search the EW-
 2080 $Z Z jj$ process, as well as the cross section measurement of inclusive EW and QCD $Z Z jj$
 2081 process in fiducial volume. Therefore, theoretical and experimental uncertainties may
 2082 affect the predicted background yields and shapes, the correction factors from detector-
 2083 level to particle-level measurement, as well as the $Z Z jj$ MD shapes and so on. Moreover,
 2084 the statistical uncertainties of simulated samples are also taken into account. Due to the
 2085 extremely low cross section of $\ell\ell\ell'\ell'$ channel, the analysis is still data statistic dominant.
 2086 This section describes the measurement of both theoretical and experimental systematics
 2087 for $Z Z jj$ productions. The systematics for fake backgrounds have been elaborated in
 2088 section 3.

2089 6.5.1 Theoretical systematics

2090 The theoretical systematics on EW- and QCD- $Z Z jj$ processes including the uncer-
 2091 tainties from PDF, QCD scale, α_S and parton showering variations are summarized in ta-

ble 6.6. The PDF uncertainty is estimated from the envelop of NNPDF internal variations and the difference between nominal and alternative PDF sets, following the PDF4LHC as introduced in section 2.2.1. The QCD scale uncertainty is estimated by varying the nominal renormalization scale (μ_R) and factorisation scale (μ_F) by a factor of 0.5 or 2.0. There are seven different configurations being considered, where the maximum of variations is chosen as final uncertainty. The parton showering uncertainty is estimated by comparing events with different parton showering setting between the nominal Pythia8 and the alternative Herwig7^[93-94] algorithm. The α_S uncertainty is estimated by varying the value of α_S within ± 0.001 . Due to the lack of simulation sample for alternative parton showering on QCD- $Z Z jj$ process, the value of parton showering component is taken from the measurement of EW process.

Process	EW- $Z Z jj$	QCD- $Z Z jj$
PDFs	NNPDF30lo (nominal), CT14lo	NNPDF30nnlo (nominal), MMHT2014nnlo68cl, CT14nnlo
α_S	0.118	0.117, 0.118 (nominal), 0.119
QCD scale ($[\mu_R, \mu_F]$)	[0.5,0.5], [0.5,1], [1,0.5], [1,1], [1,2], [2,1], [2,2]	[0.5,0.5], [0.5,1], [1,0.5], [1,1], [1,2], [2,1], [2,2]
Parton showering algorithm	Pythia8, Herwig7	-

Table 6.6 Summary of different variations for EW- and QCD- $Z Z jj$ theoretical uncertainties measurement.

Table 6.7 summarizes the uncertainties of each theoretical components in fiducial volume of SR, while table 6.8 shows the numbers in QCD-enriched CR region. For QCD process, the uncertainty is QCD scale dominant. Both of them are taken as inputs for statistical fit.

Process	PDF (%)	α_S (%)	QCD scale (%)	Parton shower (%)
EW	+5.9 -5.9		+6.1 -5.6	+3.3 -3.3
qqQCD	+2.0 -1.0	+2.6 -2.6	+34.2 -22.8	

Table 6.7 Summary of theoretical uncertainties for the fiducial volume (SR) for both EW and QCD qq -initial processes.

Process	PDF (%)	α_S (%)	QCD scale (%)	Parton shower (%)
EW $\ell\ell'\ell'\ell'$	+6.1 -6.1		+0.8 -1.1	+10.1 -10.1
qqQCD $\ell\ell'\ell'\ell'$	+2.0 -1.0	+2.6 -2.6	+31.5 -22.0	

Table 6.8 Summary of theoretical uncertainties for the control region for EW and qqQCD processes.

2107 The uncertainties of QCD gg -induced process ($gg \rightarrow ZZ$) as the function of MD discriminant is shown in figure 6.7 for both fiducial volume (SR) and QCD CR.

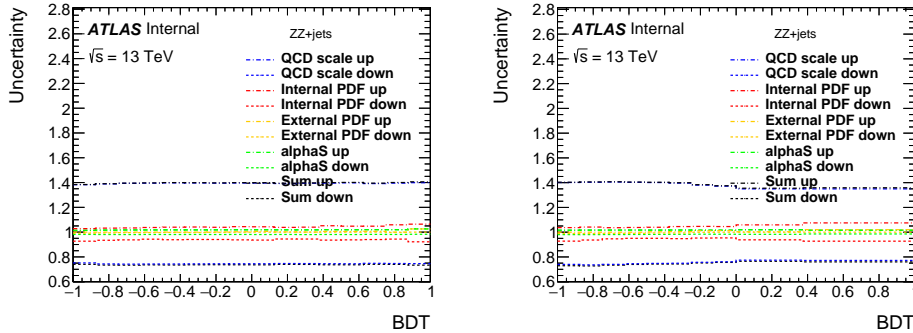


Fig. 6.7 The theoretical uncertainties for $gg \rightarrow ZZ$ background in particle-level SR (left) and CR (right).

2109 6.5.2 Experimental systematics

2110 The dominant experimental uncertainties are from the luminosity uncertainty, the mo-
 2111 mentum scale and resolution of leptons and jets, as well as the lepton reconstruction and
 2112 selection efficiency. Some smaller uncertainties, such as trigger efficiency and pile-up
 2113 correction, are also considered. Table 6.9 lists the major systematic components from
 2114 leptons and jets for signal and major background processes in $\ell\ell\ell'\ell'$ channel. The to-
 2115 tal uncertainties for sources from electron, muon and jet respectively, as well as the sum
 2116 (quadratic sum) of them are also summarized in this table.

name	EW- $Z Z jj$	QCD qq -initial	QCD gg
nominal yield	20.61	76.69	13.10
EG_RESOLUTION_ALL	$\pm^{0.00\%}_{0.03\%}$	$\pm^{0.02\%}_{0.04\%}$	$\pm^{0.01\%}_{1.41\%}$
EG_SCALE_ALL	$\pm^{0.03\%}_{0.05\%}$	-0.04%	$\pm^{0.01\%}_{0.06\%}$
EL_EFF_ID_TOTAL_1NPCOR_PLUS_UNCOR	$\pm^{2.66\%}_{2.58\%}$	$\pm^{2.60\%}_{2.53\%}$	$\pm^{2.65\%}_{2.57\%}$
EL_EFF_Iso_TOTAL_1NPCOR_PLUS_UNCOR	$\pm 0.70\%$	$\pm 0.47\%$	$\pm 0.42\%$
EL_EFF_Reco_TOTAL_1NPCOR_PLUS_UNCOR	$\pm 0.55\%$	$\pm 0.55\%$	$\pm 0.63\%$
JET_EtaIntercalibration_NonClosure	-0.01%	-0.03%	0%
JET_GroupedNP_1	$\pm 1.97\%$	$\pm^{11.82\%}_{10.14\%}$	$\pm^{16.21\%}_{12.92\%}$
JET_GroupedNP_2	$\pm 0.23\%$	$\pm 1.26\%$	+5.3%
JET_GroupedNP_3	$\pm 0.55\%$	$\pm 2.94\%$	$\pm^{3.14\%}_{0.12\%}$
JET_JER_SINGLE_NP	0.11%	+5.47%	+6.31%
JET_JvtEfficiency	$\pm 0.04\%$	$\pm 0.12\%$	$\pm 0.15\%$
MUON_EFF_ISO_STAT	$\pm 0.09\%$	$\pm 0.08\%$	$\pm 0.07\%$
MUON_EFF_ISO_SYS	$\pm 0.54\%$	$\pm 0.55\%$	$\pm 0.56\%$
MUON_EFF_RECO_STAT	$\pm 0.15\%$	$\pm 0.19\%$	$\pm 0.15\%$
MUON_EFF_RECO_STAT_LOWPT	$\pm 0.06\%$	$\pm 0.02\%$	$\pm 0.03\%$
MUON_EFF_TTVA_STAT	$\pm 0.06\%$	$\pm 0.07\%$	$\pm 0.06\%$
MUON_EFF_TTVA_SYS	$\pm 0.03\%$	$\pm 0.4\%$	$\pm 0.03\%$
MUON_ID	$\pm 0.03\%$	$\pm 0.02\%$	<0.001%
MUON_MS	-0.05%	$\pm^{0.04\%}_{0.01\%}$	<0.001%
MUON_SAGITTA_RESBIAS	$\pm 0.01\%$	$\pm 0.02\%$	<0.001%
MUON_SAGITTA_RHO	+1.13%	-0.73%	$\pm 1.00\%$
MUON_SCALE	$\pm 0.02\%$	$\pm^{0.03\%}_{0.02\%}$	<0.001%
PRW_DATASF	$\pm 0.5\%$	$\pm^{0.42\%}_{1.02\%}$	$\pm^{2.17\%}_{1.46\%}$
Electron Exp.	$\pm^{2.8\%}_{2.7\%}$	$\pm^{2.70\%}_{2.62\%}$	$\pm^{2.75\%}_{2.64\%}$
Muon Exp.	$\pm 1.3\%$	$\pm 1.3\%$	$\pm 1.04\%$
Jet Exp.	$\pm 2.0\%$	$\pm^{13.39\%}_{10.64\%}$	$\pm^{18.54\%}_{13.57\%}$
Total experimental uncertainties	$\pm^{3.7\%}_{4.0\%}$	$\pm^{13.72\%}_{11.11\%}$	$\pm^{18.90\%}_{13.57\%}$

Table 6.9 Experimental systematic uncertainties in $\ell\ell'\ell'\ell'$ channel with the luminosity of 139 fb^{-1} . The “Electron Exp.”, “Muon Exp.” and “Jet Exp.” represent the quadrature of the respective sources from electron, muon, and jets.

2117 In addition, the uncertainty of the combined 2015 to 2018 integrated luminosity is
 2118 1.7%^[95] in ATLAS experiment, obtained using the LUCID-2 detector^[96] for the primary
 2119 luminosity measurements.

2120 On top of them, a systematic uncertainty for MD distribution with different pile-up
 2121 ($\langle\mu\rangle$) is also considered for QCD- $Z Z jj$ background by comparing the distributions be-

tween events with low and high pile-up conditions. A boundary of $\langle\mu\rangle = 33$ is used to defined low/high pile-up according to the average $\langle\mu\rangle$ for signal (about 34.5) and QCD background (about 33). Figure 6.8 shows the MD distribution in SR (left) and QCD CR (right) in two different PU conditions, the difference as function of MD is then taken into account as additional shape uncertainty for statistical fit.

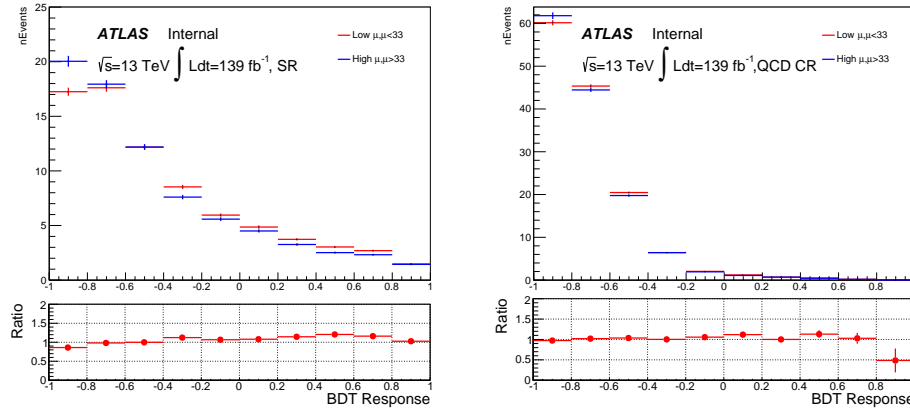


Fig. 6.8 MD distribution for QCD- $Z Z jj$ process in low and high pile-up events for SR (left) and CR (right).

Moreover, a conservative uncertainty is assigned to QCD- $Z Z jj$ process by comparing the sample modelled by Sherpa generator (nominal) with MadGraph5_aMC@NLO. The MD shape difference for both SR (left) and QCD CR (right) are shown in figure 6.9. The modelling uncertainty is then calculated from the envelop between nominal and alternative samples as function of MD as one additional shape uncertainty.

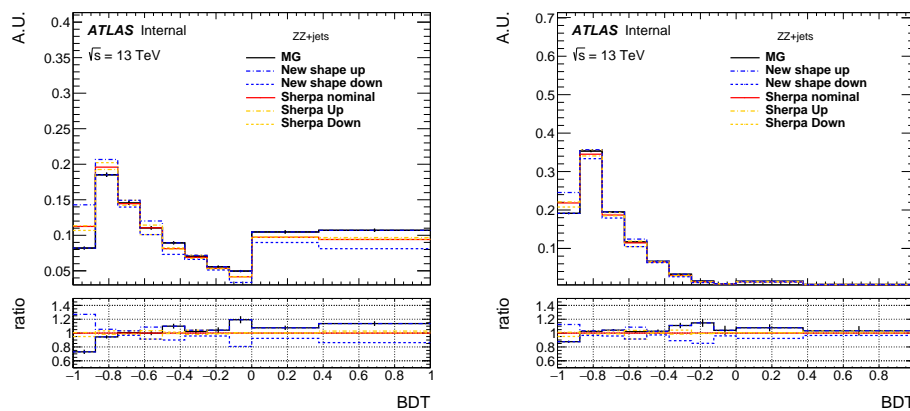


Fig. 6.9 MD shape difference for QCD $q\bar{q} \rightarrow ZZ$ background between different Sherpa theoretical uncertainties and sample from MadGraph5_aMC@NLO on SR (left) and CR (right).

2132 6.6 Measurement of fiducial cross section

2133 The fiducial cross section for inclusive $ZZjj$ production, including both EW and
 2134 QCD components, is then measured. The definition of fiducial volume, which is used for
 2135 cross section measurement, follows closely to the detector-level selection but use physics
 2136 objects at particle-level, which are reconstructed in simulation from stable final-state par-
 2137 ticles, prior to their interactions with the detector.

2138 For electrons and muons, QED final-state radiation is for the most part recovered by
 2139 adding the four-momenta of surrounding photons that are not originating from hadrons
 2140 and within an angular distance $\Delta R < 0.1$ to the lepton four-momentum, called lepton
 2141 “dressing” at truth level. Particle-level jets are built with anti- k_T algorithm with radius
 2142 parameter $R = 0.4$ using all final-state particles except leptons and neutrinos as inputs.
 2143 Comparing to the events selection at detector-level in section 6.3, at particle-level, the
 2144 selected dilepton pair mass required is relaxed to be within 60 to 120 GeV for the reasons
 2145 of reducing the migration effect, as well as being more compatibility with CMS publica-
 2146 tion^[80]. All other kinematic selections are the same as the definition at detector-level.

2147

6.6.1 Calculation of C-factor

2148 C-factor is defined as the ratio between the number of selected events at detector-level
 2149 and the number of particle-level events in fiducial volume (FV):

$$C = \frac{N_{\text{detector-level}}}{N_{\text{FV}}} \quad (6.5)$$

2150 The value of C-factor for each $ZZjj$ process are calculated from each individual simu-
 2151 lation samples as listed in table 6.10 together with their systematics.

Process	C	ΔC (stats.)	ΔC (sys.)	ΔC (theo.)
EWK $ZZjj$	0.663	± 0.002	$\pm^{0.032}_{0.031}$	NA
QCD $q\bar{q} \rightarrow ZZ$	0.702	± 0.003	$\pm^{0.061}_{0.051}$	$\pm^{0.015}_{0.018}$
QCD $gg \rightarrow ZZ$	0.741	± 0.021	$\pm^{0.143}_{0.072}$	± 0.002

Table 6.10 C Factor of different $ZZjj$ processes.

2152 Then the C from different processes are combined together to be used as inputs for
 2153 cross section calculation:

$$C = \sum_i \frac{N_{\text{FV}}^i}{\sum_j N_{\text{FV}}^j} \times C_i = 0.699 \pm 0.003(\text{stats.}) \pm^{0.011}_{0.013} (\text{theo.}) \pm 0.028(\text{exp.}) \quad (6.6)$$

2154 The stats. refers to the statistical uncertainty from MC simulation statistics. The theo.

2155 and exp. denote the theoretical and experimental uncertainties described in section 6.5.

2156 **6.6.2 Result of fiducial cross section**

2157 The cross section in fiducial volume is computed as:

$$\sigma^{FV} = \frac{N_{data} - N_{bkg}}{C \times Lumi} \quad (6.7)$$

2158 where N_{data} and N_{bkg} denote the number of events selected from detector-level selection
 2159 from data and sum of backgrounds, and C is the C-factor calculated above, Lumi repre-
 2160 sents the integrated luminosity of data from 2015 to 2018 of 139 fb^{-1} . Table 6.11 shows
 2161 the fiducial cross section for $\ell\ell\ell'\ell'$ final state measured from equation 6.7, as well as
 2162 the predicted cross section measured from MC simulation directly.

Measured fiducial σ [fb]	Predicted fiducial σ [fb]
$1.27 \pm 0.12(\text{stat}) \pm 0.02(\text{theo}) \pm 0.07(\text{exp}) \pm 0.01(\text{bkg}) \pm 0.03(\text{lumi})$	$1.14 \pm 0.04(\text{stat}) \pm 0.20(\text{theo})$

Table 6.11 Measured and predicted fiducial cross-sections in $\ell\ell\ell'\ell' jj$ final-state. Uncertainties due to different sources are presented.

2163 The measured cross section has a total uncertainty of 11%, and is found to be compat-
 2164 ible with SM prediction. This measurement is still dominant by data statistic.

2165 **6.7 Search for EW- $ZZjj$**

2166 **6.7.1 MD discriminant**

2167 To further separate the EW- $ZZjj$ component from QCD- $ZZjj$, a MD based on
 2168 Gradient Boosted Decision Tree (BDT) algorithm^[97] is trained with simulated events
 2169 via TMVA framework^[69]. Training is performed between EW (signal) and QCD (back-
 2170 ground) processes. Twelve event kinematic variables sensitive to the characteristics of
 2171 the EW signal are used as input features in training. Table 6.12 lists those input variables
 2172 with the order of their importance in BDT response provided by TMVA tool. One can see
 2173 the jet-related information provides larger sensitivity. Then the MD distributions in both
 2174 SR and QCD CR region are used for statistical fit.

2175 **6.7.2 Fitting procedure**

2176 A profile likelihood fit, as described in chapter 5, is performed on MD discriminant to
 2177 extract the EW- $ZZjj$ signal from backgrounds. The binning of MD distributions in SR

Rank	Variables	Description
1	m_{jj}	Dijet invariant mass
2	p_T^{j1}	p_T of the leading jet
3	p_T^{j2}	p_T of the sub-leading jet
4	$\frac{p_T(ZZjj)}{H_T(ZZjj)}$	p_T of the $Z Z jj$ system divided by the scalar p_T sum of Z bosons and two jets
5	$y_{j1} \times y_{j2}$	Product of jet rapidities
6	Δy_{jj}	Rapidity difference between two jets
7	Y_{Z2}^*	Rapidity of the second Z boson
8	Y_{Z1}^*	Rapidity of the Z boson reconstructed from the lepton pair with the mass closer to the Z boson mass
9	p_T^{ZZ}	p_T of 4l system
10	m_{ZZ}	Invariant mass of 4l system
11	p_T^{Z1}	p_T of the Z boson reconstructed from the lepton pair with the mass closer to the Z boson mass
12	$p_T^{\ell3}$	p_T of the third lepton

Table 6.12 Input features for the training of MD.

is optimized to maximize the sensitivity for detecting EW signal. The normalization of QCD- $Z Z jj$ production (μ_{QCD}^{III}) in $\ell\ell\ell'\ell'$ channel is determined by data from simultaneously fit in SR and QCD CR as described in section 6.4. The signal strength of EW- $Z Z jj$ production (μ_{EW}) is taken as parameter of interest and floated in the fit. The effects of the uncertainties related to normalizations and shapes described previously in section 6.5 of background processes in the MD distribution are all taken into account.

In most case, a common nuisance parameter is used for each source of systematic in all bins and all categories. The statistical uncertainties for simulated samples are uncorrelated among all bins, and the background uncertainties only applied to their corresponding backgrounds. Furthermore, to be more conservative, the generator modelling uncertainty for QCD- $Z Z jj$ production mentioned in section 6.5 is separated to be two nuisance pa-

2189 parameters in low and high MD region.

2190 **6.7.3 Result of fit**

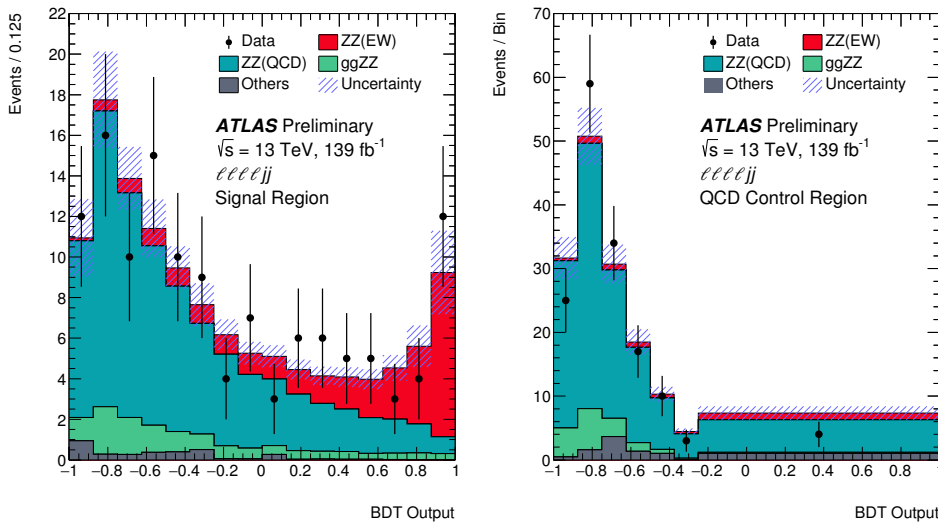
2191 The results of fitting to $\ell\ell\ell'\ell'$ final state are presented in table 6.13. To drive expected
 2192 results, the observed data is used for QCD CR to extract normalization factor of QCD
 2193 component (μ_{QCD}^{III}), while in SR, asimov data built from background prediction and signal
 2194 model with SM assumed cross section is used.

	μ_{EW}	$\mu_{QCD}^{\ell\ell\ell'jj}$	Significance Obs. (Exp.)
$\ell\ell\ell'jj$	1.54 ± 0.42	0.95 ± 0.22	$5.48 (3.90) \sigma$

2195 **Table 6.13** Observed μ_{EW} and $\mu_{QCD}^{\ell\ell\ell'jj}$, as well as the observed and expected significance from
 2196 the individual $\ell\ell\ell'\ell'$ channel. The full set of systematic uncertainties are included.

2197 As a conclusion, the background-only hypothesis is rejected at 5.5σ (3.9σ) for ob-
 2198 served (expected) data, which leads to the observation of EW- $ZZjj$ production.

2199 Figure 6.10 shows the post-fit MD distributions for $\ell\ell\ell'\ell'$ channel in SR (left) and
 2200 QCD CR (right). The EW- $ZZjj$ cross section measured in $\ell\ell\ell'\ell'$ channel is extracted
 2201 to be 0.94 ± 0.26 fb.



2202 **Fig. 6.10** Observed and post-fit expected multivariate discriminant distributions after the sta-
 2203 tistical fit in the $\ell\ell\ell'\ell'$ SR (left) and QCD CR (right). The error bands include the
 2204 experimental and theoretical uncertainties, as well as the uncertainties in μ_{EW} and
 2205 $\mu_{QCD}^{\ell\ell\ell'jj}$. The error bars on the data points show the statistical uncertainty on data.

2206

2207 Figure 6.11 shows the m_{jj} distribution in SR (left) and QCD CR (right), where the
 2208 normalization of EW and QCD processes are scaled according to their observed value in
 2209 table 6.13. High m_{jj} region is more sensitive for EW- $ZZjj$ events detection from this

2203 figure. Figure 6.12 shows the spectrum of invariant mass of $\ell\ell\ell'\ell'$ system (m_{ZZ}) in SR
 2204 also with the normalization of EW and QCD processes scaled.

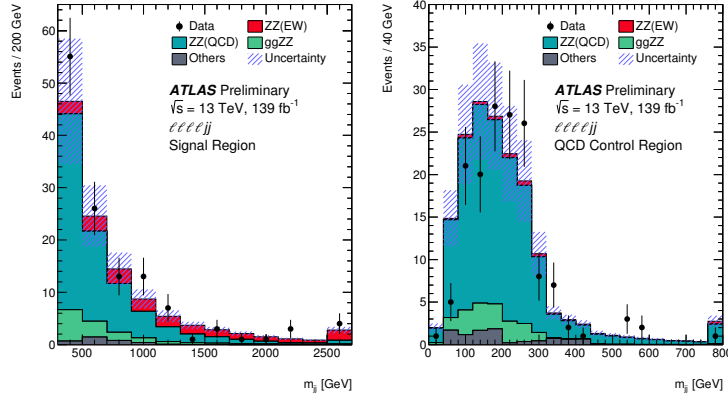


Fig. 6.11 Observed and post-fit expected m_{jj} distributions in SR (left) and QCD CR (right). The error bands include the expected experimental and theoretical uncertainties. The error bars on the data points show the statistical uncertainty. The contributions from the QCD and EW production of $Z Z j j$ events are scaled by 0.96 and 1.35, respectively, corresponding to the observed normalization factors in the statistical fit. The last bin includes the overflow events.

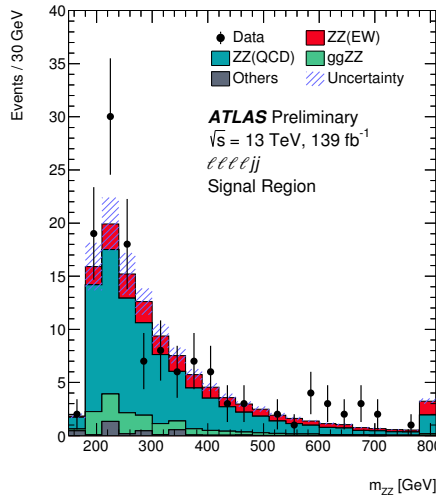


Fig. 6.12 Observed and post-fit expected m_{ZZ} spectrum in SR. The error bands include the expected experimental and theoretical uncertainties. The error bars on the data points show the statistical uncertainty. The contributions from the QCD and EW production of $Z Z j j$ events are scaled by 0.96 and 1.35, respectively, corresponding to the observed normalization factors in the statistical fit. The last bin includes the overflow events.

2205 Figure 6.13 is the display of one event candidate of EW- $Z Z j j$ production in $2e2\mu$
 2206 final state with two jets in forward and backward region.

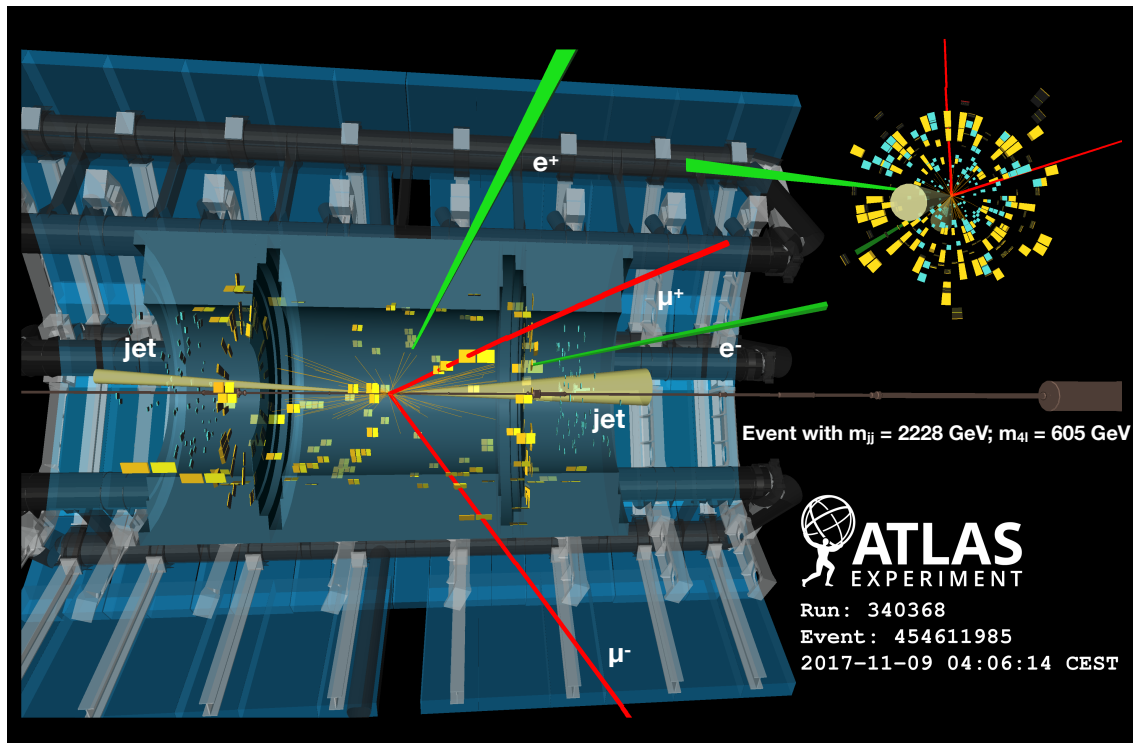


Fig. 6.13 Display of an event candidate of EW- $Z Z jj$ production in $2e2\mu$ channel in last MD bin ($0.875 < \text{MD} < 1.0$). The invariant mass of the di-jet (four-lepton) system is 2228 (605) GeV.

2207 6.8 Prospect study of EW- $Z Z jj$ production in HL-LHC

2208 The High-Luminosity Large Hadron Collider (HL-LHC) project aims to increase the
 2209 luminosity by a factor of 10 beyond the LHC's design value to increase the potential for
 2210 discoveries after 2025. The expected luminosity will reach 3000 fb^{-1} with the centre-of-
 2211 mass energy of 14 TeV.

2212 As introduced in previous sections, with full run-2 data of 139 fb^{-1} collected by AT-
 2213 LAS detector at the LHC, the EW- $Z Z jj$ production is the last channel of observation for
 2214 VBS processes with massive bosons due to its very low cross section in $Z Z$ channel. So
 2215 we expect that this channel will benefit significantly from the increased luminosity at the
 2216 HL-LHC, and can be studied in great details for this known mechanism.

2217 In this section, a prospective study is performed for EW- $Z Z jj$ production at the HL-
 2218 LHC in the $\ell\ell\ell'\ell'$ channel. The study uses 3000 fb^{-1} of simulated pp collision data at a
 2219 centre-of-mass energy of 14 TeV as expected to be recorded by the ATLAS detector at the
 2220 HL-LHC. All simulated events are produced at particle-level, and the detector effects of
 2221 leptons and jets reconstruction and identification are estimated by corrections assuming
 2222 the mean number of interactions per bunch crossing ($\langle\mu\rangle$) of 200.

6.8.1 The ATLAS detector at HL-LHC

As the expectation of HL-LHC, the new Inner Tracker (ITk)^[98] will extend the tracking acceptance capability of ATLAS detector to pseudorapidity ($|\eta|$) up to 4.0. By including a forward muon trigger, the upgraded Muon Spectrometer^[99] is also expected to provide muon identification capabilities to $|\eta|$ up to 4.0. In addition, the new high granularity timing detector (HGTD)^[100] designed to mitigate the pile-up (PU) effects is also expected to be installed in the forward region of $2.4 < |\eta| < 4.0$. More details of expected performance of the upgraded ATLAS detector at the HL-LHC has been reported in Ref.^[101]

6.8.2 Simulation

The analysis is performed using particle-level events. The samples are generated at $\sqrt{s} = 14$ TeV. The signal in this analysis is EW- $ZZjj$ process, while only the dominant irreducible background of QCD- $ZZjj$ is considered. Both signal and background are generated using Sherpa with the NNPDF3.0NNLO PDF set. The signal sample is modelled with two jets at Matrix Element (ME) level. The background is generated with up to one (three) outgoing partons at NLO (LO) in pQCD. As a quick study, other minor backgrounds such as fake backgrounds from $Z+jets$ and top-quark processes, as well as Diboson without 4l final-state and Triboson processes are not considered in this analysis. Furthermore, for hard scattering events, the pile-up collisions are set with a mean value of 200 interactions per bunch crossing. Signal and background yields are then scaled to an integrated luminosity of 3000 fb^{-1} as expected at the HL-LHC.

6.8.3 Event selection

The analysis selection follows closely to the one in ATLAS run-2 analysis as described in section 6.3. Here are some changes according to the expectation of the HL-LHC scenario for ATLAS detector:

- Extend the lepton (both electron and muon) identification to $|\eta| < 4.0$
- Pile-up (PU) jet suppression is applied with a PU rejection factor of 50 for all PU jets in the region of $|\eta| < 3.8$, based on the expected ATLAS detector performance at the HL-LHC.
- The jets are required to have $p_T > 30$ (70) GeV in the $|\eta| < 3.8$ ($3.8 < |\eta| < 4.5$) region.
- For two selected jets, tighten the m_{jj} requirement to be $m_{jj} > 600$ GeV, and require $\Delta\eta_{jj} > 2$.

In addition, a fiducial volume, used to study the expected precision of the cross-section measurements, is defined at particle-level with the same kinematic requirements listed above.

Table 6.14 summarized the number of selected signal and background events normalized to 3000 fb^{-1} . In addition to the *baseline* selection listed above, to compare the different detector scenarios at the HL-LHC, two alternative selections are also studied:

1. Reduce the lepton η region to 2.7, to understand the effect due to forward lepton reconstruction and identification with the upgraded ATLAS detector.
2. Only apply the PU jet suppression with region $|\eta| < 2.4$, to measure the improvement of *baseline* by extending the rejection range of PU jets at the HL-LHC with the installation of HGTD.

Selection	$N_{\text{EW-ZZjj}}$	$N_{\text{QCD-ZZjj}}$	$N_{\text{EW-ZZjj}} / \sqrt{N_{\text{QCD-ZZjj}}}$
Baseline	432 ± 21	1402 ± 37	11.54 ± 0.58
Leptons with $ \eta < 2.7$	373 ± 19	1058 ± 33	11.46 ± 0.62
PU jet suppression only in $ \eta < 2.4$	536 ± 23	15470 ± 120	4.31 ± 0.19

Table 6.14 Comparison of event yields for signal ($N_{\text{EW-ZZjj}}$) and background ($N_{\text{QCD-ZZjj}}$) processes, and expected significance of EW- $ZZjj$ processes, normalized to 3000 fb^{-1} data at 14 TeV, with baseline and alternative selections. Uncertainties in the table refer to expected data statistical uncertainty at 14 TeV with 3000 fb^{-1} .

From this table, one can see the extended track coverage increases the $\ell\ell\ell'\ell'jj$ events by 15 to 30%, via improving the lepton efficiency. But the significance of searching for EW- $ZZjj$ process does not improve so much due to the large increment of background events.

Figure 6.14 shows the kinematic distributions of di-jet invariant mass (m_{jj}), the ZZ invariant mass (m_{ZZ}) and the ϕ separation of two Z bosons ($|\Delta\phi(ZZ)|$) as well as the centrality of the ZZ system. The ZZ centrality is defined as:

$$ZZ \text{ centrality} = \frac{|y_{ZZ} - (y_{j1} + y_{j2})/2|}{|y_{j1} - y_{j2}|} \quad (6.8)$$

To measure the event yield, the top panel shows the stack distribution for EW- and QCD- $ZZjj$ processes, while bottom panel is the ratio between two processes.

6.8.4 Systematics

According to studies in section 6.5, the dominant systematic in $\ell\ell\ell'\ell'$ channel is from theoretical systematic for QCD- $ZZjj$ background process. Different sizes of systematics

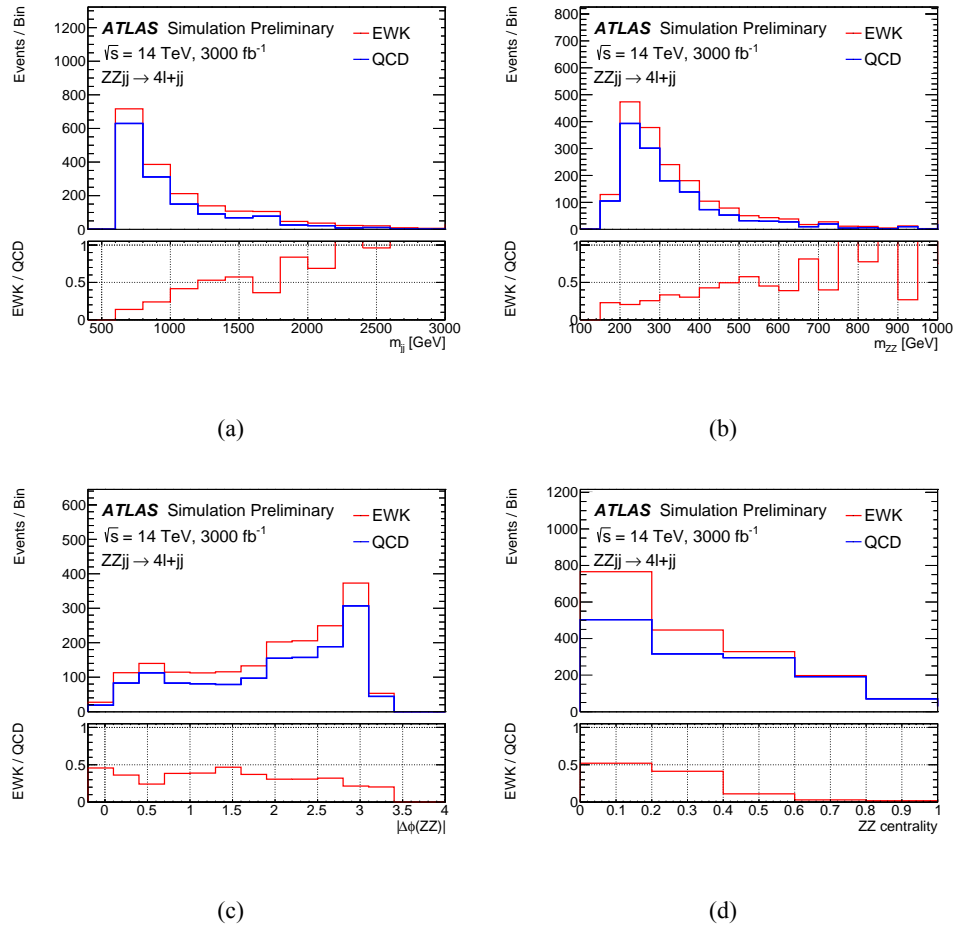


Fig. 6.14 Detector-level distributions of EW- and QCD- $Z Z j j$ processes with selected events in defined phase space at 14 TeV of (a) m_{jj} , (b) m_{ZZ} , (c) $|\Delta\phi(ZZ)|$, (d) ZZ centrality, normalized to 3000 fb^{-1} .

have been studied, at a factor of 5, 10 and 30% on background modelling. The 5% uncertainty is an optimal estimation when there is enough data events from QCD-enriched control region at the HL-LHC that can be used to constrain the theoretical normalization on QCD- $Z Z j j$ process. The 30% one is a conservative estimation, in which the uncertainties are directly calculated from different PDF sets and QCD renormalization and factorization scales, following recommendation from the PDF4LHC mentioned in section 6.5.

For experimental sources, the jet systematics have been checked following the setting provided by the HL-LHC in Ref.^[101], and the uncertainties are within 5% level, which is smaller than run-2 measurement at 10%. Figure 6.15 depicts the up and down variations for jet uncertainty provided by the HL-LHC performance tool as function of dijet invariant mass (m_{jj}). Therefore, a conservative 5% uncertainty is used as experimental uncertainty.

Since the final result relies greatly on the uncertainties, especially the theoretical un-

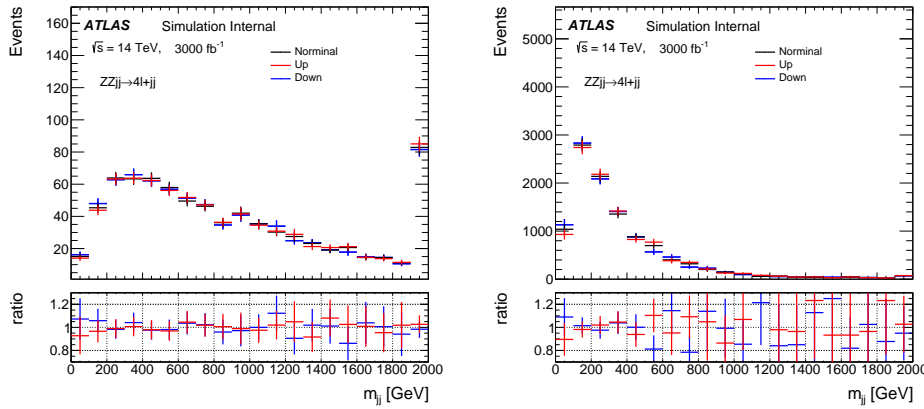


Fig. 6.15 Jet variations on m_{jj} distribution for EW- $Z Z jj$ (left) and QCD- $Z Z jj$ (right) processes with luminosity of 3000 fb^{-1} at 14 TeV. Upgrade Performance Function is used to extract the uncertainties with *baseline* setting.

certainties on QCD- $Z Z jj$ production. So results with different uncertainty conditions are shown as below:

- The case with statistical uncertainty of simulated samples only.
- The case with statistical and experimental uncertainties (5%)
- The case with statistical, experimental and additional theoretical uncertainties at 5%, 10% and 30% levels respectively.

Three different sources of uncertainties are treated as uncorrelated and summed up quadratically.

6.8.5 Results

In this analysis, instead of a statistical fit, the expected significance of EW- $Z Z jj$ production is calculated as:

$$\text{Significance} = \frac{S}{\sqrt{\sigma(B)_{\text{stat.}}^2 + \sigma(B)_{\text{syst.}}^2}}, \quad (6.9)$$

where S presents the number of selected signal events, and $\sigma(B)_{\text{stat.}}$ and $\sigma(B)_{\text{syst.}}$ denote the statistical and systematic (exp. + theo.) uncertainties from background processes. The statistical uncertainty is computed from expected data yield with an integrated luminosity of 3000 fb^{-1} .

Based on baseline selection of $m_{jj} > 600 \text{ GeV}$, an additional scan over different m_{jj} cuts is also performed with a step of 50 GeV under different systematic conditions, as shown in figure 6.16.

In addition, the expected differential cross section of EW- $Z Z jj$ process is measured in the defined phase space at 14 TeV, as a function of m_{ZZ} and m_{jj} , shown in figure 6.17.

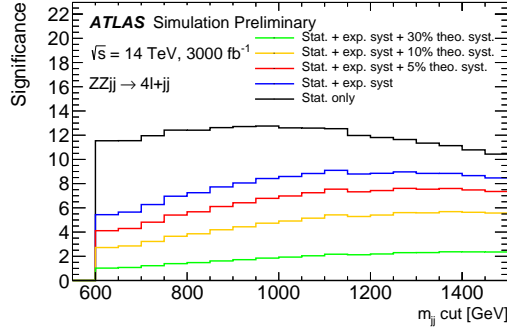


Fig. 6.16 The expected significance of EW-ZZjj processes as a function of different m_{jj} cut with 3000 fb^{-1} , under conditions of different sizes of theoretical uncertainties on the QCD-ZZjj background modelling. The statistical uncertainty is estimated from expected data yield at 14 TeV with 3000 fb^{-1} . Different uncertainties are summed up quadratically.

The expected differential cross sections are calculated as:

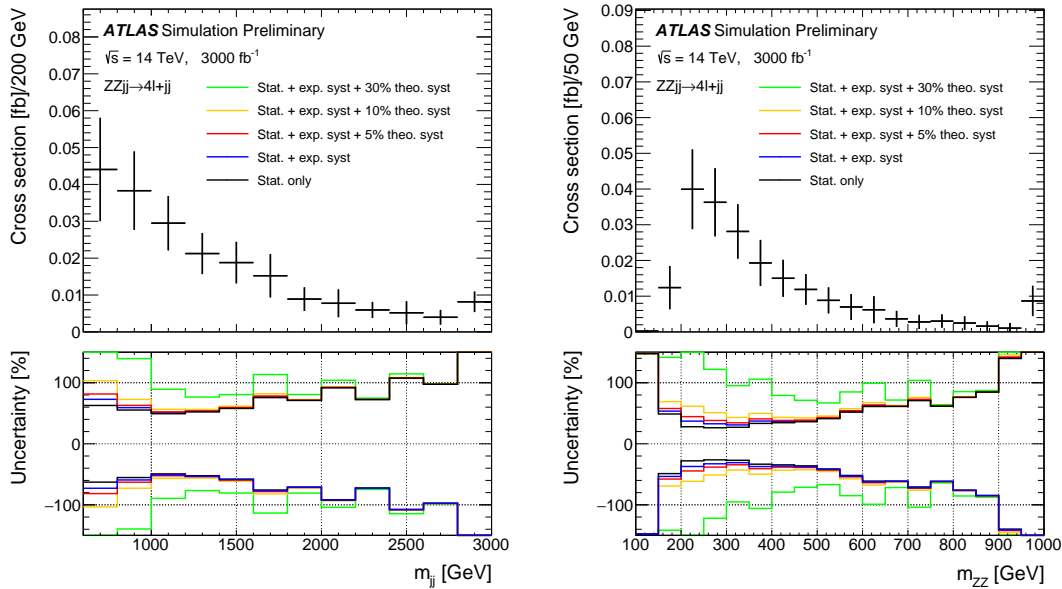


Fig. 6.17 The projected differential cross-sections at 14 TeV for the EW-ZZjj processes as a function of m_{jj} (left) and m_{ZZ} (right). The top panel shows measurement with statistical only case, where statistical uncertainty is estimated from expected data yield at 14 TeV with 3000 fb^{-1} . The bottom panel shows impact of different sizes of systematic uncertainties.

$$\sigma = \frac{N_{\text{pseudo-data}} - N_{\text{QCD-ZZjj}}}{L * C_{\text{EW-ZZjj}}} \quad (6.10)$$

$$C_{\text{EW-ZZjj}} = \frac{N_{\text{EW-ZZjj}}^{\text{det.}}}{N_{\text{EW-ZZjj}}^{\text{part.}}}$$

2313 where $N_{\text{pseudo-data}}$ denotes the expected number of data events with 3000 fb^{-1} luminosity

at 14 TeV, and $N_{QCD-ZZjj}$ and $N_{EW-ZZjj}$ are the number of predicted events of QCD- $ZZjj$ and EW- $ZZjj$ processes in particle-level. The $C_{EW-ZZjj}$ factor represents the detector efficiency for EW- $ZZjj$ processes introduced in section 6.6.1. The interference between EW- and QCD- $ZZjj$ processes is ignored due to its minor contribution.

The value of expected integrated cross section as well as its uncertainty under different systematic conditions are shown in table 6.15 with 3000 fb^{-1} luminosity at 14 TeV. The statistical uncertainty is at 10% level when with such large luminosity. The result is dominated by systematics and can reach 100% level when theoretical modelling uncertainty is 30% for QCD- $ZZjj$ processes.

	Cross section [fb]	Stat. only	Plus exp.	Plus 5% theo.	Plus 10% theo.	Plus 30% theo.
EW- $ZZjj$	0.21	± 0.02	± 0.04	± 0.05	± 0.08	± 0.21

Table 6.15 Summary of expected cross-section measured with different theoretical uncertainties. The statistical uncertainty is computed from expected data yield with 3000 fb^{-1} at 14 TeV. Different uncertainties are treated as uncorrelated and summed quadratically.

2323 6.9 Conclusion

2324 The fiducial cross section for inclusive $Z Z jj$ production is measured in this section,
2325 with a total relative uncertainty of 11% for the $\ell\ell\ell'\ell'$ final state, and found to be com-
2326 patible with the SM prediction. The observation of electroweak production of two jets in
2327 association with a Z -boson pair decay to $\ell\ell\ell'\ell'$ final state using 139 fb^{-1} of 13 TeV pp
2328 collision data collected by ATLAS experiment at the LHC is presented in this section.
2329 The search for electroweak production of two jets in association with a Z -boson pair is
2330 based on multivariate discriminants (MD) to enhance the separation between the signal
2331 and backgrounds. In $\ell\ell\ell'\ell'$ final state, the background-only hypothesis is rejected with
2332 an observed (expected) significance of 5.5 (3.9) σ , which gives the first observation of
2333 electroweak production in $Z Z jj$ channel.

2334 In addition, the prospective study for the EW- $Z Z jj$ production at the HL-LHC in
2335 the $\ell\ell\ell'\ell'$ channel, using 3000 fb^{-1} simulated pp collision data at a centre-of-mass
2336 energy of 14 TeV has been presented. The precision of the expected measurements of the
2337 integrated and differential cross sections as a function of dijet or $\ell\ell\ell'\ell'$ invariant mass are
2338 shown. Under the assumption of theoretical uncertainty for the QCD- $Z Z jj$ processes and
2339 experimental uncertainty for jets being constraint at 5% level respectively, with statistical
2340 uncertainty in 3000 fb^{-1} being considered, the observation of the EW- $Z Z jj$ process can
2341 reach a significance of 7σ .

2342 **Chapter 7 Search for heavy resonances decaying into**
2343 **a pair of Z bosons in $\ell\ell\ell'\ell'$ final state using pp**
2344 **collision data collected by ATLAS detector from 2015 to**
2345 **2018**

2346 **7.1 Introduction**

2347 A new particle was discovered by the ATLAS and CMS Collaborations at the LHC^[3-4]
2348 in 2012. Both two experiments have confirmed that the properties including spin, cou-
2349 plings and parity of this new particle are consistent with Higgs boson predicted in the
2350 Standard Model (SM), which is an important milestone in understanding of the mecha-
2351 nism of EWSB. Nevertheless, the possibility that this newly discovered particle is just a part
2352 of the extended Higgs sector as predicted by various extensions in the SM cannot be ruled
2353 out. There are many models predicted the existence of new heavy resonances decaying
2354 into dibosons, such as a heavy spin-0 neutral Higgs boson^[102] and the two-Higgs-doublet
2355 models (2HDM)^[6], as well as the spin-2 Kaluza–Klein (KK) excitations of the graviton
2356 (G_{KK})^[103].

2357 Though with smaller branching ratio comparing to semileptonic or fully hadronic de-
2358 cay channels, the $\ell\ell\ell'\ell'$ final state has its unique sensitivity in mass range smaller than
2359 1 TeV region due to its good mass resolution and relative smaller experimental and the-
2360 oretical systematics. This section presents the search for heavy resonance decaying into
2361 a pair of Z bosons to the $\ell\ell\ell'\ell'$ final state, in which ℓ denotes to either an electron
2362 or a muon. Several signal hypotheses are considered. The first hypothesis is a heavy
2363 Higgs boson (spin-0 resonance) under the narrow-width approximation (NWA). Then as
2364 several theoretical models prefer non-negligible natural widths, the models under large-
2365 width approximation (LWA), assuming widths of 1%, 5%, 10% and 15% of the resonance
2366 mass, are also studied. In addition, the graviton excitations (spin-2 resonance) under the
2367 Randall–Sundrum model are also searched. It is assumed that the heavy resonance is
2368 produced predominantly via the gluon-gluon Fusion (ggF) and the Vector Boson Fusion
2369 (VBF) productions, but with the unknown ratio of two production rates. So the results are
2370 separated for ggF and VBF production modes. To gain more sensitivity, the $\ell\ell\ell'\ell'$ events
2371 are classified into ggF- and VBF-enriched categories. Moreover, for the NWA model, the
2372 categorizations are studied under both cut-based and multivariate (MVA) -based methods,
2373 the details of categorization are shown in following sections.

2374 The search uses the four-lepton invariant mass in the range of 200 GeV to 2000 GeV for
 2375 signal hypothesis of spin-0 resonance under the NWA model, and from 400 GeV to
 2376 2000 GeV for the one under the LWA models. And the spin-2 graviton signals are searched
 2377 in the mass range from 600 GeV to 2000 GeV. The data collected by ATLAS detector at
 2378 the LHC from 2015 to 2018 at the centre-of-mass energy of 13 TeV is used. In case of no
 2379 excess, upper limits on the production rate of different signal hypotheses are computed
 2380 from statistical fits to m_{4l} distribution.

2381 **7.2 Data and MC samples**

2382 **7.2.1 Data samples**

2383 The data used in this analysis are collected by ATLAS detector at the centre-of-mass
 2384 energy of 13 TeV during the years of 2015 to 2018. Only events passing the latest Good
 2385 Run List (GRL) released by the Data Quality group from ATLAS experiment as listed in
 2386 section 6.2.1 corresponding to an integrated luminosity of $139.0 \pm 2.4 \text{ fb}^{-1}$ are used.
 2387 Table 7.1 listed the recorded integrated luminosity, average and peak pile-up of each year's
 data.

Table 7.1 Summary of the recorded integrated luminosity (lumi), average and peak pile-up (PU) of data from 2015 to 2018.

Year	recorded integrated lumi	lumi after GRL	average PU	peak PU
2015	3.86 fb^{-1}	36.2 fb^{-1}	13.4	28.1
2016	35.6 fb^{-1}		25.1	52.2
2017	46.9 fb^{-1}	44.3 fb^{-1}	37.8	79.8
2018	60.6 fb^{-1}	58.5 fb^{-1}	36.1	88.6

2388 **7.2.2 Background MC simulations**

2390 Background processes considered in this analysis include ZZ ($q\bar{q} \rightarrow ZZ$, $gg \rightarrow ZZ$), triboson (WWZ , WZZ , ZZZ), $Z+jets$ and top-quark ($t\bar{t}$, ttV) processes.

2392 The QCD $q\bar{q} \rightarrow ZZ$ process is modelled using Sherpa 2.2.2^[83] with the
 2393 NNPDF3.0NNLO^[84] PDF, where events with up to one (three) outgoing partons are gen-
 2394 erated at NLO (LO) in pQCD. The production of ZZ from the gluon-gluon initial state
 2395 with a four-fermion loop or with an exchange of the Higgs boson, which has an order
 2396 of α_S^4 in QCD, is not included in this Sherpa simulation. So a separate gg induced ZZ
 2397 sample including the continuum background, the SM Higgs boson, and the interference
 2398 contribution is modelled using Sherpa 2.2.2 with the NNPDF3.0NNLO PDF set, and with

2399 an additional 1.7 k-factor^[85] being applied. The EW- $ZZjj$ production is simulated using
2400 Sherpa 2.2.2 with the NNPDF3.0NNLO PDF, and the $ZZZ \rightarrow \ell\ell\ell'\ell'qq$ process is also
2401 taken into account in this sample.

2402 The $Z+jets$ events are generated using Sherpa 2.2.2 with the NNPDF3.0NNLO PDF,
2403 in which the ME is calculated for up to two partons with next-to-leading-order (NLO)
2404 accuracy in pQCD and up to four partons with LO accuracy. The $Z+jets$ events are
2405 normalized using the next-to-next-to-leading-order (NNLO) cross section. The triboson
2406 processes with full leptonic decays and at least four prompt charged leptons are generated
2407 using Sherpa 2.1.1. For top-quark pair ($t\bar{t}$) production and the single top-quark produc-
2408 tions in t -channel, s -channel and Wt -channel, the Powheg-Box v2 is used with the CT10
2409 PDF. The productions of $t\bar{t}$ in association with Z boson(s) (ttZ) is modelled with Mad-
2410 Graph5_aMC@NLO.

2411 7.2.3 Signal MC simulations

2412 One model considered in this analysis is heavy spin-0 resonance under the Narrow
2413 Width Approximation (NWA) simulated using Powheg-Box v2 MC event generator with
2414 the CT10 PDF. The gluon-gluon fusion (ggF) production mode and vector-boson fusion
2415 (VBF) production mode are calculated separately with matrix elements up to NLO in
2416 QCD. The Powheg-Box is interfaced to Pythia8 for parton showering, and for decaying
2417 the Higgs boson into the $H \rightarrow ZZ \rightarrow \ell\ell\ell'\ell'$ final states. Events of NWA signal are
2418 generated at mass points between 200 GeV to 2000 GeV using the step of 100 (200) GeV up
2419 to (above) 1 TeV in both ggF and VBF production modes.

2420 In addition, heavy Higgs boson events under the Large Width Approximation (LWA)
2421 with widths of 1%, 5%, 10% and 15% of the boson mass are generated using Mad-
2422 Graph5_aMC@NLO 2.3.2 interfaced to Pythia8. Only ggF production is consid-
2423 ered. Mass points between 400 GeV to 2000 GeV are simulated with the step of 100
2424 (200) GeV up to (above) 1 TeV. To describe jet multiplicity, MadGraph5_aMC@NLO is
2425 used to simulated process of $pp \rightarrow H + \geq 2\text{jets}$ at NLO in QCD with the FxFx merging
2426 scheme^[104].

2427 Spin-2 Kaluza–Klein (KK) gravitons (G_{KK}) from the Bulk Randall–Sundrum
2428 model^[105] are also studies in this analysis. Events are generated by Mad-
2429 Graph5_aMC@NLO at LO in QCD, which is then interfaced to Pythia8 for parton show-
2430 ering. The G_{KK} -gluon coupling $k/\overline{M}_{\text{Planck}}$, where k is the curvature scale of the extra
2431 dimension and $\overline{M}_{\text{Planck}}$ is the reduced Planck mass, is set to 1. The width of the resonance
2432 is correlated with the coupling $k/\overline{M}_{\text{Planck}}$ and in this configuration is around $\square 6\%$ of its

2433 mass. The mass of the G_{KK} is the only free parameter in this simplified model. Mass
2434 points between 600 GeV to 2 TeV with 200 GeV spacing were generated.

2435

7.3 Analysis selections

2436

7.3.1 Objects selection

2437 Similar to VBSZZ analysis in section 6.3, the selection of this analysis relies on the
2438 definition of multiple objects: *electrons*, *Muons*, and *jets*. Details of definitions for each
2439 object are described as below:

2440 **Electron:** As described in section 4.2.3, electrons are reconstructed from energy
2441 deposits in the EM calorimeter matched to a track in the inner detector. The electron
2442 candidates satisfying the *Loose* criterion valuing by the likelihood-based (LH) method
2443 are selected, with a selection efficiency ranging from 90% for transverse momentum
2444 $p_T = 20$ GeV to 96% for $p_T > 60$ GeV. In addition, the electrons are required to have
2445 $p_T > 7$ GeV, $|\eta| < 2.47$ and $|z_0 \sin\theta| < 0.5$ mm.

2446 **Muon:** To increase the acceptance range in reco-level for $\ell\ell\ell'\ell'$ channel, all four
2447 types of muons (CB, ST, CT, ME muons, described in section 4.2.4) are used. The CT
2448 muons are required to pass $p_T > 15$ GeV and $|\eta| < 0.1$, while the ST muons are also
2449 limited in $|\eta| < 0.1$ region. The ME muons are only used in the region of $2.5 < |\eta| < 2.7$.
2450 And at most one CT, ST or ME muon is allowed in one $\ell\ell\ell'\ell'$ quadruplet. The Muon
2451 candidates are required to pass $p_T > 5$ GeV and $|\eta| < 2.7$, and satisfy the *Loose* identifi-
2452 cation criterion with an efficiency of at least 98.5%. The impact parameter requirements
2453 of $|d_0| < 1$ mm and $|z_0 \sin\theta| < 0.5$ mm are further applied.

2454 **Jets:** Jets are clustered using the anti- k_t algorithm with radius parameter $R = 0.4$ im-
2455 plemented in the FastJet package as described in section 4.2.5. The ‘particle flow’ (PFlow)
2456 objects^[106], which combines measurements from both the tracker and the calorimeter,
2457 are used as inputs to the FastJet package. The energy deposited in the calorimeter by
2458 all charged particles is removed, and the jet reconstruction is performed on an ensem-
2459 ble of PFlow objects consisting of the remaining calorimeter energy and tracks which
2460 are matched to the hard interaction. This improves the accuracy of the charged-hadron
2461 measurement, while retaining the calorimeter measurements of neutral-particle energies.
2462 Compared to only using topological clusters, jets reconstructed with the particle flow algo-
2463 rithm with $p_T > 30$ GeV have approximately 10% better transverse momentum resolution.
2464 The jets used in this analysis are then required to have $p_T > 30$ GeV and $|\eta| < 4.5$. To
2465 further reduce the effects of pile-up jets, a jet vertex tagger (JVT) is applied to jets with

2466 $p_T < 60$ GeV and $|\eta| < 2.4$.

2467 **Overlap removal:** As the selected jet and lepton candidates can be reconstructed
 2468 from same detector information, an overlap-removal procedure is applied. For electron
 2469 and muon sharing the same ID track, the electron is selected in the case that the muon is
 2470 calorimeter-tagged and does not have a MS track, or is a segment-tagged muon, otherwise
 2471 the muon is selected. The jet overlapping with electron (muon) within a cone of size of
 2472 $\Delta R \equiv \sqrt{(\Delta\eta)^2 + (\Delta\phi)^2} = 0.2(0.1)$ are removed.

2473 **7.3.2 Event selection**

2474 First of all, the four-lepton events are required to pass single or multi-lepton triggers.
 2475 Due to the increasing of peak luminosity and pile-up, the p_T and E_T thresholds of triggers
 2476 increase slightly during the data-taking periods from 2015 to 2018. Table 7.2 summarizes
 2477 the triggers used for $\ell\ell\ell'\ell'$ channel. The overall trigger efficiency for selected signal
 2478 events passing final selection is around 98%.

**Table 7.2 Summary of the p_T (E_T) trigger thresholds (in GeV) employed for the muon (electron)
 trigger selection in the year of 2015, 2016, 2017, and 2018.**

Trigger item	Trigger threshold			
	2015	2016	2017	2018
single muon	$\mu 20; \mu 50; \mu 60$	$\mu 24; \mu 26; \mu 40; \mu 50$	$\mu 26; \mu 50; \mu 60$	$\mu 26; \mu 50; \mu 60$
single electron	$e24; e60; e120$	$e26; e60; e140; e300$	$e26; e60; e140; e300$	$e26; e60; e140; e300$
dimuon	$2\mu 10; \mu 18_{-\mu 8}$	$2\mu 10; 2\mu 14; \mu 22_{-\mu 8}$	$2\mu 14; \mu 22_{-\mu 8}$	$2\mu 14; \mu 22_{-\mu 8}$
dielectron	$2e12$	$2e15; 2e17$	$2e17; 2e24$	$2e17; 2e24$
electron-muon	$e24_{-\mu 8}$	$e24_{-\mu 8}; e26_{-\mu 8}$ $e17_{-\mu 14}; e7_{-\mu 24}; 2e12_{-\mu 10}; e12_{-\mu 10}$	$e26_{-\mu 8}$	$e26_{-\mu 8}$
trimuon	$\mu 18_{-2\mu 4}$	$\mu 11_{-2\mu 4}; \mu 6_{-2\mu 4}; \mu 20_{-2\mu 4}; 3\mu 4$ $3\mu 6$	$4\mu 4; \mu 20_{-2\mu 4}; 3\mu 4$	$\mu 20_{-2\mu 4}$
trilepton	$e17_{-2e9}$	$e17_{-2e9}; e17_{-2e10}$	$e24_{-2e12}$	$e24_{-2e12}$

2479 The $\ell\ell\ell'\ell'$ quadruplets are formed by two opposite-sign, same-flavour (OSSF) lepton pairs ($\ell^+\ell^-$). The p_T threshold of first three leading leptons are required to be 20, 15
 2480 and 10 GeV. If there are more than one combination of lepton pairing in quadruplet, the
 2481 pairing is selected by keeping it with the mass of lepton pairs closest (leading pair, refers
 2482 as m_{12}) and second closest (sub-leading pair, refers as m_{34}) to Z boson mass. The mass
 2483 of leading pair is required to satisfy $50 < m_{12} < 106$ GeV, while the sub-leading pair is
 2484 required to be less than 115 GeV and larger than 50 GeV.
 2485

2486 The two lepton pairs in quadruplet are required to have angular separation with $\Delta R >$
 2487 0.1. To suppress the contribution from $J/\psi \rightarrow \ell\ell$ decays, for 4 μ and 4 e quadruplets,
 2488 the events are rejected if any opposite-sign same-flavour lepton pair is found with mass

below 5 GeV. If there are more than one quadruplets from different channels in event at this point, the one with highest expected signal rate is selected in the order of 4μ , $2e2\mu$, $4e$. The transverse impact-parameter significance ($|d_0|/\sigma_{d_0}$) for muons (electrons) is than required to be smaller than 3 (5) to suppress the backgrounds from heavy-flavour hadrons.

In addition, the track- and calorimeter- based isolation criteria is required for all electrons and muons to further suppress the reducible backgrounds of $Z+jets$ and $t\bar{t}$. For lepton isolation selection, the two track- and calorimeter- based variables, $E_T^{topocone}$ and $p_T^{varcone}$ as described in section 4.2.4 (section 4.2.3) for muons (electrons), are vulnerable to pileup. For track-based variable, this is because of additional tracks in the event. The definition of $p_T^{varcone}$ attempts to limit the tracks used in the calculation to those from the vertex via a loose cut of $|z_0 \sin(\theta)| < 3$, which proved to be too loose in new pile-up regime 2017 and 2018 datasets. So new track-based variable is used, by adding a requirement that the track be used in determining the vertex, or that, if not, it both pass the cut on $|z_0 \sin(\theta)|$ and not be used in determining any other vertex, which makes the track-based variable to be more isolation-robust in the high pile-up regime. The new variable is named as $ptvarcone[cone]_TightTTVA_pt[p_T \text{ cut}]$, where [cone] is the cone size and [p_T cut] is the cutoff for including tracks in the calculation.

For calorimeter-based variable, the calculation of $E_T^{topocone}$ corrects the pile-up effects by subtracting an average pileup contribution computed over the whole detector. But with the increasing of energy density of pile-up events, the root mean square (RMS) of $E_T^{topocone}$ variable increases, which leads to the increment of possibility that the pile-up fluctuations are not be accounted for correctly. One possible solution is that use particle-flow (PFlow) method to calculate the calorimeter isolation. As part of PFlow reconstruction process, it assigns the clusters to tracks which improves the track-cluster association for better determination of the raw value of the E_T in the cone. And using PFlow jets to calculate the pileup correction provides a further improvement. So a resulting variable named $neflow-isol[cone]$ is used. Finally, a requirement of isolation, called *FixedCutPFlowLoose*, which gives better performance in high piup-up condition is applied to electrons and muons as:

$$(\max(ptcone20_TightTTVA_pt500, ptvarcone30_TightTTVA_pt500) + 0.4 \times neflow-isol20) / p_T < 0.16$$

On the top of impact parameter cut and lepton isolation cut, the four-lepton candidates are also required to originate from a common vertex to reduce $Z+jets$ and $t\bar{t}$ backgrounds. This is ensured by applying a vertex fit χ^2 cut of 4 ID tracks of lepton candidates satisfying $\chi^2/N_{dof} < 6$ (9) for events in 4μ ($4e$ and $2e2\mu$) channel(s).

To improve the mass resolution, the QED process of final state radiation (FSR) pho-

2524 tons in Z boson decays are taken into account in the reconstruction of Z bosons. The
2525 four-momentum of any reconstructed photon that is consistent with having been radiated
2526 from lepton(s) in leading pair are added into final state. Moreover, the four-momenta of
2527 leptons in both (leading and sub-leading) pairs are recomputed by performing a Z -mass-
2528 constrained kinematic fit, which uses a Breit–Wigner Z boson line-shape and Gaussian
2529 function with width set to the expected lepton resolution per lepton to model the momen-
2530 tum response function. The Z -mass-constrained mass improves the $m_{4\ell}$ resolution by up
2531 to 15% depending on m_H .

2532 In summary, table 7.3 lists a comprehensive object and event level selection as de-
2533 scribed above. Table 7.4 to 7.7 shows the cutflow of NWA ggF and VBF signal at the
2534 mass points of 600 and 1000 GeV as examples.

2535

7.3.3 Event categorizations

2536 To improve the sensitivity of search in both VBF and ggF production mode in NWA
2537 model, events are classified into the VBF- and ggF- enriched categories. With the statistic
2538 increasing in full run-2 data, a multivariate (MVA) based classifier has been studied for
2539 NWA signal, while in the meantime the traditional cut-based classifier is also used as a
2540 model-independent result for all three (NWA, LWA, graviton) models.

2541

1. Cut-based categorization

2542 There are four categories in total: one VBF-enriched category and three ggF-enriched
2543 categories. The categorization is defined based on kinematic cuts:

- 2544 • VBF-CBA-enriched category: Events have at least two selected jets as defined in
2545 section 7.3.1, with the two leading jets being separated by $|\Delta\eta_{jj}| > 3.3$ and invariant
2546 mass satisfying $m_{jj} > 400$ GeV;
- 2547 • ggF-CBA-enriched categories: The remaining events that are not classified into
2548 VBF-enriched category. Then events are categorized into three channels based on
2549 lepton-flavor, namely ggF_2e2μ, ggF_4e and ggF_4μ.

2550

2. MVA-based categorization

2551 In order to target different production modes, two types of classifiers, one dedicate to
2552 VBF production while the other one for ggF, have been trained using deep neural network
2553 technique. Details of two classifiers are described as below:

2554

DNN models

2555 Figure 7.1 shows the architecture of VBF (left) and ggF (right) network. The VBF
2556 network includes three parts: two recurrent neural networks (RNNs) and one multilayer
2557 perceptron (MLP). The ggF network consists of one RNN and one MLP.

Table 7.3 Summary of the object and event selection requirements.

Physics Objects	
Electrons	
Loose Likelihood quality electrons with hit in innermost layer, $E_T > 7$ GeV and $ \eta < 2.47$	
Interaction point constraint: $ z_0 \cdot \sin \theta < 0.5$ mm (if ID track is available)	
Muons	
Loose identification with $p_T > 5$ GeV and $ \eta < 2.7$	
Calo-tagged muons with $p_T > 15$ GeV and $ \eta < 0.1$, segment-tagged muons with $ \eta < 0.1$	
Stand-alone and silicon-associated forward restricted to the $2.5 < \eta < 2.7$ region	
Combined, stand-alone (with ID hits if available) and segment-tagged muons with $p_T > 5$ GeV	
Interaction point constraint: $ d_0 < 1$ mm and $ z_0 \cdot \sin \theta < 0.5$ mm (if ID track is available)	
Jets	
anti- k_T jets with <i>bad-loose</i> identification, $p_T > 30$ GeV and $ \eta < 4.5$	
Overlap removal	
Jets within $\Delta R < 0.2$ of an electron or $\Delta R < 0.1$ of a muon are removed	
Vertex	
At least one collision vertex with at least two associated track	
Primary vertex	
Vertex with the largest p_T^2 sum	
Event Selection	
Quadruplet Selection	<ul style="list-style-type: none"> - Require at least one quadruplet of leptons consisting of two pairs of same-flavour opposite-charge leptons fulfilling the following requirements: - p_T thresholds for three leading leptons in the quadruplet: 20, 15 and 10 GeV - Maximum one calo-tagged or stand-alone muon or silicon-associated forward per quadruplet - Leading di-lepton mass requirement: $50 < m_{12} < 106$ GeV - Sub-leading di-lepton mass requirement: $50 < m_{34} < 115$ GeV - $\Delta R(\ell, \ell') > 0.10$ for all leptons in the quadruplet - Remove quadruplet if alternative same-flavour opposite-charge di-lepton gives $m_{\ell\ell} < 5$ GeV - Keep all quadruplets passing the above selection
Isolation	<ul style="list-style-type: none"> - Contribution from the other leptons of the quadruplet is subtracted - FixedCutPFlowLoose WP for all leptons
Impact Parameter	<ul style="list-style-type: none"> - Apply impact parameter significance cut to all leptons of the quadruplet
Significance	<ul style="list-style-type: none"> - For electrons: $d_0/\sigma_{d_0} < 5$ - For muons: $d_0/\sigma_{d_0} < 3$
Best Quadruplet	<ul style="list-style-type: none"> - If more than one quadruplet has been selected, choose the quadruplet with highest Higgs decay ME according to channel: 4μ, $2e2\mu$, $2\mu2e$ and $4e$
Vertex Selection	<ul style="list-style-type: none"> - Require a common vertex for the leptons: - $\chi^2/\text{ndof} < 5$ for 4μ and < 9 for others decay channels

Table 7.4 Cutflow table for a narrow-width ggF signal sample at $m_H = 600$ GeV. N_{event} denotes the number of events selected after each cut is applied, normalized to 139 fb^{-1} , according to the expected upper limit on the cross section. The acceptances (the proportion of events selected relative to the initial number of events) are also included.

	N_{event}	$N_{\text{event}}/\text{BR}(ZZ \rightarrow \ell\ell\ell'\ell')$	Acc. [%]	Acc. · $\text{BR}(ZZ \rightarrow \ell\ell\ell'\ell') \cdot 1000$
Initial	17.902	3 964.3	100.00	4.516
Lepton selection	6.247	1 383.4	34.90	1.576
SFOS	5.758	1 275.1	32.16	1.453
Kinematic cuts	5.754	1 274.2	32.14	1.452
Z_1 Mass	5.726	1 267.9	31.98	1.444
Z_2 Mass	5.112	1 132.0	28.56	1.290
J/ψ Veto	5.111	1 131.9	28.55	1.289
ΔR	5.111	1 131.7	28.55	1.289
Isolation	4.864	1 077.0	27.17	1.227
Impact parameters	4.796	1 062.1	26.79	1.210
Vertex requirement	4.786	1 059.8	26.73	1.207
Trigger	4.783	1 059.1	26.72	1.207
“Badjet” veto	4.763	1 054.7	26.61	1.201

Table 7.5 Cutflow table for a narrow-width ggF signal sample at $m_H = 1000$ GeV. N_{event} denotes the number of events selected after each cut is applied, normalized to 139 fb^{-1} , according to the expected upper limit on the cross section. The acceptances (the proportion of events selected relative to the initial number of events) are also included.

	N_{event}	$N_{\text{event}}/\text{BR}(ZZ \rightarrow \ell\ell\ell'\ell')$	Acc. [%]	Acc. · $\text{BR}(ZZ \rightarrow \ell\ell\ell'\ell') \cdot 1000$
Initial	5.603	1 240.8	100.00	4.516
Lepton selection	2.141	474.1	38.21	1.725
SFOS	1.944	430.5	34.70	1.567
Kinematic cuts	1.943	430.3	34.68	1.566
Z_1 Mass	1.932	427.8	34.48	1.557
Z_2 Mass	1.715	379.7	30.61	1.382
J/ψ Veto	1.715	379.7	30.60	1.382
ΔR	1.714	379.6	30.60	1.382
Isolation	1.640	363.2	29.27	1.322
Impact parameters	1.620	358.6	28.90	1.305
Vertex requirement	1.616	357.8	28.84	1.302
Trigger	1.615	357.7	28.83	1.302
“Badjet” veto	1.609	356.2	28.71	1.297

Table 7.6 Cutflow table for a narrow-width VBF signal sample at $m_H = 600$ GeV. N_{event} denotes the number of events selected after each cut is applied, normalized to 139 fb^{-1} , according to the expected upper limit on the cross section. The acceptances (the proportion of events selected relative to the initial number of events) are also included.

	N_{event}	$N_{\text{event}}/\text{BR}(ZZ \rightarrow \ell\ell\ell'\ell')$	Acc. [%]	Acc. · $\text{BR}(ZZ \rightarrow \ell\ell\ell'\ell') \cdot 1000$
Initial	12.143	2 688.9	100.00	4.516
Lepton selection	4.307	953.7	35.47	1.602
SFOS	3.975	880.2	32.74	1.478
Kinematic cuts	3.972	879.6	32.71	1.477
Z_1 Mass	3.953	875.4	32.56	1.470
Z_2 Mass	3.545	785.0	29.19	1.318
J/ψ Veto	3.545	785.0	29.19	1.318
ΔR	3.544	784.9	29.19	1.318
Isolation	3.418	756.9	28.15	1.271
Impact parameters	3.368	745.9	27.74	1.253
Vertex requirement	3.362	744.5	27.69	1.250
Trigger	3.360	744.0	27.67	1.250
“Badjet” veto	3.340	739.7	27.51	1.242

Table 7.7 Cutflow table for a narrow-width VBF signal sample at $m_H = 1000$ GeV. N_{event} denotes the number of events selected after each cut is applied, normalized to 139 fb^{-1} , according to the expected upper limit on the cross section. The acceptances (the proportion of events selected relative to the initial number of events) are also included.

	N_{event}	$N_{\text{event}}/\text{BR}(ZZ \rightarrow \ell\ell\ell'\ell')$	Acc. [%]	Acc. · $\text{BR}(ZZ \rightarrow \ell\ell\ell'\ell') \cdot 1000$
Initial	3.827	847.4	100.00	4.516
Lepton selection	1.474	326.5	38.53	1.740
SFOS	1.351	299.1	35.30	1.594
Kinematic cuts	1.350	299.0	35.28	1.593
Z_1 Mass	1.341	297.0	35.04	1.583
Z_2 Mass	1.195	264.6	31.23	1.410
J/ψ Veto	1.195	264.6	31.23	1.410
ΔR	1.195	264.6	31.22	1.410
Isolation	1.161	257.1	30.34	1.370
Impact parameters	1.148	254.1	29.99	1.354
Vertex requirement	1.146	253.8	29.95	1.352
Trigger	1.145	253.6	29.93	1.352
“Badjet” veto	1.139	252.2	29.77	1.344

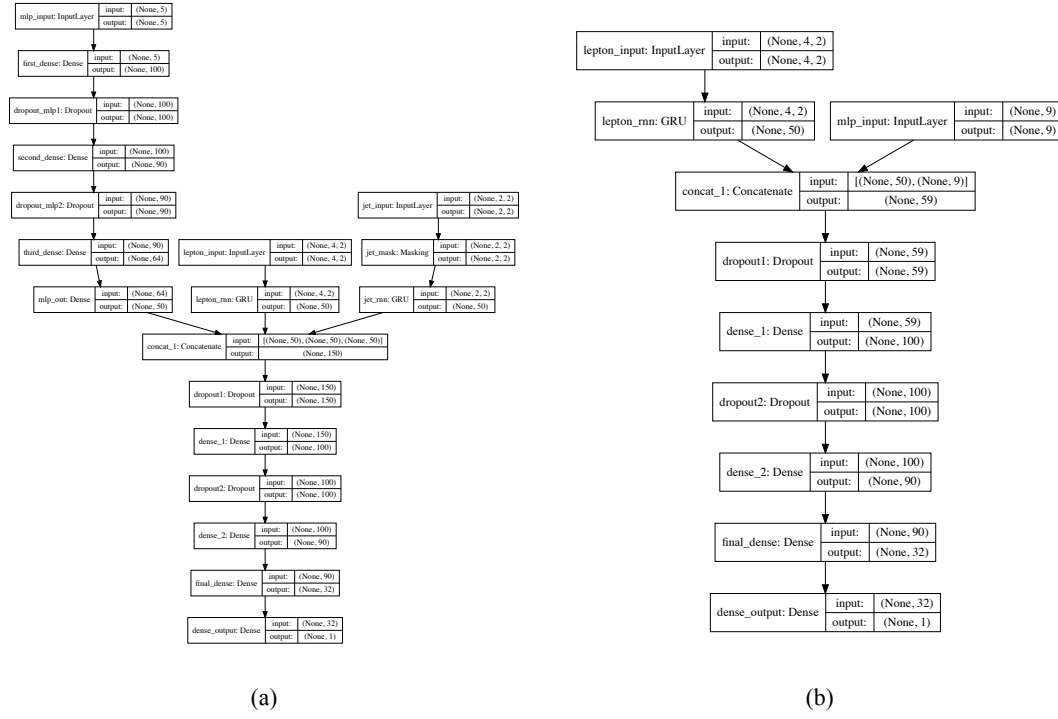


Fig. 7.1 (a) VBF DNN architecture diagram. (b) ggF DNN architecture.

For training, the VBF and ggF signal samples at the masses of 200, 300, 400, 500, 600, 700, 800, 900, 1000, 1200, 1400 GeV are used with positive label. The VBF (ggF) signals are only used for VBF (ggF) classifier. The background including simulated samples of QCD and EW $q\bar{q} \rightarrow ZZ$ processes as well as $gg \rightarrow ZZ$ process summed according to their cross section are assigned with negative labels. In addition to the selections described in section 7.3.2, the events used for VBF network are required to have $N_{\text{jets}} \geq 2$, while $N_{\text{jets}} < 2$ is required for events in ggF network.

In order to assign equivalent importance to signals with different mass assumptions, during the training, signal events are reweighted to follow the $m_{4\ell}$ distribution from background, as shown in figure 7.2 (figure 7.3) before (left) and after(right) reweighting for VBF (ggF) samples.

Input features

Table 7.8 (table 7.9) lists the input features used for VBF (ggF) network during the training. For VBF network, one RNN (the other one) takes the p_T and η of p_T -ordered four leptons (two leading jets) as input features, which intends to study the time relationship from particle decay between leptons (jets). For ggF network, the only one RNN model takes the p_T and η of p_T -ordered four leptons as inputs.

Evaluation of models

Figure 7.4 shows the output of “ggF-classifier” and “VBF-classifier” for data, SM

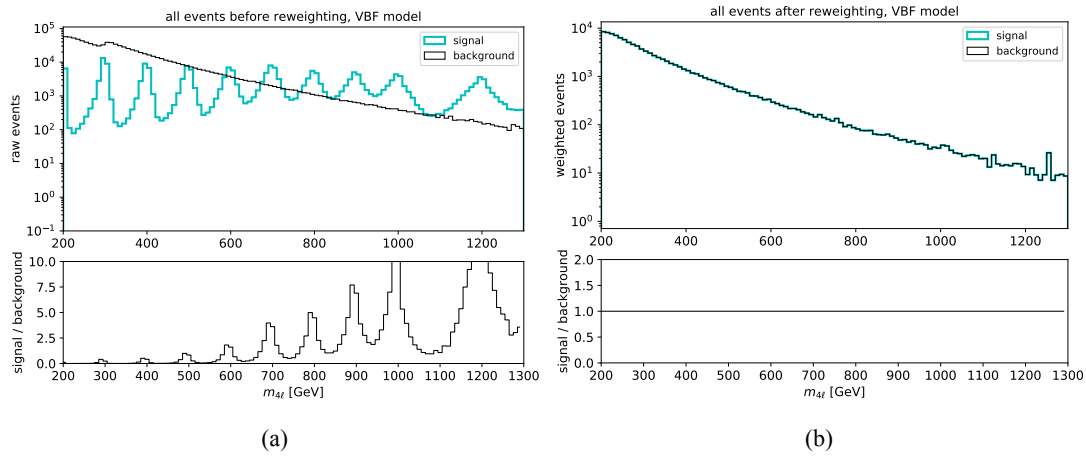


Fig. 7.2 (a) $m_{4\ell}$ distribution of raw (unweighted) training events for VBF signal (blue) and background (black); (b) $m_{4\ell}$ distribution of weighted VBF signal (blue) and background (black) used at training time.

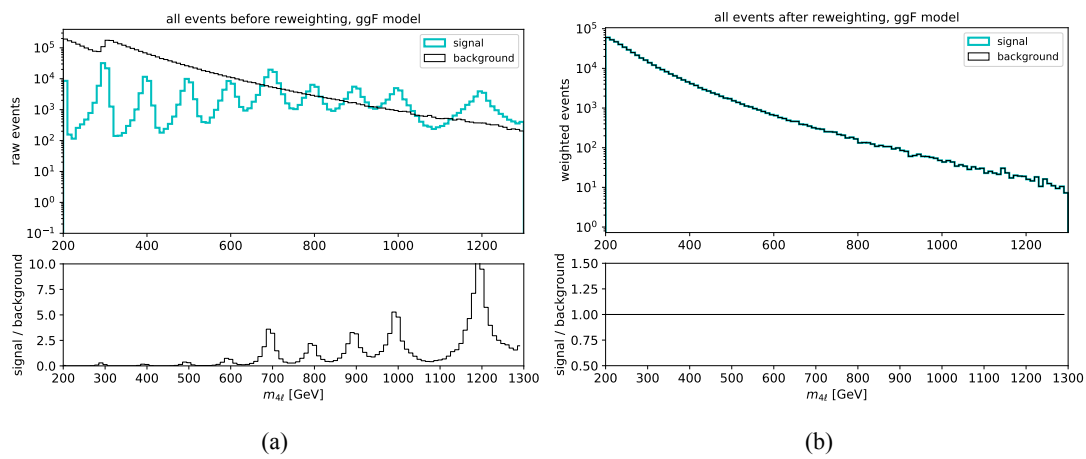


Fig. 7.3 (a) $m_{4\ell}$ distribution of raw (unweighted) training events for ggF signal (blue) and background (black); (b) $m_{4\ell}$ distribution of weighted ggF signal (blue) and background (black) used at training time.

Table 7.8 Input features used in the “VBF-classifier” for the $\ell\ell\ell'\ell'$ analysis. The RNN stands for the recurrent neural network and MLP for the multilayer perceptron.

Model	Inputs	Description
RNN	$p_T^{j0,j1}$	transverse momenta of the two leading jets
	$\eta^{j0,j1}$	pseudorapidity of the two leading jets
	$p_T^{\ell0,\ell1,\ell2,\ell3}$	transverse momenta of the four leptons
	$\eta^{\ell0,\ell1,\ell2,\ell3}$	pseudorapidity of the four leptons
MLP	$m_{4\ell}$	invariant mass of the four lepton system
	m_{jj}	invariant mass of the two leading jet system
	p_T^{jj}	transverse momentum of the two leading jet system
	$\Delta\eta_{H,j}$	difference in pseudorapidity between the four lepton system and the leading jet
	$\min\Delta R_{jZ}$	minimum distance between one of the two lepton pairs and a jet

2577 backgrounds and an example signal at 600 GeV. The ggF and VBF signals cross section
 2578 are set to be one hundred times of their observed upper limit described in section 7.7.3 for
 2579 ggF output and fifty times of the observed upper limit for VBF output for best visibility.

2580 Then the optimal cut at output score from each classifier is chosen based on an overall
 2581 good performance of classifier to have a large significance improvement while retaining
 2582 a high signal efficiency. Figure 7.5 shows the significance improvements of MVA-based
 2583 cuts when comparing with cut-based one at different VBF (left) and ggF (right) mass
 2584 samples, where the significance is calculated as:

$$Z = \sqrt{2 \left(n \ln \left[\frac{nb + \sigma^2}{b^2 + n\sigma^2} \right] - \frac{b^2}{\sigma^2} \ln \left[1 + \frac{\sigma^2(n-b)}{b(b+\sigma^2)} \right] \right)} \quad (7.1)$$

2585 Cut at 0.5 (0.8) for VBF (ggF) classifier is chosen as shown in solid lines.

2586 Then the events passing VBF classifier are categorized into VBF-MVA-enriched category.
 2587 Otherwise, the events failing VBF classifier but passing ggF classifier are categorized into ggF-MVA-high category, which is further split into 3 channels. All remaining
 2588 events are sorted into one additional ggF-MVA-low category. Thus there are five categories defined in MVA-based categorization. In summary, cuts applied in categorization
 2589 are defined as follow, and these different phase spaces are also illustrated in figure 7.6.

- 2592 • VBF-MVA-enriched category: Events have at least two selected jets ($N_{\text{jets}} \geq 2$),
 2593 and with $DNN_{\text{VBF}} > 0.8$;

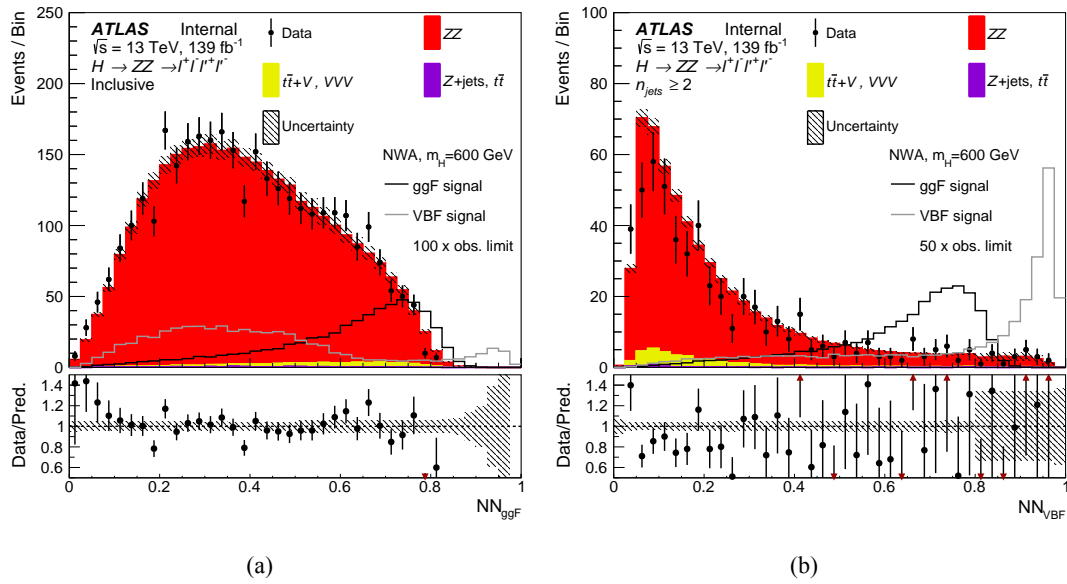


Fig. 7.4 The output score of “ggF-classifier” (a) and “VBF-classifier” (b) with the events passing the common event selections for the data, the SM backgrounds and an example of a NWA signal with a mass of 600 GeV. For the “VBF-classifier”, an additional requirement of at least two jets in the event is applied. The signals cross section are set to one hundred times of the observed limit for the “ggF-classifier” and fifty times of the observed limit for the “VBF -classifier”. The ZZ backgrounds are scaled by the normalisation factors shown in Table 7.15. The lower panels show the ratio of data to prediction. Only statistical and experimental systematic uncertainties are included.

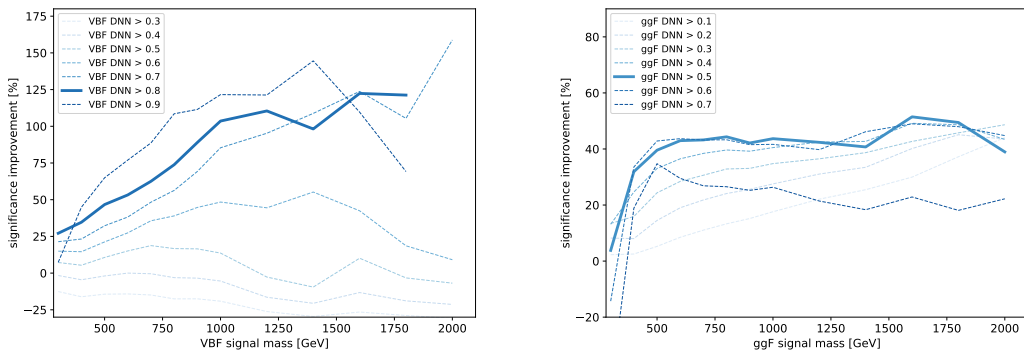


Fig. 7.5 Significance improvements of the MVA-based over the cut-based categorization of the VBF (ggF) category for VBF (ggF) signal samples from 300 to 2000 GeV for seven different cuts on the VBF (ggF) output score. The optimal cut of 0.8 (0.5) for VBF (ggF) score is chosen as the solid line, while other alternative cuts are plotted with dashed lines. For VBF category, results at 2000 GeV for cuts of 0.8 and 0.9 are missing due to a lack of background events passing this tight selection.

Table 7.9 Input features used in the “ggF-classifier” for the $\ell\ell\ell'\ell'$ analysis. The RNN stands for the recurrent neural network and MLP for the multilayer perceptron.

Model	Inputs	Description
RNN	$p_T^{\ell0,\ell1,\ell2,\ell3}$	transverse momenta of the four leptons
	$\eta^{\ell0,\ell1,\ell2,\ell3}$	pseudorapidity of the four leptons
MLP	$m_{4\ell}$	invariant mass of the four lepton system
	$p_T^{4\ell}$	transverse momentum of the four lepton system
	$\eta^{4\ell}$	pseudorapidity of the four lepton system
	$\cos \theta^*$	production angle of the leading Z defined in the four lepton rest frame
	$\cos \theta_1$	angle between the negative final state lepton and the direction of flight of leading Z in the Z rest frame
	$\cos \theta_2$	angle between the negative final state lepton and the direction of flight of sub-leading Z in the Z rest frame
	Φ	angle between the decay planes of the four final state leptons expressed in the four lepton rest frame
	p_T^{j0}	transverse momentum of the leading jet
	η^{j0}	pseudorapidity of the leading jet

- 2594 • ggF-MVA-high categories: ($N_{\text{jets}} \geq 2 \ \&\& \ DNN_{\text{VBF}} \leq 0.8 \ \&\& \ DNN_{\text{ggF}} >$
 2595 $0.5) || (N_{\text{jets}} < 2 \ \&\& \ DNN_{\text{ggF}} > 0.5);$
 2596 • ggF-MVA-low category: All remaining events that fail VBF and ggF cuts men-
 2597 tioned above.

2598 7.3.4 Signal acceptance

2599 The signal acceptance is defined as the ratio of events passing all analysis selection in
 2600 each category to the total number of simulated events in whole phase space. In denom-
 2601 inator, the events with τ final states are not taken into account. And the contribution of
 2602 τ -lepton decay to electrons and muons final states is found to be negligible.

2603 Figure 7.7 and 7.8 show the acceptance of NWA signals in DNN- and Cut- based
 2604 categorization, estimated by merging the three signal MC campaigns, mc16a, mc16d and
 2605 mc16e. A 3-rd order polynomial fit is applied for each category.

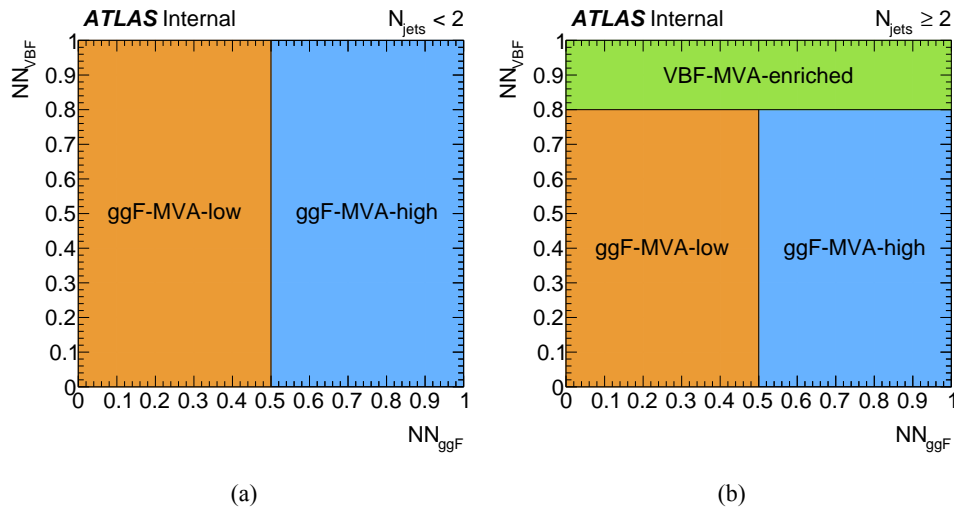


Fig. 7.6 Illustration of the MVA-based VBF and ggF event classification for events with (a) $N_{\text{jets}} < 2$ and (b) $N_{\text{jets}} \geq 2$.

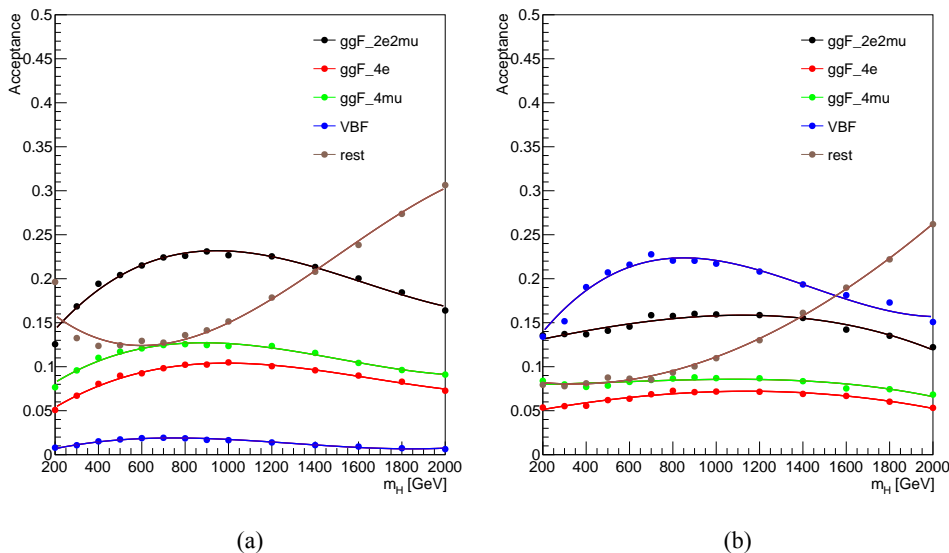


Fig. 7.7 NWA acceptance as a function of m_H for the MVA-based categorization for the samples of (a) ggF production; (b) VBF production.

7.4 Background estimation

In this analysis, 97% of total expected background events are from irreducible ZZ backgrounds, which includes about 86% quark-antiquark annihilation ($q\bar{q} \rightarrow ZZ$), 10% of gluon-induced production ($gg \rightarrow ZZ$) and around 1% of EW vector boson scattering ($q\bar{q} \rightarrow ZZ$ EW) contribution. For $q\bar{q} \rightarrow ZZ$ EW, although it has small contribution in total background events after analysis selection, it's important for VBF category with about 16% contribution.

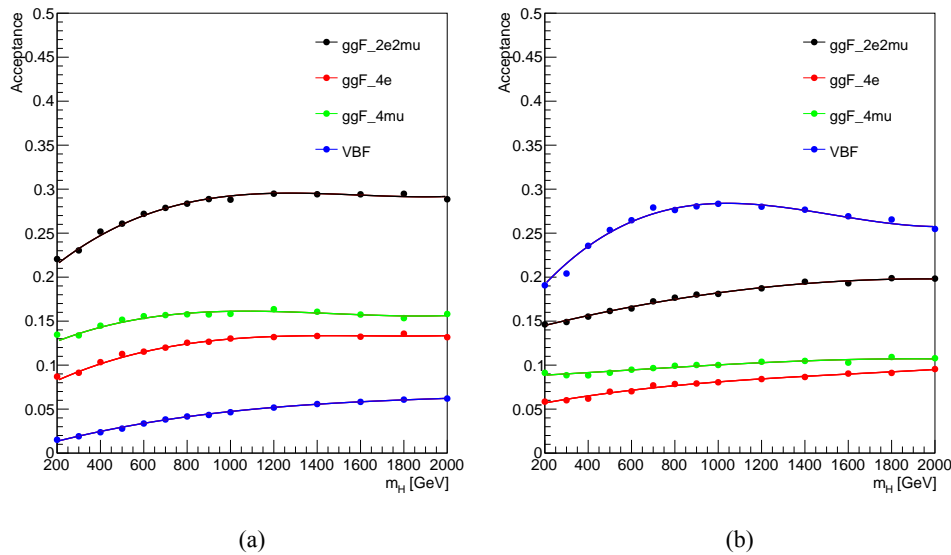


Fig. 7.8 NWA acceptance as a function of m_H for the Cut-based categorization for the samples of (a) ggF production mode; (b) VBF production mode.

2613 In addition to irreducible backgrounds, events from $Z+jets$ and $t\bar{t}$ processes, represent
 2614 as reducible backgrounds, contribute at a few percent level and can be measured using data
 2615 driven method that will be described briefly later. Additional background called ‘Others’,
 2616 including ttV and triple-V (VVV) processes, has tiny contribution and is estimated from
 2617 MC simulation directly.

2618 7.4.1 Irreducible backgrounds

2619 The Irreducible backgrounds have events with four prompt leptons. The normalization
 2620 of two dominant backgrounds $q\bar{q} \rightarrow ZZ$ and $gg \rightarrow ZZ$ are taken from data by statistical
 2621 fit, and the normalization of small $q\bar{q} \rightarrow ZZ$ EW background is measured directly from
 2622 MC simulation.

2623 The $m_{4\ell}$ shapes of all three background components are taken from MC samples and
 2624 then parameterized by an empirical function for each of them in each category respec-
 2625 tively. Details of background modellings are illustrated as below:

2626 The empirical function used for background parameterization is:

$$f(m_{4\ell}) = C_0 H(m_0 - m_{4\ell}) f_1(m_{4\ell}) + H(m_{4\ell} - m_0) f_2(m_{4\ell}), \quad (7.2)$$

where,

$$f_1(x) = \left(\frac{x - a_4}{a_3} \right)^{a_1-1} \left(1 + \frac{x - a_4}{a_3} \right)^{-a_1-a_2},$$

$$f_2(x) = \exp \left[b_0 \left(\frac{x - b_4}{b_3} \right)^{b_1-1} \left(1 + \frac{x - b_4}{b_3} \right)^{-b_1-b_2} \right],$$

$$C_0 = \frac{f_2(m_0)}{f_1(m_0)}.$$

The function consists of two parts, the first part f_1 describes the $m_{4\ell}$ spectrum in low mass region where both Z bosons decay on-shell, while the second one f_2 covers distribution at high mass tail. The transition between the low- and high- mass parts is presented in function 7.2 by the Heaviside step function $H(x)$ at the transition point m_0 . The m_0 is chosen to optimize the smoothness of the function, and practically $m_0 = 260$ (350) GeV is used for $q\bar{q} \rightarrow ZZ$ ($gg \rightarrow ZZ$ and $q\bar{q} \rightarrow ZZ$ EW). Besides, the continuity of two functions at m_0 is ensured by the factor C_0 applied to f_1 . The coefficients a_i in f_1 and b_i in f_2 are shape parameters obtained by fitting to $m_{4\ell}$ distribution from each MC simulated sample.

Figure 7.9 to 7.11 shows the fitting results of $q\bar{q} \rightarrow ZZ$, $gg \rightarrow ZZ$, $q\bar{q} \rightarrow ZZ$ EW backgrounds in four cut-based categories (ggF-CBA-enriched- $2e2\mu$, ggF-CBA-enriched- $4e$, ggF-CBA-enriched- 4μ and VBF-CBA-enriched). Figure 7.12 to 7.14 shows the fitting results of those backgrounds in five MVA-based categories (ggF-MVA-high- $2e2\mu$, ggF-MVA-high- $4e$, ggF-MVA-high- 4μ , ggF-MVA-low and VBF-MVA-enriched).

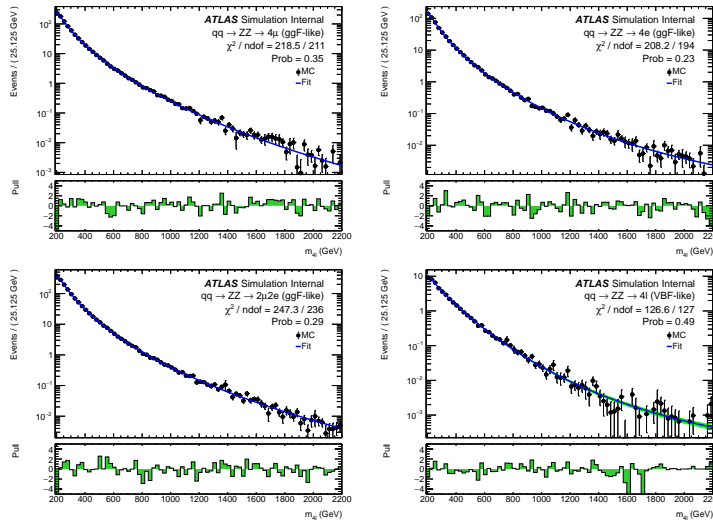


Fig. 7.9 Distributions of the $m_{4\ell}$ invariant mass fit projections of the $q\bar{q} \rightarrow ZZ$ background samples for the 4μ , $4e$ and $2\mu2e$ final states in the ggF-CBA-enriched category, and the 4ℓ inclusive VBF-CBA-enriched category. Cut-based categorization is used.

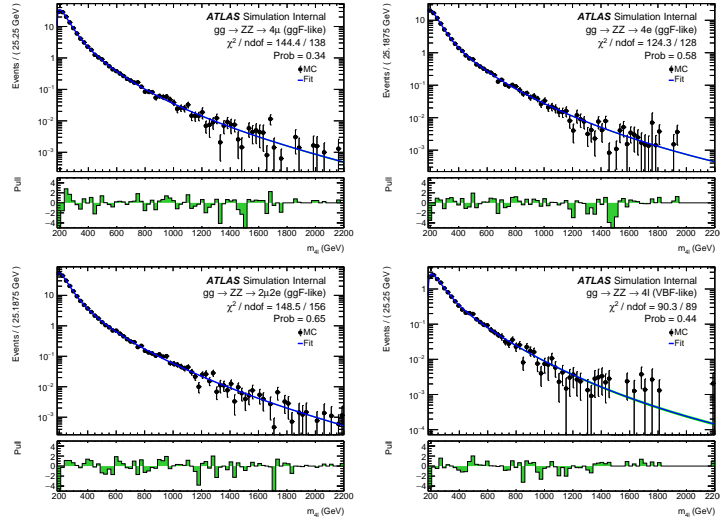


Fig. 7.10 Distributions of the $m_{4\ell}$ invariant mass fit projections of the $gg \rightarrow ZZ$ background samples for the 4μ , $4e$ and $2\mu2e$ final states in the ggF-CBA-enriched category, and the 4ℓ inclusive VBF-CBA-enriched category. Cut-based categorization is used.

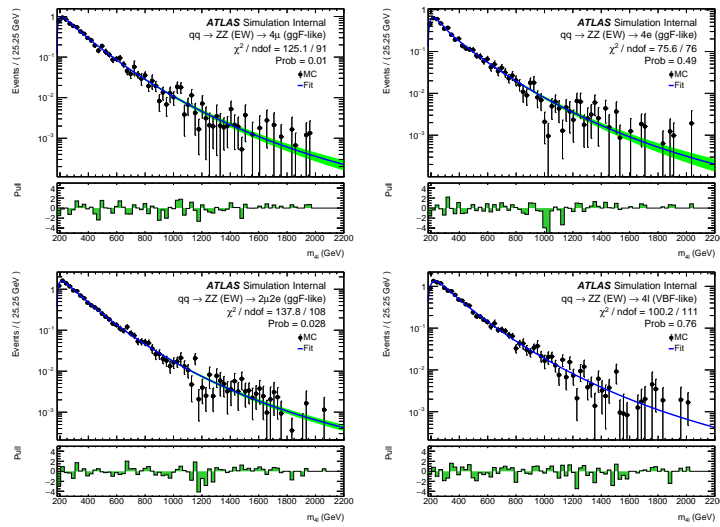


Fig. 7.11 Distributions of the $m_{4\ell}$ invariant mass fit projections of the $q\bar{q} \rightarrow ZZ$ (EW) background samples for the 4μ , $4e$ and $2\mu2e$ final states in the ggF-CBA-enriched category, and the 4ℓ inclusive VBF-CBA-enriched category. Cut-based categorization is used.

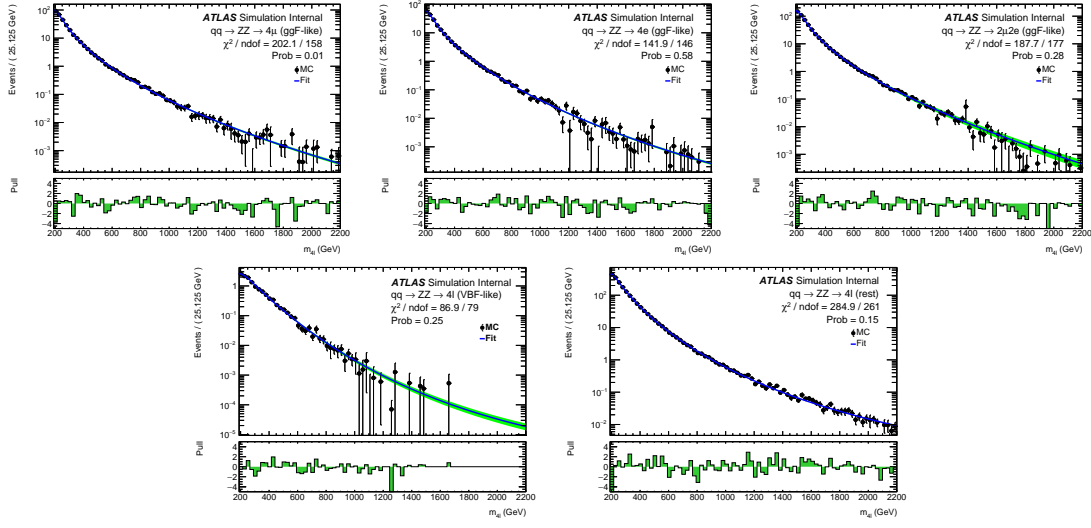


Fig. 7.12 Distributions of the $m_{4\ell}$ invariant mass fit projections of the $q\bar{q} \rightarrow ZZ$ background samples for the 4μ , $4e$ and $2\mu2e$ final states in the ggF-MVA-high category, the 4ℓ inclusive ggF-MVA-low category and VBF-MVA-enriched category. DNN-based categorization is used.

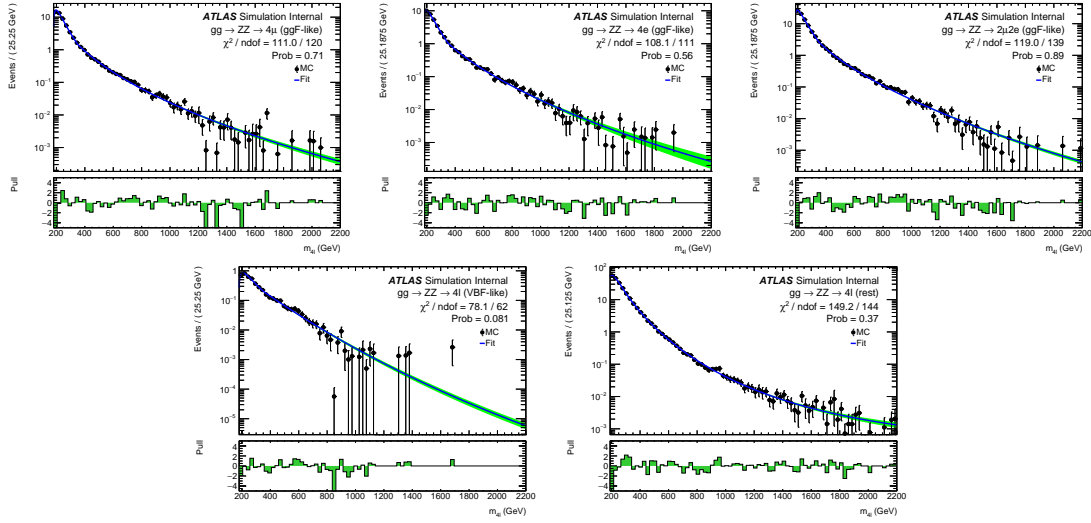


Fig. 7.13 Distributions of the $m_{4\ell}$ invariant mass fit projections of the $gg \rightarrow ZZ$ background samples for the 4μ , $4e$ and $2\mu2e$ final states in the ggF-MVA-high category, the 4ℓ inclusive ggF-MVA-low category and VBF-MVA-enriched category. DNN-based categorization is used.

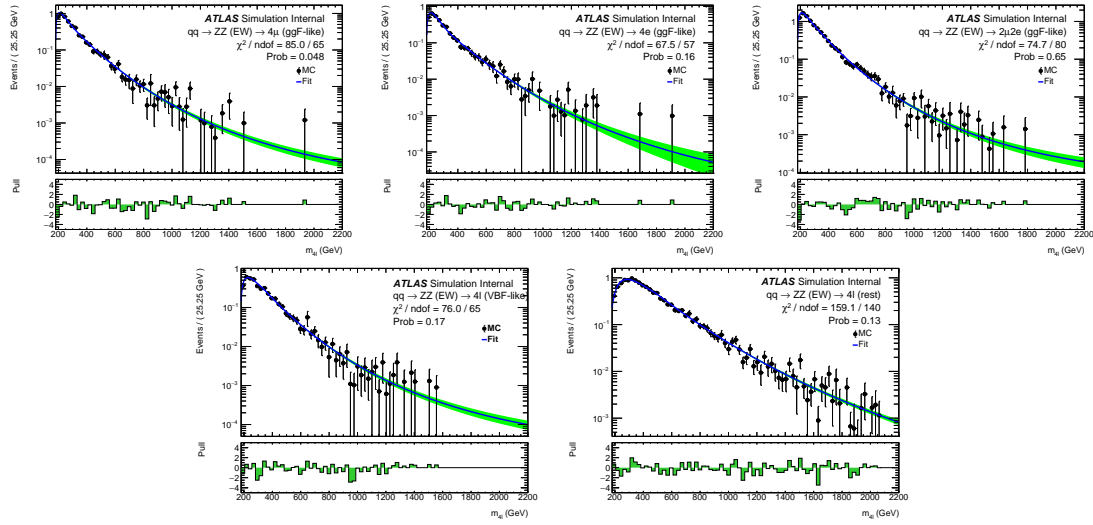


Fig. 7.14 Distributions of the $m_{4\ell}$ invariant mass fit projections of the $q\bar{q} \rightarrow ZZ$ (EW) background samples for the 4μ , $4e$ and $2\mu2e$ final states in the ggF-MVA-high category, the 4ℓ inclusive ggF-MVA-low category and VBF-MVA-enriched category. DNN-based categorization is used.

2641 7.4.2 Reducible backgrounds

2642 Similar as section 6.4, the reducible backgrounds include $Z+jets$ (consists of both
 2643 heavy- and light-flavour jets), top quark pair, and WZ production, which contain fake
 2644 and non-isolated leptons. The simulations are not very robust in terms of the selection
 2645 efficiencies. Thus, the data-driven method is applied to estimate the normalization of
 2646 those processes in different control regions (CRs). The estimations in this analysis are
 2647 performed separately for $\ell\ell + \mu\mu$ and $\ell\ell + ee$ final states, with slightly different ap-
 2648 proaches for “muon” and “electron” backgrounds.

2649 The “electron” backgrounds mostly come from process of a Z boson with light-
 2650 flavour jets ($Z+LF$) misidentified as electrons. The large contribution of “muon” back-
 2651 grounds come from heavy-flavour jets produced in association with a Z boson ($Z+HF$)
 2652 or in the decays of top quark. The estimations are done following the common H4l stud-
 2653 ies without a specific $m_{4\ell}$ range requirement^[107], and then the corresponding fraction of
 2654 event yield in $m_{4\ell} > 200$ GeV is calculated from MC simulation.

2655 $\ell\ell + \mu\mu$ final states

2656 The normalizations of “muon” backgrounds are extracted from simultaneous fits of
 2657 the leading lepton pair’s invariant mass (m_{12}) in four orthogonal CRs:

- 2658 • **Inverted d_0 CR:** this CR is formed by inverting the d_0 selection for at least one
 2659 lepton in subleading lepton pair while the leptons in leading pair are required to
 2660 pass all standard selection. This CR enhances $Z+HF$ and $t\bar{t}$ as leptons from heavy-

flavour hadronic decays are characterised by large d_0 .

- $e\mu + \mu\mu$ **CR**: this CR is formed using an opposite-charge different-flavour dilepton in leading pair. It aims to enhance $t\bar{t}$ background as the leading lepton pair cannot come from Z boson decay.
- **Inverted isolation CR**: in this CR, leptons in leading pair are required to satisfy all standard analysis selection, while for leptons in subleading pair, they are required to pass d_0 selection but have at least one of them failing isolation selection. This CR enhances the events from $Z+LF$ processes while suppress $Z+HF$ by d_0 cut.
- **Same-sign CR**: in this CR, the leptons in subleading pair are required to have same-charge, while the leading pair still passes standard selection. This CR is not dominant by any specific background since all reducible backgrounds could have sizable contribution in it.

The fit results of normalizations are then propagated to signal region (SR) by applying transfer factors to account the difference of selection efficiencies between SR and CRs.

The transfer factors are computed using $Z + \mu$ MC samples.

$\ell\ell + ee$ final states

The “electron” backgrounds are estimated in $3\ell + X$ CR, where X denotes the lower p_T electron in the subleading pair. The selection and identification criterias for X are relaxed , while other three leptons must satisfy the standard selection. In this case, X could be a light-flavour jet, a photon conversion or an electron from heavy-flavour hadron decay. Moreover, the subleading pair is required to have same charge dilepton to ensure the orthogonality to the signal region. The normalization of backgrounds are obtained based on a fit to the number of hits in the innermost ID layer in CR, and the transfer factors are computed from $Z + e$ simulated sample.

The $m_{4\ell}$ shapes of reducible backgrounds are obtained from MC simulation in signal region, and then smoothed by an one-dimensional kernel estimation, which models the input data as a superposition of Gaussian kernels, one for each data point with contributing $1/N$ to total integral N ^[108]. The difference from using different smoothing strength (ρ) in kernel estimation is taken into account as additional shape uncertainties for these reducible backgrounds.

7.5 Signal modelling

The parameterization of $m_{4\ell}$ distributions based on simulated samples for signals are described in this section. Several signal models are studied, including heavy Higgs like

2694 narrow-width signal (NWA) and large-width signal (LWA), as well as the modelling of
2695 Randall-Sundrum graviton (RSG) signal.

2696 7.5.1 Modelling of narrow-width signal

2697 For narrow-width (NWA) signal, the $m_{4\ell}$ width is totally determined by detector reso-
2698 lution, which is modelled by the sum of a Crystal Ball (C) function^[109-110] and a Gaussian
2699 (G) function:

$$P_s(m_{4\ell}) = f_C \cdot C(m_{4\ell}; \mu, \sigma_C, \alpha_C, n_C) + (1 - f_C) \cdot G(m_{4\ell}; \mu, \sigma_G) \quad (7.3)$$

2700 The two functions share the same central value μ , while the resolution parameters, σ_C
2701 and σ_G , are different. In the Crystal Ball function, the parameters α_C and n_C model the
2702 shape of non-Gaussian tail, and the fraction parameter f_C is used to ensure the relative
2703 normalization between two functions.

2704 The parameters are obtained by fitting to signal MC simulations combining the mc16a,
2705 mc16d and mc16e campaigns for each category at each mass points from 200 GeV to
2706 2000 GeV respectively, and the shape of ggF and VBF signals are found to be similar.
2707 Figure 7.15 shows the $m_{4\ell}$ distribution and fitted curves for ggF production at mass from
2708 200 GeV to 2000 GeV in $2e2\mu$ channel as examples.

2709 Then the $C + G$ parameters are fitted with a polynomial function as the function of
2710 generated mass points (m_H), as an example shown in figure 7.16 for $2e2\mu$ channel. The
2711 fitting quality can be measured by the Pearson's χ^2 , which is within 3 (2) for $2e2\mu$ (4e
2712 and 4μ) channel.

2713 In addition, possible difference on the signal yield extracted from parameterization and
2714 MC simulation is studied. Figure 7.17 shows this difference by computing $\frac{N_{\text{reco}} - N_{\text{fit}}}{N_{\text{fit}}}$, where
2715 N_{reco} denotes the total number of reconstructed events observed from MC simulation at
2716 that mass point and N_{fit} depicts the number of events obtained from the fitted PDF. The
2717 differences are treated as an additional systematic uncertainty with the value of 2% (1%)
2718 for $2e2\mu$ (4e and 4μ) channel in statistical fit.

2719 In summary, the final interpolated signal shapes for the ggF production mode are
2720 shown together in figure 7.18 for mass points with step of 100 GeV from 200 GeV to
2721 3000 GeV.

2722 7.5.2 Modelling of large-width signal

2723 The $m_{4\ell}$ shape of heavy Higgs model in large-width (LWA) hypothesis can be de-
2724 scribed by a convolution of a truth distribution and a resolution from detector effect. The

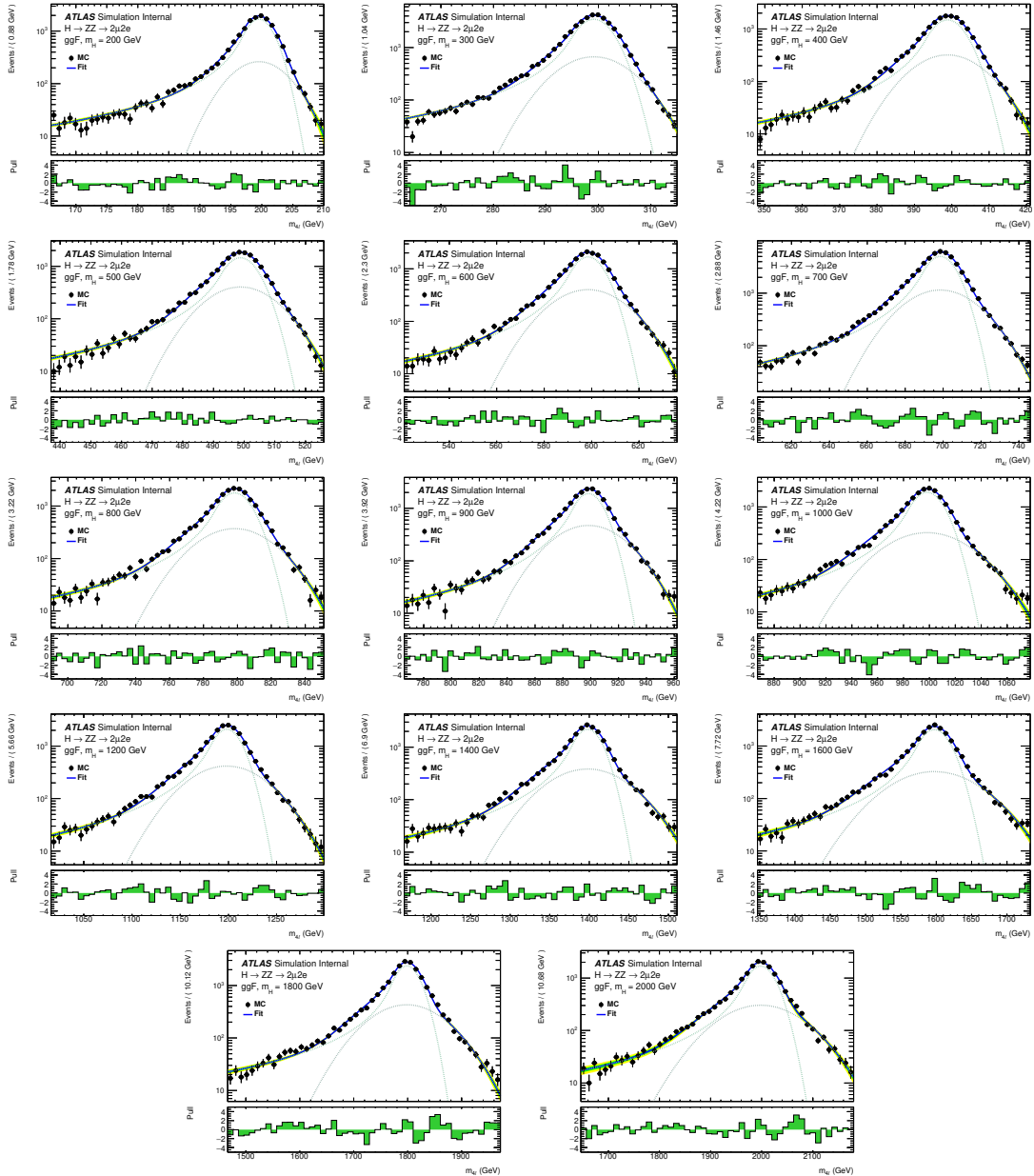


Fig. 7.15 Distributions of the $m_{2\mu 2e}$ and fit projection for signal samples between 200 to 3000 GeV for ggF production mode. Three MC campaigns, mc16a, mc16d and mc16e, are combined. The lower panel in each plot shows the pull distribution.

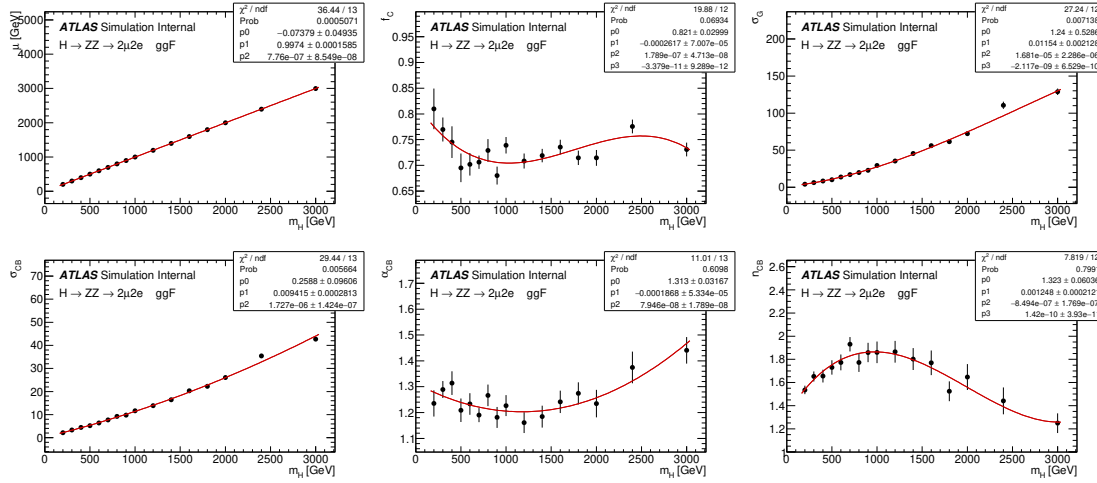


Fig. 7.16 Polynomial fits of the parameters μ , f_C , σ_G , σ_C , n_c and α_C for the signal $\mathcal{C} + \mathcal{G}$ model in the $2\mu 2e$ channel as a function of m_H for the ggF production mode. The combination of the mc16a, mc16d and mc16e MC campaigns is used.

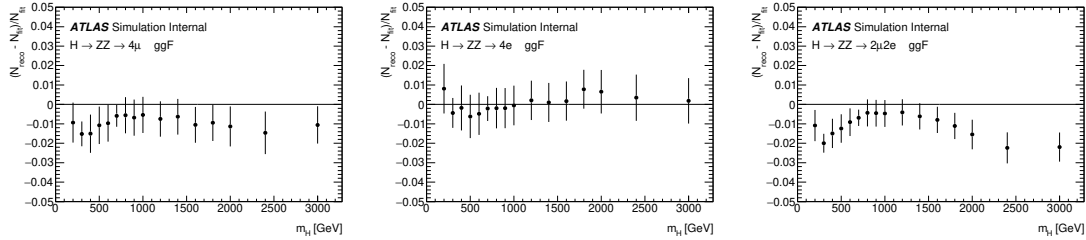


Fig. 7.17 The difference between MC simulation and parameterization of 4μ (left), $4e$ (middle) and $2\mu 2e$ (right) for the ggF production mode. The combination of the mc16a, mc16d and mc16e MC campaigns is used.

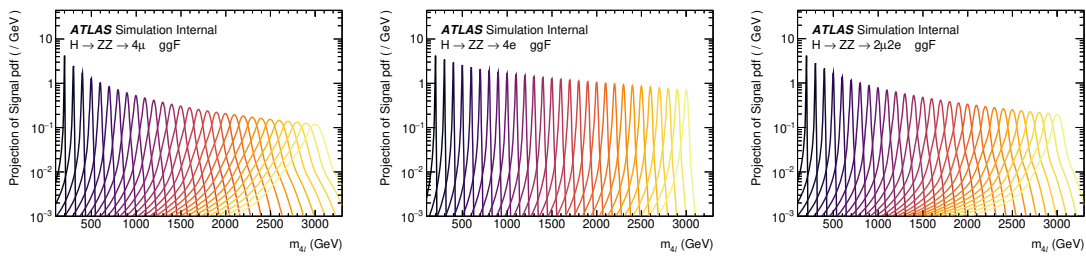


Fig. 7.18 The final signal shapes for the ggF production mode, interpolated from the polynomial fit parameters.

detector resolution effect is the one modelled by the function described in NWA parameterization, as in NWA model the truth level width is negligible.

The differential parton cross section for the heavy Higgs model can be written as^[111]:

$$\sigma_{gg \rightarrow H \rightarrow ZZ}(s) = \frac{1}{2s} \int d\Omega |A_{gg \rightarrow H}(s, \Omega)|^2 \frac{1}{|s - s_H|^2} |A_{H \rightarrow ZZ}(s, \Omega)|^2 \quad (7.4)$$

where $A_{gg \rightarrow H}(s, \Omega)$ and $A_{H \rightarrow ZZ}(s, \Omega)$ are corresponding Higgs production and decay amplitudes, and $\frac{1}{|s - s_H|}$ denotes the Higgs propagator and Ω represents the phase space of the process.

Using the definition of a partial width,

$$\Gamma_{H \rightarrow F}(s) = \frac{1}{2\sqrt{s}} \int d\Omega |A_{H \rightarrow F}(s, \Omega)|^2 \quad (7.5)$$

the parton cross section can be rewritten as,

$$\sigma_{gg \rightarrow H \rightarrow ZZ}(s) = 2 \frac{1}{|s - s_H|^2} \times \Gamma_{H \rightarrow gg}(s) \times \Gamma_{H \rightarrow ZZ}(s) \quad (7.6)$$

with the components computed in Ref^[111-112]:

$$\begin{aligned} \frac{1}{s - s_H} &= \frac{1 + i \cdot \bar{\Gamma}_H / \bar{m}_H}{s - \bar{m}_H^2 + i \cdot s \cdot \bar{\Gamma}_H / \bar{m}_H} \\ \bar{m}_H &= \sqrt{\bar{\Gamma}_H^2 + m_H^2} \\ \bar{\Gamma}_H &= \bar{m}_H \cdot \frac{\Gamma_H}{m_H} \end{aligned} \quad (7.7)$$

$$\Gamma_{H \rightarrow ZZ}(s) = C \cdot s^{\frac{3}{2}} \cdot \left[1 - \frac{4m_Z^2}{s} + \frac{3}{4} \left(\frac{4m_Z^2}{s} \right)^2 \right] \cdot \left[1 - \frac{4m_Z^2}{s} \right]^{\frac{1}{2}} \quad (7.8)$$

$$\begin{aligned} \Gamma_{H \rightarrow gg}(s) &= C \cdot s^{\frac{3}{2}} \cdot |A_t(\tau_t)|^2 \\ A_t(\tau) &= 2 \frac{\tau + (\tau - 1)f(\tau)}{\tau^2} \\ \tau_t &= \frac{s}{4m_t^2} \end{aligned} \quad (7.9)$$

$$f(\tau) = \begin{cases} \arcsin^2(\sqrt{\tau}), & \tau \leq 1 \\ -\frac{1}{4} \left[\log \frac{1+\sqrt{1-\tau^{-1}}}{1-\sqrt{1-\tau^{-1}}} - i\pi \right]^2, & \tau > 1 \end{cases}$$

where m_f stands for the mass of a fermion f , and Γ_H denotes an assumed total width of the heavy Higgs boson.

At the LHC, the $m_{4\ell}$ line shape can be defined by a hadron cross section that is derived from equation 7.6 by multiplication with gluon-gluon luminosity \mathcal{L}_{gg} described in^[113]. Meanwhile, the cross section is rewritten as a function of $m_{4\ell}$ instead of s , which will give an extra power of mass dependence in the formula:

$$\sigma_{pp \rightarrow H \rightarrow ZZ}(m_{4\ell}) = 2 \cdot m_{4\ell} \cdot \mathcal{L}_{gg} \cdot \frac{1}{|s - s_H|^2} \cdot \Gamma_{H \rightarrow gg}(m_{4\ell}^2) \cdot \Gamma_{H \rightarrow ZZ}(m_{4\ell}^2) \quad (7.10)$$

The analytical shapes of truth level $m_{4\ell}$ distribution of gg2VV MC samples is shown on figure 7.19.

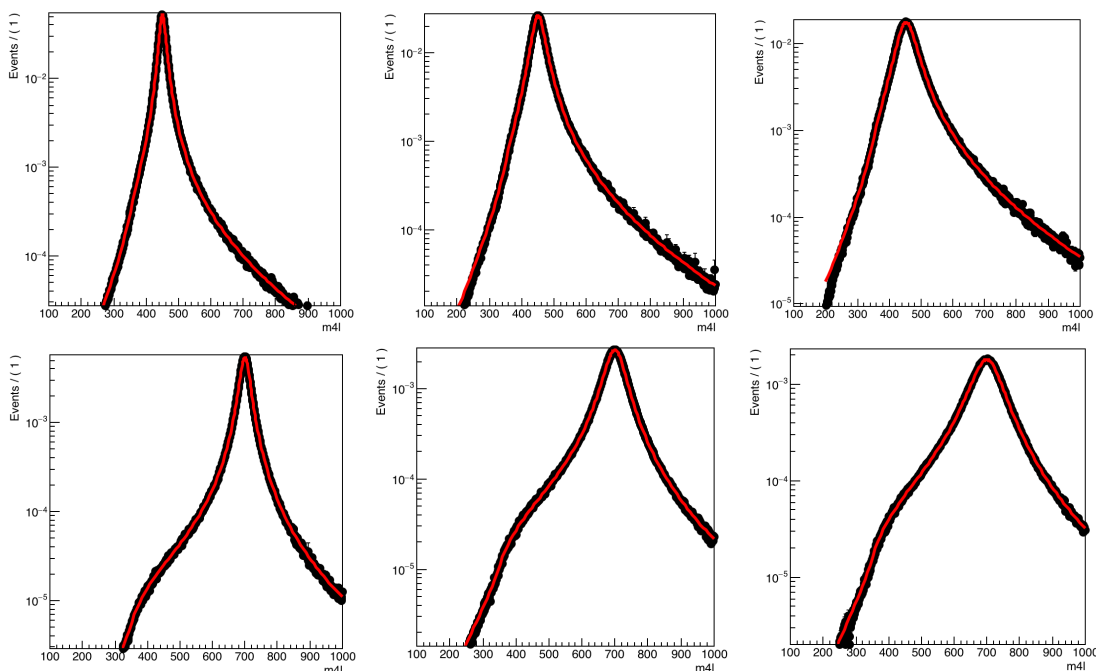


Fig. 7.19 Comparison of the analytical shape to a truth $m_{4\ell}$ distribution of gg2VV MC samples for $m_H = 450$ GeV (top), 700 GeV (bottom) and width equal to 5% (left), 10% (middle), 15% (right) of the mass.

The reconstruction level signal shape can then be modelled by the analytical truth shape convoluted with detector effects modelled in section 7.5.1. A comparison between the modelled shape and reconstruction level MC simulation for signal mass above 400 GeV (for ggF production in $2e2\mu$ channel as an example) are shown in figure 7.20, the shapes are well compatible between each other. This modelling is not valid for lower masses due to the rapid change of detector resolution.

7.5.3 Modelling of interference

There are three processes sharing the same gg initial state and ZZ final state:

- The SM $gg \rightarrow ZZ$ process with an amplitude A_B

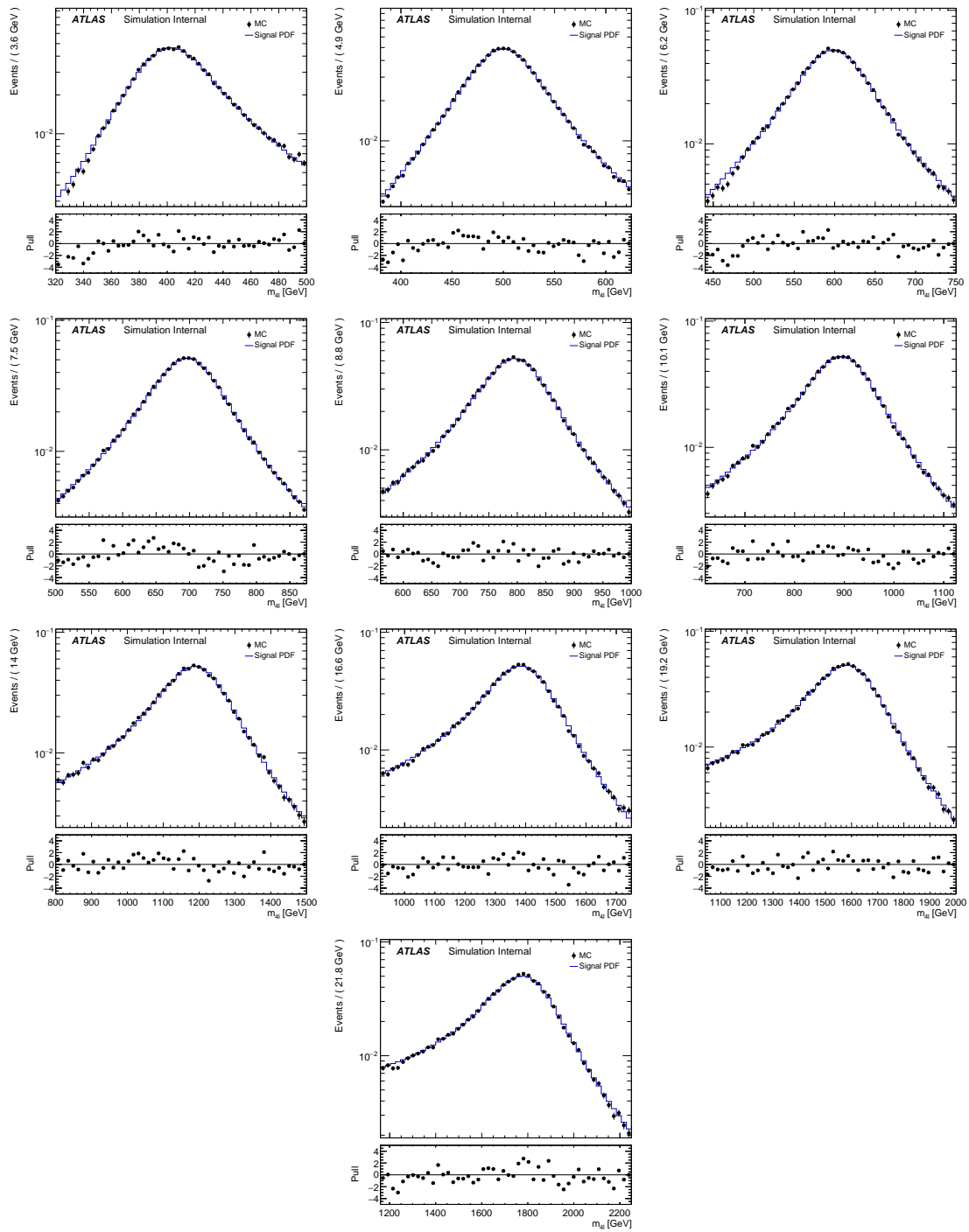


Fig. 7.20 Comparison between the analytical shape convoluted with detector effects and the reconstructed $m_{2\mu 2e}$ MC distribution for mass points ranging from 400 to 1800 GeV and width equal to 15% of the mass.

- 2750 • The SM (light) Higgs at mass of around 125 GeV with an amplitude A_h
- 2751 • The BSM heavy Higgs we are searching in this analysis with an amplitude A_H

2752 The three processes can interfere with each other due to the same initial and final states.

2753 The parton cross section for these processes can be written as:

$$\begin{aligned}
 \sigma_{gg \rightarrow (X) \rightarrow ZZ}(s) &= \frac{1}{2s} \int d\Omega |A_h(s, \Omega) + A_H(s, \Omega) + A_B(s, \Omega)|^2 \\
 &= \frac{1}{2s} \int d\Omega \left(|A_h(s, \Omega)|^2 + |A_H(s, \Omega)|^2 + |A_B(s, \Omega)|^2 \right) + \\
 &\quad + \frac{1}{s} \int d\Omega \left(\text{Re}[A_h(s, \Omega) \cdot A_B^*(s, \Omega)] \right. \\
 &\quad \left. + \text{Re}[A_H(s, \Omega) \cdot A_B^*(s, \Omega)] + \text{Re}[A_H(s, \Omega) \cdot A_h^*(s, \Omega)] \right) \\
 &\quad + \frac{1}{s} \text{Re} \left[\frac{1}{s - s_H} \int d\Omega \cdot A_H^P(s, \Omega) \cdot A_H^D(s, \Omega) \cdot A_B^*(s, \Omega) \right] \\
 &\quad + \frac{1}{s} \int d\Omega \cdot \text{Re} \left[A_H^P(s, \Omega) \cdot \frac{1}{s - s_H} \cdot A_H^D(s, \Omega) \cdot A_h^{P*}(s, \Omega) \cdot \frac{1}{(s - s_h)^*} \cdot A_h^{D*}(s, \Omega) \right]
 \end{aligned} \tag{7.11}$$

2754 The first term in equation 7.11 denotes the on-shell SM Higgs contribution, which is
 2755 negligible in this analysis. The second term corresponds to the heavy Higgs contribution,
 2756 whose line shape has been described in previous section. The third term is the $gg \rightarrow ZZ$
 2757 continuum process, while the forth term is the interference between SM Higgs and $gg \rightarrow$
 2758 ZZ continuum. The fifth and sixth terms are the interferences between heavy Higgs and
 2759 $gg \rightarrow ZZ$ continuum (H-B), and between heavy Higgs and SM Higgs (H-h) that we
 2760 are interested in. More details about the parameterization of these two interferences are
 2761 described as below.

2762 1. Interference between heavy Higgs and $gg \rightarrow ZZ$ continuum

2763 The parton cross section of this interference term has been written down in equa-
 2764 tion 7.11. By assuming that this function has a smooth behaviour, it can be replaced with
 2765 complex polynomial:

$$\int d\Omega \cdot A_H^P(s, \Omega) \cdot A_H^D(s, \Omega) \cdot A_B^*(s, \Omega) \approx (a_0 + a_1 \cdot \sqrt{s} + \dots) + i \cdot (b_0 + b_1 \cdot \sqrt{s} + \dots) \tag{7.12}$$

2766 The parameters a_i and b_i can be extracted by fitting to the $m_{4\ell}$ distribution from truth
 2767 level MC simulation after analysis selection. Since the signal mass and width does not
 2768 enter into this function, the parameters should be independent for every tested signal hy-
 2769 pothesis.

2770 Same as description for equation 7.10, the parton cross section can be transformed

2771 into a hadron cross section as a function of $m_{4\ell}$:

$$\sigma_{pp}(m_{4\ell}) = \mathcal{L}_{gg} \cdot \frac{1}{m_{4\ell}} \cdot \text{Re} \left[\frac{1}{s - s_H} \cdot ((a_0 + a_1 \cdot m_{4\ell} + \dots) + i \cdot (b_0 + b_1 \cdot m_{4\ell} + \dots)) \right] \quad (7.13)$$

2772 where the propagators are shown in equation 7.7.

2773 Figure 7.21 shows the distributions of interference function obtained by simultaneous
2774 fitting to $m_{4\ell}$ shape from truth level H-B interference simulation at different mass in $2e2\mu$
2775 channel as an example.

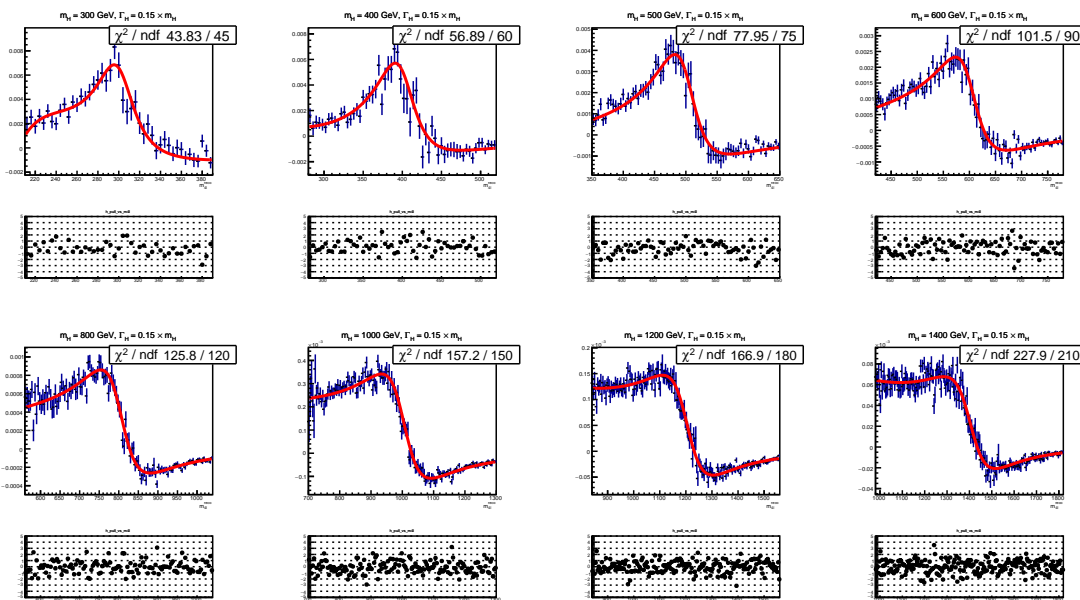


Fig. 7.21 The interference (H-B) model fitted to the truth $m_{4\ell}$ MC distribution after signal region selection for $2\mu2e$ channel.

2776 **2. Interference between heavy Higgs and SM Higgs**

2777 The parton cross section of this interference term has been written down in equa-
2778 tion 7.11. By assuming the production and decay amplitudes are the same for heavy
2779 Higgs boson and SM Higgs boson, the cross section function can be simplified to:

$$\sigma_{gg}(s) = \frac{1}{s} \int d\Omega \cdot \text{Re} \left[\frac{1}{s - s_H} \cdot \frac{1}{(s - s_h)^*} \right] \cdot |A_{gg \rightarrow H}(s, \Omega)|^2 |A_{H \rightarrow ZZ}(s, \Omega)|^2 \quad (7.14)$$

2780 Taking into account Equation 7.5:

$$\sigma_{gg}(s) = 4 \cdot \text{Re} \left[\frac{1}{s - s_H} \cdot \frac{1}{(s - s_h)^*} \right] \cdot \Gamma_{H \rightarrow gg}(s) \cdot \Gamma_{H \rightarrow ZZ}(s) \quad (7.15)$$

2781 where the propagators are described in equation 7.7, and the partial widths are de-
2782 scribed in equations 7.8 and 7.9.

2783 Same as previous procedure, the parton cross section can be transformed to a hadron
 2784 cross section as a function of $m_{4\ell}$:

$$\sigma_{pp}(m_{4\ell}) = 4 \cdot m_{4\ell} \cdot \mathcal{L}_{gg} \cdot \text{Re} \left[\frac{1}{s - s_H} \cdot \frac{1}{(s - s_h)^*} \right] \cdot \Gamma_{H \rightarrow gg}(m_{4\ell}) \cdot \Gamma_{H \rightarrow ZZ}(m_{4\ell}) \quad (7.16)$$

2785 The modelling procedure of interference is the same as the way for large-width signal
 2786 described in section 7.5.2. The truth line shape is measured as analytical function from
 2787 equation 7.16, and then convolute with detector effect from NWA parameterization to get
 2788 the reconstruction level shape.

2789 For LWA signal model, these two interferences are carefully token into account, and
 2790 the integration of the pure LWA signal with the interferences is used for further studies.
 2791 Figure 7.22 shows the signal model for large-width scenario at mass points of 400 GeV,
 2792 600 GeV, 800 GeV, for three different signal widths: 5%, 10%, 15%, with and without
 2793 interference. Additionally, the contribution of the interference between heavy Higgs and
 2794 SM Higgs (H-h) is shown together with the one between heavy Higgs and SM $gg \rightarrow$
 2795 ZZ background (H-b). One can see the interference effect on signal shape becomes less
 2796 important when going to higher mass.

2797 7.5.4 Modelling of spin-2 RS Graviton signal

2798 The search for Randall-Sundrum (RS) graviton is performed in mass region between
 2799 600 to 2000 GeV. The width of resonance is determined by the $k/\overline{M}_{\text{Planck}}$, which, as
 2800 mentioned in section 7.2.3, is set to be 1. In this configuration, the width of signal is
 2801 expected to be about 6% of its mass.

The reconstructed $m_{4\ell}$ lineshape of graviton is also built by convolving the truth-level lineshape with a detector resolution function, where the detector resolution effect is modelled by a Gaussian + Crystal Ball function, whose parameters are taken from the NWA signal parameterization in section 7.5.1. And for truth-level shape, for graviton, it's modelled as the product of a relativistic Breit-Wigner (RBW) term, a term corresponding to the squared matrix element of the production process and a parton luminosity term \mathcal{L} as given in [114]. So the truth lineshape of $m_{4\ell}$ is token from:

$$m_{4\ell}^{\text{Truth}} \sim \mathcal{L}_{gg} \cdot s^2 \cdot \frac{s(1+s)(1+2s+2s^2)}{(s^2 - m_G^2)^2 + m_G^2 \Gamma^2}$$

2802 The truth-level signal model is extracted by fitting to MC simulation at truth-level with
 2803 the mass m_G and width Γ parameters floating at each mass points respectively. And then

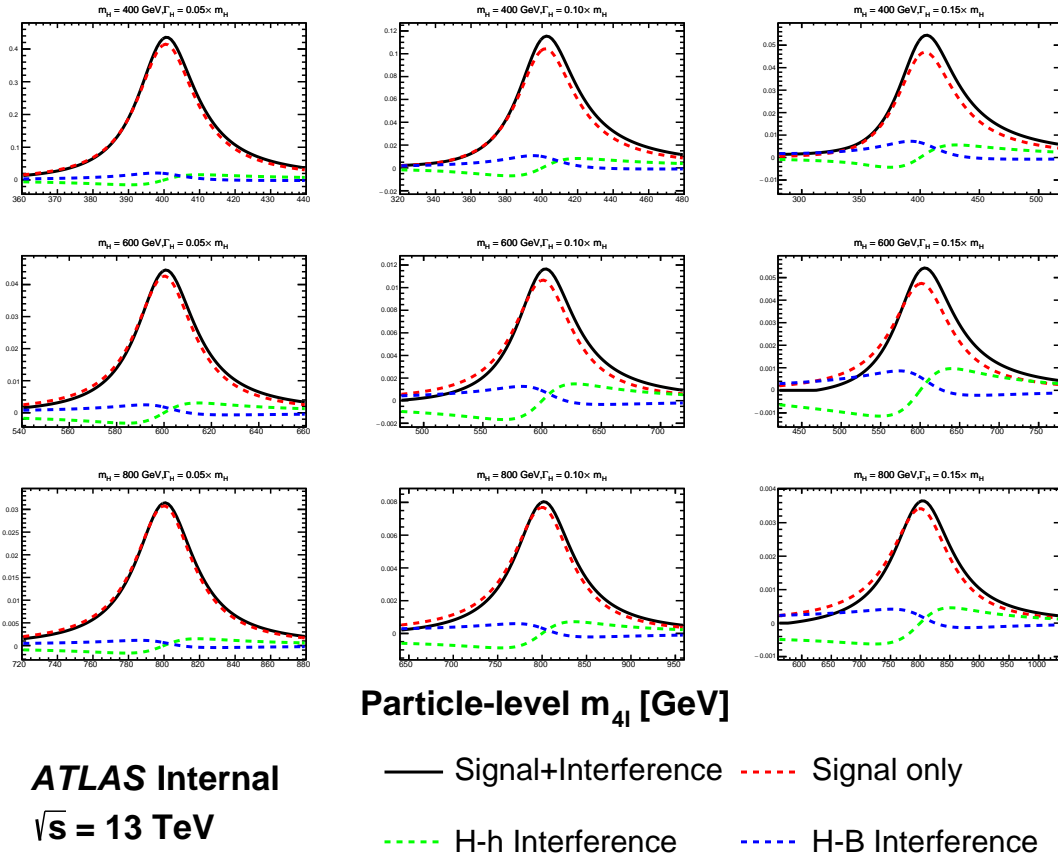


Fig. 7.22 The signal modelling for the large-width scenario at m_H of 400 GeV (top), 600 GeV (middle) and 800 GeV (bottom), as well as three different signal width: 5% (left), 10% (middle) and 15% (right). The contribution of the interference between heavy Higgs and SM Higgs (H-h) is shown together with the one between heavy Higgs and SM $gg \rightarrow ZZ$ background (H-b).

2804 the two parameters are parameterized as the function of m_H by a linear fit as shown in
 2805 figure 7.23.

2806 The final signal model is obtained by convolving the truth-level lineshape with the
 2807 detector resolution function. To verify the result, figure 7.24 compares the $m_{4\ell}$ lineshape
 2808 from parameterization with the one observed from reconstructed-level MC simulation in
 2809 $2e2\mu$ channel at masses of 600 GeV, 1600 GeV and 2000 GeV as examples.

2810 7.6 Systematic uncertainties

2811 This section describes the sources and value of theoretical and experimental system-
 2812 atic uncertainties considered in this analysis. In addition, as mentioned in previous sec-
 2813 tions, the uncertainties of irreducible background modelling, reducible background shape
 2814 smoothing procedure and signal yield difference between simulation and parameterization

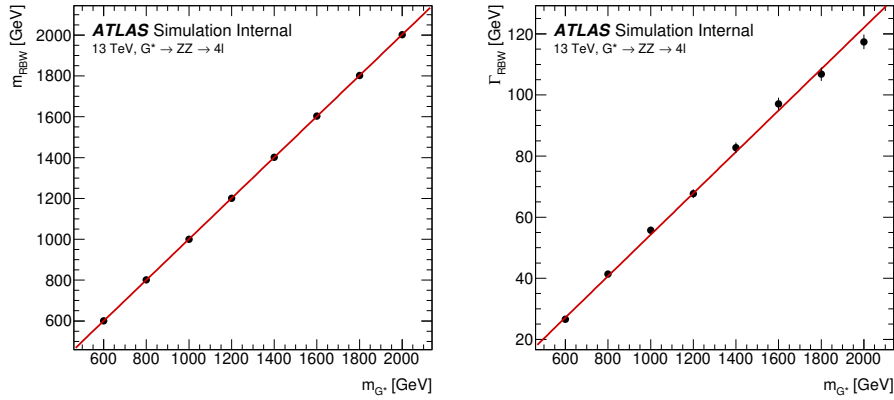


Fig. 7.23 Fitted parameters of the graviton RBW, m_{RBW} and Γ_{RBW} , as a function of the graviton resonance mass, m_G .

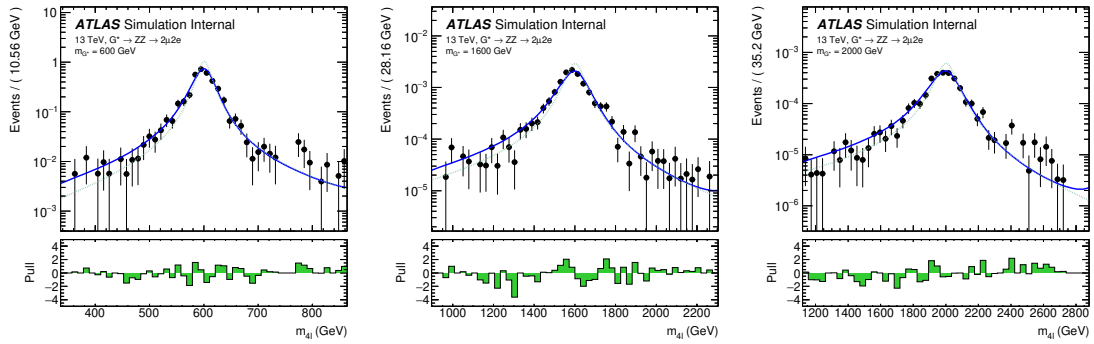


Fig. 7.24 Reconstructed m_{4l} distributions in the $2\mu 2e$ channel with the final signal model superimposed for each RS graviton signal sample at masses of 600 GeV, 1600 GeV and 2000 GeV. The lower panel in each plot shows the pull distribution. The dashed green lines show the truth-level graviton signal models for reference.

2815 are all taken into account.

2816 7.6.1 Theoretical uncertainties

2817 The theoretical modelling uncertainties include the PDF variations, missing QCD
 2818 higher-order corrections via the variations of factorisation and renormalization scales, and
 2819 the parton showering uncertainties.

2820 1. Theoretical uncertainties for signal

2821 The PDF, QCD scale and parton showering uncertainties affecting the acceptance dif-
 2822 ference originating from analysis selection for signal are taken into account in different
 2823 categories. The acceptance uncertainties are calculated on the acceptance factor which
 2824 extrapolates from the fiducial space to the full phase space by a simple ratio:

$$A = \frac{N_{fiducial}}{N_{total}} \quad (7.17)$$

For PDF uncertainties, the standard derivations of 100 PDF replicas of NNPDF3.0 NNLO, as well as comparison to two external PDF sets: MMHT2014 NNLO, CT14 NNLO are considered. For missing QCD higher-order corrections, the effects are studied with truth events by comparing weights corresponding to variations of the renormalization and factorization scale factors, up and down by a factor of two, and the envelop of different variations is used. The parton showering uncertainties are estimated by comparing events with different setting via Pythia8.

Systematic uncertainties are studied for both cut- and MVA- based event categorizations, in two different categories: the inclusive ggF-CBA-enriched and VBF-CBA-enriched category for cut-based analysis and in three different categories: inclusive ggF-MVA-high, ggF-MVA-low and VBF-MVA-enriched category for MVA-based one. This section shows the MVA-based results as an example.

Table 7.10 and 7.11 show the theoretical uncertainties mentioned above for ggF and VBF signal respectively in MVA-based categorization.

Table 7.10 Summary of acceptance uncertainties of PDF, QCD scale and parton shower variations for ggF production. The MVA-based categorization is used.

Categories	PDF	QCD Scale	Parton Shower
ggF-MVA-high	0.40%	0.06%	2.03%
ggF-MVA-low	0.56%	0.07%	4.86%
VBF-MVA-enriched	0.53%	0.09%	3.43%

Table 7.11 Summary of acceptance uncertainties of PDF, QCD scale and parton shower variations for VBF production. The MVA-based categorization is used.

Categories	PDF	QCD Scale	Parton Shower
ggF-MVA-high	0.18%	1.20%	0.41%
ggF-MVA-low	0.43%	0.26%	0.36%
VBF-MVA-enriched	0.23%	3.19%	0.85%

2. Theoretical uncertainties for SM background processes

The theoretical uncertainties of irreducible ZZ backgrounds are considered in terms of both the variations of shape of $m_{4\ell}$ distributions and the acceptance originating from the event selection.

The PDF and QCD scale uncertainties are considered by using the same method as described for signal. The parton showering uncertainties for those Sherpa samples are evaluated by varying the resummation scale by a factor of 2, changing the CKKW setting and using different showering option, following the PMG recommendation in ref.^[115], and the quadratic sum between the uncertainties in different kinds of showering option

2848 is taken as final result of uncertainties. Moreover, the shape uncertainty associated with
2849 electroweak higher-order correction for $q\bar{q} \rightarrow ZZ$ process is also taken into account.

2850 Same as for signals, these theoretical uncertainties for irreducible backgrounds are
2851 studied for both cut- and MVA- based event categorizations. The value of shape uncer-
2852 tainties vary from less than 1% at low mass region to 50% at high mass tail due to large
2853 statistic fluctuation. As for the acceptance uncertainties, the values vary from about 1%
2854 for PDF variations to 40% for parton showering variations. The VBF category has relative
2855 larger uncertainties.

2856 Table 7.12 summarizes the acceptance uncertainties of PDF, QCD scale, and parton
2857 showering variations for the dominant background: $q\bar{q} \rightarrow ZZ$.

**Table 7.12 Summary of acceptance uncertainties of PDF, scale, and parton showering varia-
tions for QCD $q\bar{q} \rightarrow ZZ$ background. The MVA-based categorization is used.**

Categories	PDF	QCD Scale	Parton showering
ggF-MVA-high	1.15%	10.16 %	3.71%
ggF-MVA-low	1.04%	3.26 %	3.80%
VBF-MVA-enriched	2.91%	27.90 %	23.82%

2858

7.6.2 Experimental systematics

2859 The signal and background predictions used in this analysis are also affected by
2860 various sources of experimental systematic uncertainties. Similar as described in sec-
2861 tion 6.5.2, the dominant experimental uncertainties in this analysis come from the en-
2862 ergy/momentum scales and reconstruction and identification efficiencies of the leptons
2863 and jets, as well as the luminosity uncertainty. The systematic uncertainties are calculated
2864 using the recommendations from the Combined Performance (CP) groups of ATLAS ex-
2865 periment. Table 7.13 summarizes the experimental systematics considered in this analysis
2866 that affect either the normalization of total event yield or the shape of $m_{4\ell}$ distribution.
2867 The impact of those systematics in statistical fit are studied in section 7.7.

2868

7.7 Results in $\ell\ell\ell'\ell'$ channel

2869 The statistical treatment in searching for heavy resonances in $ZZ \rightarrow \ell\ell\ell'\ell'$ final
2870 state is described in this section. Results are presented in both cut- and MVA- based
2871 analysis.

2872 7.7.1 Statistical procedure

2873 The upper limits on heavy resonances are obtained using the unbinned profile likelihood fits. $m_{4\ell}$ is the discriminant. The likelihood function is a product of a Poisson term
 2874 representing the probability of observing n events and a weighted sum of both signal and
 2875 background probability distribution functions (PDFs) evaluated at all observed events.

$$L(x_1..x_n|\sigma_{ggF}, \sigma_{VBF}) = \text{Pois}(n|S_{ggF} + S_{VBF} + B) \left[\prod_{i=1}^n \frac{S_{ggF}f_{ggF}(x_i) + S_{VBF}f_{VBF}(x_i) + Bf_B(x_i)}{S_{ggF} + S_{VBF} + B} \right] \quad (7.18)$$

2877 where f_X s are the probability distribution functions of signal and backgrounds modelled
 2878 in section 7.5 and 7.4, S_X and B are the normalizations of signal and sum of backgrounds.

2879 The parameters of interest (POI) in the search is σ_{ggF} (and σ_{VBF} only for NWA signal),
 2880 which is the cross section of signal model in ggF (and VBF) production mode. In the case
 2881 of there are two POIs, when testing one POI, the other one is profiled along with other
 2882 nuisance parameters (except left unconstrained) during the minimization. These POIs
 2883 enter the likelihood inside the expected signal yields S_{ggF} and S_{VBF} as:

$$S_{ggF(VBF)} = \sigma_{ggF(VBF)} \times BR(S \rightarrow ZZ) \times A \times C \times \int \mathcal{L} \quad (7.19)$$

2884 where $A \times C$ is the signal acceptance as parameterized in 7.3.4, and $\int \mathcal{L} = 139 \text{ fb}^{-1}$ is the
 2885 integrated luminosity of the dataset.

2886 The dependence of the expected number of signal and background events (normaliza-
 2887 tions) and the shape of the PDFs on the systematic uncertainties measured in section 7.6
 2888 is described by a set of nuisance parameters (NPs) θ_i . The Gaussian constraints are ap-
 2889 plied to those NPs. The constraints are implemented as additional ‘penalty’ terms added
 2890 to the likelihood which increase the negative log-likelihood when any nuisance parameter
 2891 is shifted from its nominal value. The final likelihood function $L(\sigma_{ggF}, \sigma_{VBF}, m_H, \theta_i)$ is
 2892 therefore a function of σ_{ggF} , σ_{VBF} , m_H , and θ_i .

2893 Furthermore, the normalization of SM background $pp \rightarrow ZZ$, including both $q\bar{q} \rightarrow$
 2894 ZZ and $gg \rightarrow ZZ$, is a free parameter (μ_{ZZ}) and profiled during the minimization.
 2895 Floating ZZ normalization in fit takes the advantage of reducing the dependence on the-
 2896 ory predictions and their associated uncertainties, especially given that the increased data
 2897 luminosity would provide precise determination of the SM ZZ background rate.

2898 At the end, the upper limit on production cross-section $\sigma_{ggF(VBF)}$ at a given heavy
 2899 resonance model is obtained by setting the mass of signal m_H parameter as constant at the
 2900 desired value, and maximising the likelihood function with respect to nuisance parame-
 2901 ters. The $CL_s^{[116]}$ method is used to obtain exclusion limits.

2902 7.7.2 For to likelihood function under background-only hypothesis for
2903 MVA-based analysis

2904 Both MVA- and cut-based analysis are studied by performing likelihood fit to the
2905 (pseudo-) data under the background-only hypothesis and under different signal models.
2906 Due to the same background estimation and modelling procedures, as well as the same
2907 method of systematic measurements, this section only shows the results of background-
2908 only fits for MVA-based analysis under the model of heavy Higgs resonance with narrow-
2909 width as an example. The final results of interpretation in both MVA- and cut- based
2910 analysis in all signal models described in section 7.5 will be measured in next section.

2911 First of all, table 7.14 summarized the expected and observed number of events for
2912 region of $m_{4\ell} > 200$ GeV together with their systematic uncertainties after background-
2913 only fit. The post-fit $m_{4\ell}$ spectrum in each category is shown in figure 7.25.

2914 To inspect the likelihood model, pulls and constraints as well as the correlation matrix
2915 of NPs are studied by performing a background only fit. Figure 7.26 shows the pulls and
2916 constraints when fitting to pseudo-data (top) and observed data (bottom). Figure 7.27
2917 shows the correlation matrix, only for NPs with correlation between each others greater
2918 than 0.1 when fitting to pseudo-data. The normalization of ZZ background is taken from
2919 data for one category each, as shown in table 7.15.

2920 The impact of a systematic uncertainty on the result depends on the production mode
2921 and the mass hypothesis. To check the impact of systematic uncertainties on expected sig-
2922 nal sensitivity, a NP ranking study is performed using signal injected Asimov data with
2923 the injected cross section close to 95% CLs upper limit at the masses of 400 GeV and
2924 1000 GeV. The results are shown in table 7.16. For ggF production, at lower masses, the
2925 systematic uncertainties of parton showering variation for signal, the luminosity uncer-
2926 tainty, and the parametrization of signal acceptance dominate, while at higher masses, the
2927 shape uncertainties from PDF variation for ZZ ($q\bar{q} \rightarrow ZZ$ and $gg \rightarrow ZZ$) background
2928 become important, as also seen in VBF production mode. In addition for VBF, jet related
2929 uncertainties become more important comparing to ggF production. Moreover, the domi-
2930 nate uncertainties include the acceptance uncertainty from QCD scale variation for signal
2931 and the luminosity uncertainty.

2932 7.7.3 Interpretations

2933 1. Spin-0 resonance with NWA

2934 In the absence of a specific model, the ratio of ggF and VBF production mode is un-
2935 known for this additional heavy scalar. For this reason, the fits for ggF and VBF processes

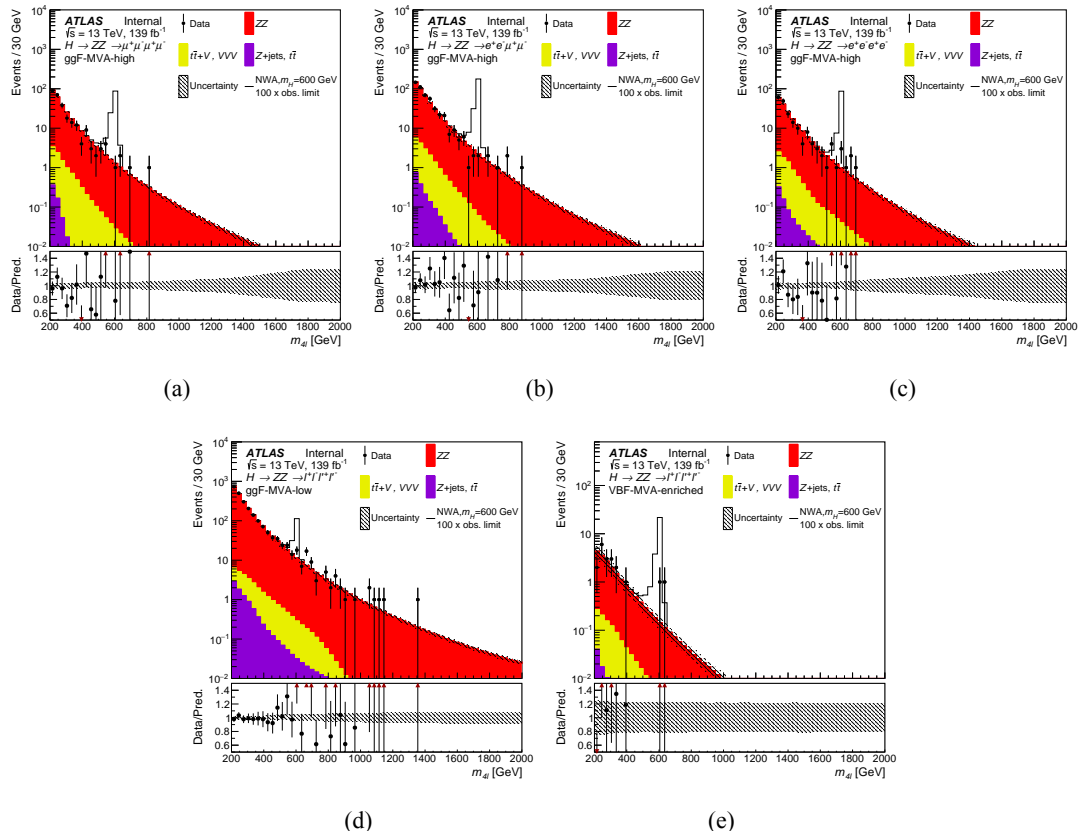


Fig. 7.25 Distribution of the four-lepton invariant mass $m_{4\ell}$ in the $\ell\ell\ell'\ell'$ search for (a), (b), (c) the ggF-MVA-high categories, (d) the ggF-MVA-low category and (e) the VBF-MVA-enriched category. The backgrounds are determined from a combined likelihood fit to the data under the background-only hypothesis. The simulated signal at 600 GeV is normalized to a cross section corresponding to one hundred times the observed upper limit given in section 7.7.3. The error bars on the data points indicate the statistical uncertainty, while the systematic uncertainty in the prediction is shown by the hatched band. The lower panels show the ratio of data to prediction.

are done separately, and in each case the cross section of the untested process is allowed to be a free parameter in the statistical fit. The observed and expected upper limit at 95% confidence level (CL) on the $\sigma \times BR(H \rightarrow ZZ)$ of a narrow scalar resonance for both ggF (left) and VBF (right) production mode with the integrated luminosity of 139 fb^{-1} is shown in figure 7.28 (7.29) for MVA- (cut-) based analysis. No excess over 2σ is found.

2. Spin-0 resonance with LWA

In the case of LWA model, only ggF production mode is studied. The interference between the heavy scalar and SM Higgs boson ($H-h$), as well as the heavy scalar and SM $gg \rightarrow ZZ$ continuum background ($H-B$) as modelled in section 7.5.3 are taken into account. The upper limit at 95% confidence level (CL) on ggF cross section times branch ratio ($\sigma_{ggF} \times BR(H \rightarrow ZZ)$) is shown in figure 7.30 for a width of 1, 5, 10 and 15% of

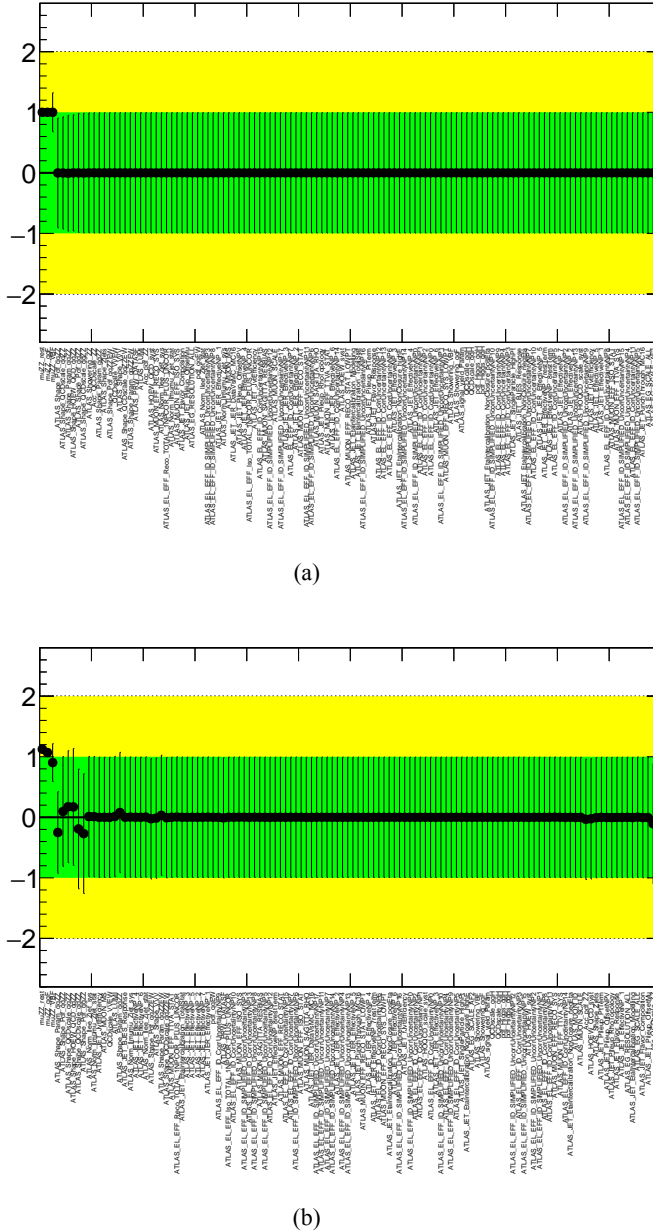
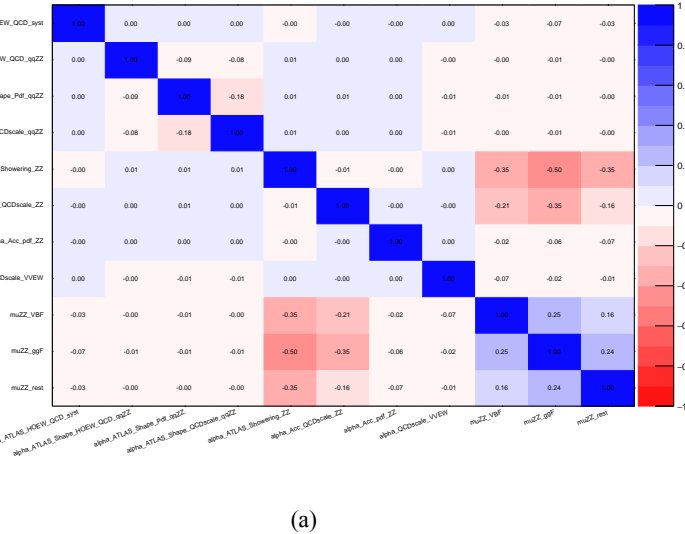


Fig. 7.26 Pulls and constraints of nuisance parameters after a background only fit to (a) Asimov data and (b) observed data in the $\ell\ell\ell'\ell'$ channel. The Asimov data is generated with background data only, and the observed data includes datasets from 2015 to 2018.

2947 m_H .

2948 3. Spin-2 RS Graviton resonance

2949 The observed and expected 95% upper limit on the cross section times branching ratio
 2950 for RS Graviton (RSG) scenario is shown in figure 7.31. Same as LWA case, only $4e$,
 2951 4μ and $2e2\mu$ channel of ggF production mode are used. On top of the expected and
 2952 observed upper limits in this model, a predicted cross section as function of mass provided
 2953 by theorist is also shown in the figure. Comparing with the observed result provided by
 2954 $ZZ \rightarrow \ell\ell\ell'\ell'$ decay, this spin-2 graviton is excluded up to a mass of 1500 GeV.



(a)

Fig. 7.27 Correlation of nuisance parameters after a background only fit to Asimov data in the $\ell\ell\ell'\ell'$ channel. The Asimov data is generated with background data only.

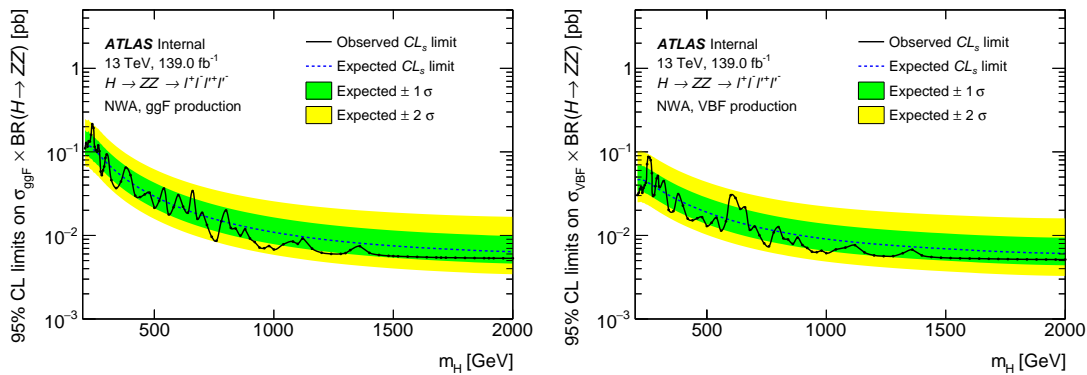


Fig. 7.28 The expected and observed upper limits at 95% CL on $\sigma \times BR(H \rightarrow ZZ)$ using the MVA-based analysis for ggF (left) and VBF (right) production. The green and yellow bands represent the $\pm 1\sigma$ and $\pm 2\sigma$ uncertainties in the expected limits.

4. Summary of interpretation

As a summary, figure 7.32 shows the comparison of expected and observed 95% CL upper limits between different models described above.

Figure 7.33 compares the expected 95% CL upper limits as a function of the NWA resonance mass in this analysis with full run-2 data and the one in previous publication^[117] with the integrated luminosity of 36.1 fb^{-1} . With a significant increase of integrated luminosity and an improved analysis strategy, comparing to the previous publication, the expected sensitivities of searching for narrow-width heavy resonance reduce by up to 70% in MVA-based analysis, where 50% of reduction is due to luminosity increase while other improvement mainly comes from inviting multivariate method.

Figure 7.34 shows the display of one candidate event passing analysis selection in

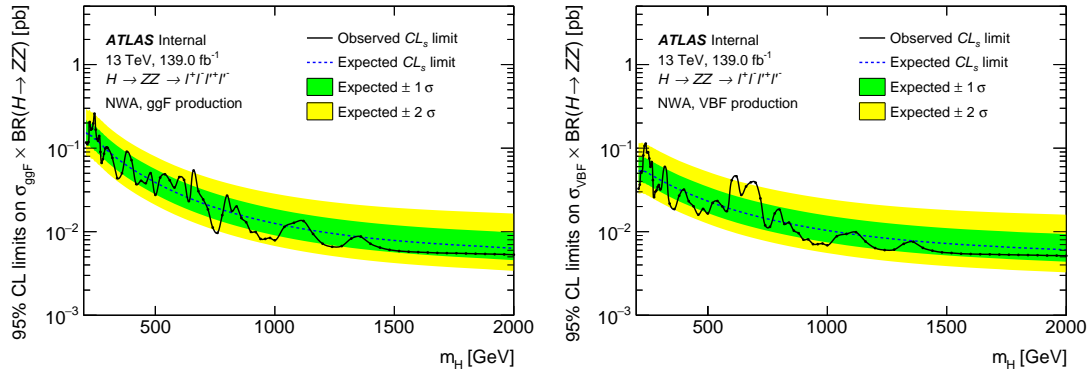


Fig. 7.29 The expected and observed upper limits at 95% CL on $\sigma \times BR(H \rightarrow ZZ)$ using the cut-based analysis for ggF (left) and VBF (right) production. The green and yellow bands represent the $\pm 1\sigma$ and $\pm 2\sigma$ uncertainties in the expected limits.

2966 four-muon final state with four-muon invariant mass of 1.34 TeV.

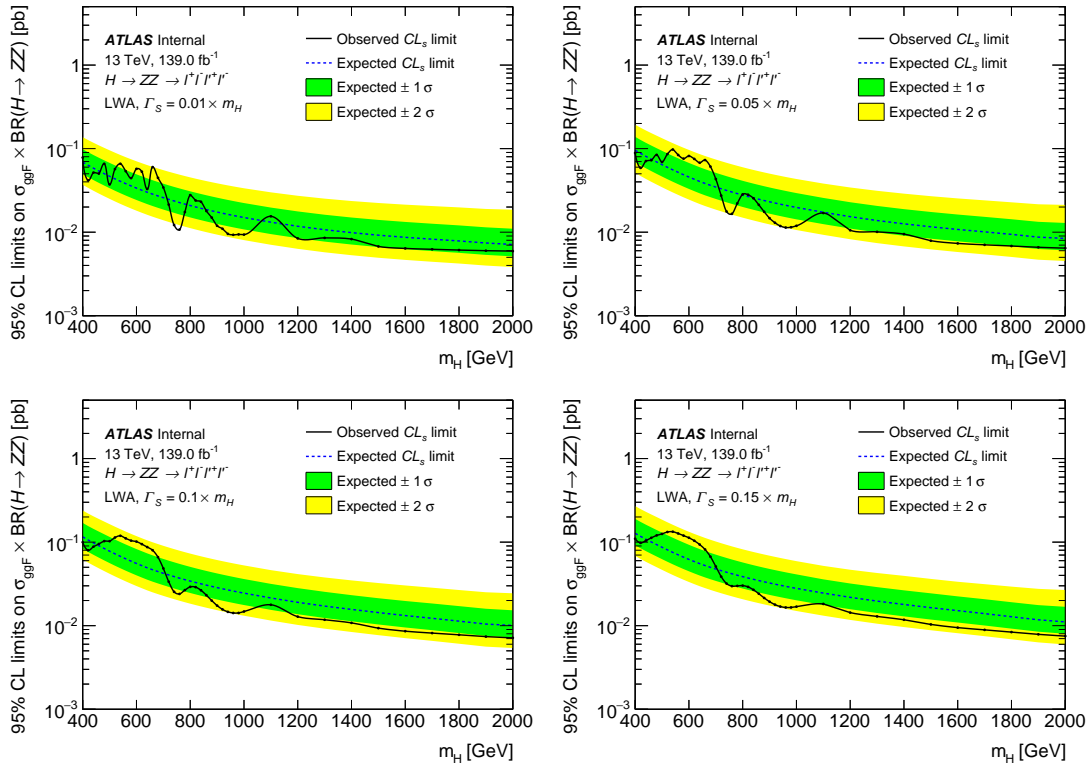


Fig. 7.30 The upper limits at 95% confidence level on $\sigma_{ggF} \times BR(H \rightarrow ZZ)$ as a function of the heavy resonance mass m_H for the ggF production mode with an intrinsic width of 1% (top left), 5% (top right), 10% (bottom left) and 15% (bottom right) for both the case where interference with Standard Model processes is considered. The green and yellow bands represent the $\pm 1 \sigma$ and $\pm 2 \sigma$ uncertainties in the expected limits.

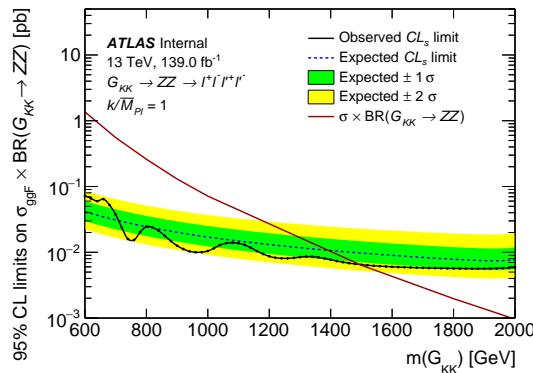


Fig. 7.31 The upper limits at 95% confidence level on $\sigma_{ggF} \times BR(G_{KK} \rightarrow ZZ)$ as a function of the heavy resonance mass $m(G_{KK})$ for the ggF production mode in RS Graviton model. The green and yellow bands represent the $\pm 1 \sigma$ and $\pm 2 \sigma$ uncertainties in the expected limits.

Table 7.13 A list of the experimental systematics considered in this analysis. The NPs have been separated by whether they only affect the normalisation (left column) or if they affect the shape (right column) of the $m_{4\ell}$ distribution. They are further subdivided into the primary objects that they affect.

Normalisation NPs	Shape NPs
Electrons	
EL_EFF_ID_CorrUncertaintyNP[0-15]	EG_RESOLUTION_ALL
EL_EFF_ID_SIMPLIFIED_UncorrUncertaintyNP[0-17]	EG_SCALE_ALLCORR
EL_EFF_Iso_TOTAL_1NPCOR_PLUS_UNCOR	EG_SCALE_E4SCINTILLATOR
EL_EFF_Reco_TOTAL_1NPCOR_PLUS_UNCOR	EG_SCALE_LARCALIB_EXTRA2015PRE EG_SCALE_LARTEMPERATURE_EXTRA2015PRE EG_SCALE_LARTEMPERATURE_EXTRA2016PRE
Muons	
MUON_EFF_ISO_STAT	MUON_ID
MUON_EFF_ISO_SYS	MUON_MS
MUON_EFF_RECO_STAT	MUON_SAGITTA_RESBIAS
MUON_EFF_RECO_STAT_LOWPT	MUON_SAGITTA_RHO
MUON_EFF_RECO_SYS	MUON_SCALE
MUON_EFF_RECO_SYS_LOWPT	
MUON_EFF_TTVA_STAT	
MUON_EFF_TTVA_SYS	
Jets	
	JET_BJES_Response JET_EffectiveNP_[1-7] JET_EffectiveNP_8restTerm JET_EtaIntercalibration_Modelling JET_EtaIntercalibration_NonClosure_highE JET_EtaIntercalibration_NonClosure_negEta JET_EtaIntercalibration_NonClosure_posEta JET_EtaIntercalibration_TotalStat JET_Flavor_Composition JET_Flavor_Response JET_JER_DataVsMC JET_JER_EffectiveNP_[1-6] JET_JER_EffectiveNP_7restTerm JET_Pileup_OffsetMu JET_Pileup_OffsetNPV JET_Pileup_PtTerm JET_Pileup_RhoTopology JET_PunchThrough_MC16 JET_SingleParticle_HighPt
Other	
HOEW_QCD_syst	
HOEW_syst	
HOQCD_scale_syst	
PRW_DATASF	

Table 7.14 Expected and observed numbers of events for $m_{4\ell} > 200$ GeV, together with their systematic uncertainties, for three MVA-based categories. The expected number of events, as well as their uncertainties, are obtained from a likelihood fit to the data under the background-only hypothesis. The uncertainties of the ZZ normalisation factors, presented in table 7.15, are also taken into account.

Process	VBF-enriched category	ggF-enriched categories			the “rest” category
		4 μ channel	2e2 μ channel	4e channel	
$q\bar{q} \rightarrow ZZ$	11 ± 4	232 ± 10	389 ± 17	154 ± 7	2008 ± 47
$gg \rightarrow ZZ$	3 ± 2	37 ± 6	64 ± 10	26 ± 4	247 ± 19
ZZ (EW)	4.1 ± 0.4	4.5 ± 0.2	7.5 ± 0.4	3 ± 0.2	14.3 ± 0.7
$Z+jets, t\bar{t}$	0.08 ± 0.02	0.6 ± 0.1	1.7 ± 0.4	0.8 ± 0.1	8.8 ± 2.1
$t\bar{t}V, VVV$	0.97 ± 0.1	9.8 ± 0.2	17.5 ± 0.4	7.8 ± 0.2	21.9 ± 0.5
Total background	19 ± 4.5	285 ± 11.7	479 ± 19.7	192 ± 8.1	2301 ± 50.7
Observed	19	271	493	191	2301

Table 7.15 ZZ normalization factor in each category, obtained from a likelihood fit to the data under the background-only hypothesis.

Normalization factor	Fitted value
$\mu_{ZZ}^{ggF-MVA-high}$	1.07 ± 0.047
$\mu_{ZZ}^{ggF-MVA-low}$	1.12 ± 0.026
$\mu_{ZZ}^{VBF-MVA-enriched}$	0.91 ± 0.314

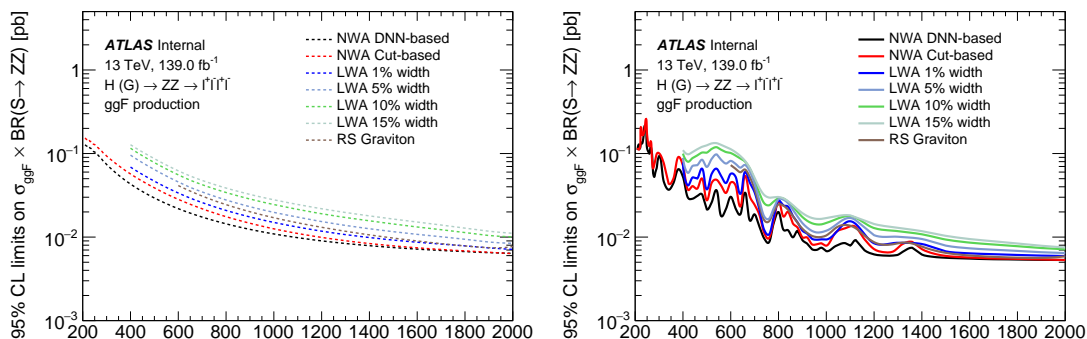


Fig. 7.32 The expected (left) and observed (right) upper limits at 95% confidence level on $\sigma \times BR(S \rightarrow ZZ)$ for ggF production mode at different assumptions.

Table 7.16 Impact of the leading systematic uncertainties, the data statistic uncertainties, as well as the total uncertainties on the predicted signal event yield with the cross section times branching ratio being set to the expected upper limit, expressed as a percentage of the signal yield for the ggF (left) and VBF (right) production modes at $m_H = 400$ and 1000 GeV.

ggF production		VBF production	
Systematic source	Impact [%]	Systematic source	Impact [%]
$m_H = 400$ GeV			
Parton showering of ggF	2.3	QCD scale of VBF	2.7
Luminosity	1.8	Jet flavor composition	2.5
PDF of $q\bar{q} \rightarrow ZZ$	1.6	Luminosity	1.8
Signal yield parameterization	1.4	Jet energy scale (in-su calibration)	1.6
Data stat. uncertainty	48	Data stat. uncertainty	57
Total Uncertainty	49	Total Uncertainty	58
$m_H = 1000$ GeV			
PDF of $q\bar{q} \rightarrow ZZ$	2.5	QCD scale of VBF	2.3
Parton showering of ggF	2.4	PDF of $q\bar{q} \rightarrow ZZ$	2.2
PDF of $gg \rightarrow ZZ$	1.9	Luminosity	1.8
Luminosity	1.8	PDF of $gg \rightarrow ZZ$	1.6
Data stat. uncertainty	84	Data stat. uncertainty	92
Total Uncertainty	86	Total Uncertainty	93

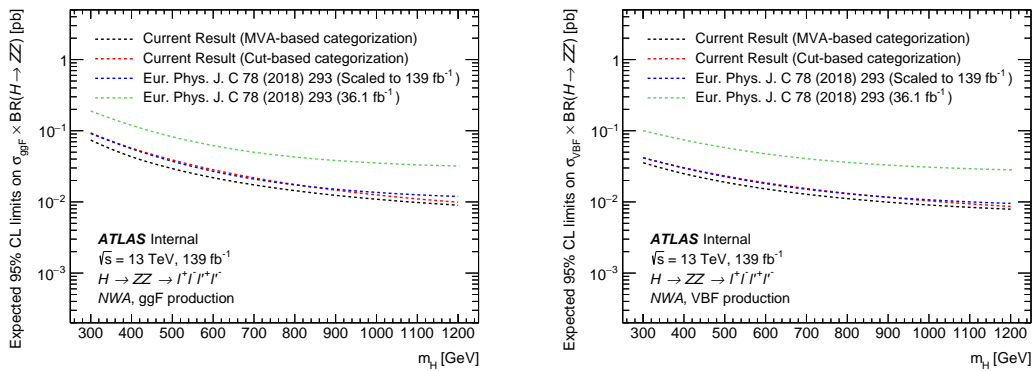


Fig. 7.33 Comparisons of the expected upper limits at 95% CL on the cross section times branching ratio as a function of the heavy resonance mass m_H for the ggF production mode (left) and for the VBF production mode (right) in the case of the NWA. The expected limits from the previous publication are shown in the green dashed line and are projected to the 139 fb^{-1} as shown in the blue dashed line. In addition, the current results based on either cut-based categorisation or the multivariate-based categorisation are shown in red and black lines.

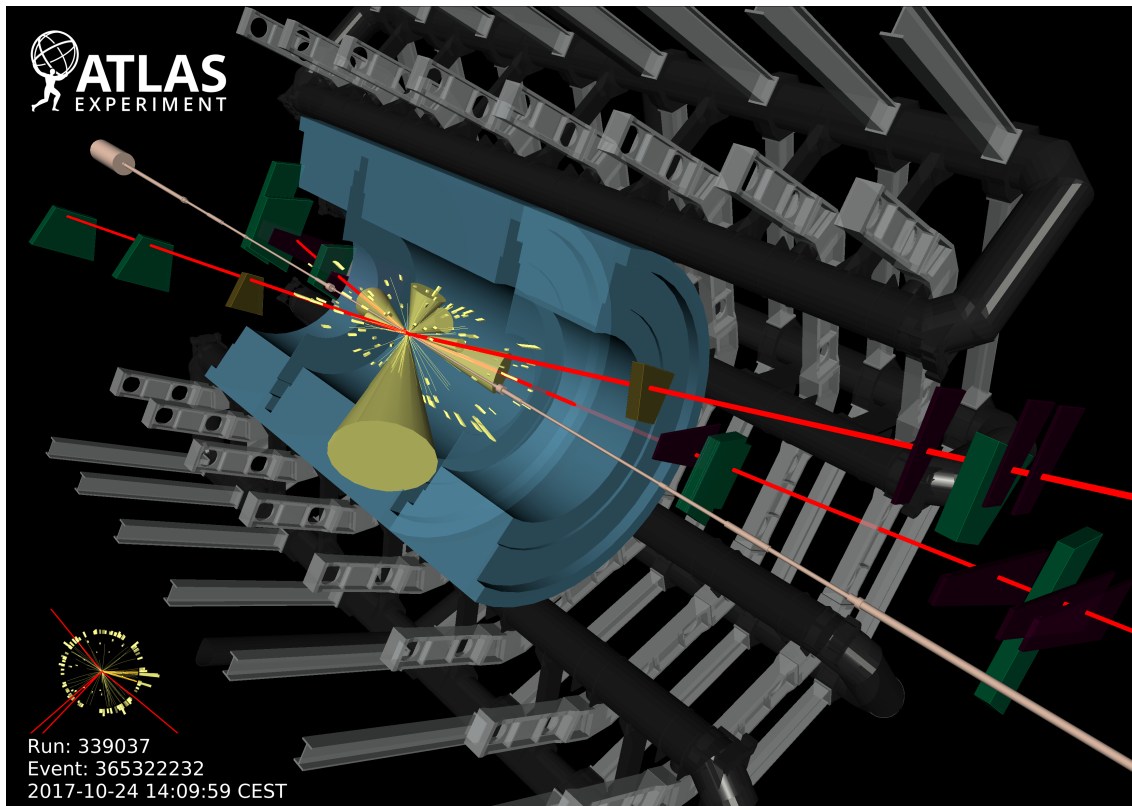


Fig. 7.34 Display of one candidate event in 4μ final state with the mass of 1.35 TeV.

2967 7.8 Conclusion

2968 Searches of heavy resonances decaying into a pair of Z boson to $\ell\ell\ell'\ell'$ final state
2969 are performed using 139 fb^{-1} of 13 TeV pp collision data collected by ATLAS experiment
2970 at the LHC. The results are interpreted as 95% CL upper limits on the production cross
2971 section of a spin-0 and spin-2 resonances under different theoretical models. The search
2972 range of the hypothetical resonances is between 200 GeV to 2000 GeV depending on the
2973 signal model.

2974 The spin-0 resonance is assumed to be a heavy Higgs like scalar produced predom-
2975 inantly from gluon–gluon fusion (ggF) and vector-boson fusion (VBF) decays, and it is
2976 studied under both the narrow-width approximation and with the large-width assumption.
2977 For narrow-width approximation, limits on cross section of heavy scalar decaying into
2978 two Z bosons are set separately for ggF and VBF production modes, under DNN- and
2979 cut- based analysis. In DNN-based analysis, the 95% CL upper limit range is from 215 fb
2980 at $m_H = 240 \text{ GeV}$ to 5.3 fb at $m_H = 2000 \text{ GeV}$ for ggF production mode, and from 87 fb
2981 at $m_H = 255 \text{ GeV}$ to 5.1 fb at $m_H = 1960 \text{ GeV}$ for VBF production mode. In cut-based
2982 analysis, the 95% CL upper limit range is from 259 fb at $m_H = 245 \text{ GeV}$ to 5.3 fb at
2983 $m_H = 2000 \text{ GeV}$ for ggF production mode, and from 113 fb at $m_H = 240 \text{ GeV}$ to 5.1 fb
2984 at $m_H = 2000 \text{ GeV}$ for VBF production mode. DNN-based analysis gains about 20% im-
2985 provement on upper limits at lower mass region comparing to the cut-based analysis, while
2986 for mass above 1500 GeV, both analyses perform closely. For large-width approximation,
2987 limits are studied on ggF production rate at four different widths assumptions: 1%, 5%,
2988 10% and 15% of resonance’s mass, with the interference between the heavy scalar and the
2989 SM Higgs boson as well as the heavy scalar and the SM $gg \rightarrow ZZ$ continuum background
2990 taken into account. The maximum and minimum of upper limits are obtained as 78 fb at
2991 $m_H = 400 \text{ GeV}$ to 5.9 fb at $m_H = 2000 \text{ GeV}$ for 1% width; 98 fb at $m_H = 540 \text{ GeV}$ to 6.4
2992 fb at $m_H = 2000 \text{ GeV}$ for 5% width; 119 fb at $m_H = 540 \text{ GeV}$ to 7.1 fb at $m_H = 2000 \text{ GeV}$
2993 for 10% width; 133 fb at $m_H = 540 \text{ GeV}$ to 7.5 fb at $m_H = 2000 \text{ GeV}$ for 15% width.
2994 Last but not least, the framework of the Randall–Sundrum model with a graviton excita-
2995 tion spin-2 resonance with $m(G_{KK}) < 1500 \text{ GeV}$ is excluded at 95% CL.

2996

Chapter 8 Summary

2997 On December 3rd, 2018, the LHC finished its second run (run-2) after three fantastic
2998 years. Thanks to run-2 with largely increased statistic, we now know the masses of the
2999 Higgs boson, top quark and W boson to considerably greater precision. And also confirm
3000 the Standard Model as a stable theory.

3001 In this dissertation, various physics processes in $ZZ \rightarrow \ell\ell\ell'\ell'$ final state are studied,
3002 taking the advantage of full run-2 pp collision data in the LHC. Using this signature,
3003 we measured the fiducial cross section of ZZ production to $\ell\ell\ell'\ell' jj$ channel in SM,
3004 which is an important physics process and major background in many analysis with ZZ
3005 production, eg. Higgs analysis (HZZ). In addition, we searched the electroweak ZZ
3006 production via vector boson scattering in associated with 2-jet process in $\ell\ell\ell'\ell'$ final
3007 state. In the meantime, the searches of heavy resonances decaying into a pair of Z bosons
3008 to $\ell\ell\ell'\ell'$ final state for several different hypothetical resonances are conducted in this
3009 dissertation. The results of several analyses are summarized as below:

3010 **Measurement of fiducial cross section of ZZ production in $\ell\ell\ell'\ell' jj$ final state**

3011 The fiducial cross section of inclusive SM $ZZ \rightarrow \ell\ell\ell'\ell'$ production is measured to
3012 be:

$$\sigma_{ZZ \rightarrow \ell\ell\ell'\ell'}^{fid} = 1.27 \pm 0.12(stat) \pm 0.02(theo) \pm 0.07(exp) \pm 0.01(bkg) \pm 0.03(lumi) \quad (8.1)$$

3013 which is found to be compatible with the SM prediction. The ZZ cross section is calcu-
3014 lated with up to one (three) outgoing partons at NLO (LO) using Sherpa 2.2.2 for QCD
3015 production, and in LO using MadGraph5_aMC@NLO 2.6.1 for EW production. The to-
3016 tal uncertainty is 11%, the analysis is still data static dominant (data statistic uncertainty
3017 is about 9.5%).

3018 **Observation of electroweak ZZ production in $\ell\ell\ell'\ell' jj$ final state**

3019 Thanks to the largely increased data statistic collected by ATLAS experiment in the
3020 LHC run-2, the electroweak ZZ production (EW- $ZZjj$) to $\ell\ell\ell'\ell'$ channel in associa-
3021 tion with two jets is observed with a significant deviation from the background-only
3022 hypothesis. The signal strength of EW- $ZZjj$ production, the normalization of QCD-
3023 $ZZjj$ production, as well as the observed and expected statistical significance measured

3024 in $\ell\ell\ell'\ell' jj$ channel are found to be:

$$\begin{aligned}\mu_{\text{EW}} &= 1.54 \pm 0.42 \\ \mu_{\text{QCD}} &= 0.95 \pm 0.22\end{aligned}\quad (8.2)$$

Obs. (Exp.) Significance = 5.48 (3.90) σ

3025 Then in this dissertation, the differential cross section and expected significance of
 3026 EW- $ZZjj$ production, using 3000 fb^{-1} simulated pp collision data at a centre-of-mass
 3027 energy of 14 TeV to be recorded by ATLAS experiment at the HL-LHC, are studied via
 3028 simulations. The HL-LHC will for sure give us more opportunity to probe rare process
 3029 like $ZZ \rightarrow \ell\ell\ell'\ell'$ in the future.

3030 Searches of heavy ZZ resonances in $\ell\ell\ell'\ell'$ final state

3031 Searches of heavy ZZ resonances are performed in four-lepton invariant mass $m_{4\ell}$
 3032 range from 200 GeV to 2000 GeV. Data are found to agree with the background-only
 3033 hypothesis, and 95% CL upper limits are set on the production rate under the models of:

- Spin-0 heavy Higgs under narrow-width approximation (NWA).

3035 Search range is from 200 GeV to 2000 GeV.

3036 In DNN-based analysis, the limits are range from 215 fb at $m_H = 240$ GeV to 5.3
 3037 fb at $m_H = 2000$ GeV for ggF production mode, and from 87 fb at $m_H = 255$ GeV
 3038 to 5.1 fb at $m_H = 1960$ GeV for VBF production mode.

3039 The DNN-based analysis is found to be at most 20% better than cut-based results.

- Spin-0 heavy Higgs under large-width approximation (LWA) with the width of 1,
 3041 5, 10, 15% of its mass.

3042 Search range is from 400 GeV to 2000 GeV, and only ggF production is studied.

3043 The maximum and minimum of upper limits are obtained as 78 fb at $m_H = 400$ GeV
 3044 to 5.9 fb at $m_H = 2000$ GeV for 1% width; 98 fb at $m_H = 540$ GeV to 6.4 fb at $m_H =$
 3045 2000 GeV for 5% width; 119 fb at $m_H = 540$ GeV to 7.1 fb at $m_H = 2000$ GeV for
 3046 10% width; 133 fb at $m_H = 540$ GeV to 7.5 fb at $m_H = 2000$ GeV for 15% width.

- Spin-2 graviton excitation under the Randall–Sundrum model.

3048 Search range is from 600 GeV to 2000 GeV, and only ggF production is studied.

3049 The maximum and minimum of limits are 73 fb at $m_H = 600$ GeV and 5.6 fb
 3050 at $m_H = 1880$ GeV for ggF production mode. And the mass of graviton below
 3051 1500 GeV is excluded comparing the observed results with theoretical prediction.

3053 In summary, the $ZZ \rightarrow \ell\ell\ell'\ell'$ production presented in this dissertation are consis-
 3054 tent with SM prediction. This result completes the observation of weak boson scattering

3055 for massive bosons, which is a new milestone reached in the study of electroweak sym-
3056 metry breaking. In the meantime, no indication of new physics is observed. We are
3057 looking forward the HL-LHC, with greatly increased luminosity and higher centre-of-
3058 mass energy, which should enhance the sensitivity for new physics search and precise
3059 measurement for rare process like $\ell\ell\ell'\ell'$ final state.

3060

Bibliography

- 3061 [1] LANGACKER P. Introduction to the Standard Model and Electroweak Physics[C/OL]//
3062 Proceedings of Theoretical Advanced Study Institute in Elementary Particle Physics on The
3063 dawn of the LHC era (TASI 2008): Boulder, USA, June 2-27, 2008. 2010: 3-48. DOI:
3064 [10.1142/9789812838360_0001](https://doi.org/10.1142/9789812838360_0001).
- 3065 [2] PICH A. Electroweak Symmetry Breaking and the Higgs Boson[J/OL]. Acta Phys. Polon.,
3066 2016, B47:151. DOI: [10.5506/APhysPolB.47.151](https://doi.org/10.5506/APhysPolB.47.151).
- 3067 [3] Observation of a new particle in the search for the standard model higgs boson with the atlas
3068 detector at the lhc[J/OL]. Physics Letters B, 2012, 716(1):1 - 29. <http://www.sciencedirect.com/science/article/pii/S037026931200857X>. DOI: <https://doi.org/10.1016/j.physletb.2012.08.020>.
- 3070 [4] Observation of a new boson at a mass of 125 gev with the cms experiment at the lhc[J/OL].
3071 Physics Letters B, 2012, 716(1):30 - 61. <http://www.sciencedirect.com/science/article/pii/S0370269312008581>. DOI: <https://doi.org/10.1016/j.physletb.2012.08.021>.
- 3073 [5] PROFUMO S, RAMSEY-MUSOLF M J, SHAUGHNESSY G. Singlet higgs phenomenology
3074 and the electroweak phase transition[J/OL]. Journal of High Energy Physics, 2007, 2007(08):
3075 010-010. <https://doi.org/10.1088%2F1126-6708%2F2007%2F08%2F010>. DOI: [10.1088/1126-6708/2007/08/010](https://doi.org/10.1088/1126-6708/2007/08/010).
- 3077 [6] BRANCO G, FERREIRA P, LAVOURA L, et al. Theory and phenomenology of two-higgs-
3078 doublet models[J/OL]. Physics Reports, 2012, 516(1):1 - 102. <http://www.sciencedirect.com/science/article/pii/S0370157312000695>. DOI: <https://doi.org/10.1016/j.physrep.2012.02.002>.
- 3080 [7] DREMIN I M. Soft and hard processes in QCD[J/OL]. JETP Lett., 2005, 81:307-310. DOI:
3081 [10.1134/I.1944068](https://doi.org/10.1134/I.1944068).
- 3082 [8] WOMERSLEY J. QCD at the Tevatron: Status and prospects[C/OL]//Proceedings, 5th Inter-
3083 national Symposium on Radiative Corrections - RADCOR 2000. 2000. <http://www.slac.stanford.edu/econf/C000911/>.
- 3085 [9] LIN H W, et al. Parton distributions and lattice QCD calculations: a community white paper
3086 [J/OL]. Prog. Part. Nucl. Phys., 2018, 100:107-160. DOI: [10.1016/j.ppnp.2018.01.007](https://doi.org/10.1016/j.ppnp.2018.01.007).
- 3087 [10] COLLINS J C, SOPER D E, STERMAN G F. Factorization of Hard Processes in QCD[J/OL].
3088 Adv. Ser. Direct. High Energy Phys., 1989, 5:1-91. DOI: [10.1142/9789814503266_0001](https://doi.org/10.1142/9789814503266_0001).
- 3089 [11] STIRLING W J. Perturbative QCD[J/OL]. 2000(CERN-OPEN-2000-296):40 p. <https://cds.cern.ch/record/1194745>. DOI: [10.5170/CERN-2000-007.305](https://doi.org/10.5170/CERN-2000-007.305).
- 3091 [12] GROJEAN C. Higgs Physics[J/OL]. 2017(arXiv:1708.00794):143-158. 12 p. <https://cds.cern.ch/record/2243593>. DOI: [10.5170/CERN-2016-005.143](https://doi.org/10.5170/CERN-2016-005.143).

- 3093 [13] Cern yellow reports: Monographs: Handbook of LHC Higgs Cross Sections: 4. Deciphering
3094 the Nature of the Higgs Sector[M/OL]. 2016. <https://cds.cern.ch/record/2227475>. DOI: [10.23731/CYRM-2017-002](https://doi.org/10.23731/CYRM-2017-002).
- 3096 [14] HEINEMEYER S. Cern yellow reports: Monographs: Handbook of LHC Higgs Cross Sec-
3097 tions: 3. Higgs Properties: Report of the LHC Higgs Cross Section Working Group[M/OL].
3098 2013. <https://cds.cern.ch/record/1559921>. DOI: [10.5170/CERN-2013-004](https://doi.org/10.5170/CERN-2013-004).
- 3099 [15] CHANG J, CHEUNG K, LU C T, et al. *ww* scattering in the era of post-higgs-boson discovery
3100 [J/OL]. Phys. Rev. D, 2013, 87:093005. <https://link.aps.org/doi/10.1103/PhysRevD.87.093005>.
- 3101 [16] BRUNING O S, COLLIER P, LEBRUN P, et al. LHC Design Report Vol.1: The LHC Main
3102 Ring[J]. 2004.
- 3103 [17] BUNING O, COLLIER P, LEBRUN P, et al. LHC Design Report. 2. The LHC infrastructure
3104 and general services[J]. 2004.
- 3105 [18] BENEDIKT M, COLLIER P, MERTENS V, et al. LHC Design Report. 3. The LHC injector
3106 chain[J]. 2004.
- 3107 [19] EVANS L, BRYANT P. LHC machine[J/OL]. Journal of Instrumentation, 2008, 3(08):S08001-
3108 S08001. <https://doi.org/10.1088%2F1748-0221%2F3%2F08%2Fs08001>. DOI: [10.1088/1748-0221/3/08/s08001](https://doi.org/10.1088/1748-0221/3/08/s08001).
- 3110 [20] MOBS E. The CERN accelerator complex. Complexe des accélérateurs du CERN[J/OL]. 2016.
3111 <https://cds.cern.ch/record/2197559>.
- 3112 [21] COLLABORATION A. The ATLAS experiment at the CERN large hadron collider[J/OL].
3113 Journal of Instrumentation, 2008, 3(08):S08003-S08003. <https://doi.org/10.1088%2F1748-0221%2F3%2F08%2Fs08003>. DOI: [10.1088/1748-0221/3/08/s08003](https://doi.org/10.1088/1748-0221/3/08/s08003).
- 3115 [22] PEREZ G. Unitarization models for vector boson scattering at the lhc[D/OL]. 2018. DOI:
3116 [10.5445/IR/1000082199](https://doi.org/10.5445/IR/1000082199).
- 3117 [23] PEQUENAO J. Computer generated image of the whole ATLAS detector[Z/OL]. 2008. <https://cds.cern.ch/record/1095924>.
- 3119 [24] MCFAYDEN J. The lhc and atlas detector. in: Third generation susy and $t^-t^+ + z$ productin.
3120 [D/OL]. 2014. DOI: [10.1007/978-3-319-07191-6_2](https://doi.org/10.1007/978-3-319-07191-6_2).
- 3121 [25] COLLABRATION A. Operation and performance of the ATLAS semiconductor tracker. Op-
3122 eration and performance of the ATLAS semiconductor tracker[J/OL]. JINST, 2014, 9(CERN-
3123 PH-EP-2014-049. CERN-PH-EP-2014-049):P08009. 80 p. <https://cds.cern.ch/record/1698966>.
3124 DOI: [10.1088/1748-0221/9/08/P08009](https://doi.org/10.1088/1748-0221/9/08/P08009).
- 3125 [26] ATLAS pixel detector electronics and sensors[J/OL]. Journal of Instrumentation, 2008, 3(07):
3126 P07007-P07007. <https://doi.org/10.1088%2F1748-0221%2F3%2F07%2Fp07007>. DOI: [10.1088/1748-0221/3/07/p07007](https://doi.org/10.1088/1748-0221/3/07/p07007).

Bibliography

- 3128 [27] MULLIER G. The upgraded pixel detector of the atlas experiment for run-2 at the large hadron
3129 collider[J/OL]. Journal of Instrumentation, 2016, 11:C02061-C02061. DOI: [10.1088/1748-0221/11/02/C02061](https://doi.org/10.1088/1748-0221/11/02/C02061).
- 3131 [28] The silicon microstrip sensors of the atlas semiconductor tracker[J/OL]. Nuclear Instruments
3132 and Methods in Physics Research Section A: Accelerators, Spectrometers, Detectors and Asso-
3133 ciated Equipment, 2007, 578(1):98 - 118. <http://www.sciencedirect.com/science/article/pii/S0168900207007644>. DOI: <https://doi.org/10.1016/j.nima.2007.04.157>.
- 3135 [29] SULTAN D M S. Development of small-pitch, thin 3d sensors for pixel detector upgrades at
3136 hl-lhc[D/OL]. 2017. DOI: [10.13140/RG.2.2.36253.82403/1](https://doi.org/10.13140/RG.2.2.36253.82403/1).
- 3137 [30] The ATLAS transition radiation tracker (TRT) proportional drift tube: design and performance
3138 [J/OL]. Journal of Instrumentation, 2008, 3(02):P02013-P02013. <https://doi.org/10.1088%2F1748-0221%2F3%2F02%2Fp02013>. DOI: [10.1088/1748-0221/3/02/p02013](https://doi.org/10.1088/1748-0221/3/02/p02013).
- 3140 [31] BUCHANAN N, CHEN L, GINGRICH D, et al. Design and implementation of the front end
3141 board for the readout of the atlas liquid argon calorimeters[J/OL]. Journal of Instrumentation,
3142 2008, 3:P03004. DOI: [10.1088/1748-0221/3/03/P03004](https://doi.org/10.1088/1748-0221/3/03/P03004).
- 3143 [32] Technical design report atlas: ATLAS liquid-argon calorimeter: Technical Design Report
3144 [M/OL]. Geneva: CERN, 1996. <https://cds.cern.ch/record/331061>.
- 3145 [33] AAD G, ABBOTT B, ABDALLAH J, et al. Readiness of the atlas tile calorimeter for lhc
3146 collisions[J]. European Physical Journal C, 2010.
- 3147 [34] Technical design report atlas: ATLAS muon spectrometer: Technical Design Report[M/OL].
3148 Geneva: CERN, 1997. <https://cds.cern.ch/record/331068>.
- 3149 [35] SLIWA K. "ATLAS Overview and Main Results"[C]//Proceedings, International School on
3150 High Energy Physics : Workshop on High Energy Physics in the near Future. (LISHEP 2013):
3151 Rio de Janeiro, Brazil, March 17-24, 2013. 2013.
- 3152 [36] RUIZ-MARTINEZ A, COLLABORATION A. The Run-2 ATLAS Trigger System: ATL-DAQ-
3153 PROC-2016-003[R/OL]. Geneva: CERN, 2016. <https://cds.cern.ch/record/2133909>. DOI:
3154 [10.1088/1742-6596/762/1/012003](https://doi.org/10.1088/1742-6596/762/1/012003).
- 3155 [37] PÁSZTOR G. The Upgrade of the ATLAS Electron and Photon Triggers towards LHC Run 2 and
3156 their Performance: ATL-DAQ-PROC-2015-053. arXiv:1511.00334[R/OL]. Geneva: CERN,
3157 2015. <https://cds.cern.ch/record/2063746>.
- 3158 [38] COLLABORATION A. Atlas computing: Technical design report[R/OL]. Geneva: CERN.
3159 <http://atlas-computing.web.cern.ch/atlas-computing/packages/athenaCore/athenaCore.php>.
- 3160 [39] AAD G, et al. The ATLAS Simulation Infrastructure[J/OL]. Eur. Phys. J., 2010, C70:823-874.
3161 DOI: [10.1140/epjc/s10052-010-1429-9](https://doi.org/10.1140/epjc/s10052-010-1429-9).
- 3162 [40] HOCHÉ S. Introduction to parton-shower event generators[C/OL]//Proceedings, Theoretical

Bibliography

- 3163 Advanced Study Institute in Elementary Particle Physics: Journeys Through the Precision Fron-
3164 tier: Amplitudes for Colliders (TASI 2014): Boulder, Colorado, June 2-27, 2014. 2015: 235-
3165 295. DOI: [10.1142/9789814678766_0005](https://doi.org/10.1142/9789814678766_0005).
- 3166 [41] GLEISBERG T, HöCHE S, KRAUSS F, et al. Event generation with SHERPA 1.1[J/OL]. Journal of High Energy Physics, 2009, 2009(02):007-007. <https://doi.org/10.1088%2F1126-6708%2F2009%2F02%2F007>. DOI: [10.1088/1126-6708/2009/02/007](https://doi.org/10.1088/1126-6708/2009/02/007).
- 3169 [42] BÄHR M, GIESEKE S, GIGG M A, et al. Herwig++ physics and manual[J/OL]. The European Physical Journal C, 2008, 58(4):639-707. <https://doi.org/10.1140/epjc/s10052-008-0798-9>.
- 3171 [43] NASON P. A New method for combining NLO QCD with shower Monte Carlo algorithms [J/OL]. JHEP, 2004, 11:040. DOI: [10.1088/1126-6708/2004/11/040](https://doi.org/10.1088/1126-6708/2004/11/040).
- 3173 [44] FRIXIONE S, WEBBER B R. Matching NLO QCD computations and parton shower simulations[J/OL]. Journal of High Energy Physics, 2002, 2002(06):029-029. <https://doi.org/10.1088%2F1126-6708%2F2002%2F06%2F029>. DOI: [10.1088/1126-6708/2002/06/029](https://doi.org/10.1088/1126-6708/2002/06/029).
- 3176 [45] SJOSTRAND T, MRENNA S, SKANDS P Z. A Brief Introduction to PYTHIA 8.1[J/OL]. Comput. Phys. Commun., 2008, 178:852-867. DOI: [10.1016/j.cpc.2008.01.036](https://doi.org/10.1016/j.cpc.2008.01.036).
- 3178 [46] BARBERIO E, et al. The Geant4-Based ATLAS Fast Electromagnetic Shower Simulation [C/OL]//Astroparticle, particle and space physics, detectors and medical physics applications. Proceedings, 10th Conference, ICATPP 2007, Como, Italy, October 8-12, 2007. 2008: 802-806. <http://cdsweb.cern.ch/record/1064665/files/soft-conf-2007-002.pdf>. DOI: [10.1142/9789812819093_0133](https://doi.org/10.1142/9789812819093_0133).
- 3183 [47] RICHTER-WAS E, FROIDEVAUX D, POGGIOLI L. ATLFAST 2.0 a fast simulation package for ATLAS: ATL-PHYS-98-131[R/OL]. Geneva: CERN, 1998. <https://cds.cern.ch/record/683751>.
- 3186 [48] EDMONDS K, FLEISCHMANN S, LENZ T, et al. The Fast ATLAS Track Simulation (FATRAS): ATL-SOFT-PUB-2008-001. ATL-COM-SOFT-2008-002[R/OL]. Geneva: CERN, 2008. <https://cds.cern.ch/record/1091969>.
- 3189 [49] BOYD J T, COSTA M J, TONOYAN A, et al. Commissioning of the ATLAS reconstruction software with first data[J/OL]. Journal of Physics: Conference Series, 2010, 219(3):032059. <https://doi.org/10.1088%2F1742-6596%2F219%2F3%2F032059>. DOI: [10.1088/1742-6596/219/3/032059](https://doi.org/10.1088/1742-6596/219/3/032059).
- 3193 [50] CORNELISSEN T, ELSING M, FLEISCHMANN S, et al. Concepts, Design and Implementation of the ATLAS New Tracking (NEWT): ATL-SOFT-PUB-2007-007. ATL-COM-SOFT-2007-002[R/OL]. Geneva: CERN, 2007. <https://cds.cern.ch/record/1020106>.
- 3196 [51] AAD G, et al. Muon reconstruction performance of the ATLAS detector in proton-proton collision data at $\sqrt{s}=13$ TeV[J/OL]. Eur. Phys. J., 2016, C76(5):292. DOI: [10.1140/epjc/s10052-016-4080-0](https://doi.org/10.1140/epjc/s10052-016-4080-0).

- 3198 016-4120-y.
- 3199 [52] ILLINGWORTH J, KITTNER J. A survey of the hough transform[J/OL]. Computer Vision,
3200 Graphics, and Image Processing, 1988, 44(1):87 - 116. <http://www.sciencedirect.com/science/article/pii/S0734189X88800331>. DOI: [https://doi.org/10.1016/S0734-189X\(88\)80033-1](https://doi.org/10.1016/S0734-189X(88)80033-1).
- 3201 [53] Vertex Reconstruction Performance of the ATLAS Detector at 13 TeV: ATL-PHYS-PUB-2015-
3202 026[R/OL]. Geneva: CERN, 2015. <https://cds.cern.ch/record/2037717>.
- 3203 [54] AABOUD M, et al. Reconstruction of primary vertices at the ATLAS experiment in Run 1
3204 proton-proton collisions at the LHC[J/OL]. Eur. Phys. J., 2017, C77(5):332. DOI: <10.1140/epjc/s10052-017-4887-5>.
- 3205 [55] Electron efficiency measurements with the ATLAS detector using the 2015 LHC proton-proton
3206 collision data: ATLAS-CONF-2016-024[R/OL]. Geneva: CERN, 2016. <https://cds.cern.ch/reCORD/2157687>.
- 3207 [56] LAMPL W, LAPLACE S, LELAS D, et al. Calorimeter Clustering Algorithms: Description
3208 and Performance: ATL-LARG-PUB-2008-002. ATL-COM-LARG-2008-003[R/OL]. Geneva:
3209 CERN, 2008. <https://cds.cern.ch/record/1099735>.
- 3210 [57] CORNELISSEN T G, ELSING M, GAVRILENKO I, et al. The global χ^2 track fitter in ATLAS
3211 [J/OL]. Journal of Physics: Conference Series, 2008, 119(3):032013. <https://doi.org/10.1088%2F1742-6596%2F119%2F3%2F032013>. DOI: <10.1088/1742-6596/119/3/032013>.
- 3212 [58] Electron efficiency measurements with the ATLAS detector using the 2012 LHC proton-proton
3213 collision data: ATLAS-CONF-2014-032[R/OL]. Geneva: CERN, 2014. <http://cds.cern.ch/reCORD/1706245>.
- 3214 [59] LIMPER M. Track and vertex reconstruction in the ATLAS inner detector[D/OL]. 2009. <http://cds.cern.ch/record/1202457>.
- 3215 [60] AAD G, et al. Topological cell clustering in the ATLAS calorimeters and its performance in
3216 LHC Run 1[J/OL]. Eur. Phys. J., 2017, C77:490. DOI: <10.1140/epjc/s10052-017-5004-5>.
- 3217 [61] ZHENG Z. Identification of very-low transverse momentum muons with the ATLAS experi-
3218 ment: ATL-MUON-PROC-2018-018[R/OL]. Geneva: CERN, 2018. <https://cds.cern.ch/reCORD/2649299>.
- 3219 [62] CACCIARI M, SALAM G P. Pileup subtraction using jet areas[J/OL]. Physics Letters B, 2008,
3220 659(1):119 - 126. <http://www.sciencedirect.com/science/article/pii/S0370269307011094>. DOI:
3221 <https://doi.org/10.1016/j.physletb.2007.09.077>.
- 3222 [63] CACCIARI M, SALAM G P, SOYEZ G. The anti-ktjet clustering algorithm[J/OL]. Journal of
3223 High Energy Physics, 2008, 2008(04):063-063. <https://doi.org/10.1088%2F1126-6708%2F2008%2F04%2F063>. DOI: <10.1088/1126-6708/2008/04/063>.
- 3224 [64] CACCIARI M, SALAM G P, SOYEZ G. Fastjet user manual[J/OL]. The European Physical

Bibliography

- 3233 Journal C, 2012, 72(3):1896. <https://doi.org/10.1140/epjc/s10052-012-1896-2>.
- 3234 [65] AAD G, et al. Jet energy measurement and its systematic uncertainty in proton-proton collisions
3235 at $\sqrt{s} = 7$ TeV with the ATLAS detector[J/OL]. Eur. Phys. J., 2015, C75:17. DOI: [10.1140/epjc/s10052-014-3190-y](https://doi.org/10.1140/epjc/s10052-014-3190-y).
- 3237 [66] AABOUD M, et al. Jet energy scale measurements and their systematic uncertainties in proton-
3238 proton collisions at $\sqrt{s} = 13$ TeV with the ATLAS detector[J/OL]. Phys. Rev., 2017, D96(7):
3239 072002. DOI: [10.1103/PhysRevD.96.072002](https://doi.org/10.1103/PhysRevD.96.072002).
- 3240 [67] Optimisation of the ATLAS *b*-tagging performance for the 2016 LHC Run: ATL-PHYS-PUB-
3241 2016-012[R/OL]. Geneva: CERN, 2016. <https://cds.cern.ch/record/2160731>.
- 3242 [68] PIACQUADIO G, WEISER C. A new inclusive secondary vertex algorithm for b-jet tagging
3243 in ATLAS[J/OL]. Journal of Physics: Conference Series, 2008, 119(3):032032. <https://doi.org/10.1088%2F1742-6596%2F119%2F3%2F032032>. DOI: [10.1088/1742-6596/119/3/032032](https://doi.org/10.1088/1742-6596/119/3/032032).
- 3245 [69] SPECKMAYER P, HÖCKER A, STELZER J, et al. The toolkit for multivariate data analysis,
3246 TMVA 4[J/OL]. Journal of Physics: Conference Series, 2010, 219(3):032057. <https://doi.org/10.1088%2F1742-6596%2F219%2F3%2F032057>. DOI: [10.1088/1742-6596/219/3/032057](https://doi.org/10.1088/1742-6596/219/3/032057).
- 3248 [70] Performance of missing transverse momentum reconstruction with the atlas detector using
3249 proton–proton collisions at $\sqrt{s}=13$ TeV[J/OL]. The European Physical Journal C, 2018, 78(11):903. <https://doi.org/10.1140/epjc/s10052-018-6288-9>.
- 3251 [71] COWAN G, CRANMER K, GROSS E, et al. Asymptotic formulae for likelihood-based tests
3252 of new physics[J/OL]. Eur. Phys. J. C, 2011, 71:1554. DOI: [10.1140/epjc/s10052-011-1554-0](https://doi.org/10.1140/epjc/s10052-011-1554-0).
- 3253 [72] READ A L. Presentation of search results: theCLtechnique[J/OL]. Journal of Physics G:
3254 Nuclear and Particle Physics, 2002, 28(10):2693-2704. <https://doi.org/10.1088%2F0954-3899%2F28%2F10%2F313>. DOI: [10.1088/0954-3899/28/10/313](https://doi.org/10.1088/0954-3899/28/10/313).
- 3256 [73] LEE B W, QUIGG C, THACKER H B. The Strength of Weak Interactions at Very High-
3257 Energies and the Higgs Boson Mass[J/OL]. Phys. Rev. Lett., 1977, 38:883-885. DOI: [10.1103/PhysRevLett.38.883](https://doi.org/10.1103/PhysRevLett.38.883).
- 3259 [74] CHANOWITZ M S, GAILLARD M K. The TeV Physics of Strongly Interacting W's and Z's
3260 [J/OL]. Nucl. Phys., 1985, B261:379-431. DOI: [10.1016/0550-3213\(85\)90580-2](https://doi.org/10.1016/0550-3213(85)90580-2).
- 3261 [75] SZLEPER M. The Higgs boson and the physics of WW scattering before and after Higgs
3262 discovery[J]. 2014.
- 3263 [76] Evidence for electroweak production of $W^\pm W^\pm jj$ in pp collisions at $\sqrt{s} = 8$ TeV with the
3264 atlas detector[J/OL]. Phys. Rev. Lett., 2014, 113:141803. <https://link.aps.org/doi/10.1103/PhysRevLett.113.141803>.
- 3266 [77] Observation of electroweak production of a same-sign w boson pair in association with two jets
3267 in pp collisions at $\sqrt{s} = 13$ TeV with the atlas detector[J/OL]. Phys. Rev. Lett., 2019, 123:

Bibliography

- 3268 161801. <https://link.aps.org/doi/10.1103/PhysRevLett.123.161801>.
- 3269 [78] SIRUNYAN A M, et al. Observation of electroweak production of same-sign W boson pairs
3270 in the two jet and two same-sign lepton final state in proton-proton collisions at $\sqrt{s} = 13$ TeV
3271 [J/OL]. Phys. Rev. Lett., 2018, 120(8):081801. DOI: [10.1103/PhysRevLett.120.081801](https://doi.org/10.1103/PhysRevLett.120.081801).
- 3272 [79] Observation of electroweak $w\pm z$ boson pair production in association with two jets in pp col-
3273 lisions at $s=13$ tev with the atlas detector[J/OL]. Physics Letters B, 2019, 793:469 - 492.
3274 <http://www.sciencedirect.com/science/article/pii/S0370269319303211>. DOI: <https://doi.org/10.1016/j.physletb.2019.05.012>.
- 3276 [80] Measurement of vector boson scattering and constraints on anomalous quartic couplings from
3277 events with four leptons and two jets in proton–proton collisions at $s=13$ tev[J/OL]. Physics
3278 Letters B, 2017, 774:682 - 705. <http://www.sciencedirect.com/science/article/pii/S0370269317308328>. DOI: <https://doi.org/10.1016/j.physletb.2017.10.020>.
- 3280 [81] ALWALL J, FREDERIX R, FRIXIONE S, et al. The automated computation of tree-level and
3281 next-to-leading order differential cross sections, and their matching to parton shower simula-
3282 tions[J/OL]. JHEP, 2014, 07:079. DOI: [10.1007/JHEP07\(2014\)079](https://doi.org/10.1007/JHEP07(2014)079).
- 3283 [82] BALL R D, et al. Parton distributions with LHC data[J/OL]. Nucl. Phys. B, 2013, 867:244-289.
3284 DOI: [10.1016/j.nuclphysb.2012.10.003](https://doi.org/10.1016/j.nuclphysb.2012.10.003).
- 3285 [83] GLEISBERG T, HÖCHE S, KRAUSS F, et al. Event generation with SHERPA 1.1[J/OL].
3286 JHEP, 2009, 02:007. DOI: [10.1088/1126-6708/2009/02/007](https://doi.org/10.1088/1126-6708/2009/02/007).
- 3287 [84] BALL R D, et al. Parton distributions for the LHC run II[J/OL]. JHEP, 2015, 04:040. DOI:
3288 [10.1007/JHEP04\(2015\)040](https://doi.org/10.1007/JHEP04(2015)040).
- 3289 [85] CAOLA F, MELNIKOV K, RÖNTSCH R, et al. Qcd corrections to zz production in gluon
3290 fusion at the lhc[J/OL]. Phys. Rev. D, 2015, 92:094028. <https://link.aps.org/doi/10.1103/PhysRevD.92.094028>.
- 3292 [86] FRIXIONE S, RIDOLFI G, NASON P. A positive-weight next-to-leading-order Monte Carlo
3293 for heavy flavour hadroproduction[J/OL]. JHEP, 2007, 09:126. DOI: [10.1088/1126-6708/2007/09/126](https://doi.org/10.1088/1126-6708/2007/09/126).
- 3295 [87] LAI H L, et al. New parton distributions for collider physics[J/OL]. Phys. Rev. D, 2010, 82:
3296 074024. DOI: [10.1103/PhysRevD.82.074024](https://doi.org/10.1103/PhysRevD.82.074024).
- 3297 [88] ALIOLI S, NASON P, OLEARI C, et al. NLO single-top production matched with shower in
3298 POWHEG: s- and t-channel contributions[J/OL]. JHEP, 2009, 09:111. DOI: [10.1088/1126-6708/2009/09/111](https://doi.org/10.1088/1126-6708/2009/09/111).
- 3300 [89] FREDERIX R, RE E, TORRIELLI P. Single-top t-channel hadroproduction in the four-flavour
3301 scheme with POWHEG and aMC@NLO[J/OL]. JHEP, 2012, 09:130. DOI: [10.1007/JHEP09\(2012\)130](https://doi.org/10.1007/JHEP09(2012)130).

Bibliography

- 3303 [90] RE E. Single-top Wt-channel production matched with parton showers using the POWHEG
3304 method[J/OL]. Eur. Phys. J. C, 2011, 71:1547. DOI: [10.1140/epjc/s10052-011-1547-z](https://doi.org/10.1140/epjc/s10052-011-1547-z).
- 3305 [91] COLLABORATION A. ATLAS Pythia 8 tunes to 7 TeV data[M/OL]. 2014. <https://cds.cern.ch/record/1966419>.
- 3307 [92] ATLAS Collaboration. Performance of pile-up mitigation techniques for jets in pp collisions at
3308 $\sqrt{s} = 8$ TeV using the ATLAS detector[J/OL]. Eur. Phys. J. C, 2016, 76:581. DOI: [10.1140/epjc/s10052-016-4395-z](https://doi.org/10.1140/epjc/s10052-016-4395-z).
- 3310 [93] BELLM J, et al. Herwig 7.0/Herwig++ 3.0 release note[J/OL]. Eur. Phys. J. C, 2016, 76(4):
3311 196. DOI: [10.1140/epjc/s10052-016-4018-8](https://doi.org/10.1140/epjc/s10052-016-4018-8).
- 3312 [94] BAHR M, et al. Herwig++ Physics and Manual[J/OL]. Eur. Phys. J. C, 2008, 58:639-707. DOI:
3313 [10.1140/epjc/s10052-008-0798-9](https://doi.org/10.1140/epjc/s10052-008-0798-9).
- 3314 [95] Luminosity determination in pp collisions at $\sqrt{s} = 13$ TeV using the ATLAS detector at the
3315 LHC: ATLAS-CONF-2019-021[R/OL]. Geneva: CERN, 2019. [http://cds.cern.ch/record/2677054](https://cds.cern.ch/record/2677054).
- 3317 [96] The new LUCID-2 detector for luminosity measurement and monitoring in ATLAS[J/OL]. Journal
3318 of Instrumentation, 2018, 13(07):P07017-P07017. <https://doi.org/10.1088/1748-0221/2f13%2f07%2fp07017>. DOI: [10.1088/1748-0221/13/07/p07017](https://doi.org/10.1088/1748-0221/13/07/p07017).
- 3320 [97] COADOU Y. Boosted decision trees and applications[J/OL]. EPJ Web of Conferences, 2013,
3321 55:02004-. DOI: [10.1051/epjconf/20135502004](https://doi.org/10.1051/epjconf/20135502004).
- 3322 [98] COLLABORATION A. Technical Design Report for the ATLAS Inner Tracker Pixel Detector:
3323 CERN-LHCC-2017-021. ATLAS-TDR-030[R/OL]. Geneva: CERN, 2017. <https://cds.cern.ch/record/2285585>.
- 3325 [99] COLLABORATION A. Technical Design Report for the Phase-II Upgrade of the ATLAS Muon
3326 Spectrometer: CERN-LHCC-2017-017. ATLAS-TDR-026[R/OL]. Geneva: CERN, 2017. <https://cds.cern.ch/record/2285580>.
- 3328 [100] COLLABORATION A. Technical Proposal: A High-Granularity Timing Detector for the AT-
3329 LAS Phase-II Upgrade: CERN-LHCC-2018-023. LHCC-P-012[R/OL]. Geneva: CERN, 2018.
3330 <https://cds.cern.ch/record/2623663>.
- 3331 [101] Expected performance for an upgraded ATLAS detector at High-Luminosity LHC: ATL-PHYS-
3332 PUB-2016-026[R/OL]. Geneva: CERN, 2016. <https://cds.cern.ch/record/2223839>.
- 3333 [102] HILL A, VAN DER BIJ J J. Strongly interacting singlet-doublet higgs model[J/OL]. Phys. Rev.
3334 D, 1987, 36:3463-3473. <https://link.aps.org/doi/10.1103/PhysRevD.36.3463>.
- 3335 [103] DAVOUDIASL H, HEWETT J, RIZZO T. Bulk gauge fields in the randall–sundrum
3336 model1work supported by the department of energy, contract de-ac03-76sf00515.1[J/OL].
3337 Physics Letters B, 2000, 473(1):43 - 49. <http://www.sciencedirect.com/science/article/pii/S037>

Bibliography

- 3338 [0269399014306](https://doi.org/10.1016/S0370-2693(99)01430-6). DOI: [https://doi.org/10.1016/S0370-2693\(99\)01430-6](https://doi.org/10.1016/S0370-2693(99)01430-6).
- 3339 [104] FREDERIX R, FRIXIONE S. Merging meets matching in MC@NLO[J/OL]. JHEP, 2012, 12:
3340 061. DOI: [10.1007/JHEP12\(2012\)061](https://doi.org/10.1007/JHEP12(2012)061).
- 3341 [105] AGASHE K, DAVOUDIASL H, PEREZ G, et al. Warped Gravitons at the LHC and Beyond
3342 [J/OL]. Phys.Rev., 2007, D76:036006. DOI: [10.1103/PhysRevD.76.036006](https://doi.org/10.1103/PhysRevD.76.036006).
- 3343 [106] ATLAS Collaboration. Jet reconstruction and performance using particle flow with the ATLAS
3344 Detector[J/OL]. Eur. Phys. J. C, 2017, 77:466. DOI: [10.1140/epjc/s10052-017-5031-2](https://doi.org/10.1140/epjc/s10052-017-5031-2).
- 3345 [107] Measurements of higgs boson production and couplings in the four-lepton channel in pp col-
3346 lisions at center-of-mass energies of 7 and 8 tev with the atlas detector[J/OL]. Phys. Rev. D,
3347 2015, 91:012006. <https://link.aps.org/doi/10.1103/PhysRevD.91.012006>.
- 3348 [108] CRANMER K S. Kernel estimation in high-energy physics[J/OL]. Comput. Phys. Commun.,
3349 2001, 136:198-207. DOI: [10.1016/S0010-4655\(00\)00243-5](https://doi.org/10.1016/S0010-4655(00)00243-5).
- 3350 [109] OREGLIA M. A Study of the Reactions $\psi' \rightarrow \gamma\gamma\psi$ [M/OL]. SLAC, 1980. <https://www.slac.stanford.edu/cgi-wrap/getdoc/slac-r-236.pdf>.
- 3351 [110] GAISER J. Charmonium Spectroscopy From Radiative Decays of the J/ψ and ψ' [M/OL].
3353 SLAC, 1982. <https://www.slac.stanford.edu/cgi-wrap/getdoc/slac-r-255.pdf>.
- 3354 [111] GORIA S, PASSARINO G, ROSCO D. The Higgs Boson Lineshape[J/OL]. Nucl.Phys., 2012,
3355 B864:530-579. DOI: [10.1016/j.nuclphysb.2012.07.006](https://doi.org/10.1016/j.nuclphysb.2012.07.006).
- 3356 [112] SPIRA M, DJOUADI A, GRAUDENZ D, et al. Higgs boson production at the LHC[J]. Nucl.
3357 Phys., 1995, B 453:17-82.
- 3358 [113] BALL R D, et al. Parton Distribution Benchmarking with LHC Data[J/OL]. JHEP, 2013, 04:
3359 125. DOI: [10.1007/JHEP04\(2013\)125](https://doi.org/10.1007/JHEP04(2013)125).
- 3360 [114] BIJNENS J, EEROLA P, MAUL M, et al. Qcd signatures of narrow graviton resonances in
3361 hadron colliders[J/OL]. Physics Letters B, 2001, 503(3-4):341-348. DOI: [10.1016/s0370-2693\(01\)00238-6](https://doi.org/10.1016/s0370-2693(01)00238-6).
- 3363 [115] ATLAS Collaboration. PMG Systematic Uncertainty Recipes[EB/OL]. <https://twiki.cern.ch/twiki/bin/view/AtlasProtected/PmgSystematicUncertaintyRecipes>.
- 3364 [116] READ A L. Presentation of search results: The CL(s) technique[J]. J. Phys. G, 2002, 28:
3366 2693-2704.
- 3367 [117] AABOUD M, et al. Search for heavy ZZ resonances in the $\ell^+\ell^-\ell^+\ell^-$ and $\ell^+\ell^-v\bar{v}$ final states
3368 using proton–proton collisions at $\sqrt{s} = 13$ TeV with the ATLAS detector[J/OL]. Eur. Phys. J.
3369 C, 2018, 78(4):293. DOI: [10.1140/epjc/s10052-018-5686-3](https://doi.org/10.1140/epjc/s10052-018-5686-3).